SEISMIC ANALYSIS OF CONCRETE GRAVITY DAMS

A THESIS SUBMITTED TO
THE GRADUATE SCHOOL OF NATURAL AND APPLIED SCIENCES
OF
MIDDLE EAST TECHNICAL UNIVERSITY

BY

UĞUR AKPINAR

IN PARTIAL FULFILLMENT OF THE REQUIREMENTS
FOR
THE DEGREE OF DOCTOR OF PHILOSOPHY
IN
CIVIL ENGINEERING

SEPTEMBER 2019

Approval of the thesis:

SEISMIC ANALYSIS OF CONCRETE GRAVITY DAMS

submitted by **UĞUR AKPINAR** in partial fulfillment of the requirements for the degree of **Doctor of Philosophy in Civil Engineering Department, Middle East Technical University** by,

Prof. Dr. Halil Kalıpçılar
Dean, Graduate School of **Natural and Applied Sciences**   _____

Prof. Dr. Ahmet Türer
Head of Department, **Civil Engineering**   _____

Prof. Dr. Barış Binici
Supervisor, **Civil Engineering, METU**   _____

Examining Committee Members:

Prof. Dr. Ahmet Yakut
Civil Engineering Dept., METU   _____

Prof. Dr. Barış Binici
Civil Engineering, METU   _____

Assoc. Prof. Dr. Mustafa Tolga Yılmaz
Engineering Sciences Dept., METU   _____

Assoc. Prof. Dr. Alper Aldemir
Civil Engineering Dept., Hacettepe Uni.   _____

Assist. Prof. Dr. Burcu Güldür Erkal
Civil Engineering Dept., Hacettepe Uni.   _____

Date: 06.09.2019

I hereby declare that all information in this document has been obtained and presented in accordance with academic rules and ethical conduct. I also declare that, as required by these rules and conduct, I have fully cited and referenced all material and results that are not original to this work.

Name, Surname: Uğur Akpınar

Signature:

ABSTRACT

SEISMIC ANALYSIS OF CONCRETE GRAVITY DAMS

Akpınar, Uğur
Doctor of Philosophy, Civil Engineering
Supervisor: Prof. Dr. Barış Binici

September 2019, 148 pages

After the industrial revolution, energy has become one of the important issues determining the internal and external policies of the countries. Nowadays, to meet the energy needs of future generations and to reduce the damage to the environment, renewable energy sources are utilized. At this point, hydroelectric energy offers a clean and renewable energy source alternative. In addition to many built dams, the necessity of controlling existing dam stock punctuates the importance of studies on the seismic design and safety of concrete dams. In this study, the linear and nonlinear responses of concrete dams are evaluated and new simplified methods are proposed for the design and evaluation of the concrete dams. In the first part, linear response of concrete dams is examined. For this purpose, dynamic analyzes of a group of selected concrete dam sections were conducted. Analyses were carried out separately for the frequency domain where the dam-foundation-reservoir interactions can be accurately calculated and for the time domain where they can be calculated with approximate methods. By employing the results of the frequency domain solution, the tensile stresses in the heel, which is an important parameter in the design, were related to a number of engineering demand parameters. Additionally, effective damping ratios were obtained by comparing frequency and time domain solutions and a new damping ratio equation for time domain analysis was proposed. In the second part, nonlinear response of concrete dams is examined. The coupled solution of concrete nonlinearity

and the dam-foundation-reservoir interaction is still a challenge for the current practices. For this purpose, a simplified static analysis method is proposed which can estimate the nonlinear damage of concrete dams including dam-reservoir interaction. In the method, the capacity curve was obtained by pushover analysis (including inertia and hydrodynamic effects) compatible with the first mode behavior. Such nonlinear problem can be a challenge to solve by the existing tools. For this purpose, the Sequential Linear Analysis (SLA) method was adopted to obtain the capacity curve. In order to verify the simplified static analysis method, nonlinear time domain analyzes were performed with selected sections and earthquake records. The damage was estimated by both techniques and compared to evaluate the performance of the simplified solution. Finally, the performance levels for concrete dams were estimated by using the results of nonlinear time domain analysis and deterministic sensitivity analysis. The resulting fragility curves and performance levels will be important tools to assist engineers in designing and evaluating concrete dams.

ÖZ

BETON AĞIRLIK BARAJLARIN SİSMİK ANALİZİ

Akpınar, Uğur
Doktora, İnşaat Mühendisliği
Tez Danışmanı: Prof. Dr. Barış Binici

Eylül 2019, 148 sayfa

Sanayi devrimi sonrasında enerji, ülkelerin iç ve dış politikalarını belirleyen önemli parametrelerden biri haline gelmiştir. Gelecek nesillerin enerji ihtiyacını karşılamak ve çevreye verilen zararı en aza indirgeyebilmek için yenilenebilir enerji kaynaklarına yönelim ise giderek artmaktadır. Bu noktada, hidroelektrik enerji temiz ve yenilenebilir bir enerji kaynağı olarak önemli bir cazibe sunmaktadır. İnşa edilen birçok barajın yanında, mevcut baraj stoklarının kontrol edilmesi gerekliliği ise beton barajların sismik tasarım ve güvenliğine ilişkin çalışmaların önemini bir kez daha gözler önüne sermektedir. Bu çalışmada beton barajlar için kullanılan doğrusal ve doğrusal olmayan davranışları değerlendirilmiş, beton barajların tasarım ve performanslarının belirlenmesine yönelik basitleştirilmiş yöntemler geliştirilmiştir. İlk bölümde, beton barajların doğrusal davranışı irdelenmiştir. Bu amaçla seçilen beton baraj kesitlerinin dinamik analizleri yapılmıştır. Analizler, yapı-zemin-rezervuar etkilerinin doğru bir şekilde hesaplanabildiği frekans alanı ile rezervuar ve zeminin yaklaşık yöntemlerle hesaplanabildiği zaman alanı için ayrı ayrı yapılmıştır. Tasarımda önemli bir parametre olan topuktaki çekme gerilmeleri, frekans alanı çözümü yardımı ile farklı kesit, malzeme ve deprem durumları ile ilişkilendirilmiştir. Buna ek olarak, frekans ve zaman alanı çözümlerinin karşılaştırılması ile efektif sönüm oranları elde edilmiş, bu oranlar kullanılarak zaman tanım alanı analizlerine yönelik yeni bir sönüm oranı denklemi geliştirilmiştir. Çalışmanın ikinci bölümünde,

beton barajların doğrusal olmayan davranışları irdelenmiştir. Literatürde betonun doğrusal olmayan davranışı ile yapı-zemin-rezervuar etkisinin dâhil edilebildiği kabul edilebilir yöntemler bulunmamaktadır. Bu amaçla beton barajların doğrusal olmayan çatlama davranışını baraj-rezervuar etkileşimini de dâhil ederek hesaplayabilen basitleştirilmiş statik analiz yöntemi geliştirilmiştir. Birinci mod davranışı ile uyumlu yatay yük (atalet ve hidrodinamik etkiler dâhil edilerek) profili ile yapılan itme analizi sonucunda kapasite eğrisi elde edilmektedir. Kırılgan yapıdaki beton barajın itme analizi mevcut yöntemlerle çözümü zor bir problemdir. Bu amaçla yapının kapasite eğrisi için Ardışık Lineer Analiz (ALA) yöntemi kullanılmıştır. Basitleştirilmiş statik analiz yöntemin doğrulanabilmesi için seçil kesitler ve deprem kayıtları ile doğrusal olmayan zaman tanım analizleri yapılmıştır. Her iki yöntem ile belirlenen hasar durumları karşılattırılmış önerilen yöntemin yeterliliği değerlendirilmiştir. Son olarak doğrusal olmayan zaman tanım alanı analizi sonuçları kullanılarak beton barajlar için performans seviyeleri belirlenmiş ve deterministik duyarlılık analizi yapılmıştır. Çalışma sonucunda elde edilen kırılganlık eğrileri ve performans seviyeleri, beton barajların tasarım ve değerlendirilmelerinde mühendislere yardımcı olacak önemli araçlar olacaklardır.

Anahtar Kelimeler: Beton ağırlık barajı, Doğrusal olmayan analiz, Ardışık lineer analiz, Sönüm oranı, Çatlak davranışı

To My Family

ACKNOWLEDGEMENTS

TABLE OF CONTENTS

LIST OF TABLES

TABLES

LIST OF FIGURES

FIGURES

xviii

LIST OF ABBREVIATIONS

ABBREVIATIONS

ASI	Acceleration spectrum intensity
CRCM	Coaxial rotating crack model
CM F/356	Fema-356 Coefficient method
CM F/440	Fema-440 Coefficient method
CSM A/40	ATC-40 Capacity spectrum method
CSM F/440	Fema-440 Capacity spectrum method
DSF	Damping scaling factor
EM	Exact model
ER	Empty reservoir
FCM-VSRF	Fixed crack model with variable shear
FR	Full reservoir
FS	Factor of safety
HI	Housner intensity
IFMFM	Incompressible fluid massless foundation model
OBE	Operating basis earthquake
MDOF	Multi degree of freedom
PER	Post-earthquake ratio
PGA	Peak ground acceleration
PGV	Peak ground velocity
POD	The probability of damage
SDOF	Single degree of freedom
SEE	Safety evaluation earthquake
SLA	Sequentially linear analysis
THA	Time history analysis

LIST OF SYMBOLS

SYMBOLS

A	Response spectrum
A'	Target spectrum
a_x	The horizontal frequency response acceleration
B_0	Hydrodynamic parameter for the dam-reservoir interaction
B_1	Hydrodynamic parameter for the bottom wave absorption
C	The velocity of sound in water
C_1	Generalized damping with ER
$\tilde{C}_1$	Generalized damping with FR
C_i	Coefficients of the base stress distribution estimations
C_k	Coefficients of the coefficient method
C_n	Coefficients of the crack length estimation
d	Distance to the epicenter
D	The effective damping ratio
d_c	Closest distance
d_h	Hypocentral distance
d_{crest}	The crest displacement
d_{max}	The maximum crest displacement
E_c	Modulus of elasticity of the concrete
E_f	Modulus of elasticity of the foundation
E_n	Degraded modulus of elasticity at local direction n
E_t	Degraded modulus of elasticity at local direction t
E_0	Initial modulus of elasticity
E_{min}	Minimum of E_n and E_t
f_c	Compression strength
f_h	Hydrodynamic force distribution

f_i	Inertia force distribution
f_t	Tensile strength
F_1	First mode frequency
F_{st}	Hydrostatic load
G	Shear modulus
G_f	Fracture energy
H	Dam height
H_r	Reservoir height
i	Unit imaginary number
k_{ii}	Stiffness sub matrices
L_1	Generalized inertia force with ER
$\tilde{L}_1$	Generalized inertia force with FR
L_b	Dam base length
L_c	Equivalent crack length
$\tilde{m}$	The total mass of the dam per unit height
m_b	Mass sub matrix for foundation
m_d	Mass sub matrix for dam
M_1	Generalized mass with ER
$\tilde{M}_1$	Generalized mass with FR
M_L	Local magnitude
M_w	Moment magnitude
N_d	The number of structural mode shapes
p	Hydrodynamic pressure
$\bar{p}_0$	Rigid part of the hydrodynamic pressure function
$\bar{p}_i$	Flexible part of the hydrodynamic pressure function
PF_1	Modal participation factor for the fundamental mode
q	The damping coefficient for the bottom absorption
$\bar{q}$	Relative displacements at the reservoir bottom
$\bar{Q}_h$	Hydrodynamic forces at the reservoir bottom

$\bar{r}$	Relative displacements for nodes above the base
R	Reservoir condition
R^2	The coefficient of the determination
$\bar{r}_b$	Relative displacements for nodes at the base
$\overline{R}_b$	Forces on the bottom of dam at the dam-foundation intersection
R_f	Effect of flexible foundation for damping
$\bar{r}_f$	Relative displacements for nodes on the surface of the foundation
$\overline{R}_f$	Forces on the surface of the foundation
$\overline{R}_h$	Hydrodynamic forces at the upstream face
R_r	Effect of the reservoir for damping
S	Dam downstream slope
S_a	Spectral acceleration
S_{a1}	Fundamental mode spectral acceleration
S_d	Spectral displacement
$\underline{S}_f$	Condensed dynamic stiffness matrix of the foundation
SF_i	Scale factor
s_i	Shear reduction techniques
$\underline{S}_{ii}$	Sub matrices in the foundation rock substructure
T	The fundamental period of the dam (ER/FR)
T_1	The fundamental period of the dam with ER
$\tilde{T}_1$	The fundamental period of the dam with FR
t_s	Section thickness
$\bar{u}$	The horizontal displacement response
$\ddot{u}$	The horizontal acceleration response
V	Base shear
w	Excitation frequency
W	Total weight of the dam
w_0	Natural frequency of the full reservoir

w_1	Frequency of the dam on rigid foundation with ER
$\widetilde{w}_1$	Frequency of the dam on rigid foundation with FR
x_b	Distance measured from the upstream toe of the dam base
$\bar{Z}_i$	The complex valued frequency response function
1	Directional unit vector
α	Wave reflection coefficient
α_1	Modal mass coefficient for the first fundamental mode
β	Shear retention factor
β_t	Target damping ratio
ε_{cr}	Cracking strain
ε_{ii}	Local strains in perpendicular directions
ζ	Total damping ratio
ζ_1	Structural damping
ζ_f	Damping due to the dam-foundation interaction
ζ_r	Damping due to the reservoir-dam interaction
η	Ratio between the softened and initial elastic modulus
η_s	Constant hysteretic damping for the dam concrete
λ	Stress coefficient
λ_{crc}	Critical stress coefficient
λ_{min}	Minimum stress coefficient
λ_{max}	Maximum stress coefficient
λ_n	Eigenvalues for reservoir mode n
μ	The mean of the natural logarithm of a parameter
v	Poisson's ratio
ξ	Critical damping ratio
ξ_1	Damping ratio with ER
$\widetilde{\xi}_1$	Damping ratio with FR and bottom absorption
ρ_c	The density of the concrete
ρ_r	The density of the reservoir water

σ	Standard deviation of the natural logarithm of a parameter
$\sigma_{1,2}$	Principal stresses
σ_A	Stress due to Load A
σ_B	Stress due to Load B
$\bar{\sigma}_{base}^u$	Principal tensile stress vector at the dam base
σ_{max}	Envelope of the principle tensile stress demand
σ_{max}^u	Maximum principal tensile stress at the upstream toe
σ_{ii}	Local stresses in perpendicular directions
σ_{kk}	Global stresses in perpendicular directions
ϕ	Normal distribution function
ϕ_1	Horizontal component of fundamental mode shape

CHAPTER 1

INTRODUCTION

1.1. General

By the increase in energy demand in developing countries, the efficient ways of harvesting energy have gained great importance. Among the renewable resources, hydroelectric power is considered as an economical and fast utilizable energy source alternative. In this context, dams can be pointed as the most important structures for hydroelectric power generation. The potential of hydropower was utilized efficiently by the end of 1980s in most of the developed nations. However, dams are still under construction in countries with emerging economies such as Turkey and China. To meet the growing energy needs of Turkey, there have been significant investments made in recent years. With increasing interest of dam construction and operation in the private sector, dam design and build has become an important field of study in the local construction industry. For example, the number of dams constructed in Turkey since 1930's up to 2006 is about 600 whereas about 200 new dams are under planning, design or construction stage. However, along with the earthquake risk, this rapid advancement demand in the sector may lead to expensive or unsafe dam designs. In addition to that, the dams built before the current knowledge and experience are in need of seismic safety assessment.

For the case of concrete gravity dams, the stability factors are considered as the preliminary safety requirements that should be satisfied. The stability method simply checks the rigid block stability model of dams for sliding and overturning. As well as the gravity and hydrostatic forces, the earthquake effects included in a simplified manner as lateral forces. However, in order to have a detailed stress response of the concrete gravity dams, the guidelines commonly recommend conducting time history

analysis. For comprehensive dam analysis, accurately modeling of two interactions namely, dam-foundation and dam-reservoir interactions, concrete crack opening, and water penetration can be significant. Many approaches exist from the point of numerical analysis methods that deal with the problem in different degrees of complication. If the foundation properties along with the expected strong motions are to be considered, dynamic analyses are conducted in seismic design of new concrete dams and the evaluation of existing concrete dams. However, significant simulation time, convergence difficulties in brittle nonlinear problems, unrealistic performance estimations and ground motion uncertainties (Akpinar et al., 2014) usually demand the search for new solution techniques with the idea that if we will err we should do so in a simple way.

For the dams undergoing inelastic deformations, the accurate modeling of the damage becomes an important issue and requires reliable nonlinear analysis tools. Determination of tension softening behavior of plain concrete after cracking is still a challenge for computational analysis techniques. Particularly, the nonlinear analysis solutions have difficulties to converge due to the negative slopes arise in the cracked zones. At that point, sequentially linear analysis (SLA) was introduced as an alternative method to provide nonlinear solution without the need of displacement or load control (DeJong et al., 2008). The method gives a chance to analyze brittle structures (such as concrete dams). As it is seen, it is necessary to use mathematically different approaches together in order to determine seismic performance of concrete dams in a reliable way. In this context, simplified methods (SDOF models) stand out as an important tool for seismic preliminary evaluation. These methods can predict the failure mechanism of a concrete dam along with the capacity to resist the earthquake demand. In addition to that, the demand can be estimated by using the site-specific spectrum so the ground motion record dependency could be neglected. Such static nonlinear analysis techniques can be applied along with the initial hydrostatic and gravity loads as well as with the lateral hydrodynamic and inertia loads for concrete dams as an alternative not explored in detail.

Past research has been seeking answers to the question of whether the dam will remain safe after a certain earthquake event. While it is possible to design dams to sustain repairable damages after a seismic event, it is also possible that they may cause catastrophic damage depending on their characteristic properties and environmental conditions. In fact, it is reasonable to classify and select the target damage level of dams more qualitatively. In order to classify the damage, identification of cracks in the dam body may be considered as an appropriate parameter for concrete dams. Then, the probability of exceeding a specified damage states can be described as function of dam characteristics and seismic intensity parameters.

1.2. Objectives and Scope

The objective of this thesis is to evaluate seismic behavior of the concrete gravity dams within the framework of linear and nonlinear analysis techniques. Both approaches will have different objectives on their own with different challenges. Within this perspective, the thesis aims achieve the following objectives:

- Estimating the earthquake induced dam stresses for typical dam sections with various heights and material properties.
- Proposing prediction equations to estimate the maximum principal tensile stress demand and their distribution along the dam base.
- Evaluating the stress errors upon using massless foundation models with added mass approach along with the apparent damping.
- Proposing a new equation for the effective damping for use in response history analysis in the time domain for accurate stress estimations.
- Proposing a reliable and effective nonlinear analysis technique to obtain the capacity curves of concrete gravity dams.
- Developing a method by which the dam-reservoir interaction can be approximately included in the nonlinear static analysis of the concrete dams.
- Proposing an effective damage estimation and comparison technique for the highly scattered cracking schemes.

3

- Evaluating the performance of SDOF approximation on estimating seismic deformations and damage.

- Proposing an equation to estimate the crack distribution on dam body.

- Proposing performance levels for the assessment of the seismic response of the concrete dams.

- Measuring the seismic performance by establishing fragility curves and seismic parameters.

The scope of the thesis is to understand the seismic behavior of the concrete dams within the perspective of the specified objectives. At each stage of the study, existing methods were critically reviewed and methods were developed to improve the current engineering practice. The completion of the thesis focuses on obtaining solid findings about the main scopes of the subject and providing simplified methods that can be used in specifications and guidelines of concrete gravity dams.

1.3. Thesis Approach

In this section, the contents of the thesis are presented in detail and the reader is guided about what information can be found in which chapter. The thesis consists of five main chapters and the content of each chapter is explained below.

Chapter 1 is the introduction part of the thesis. This section begins by presenting a general perspective on the developments in the world and practices in literature on the subject of the thesis. The chapter defines the scope and objectives of the research and includes the research approach written as a guide.

Chapter 2 reveals the seismic behavior of the concrete gravity dams including foundation and reservoir effects. The chapter begins with the summary of the background theory and the objectives of the chapter. In the following sections, the followed linear procedures are explained along with the earthquake induced stresses and damping ratios. The section covers detailed information about the results and provides some simplified equations for the use of concrete dams. Chapter ends with summary of the conclusions of the part.

Chapter 3 investigates the deformation and the damage behavior of the concrete gravity dams under seismic excitations. The chapter begins with the summary of the background theory, objectives and the simplified procedure with SLA method. The following parts include the verification of the methods, ground motion scaling, and explanation of nonlinear static procedures. Chapter ends with detailed presentation of the main findings and summary of the conclusions of the part.

Chapter 4 is the section that presents the proposed methodology for the seismic damage assessment of the concrete gravity dams. The chapter begins with the summary of the background theory and the objectives of the chapter. Then the recommended performance levels and assessment techniques are explained for the concrete gravity dams. The following sections provide deterministic sensitivity analysis to determine the performance levels associated with the dam type and seismic level. Chapter ends with the summary of the conclusions of the part.

Chapter 5 provides a general perspective of the whole thesis with concrete explanations. It summarizes the main results of the thesis and provides recommendations for the future researches as well as further developments of the research itself.

CHAPTER 2

EARTHQUAKE STRESSES AND EFFECTIVE DAMPING

2.1. Background

Researchers have done important work in this area to understand the seismic behavior of concrete gravity dams including foundation and reservoir effects. The pioneering work of Westergaard (1933) provided means of estimating hydrodynamic pressure on rigid dams during earthquakes. The next milestone on the topic was calculation of earthquake response of rigid dams considering the compressibility effect of the water by Chopra (1966). Afterwards, studies focused on numerical investigation of dam-reservoir and dam-foundation interactions making use of the finite element method. The works of Fenves and Chopra (1984-1986) on a combined numerical-analytical technique provided means of accurate stress estimations. Their technique rigorously handled the radiation damping due to infinite reservoir and half-space foundation flexibility with a substructure approach in the frequency domain. Lotfi et al. (1987), on the other hand, considered the foundation and reservoir with consistent transmitting hyper-elements. The hyper-element technique presented by Lotfi et al. (1987) and the boundary element approach of Medina et al. (1990) included water-sediment interaction, where both studies employed the work of Fenves and Chopra (1984) as benchmark. Bougacha et al. (1993) did further work on the effect of sediments by considering the sediments as a porous medium for a better understanding of their importance in the seismic response.

All of the above studies were conducted in the frequency domain thereby permitting the evaluation of the dynamic response of dam sections by incorporating two important effects: 1) waves carrying energy from the foundation in the proximity of the dam to infinity appearing as an effective damping, 2) the compressibility of the

water and ensuring that wave reflections at boundaries are eliminated at infinite reservoir boundaries.

Nowadays, the need of estimating the potential risks and expected loss under earthquakes has shifted the engineers to conduct nonlinear analysis of structures including dams. A number of studies were conducted to investigate concrete cracking and estimate dam stability (e.g., Bhattacharjee and Leger, 1995, Mclean et al., 2006, Arici and Binici, 2011, Soysal et al., 2016). In nonlinear analysis, practicing engineers still use the massless foundation and added mass hydrodynamic models to simulate the dam-reservoir-foundation interaction due to their advantages such as allowing the use of existing software and providing computational efficiency while analyzing many alternative sections with many load cases (e.g., Javanmardi et al., 2005, Lotfi and Arabshahi, 2008). The most important prerequisite of such analyses is the selection of the effective damping, for which the seismic response and stresses can be estimated close to those obtained by using rigorous frequency domain approaches.

2.2. Objectives

The objective of this chapter is two folded: first, earthquake induced dam stresses are examined for typical dam sections with various heights and material properties by using the combined analytical-numerical technique of Fenves and Chopra (1984). Afterwards, prediction equations are developed to estimate the maximum principal tensile stress demand and their distribution along the dam base. The proposed equations can be employed in the preliminary design or seismic assessment of gravity dams. Secondly, the stress errors upon using massless foundation models with added mass approach along with the apparent damping as proposed by Fenves and Chopra (1986) are critically evaluated. A new equation for the effective damping is proposed for use in response history analysis in the time domain for accurate stress estimations. The outcomes of this study are believed to help practicing engineers in realizing and considering the importance of dam-foundation-reservoir interactions.

2.3. Earthquake Dam Stresses

2.3.1. Analysis Procedure and Cases

The literature review briefed above revealed that procedure of Fenves and Chopra (1984) is still the state of the art for the linear elastic response history analysis of gravity dams. Therefore, this procedure named as "Exact Model, EM" (Figure 2.1 (a)) and accepted as the exact solution for the seismic response history analysis. The technique of Fenves and Chopra (1984) is a frequency domain hybrid numerical and analytical finite element approach. In their approach, the equation of motion of the dam-foundation-reservoir system is solved for each excitation frequency by employing the reduced degrees of freedom obtained from Ritz procedure (Eq. (2.1)).

$$\left[-w^2 \begin{bmatrix} m_d & 0 \\ \underline{0} & m_b \end{bmatrix} + (1 + i\eta_s) \begin{bmatrix} k & k_b \\ k_b^T & k_{bb} \end{bmatrix} + \begin{bmatrix} \underline{0} & 0 \\ \underline{0} & \underline{S}_f(w) \end{bmatrix} \right] \begin{Bmatrix} \bar{r}^l(w) \\ \bar{r}_b^l(w) \end{Bmatrix}$$

$$= - \begin{Bmatrix} m_d \underline{1}^l \\ m_b \underline{1}_b^l \end{Bmatrix} + \begin{Bmatrix} \overline{R}_h^l(w) \\ -\underline{S}_{rq}\underline{S}_{qq}^{-1}\overline{Q}_h(w) \end{Bmatrix} \tag{2.1}$$

In the above equation, w is the excitation frequency, m_d and m_b are mass sub matrices for dam and foundation, η_s is the constant hysteretic damping for the dam concrete. k, k_b and k_{bb} are stiffness sub matrices for dam and foundation, $\bar{r}(w)$ and $\bar{r}_b(w)$ are relative displacements for nodes above the base and at the base. 1 is directional unit vector, $\overline{R}_h(w)$ is hydrodynamic forces at the upstream face, $\overline{Q}_h(w)$ is hydrodynamic forces at the reservoir bottom. $\underline{S}_{rr}$, $\underline{S}_{rq}$ and $\underline{S}_{qq}$ are the sub matrices in the force-displacement relation of the foundation substructure (Eq. (2.2)).

$$\begin{bmatrix} \underline{S}_{rr}(w) & \underline{S}_{rq}(w) \\ \underline{S}_{rq}^T(w) & \underline{S}_{qq}(w) \end{bmatrix} \begin{Bmatrix} \bar{r}_f(w) \\ \bar{q}(w) \end{Bmatrix} = \begin{Bmatrix} \overline{R}_f(w) \\ \overline{Q}_h(w) \end{Bmatrix} \tag{2.2}$$

$$\underline{S}_f(w) = \underline{S}_{rr}(w) - \underline{S}_{rq}(w)\underline{S}_{qq}^{-1}(w)\underline{S}_{rq}^T(w) \tag{2.3}$$

$\underline{S}_f(w)$ is the condensed dynamic stiffness matrix of the foundation (Eq. (2.3)) which is derived by equilibrium and compatibility equations at the dam-foundation

intersection ($\overline{R}_b(w) + \overline{R}_f(w) = 0$, $\overline{r}_b(w) = \overline{r}_f(w)$). In the above equations, $\overline{r}_f(w)$ is the relative displacements for nodes on the surface of the foundation at dam-foundation intersection, $\overline{q}(w)$ is the relative displacements at the reservoir bottom, $\overline{R}_f(w)$ is the forces on the surface of the foundation, and $\overline{R}_b(w)$ is the forces on the bottom of dam at the dam-foundation intersection. EM utilizes exact solution of hydrodynamic forces of an infinite channel on the upstream face of the dam and it includes the two-dimensional half space flexible foundation response under seismic excitations. In the formulation, the complex valued foundation stiffness matrix was obtained by using the numerical method proposed by Dasgupta and Chopra (1977). The bottom absorption is approximately modeled by the modification of the boundary condition at the reservoir bottom. Its effect is included by a wave reflection coefficient (α) that represents the ratio of the amplitude of reflected hydrodynamic pressure wave to the amplitude of a vertically propagating pressure wave incident on the reservoir bottom, which depends on damping coefficient of the reservoir materials, and velocity of pressure waves in water.

The flexible foundation solution of Fenves and Chopra (1984) method supplies the dynamic stiffness influence coefficients for a foundation mesh of only 8 elements with only constant values of foundation damping (for 2 %, 5 % and 10 % damping ratios). In order to overcome these restrictions, a new program to compute the foundation compliances for models with denser meshes and arbitrary foundation damping values was prepared. The influence coefficients were recalculated using the procedures of Dasgupta and Chopra (1977). In addition, a standalone user-friendly pre and post processor was prepared.

A number of dam sections representative of almost all practical cases were analyzed using the EM. The dam heights (H) were chosen as 50, 100, 150 m. Upstream face of all dam sections were vertical and the corresponding downstream slopes (S) were selected as 0.8 and 1.0. Crest length of the dams were taken as 4 m, 8 m and 12 m for the dam heights of 50, 100, and 150 m, respectively.

(a) EM: "Exact" approach   *(b)* IFMFM: "Simplified" approach
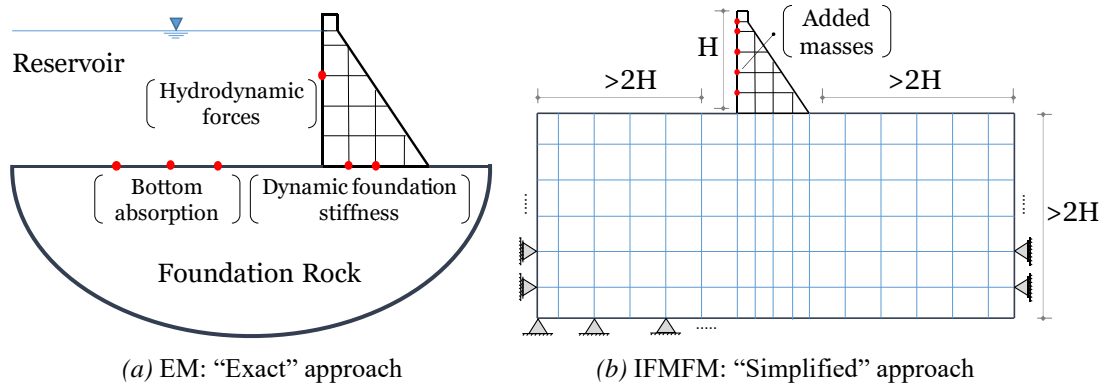
Figure 2.1. Demonstration of EM and IFMFM

Dam sections were analyzed for both the empty reservoir (ER) and full reservoir (FR) conditions to reflect the two extreme conditions. Modulus of elasticity of the concrete (E_c) for dam body was taken as 20 GPa and 30 GPa. Modulus of elasticity of the foundation (E_f) was included in the analysis as a fraction of concrete modulus of elasticity (i.e E_f/E_c = 0.5, 1, 2, 10, 50). It was identified that a flexible base solution with an E_f/E_c = 50 ratio practically corresponds to a fixed base dam without any dam-foundation interaction. This ratio was gradually reduced and a parametric study was performed. The E_f/E_c = 10 ratio was chosen as the transition parameter and corresponds to an E_f which is not very common in practice. The E_f/E_c = 2 ratio corresponds to a strong rock formation such as granite or shale. However, the most common foundation rock formation in dam structures correspond to E_f/E_c = 0.5 and E_f/E_c = 1 ratios with medium strength foundation such as sandstone or limestone. Along with the employed parameters, 120 different dam models were built. For all cases, the density of concrete and foundation material were taken as 2400 kg/m³. Poisson's ratios of concrete and foundation were assumed as 0.2 and 0.25, respectively. In order to follow the common practice, a 5% hysteretic damping ratio for the concrete and foundation was used in all analyses with EM. Wave reflection coefficient was assumed 1.0 in all analysis to reflect the insignificant sedimentation in new dams. Finite element meshes used in the analyses are presented in Figure 2.2. The mesh sizes were proportionally increased to keep constant element sizes for different section geometries. A sensitivity analysis was conducted to estimate the effect of mesh

size. A relatively fine mesh was tested for several analysis cases. If the error is evaluated with respect to maximum principle tensile stresses, finesse of mesh may affect the results 8, 10 and 12% for 50, 100 and 150 m dams, respectively.

(a) Section 1   (b) Section 2   (c) Section 3
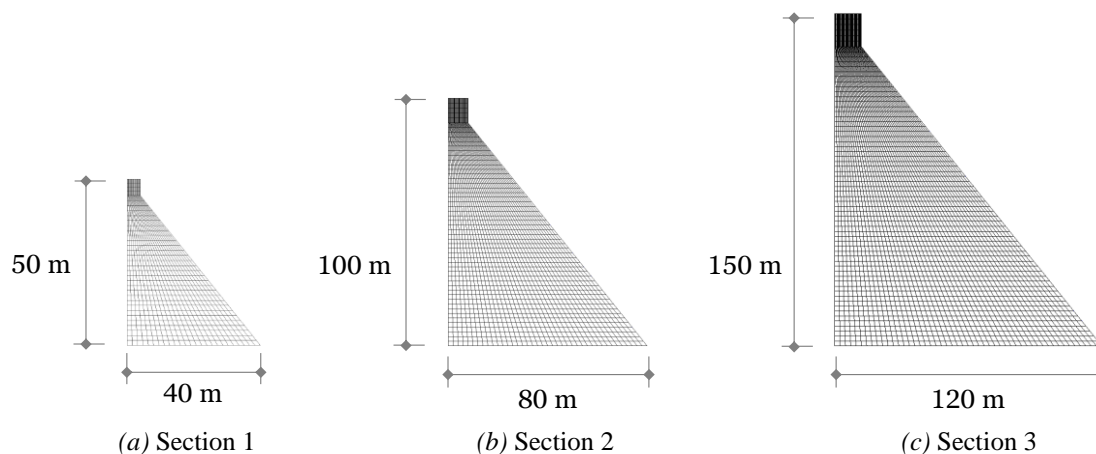
Figure 2.2. Analyzed dam sections

2.3.2. Ground Motion Records

Thirty-seven different ground motion records were utilized for the dynamic analyses of each dam section. Ground motions were selected such that shear wave velocity of the recorded motion location was greater than 750 m/s to realistically represent the foundation properties of concrete dam sites. The complete list of ground motion records is given in Table 2.1.

Table 2.1. *Details of ground motion records*

No	Earthquake	Country	Date	Site Geo.	Comp.	d (km)	M_w	PGA (g)	PGV (cm/s)
1	Vrancea	Romania	1990	Rock	EW	5	6.6(M_L)	0.024	1.90
2	Vrancea	Romania	1990	Rock	NS	5	6.6(M_L)	0.030	2.18
3	Marmara	Turkey	1999	Rock	NS	78	7.4	0.052	4.30
4	Loma Prieta	USA	1989	NEHRP(B)	115	53(d_c)	7	0.058	6.13
5	Loma Prieta	USA	1989	NEHRP(B)	205	53(d_c)	7	0.105	8.19
6	Marmara	Turkey	1999	Rock	EW	78	7.4	0.106	14.92
7	Imperial Valley	USA	1979	Granite	N45E	21.8(d_c)	6.5	0.110	5.14
8	Lazio Abruzzo	Italy	1984	Rock	EW	60	5.7	0.126	7.30
9	Lazio Abruzzo	Italy	1984	Rock	NS	60	5.7	0.132	9.47

Table 2.1. (continued)

10	Northridge	USA	1994	Rock	90	36.7(d_c)	6.7	0.133	5.34
11	Coalinga	USA	1983	Granite	315	35(d_h)	6.5	0.136	15.62
12	Campano-Luc.	Italy	1980	Rock	NS	23	6.5	0.139	20.57
13	Bucharest	Romania	1977	Rock	EW	4	6.4(M_L)	0.151	25.64
14	Marmara	Turkey	1999	Rock	NS	11	7.4	0.167	32.04
15	Coalinga	USA	1983	Granite	45	35(d_h)	6.5	0.172	15.75
16	Campano-Luc.	Italy	1980	Rock	EW	23	6.5	0.181	30.45
17	Imperial Valley	USA	1979	Granite	S45E	21.8(d_c)	6.5	0.186	8.65
18	Bucharest	Romania	1977	Rock	NS	4	6.4(M_L)	0.194	70.55
19	Campano-Luc.	Italy	1980	Rock	NS	32	6.5	0.216	33.06
20	Marmara	Turkey	1999	Rock	EW	11	7.4	0.227	54.28
21	Northridge	USA	1994	Rock	360	36.7(d_c)	6.7	0.233	7.46
22	Friuli	Italy	1976	Rock	EW	27	6.3	0.316	32.63
23	Campano-Luc.	Italy	1980	Rock	EW	32	6.5	0.323	55.36
24	Tabas	Iran	1978	Rock	N80W	11	6.4(M_L)	0.338	17.68
25	Friuli	Italy	1976	Rock	NS	27	6.3	0.357	20.62
26	Tabas	Iran	1978	Rock	N10E	11	6.4(M_L)	0.385	24.58
27	Marmara	Turkey	1999	Rock	EW	40	7.4	0.407	79.80
28	Loma Prieta	USA	1989	Rock	0	2.8(d_c)	7	0.435	31.91
29	Loma Prieta	USA	1989	Rock	90	2.8(d_c)	7	0.442	33.84
30	North P. Spr.	USA	1986	USGS(A)	180	7.3(d_c)	6.2	0.492	34.72
31	North P. Spr.	USA	1986	USGS(A)	270	7.3(d_c)	6.2	0.612	31.48
32	Morgan Hill	USA	1984	Rock	195	1.5(d_c)	6.1	0.711	51.64
33	Umbro	Italy	1997	Rock	NS	11	6	0.711	27.61
34	Umbro	Italy	1997	Rock	EW	11	6	0.760	29.86
35	Cape Mend.	USA	1992	Rock	90	15.5(d_c)	7	1.039	40.52
36	Morgan Hill	USA	1984	Rock	285	1.5(d_c)	6.1	1.298	80.79
37	Cape Mend.	USA	1992	Rock	0	15.5(d_c)	7	1.497	126.12
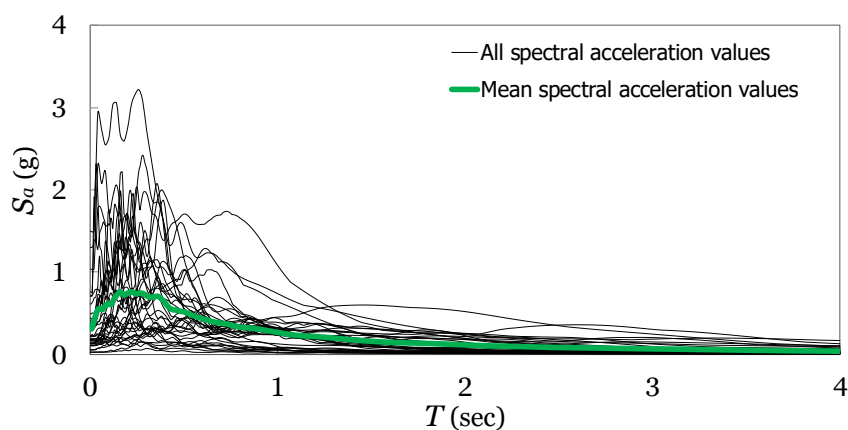
Figure 2.3. Pseudo acceleration spectrum of ground motion data set

The ranges of interest for M_w (moment magnitude), d (distance to the epicenter), PGA (peak ground acceleration) and PGV (peak ground velocity) are as follows: $5.7 < M_w < 7.4$, 4 km $< d <$ 78 km, 0.024 g $<$ PGA $<$ 1.497 g, 1.90 cm/s $<$ PGV $<$ 126.12 cm/s. M_L, d_c and d_h represent the local magnitude, closest distance and hypocentral distance, respectively. The response spectra of the ground motions are presented in Figure 2.3 for all motion records. The selected parameters (i.e. dam height, downstream slope, reservoir condition, concrete strength and E_f/E_c) resulted in 120 different cases, which were analyzed for 37 different ground motion records. The total number of conducted analyses was 4440 for the analyses using the EM.

2.3.3. Earthquake Induced Stresses

Maximum principle tensile stress values at the upstream toe excluding the static (hydrostatic and dam weight) tensile stresses (σ_{max}^u) of the concrete dam section during earthquakes is one of the most important engineering demand parameters for the selection of dam size. An appropriate concrete tensile strength should be selected based on stress demand to select an economical and safe dam section. Detailed and accurate response history analysis procedures, at early stage of design may not be possible; hence, beam analogy-based procedures are usually employed in the rigid block stability design. Due to the flexibility of dam body and foundation, such stress estimations are not accurate. Hence, the earthquake induced stresses on the dam base obtained from the EM analyses results were examined in detail in this section.

The maximum principle tensile stress values at the upstream toe at the dam base (σ_{max}^u) obtained by using EM are presented in Figure 2.4. Results are shown for different dam heights (H), and they were categorized in three PGA intervals namely, PGA $<$ 0.2g, 0.2g $<$ PGA $<$ 0.4g and PGA $>$ 0.4g separately. Horizontal axes in Figure 2.4 were arranged free of scale and actual PGA levels were given as a dashed line. Plots show the stress values and the PGA of the ground motions for different reservoir conditions. For the 50 m high dam, the mean of σ_{max}^u values obtained from 37 dynamic analyses were identified as 2.29 MPa and 2.95 MPa for ER and FR cases, respectively.

For the 100 m (150 m) dam section, these values were found as 3.57 MPa (4.49 MPa), 5.47 MPa (6.16 MPa), respectively. These results show that addition of hydrodynamic effects may increase the average σ_{max}^u values by a factor of 1.25 to 1.5. The same condition was observed for an individual result of ground motion sets such the scatter in the plots higher for the FR compared to ER cases. It can be also observed that σ_{max}^u tended to increase with increasing dam height under the same ground motion. Moreover, ground motions with lower PGAs (PGA < 0.2g) could impose high σ_{max}^u demands on 150 m high dams. This shows that ground motion variability is more important for high dams compared to lower ones.

The effect of examined parameters on σ_{max}^u values was individually studied in Figure 2.5. Average of σ_{max}^u obtained from 37 response history analysis results of each dam for ER and FR cases were used for this purpose. According to Figure 2.5(a), σ_{max}^u increased with decreasing S regardless of H or PGA. For small E_f/E_c values, the effect of S on σ_{max}^u was more influential. The effect of E_c (Figure 2.5(b)) did not lead a significant difference for low height dams as well as the ground motions in PGA < 0.2g range. However, variation in E_c while keeping E_f/E_c constant may be important for high dams located on softer foundation rock in a region of high seismic hazard. According to Figure 2.5(b), σ_{max}^u increase with decreasing E_c values for high dams. The effect of E_f/E_c on σ_{max}^u is found to be one of the most important parameters affecting σ_{max}^u values. For low height dams, E_f/E_c ratio was less influential on the average σ_{max}^u values. However, for higher dams, σ_{max}^u might increase significantly with increasing E_f/E_c, especially for high range of PGA.

(a) H = 50 m

15
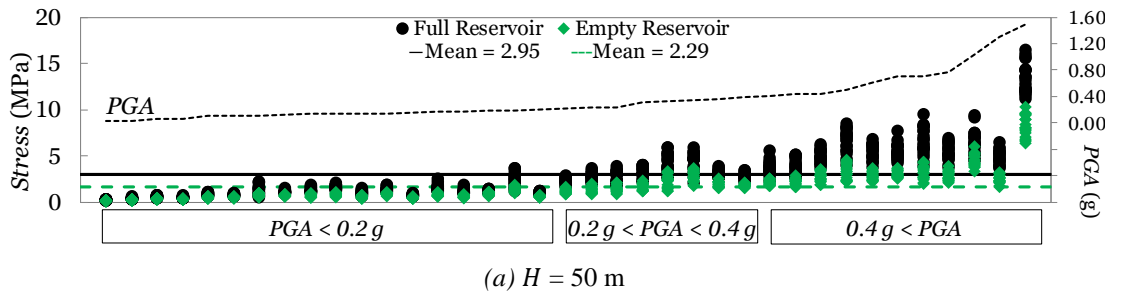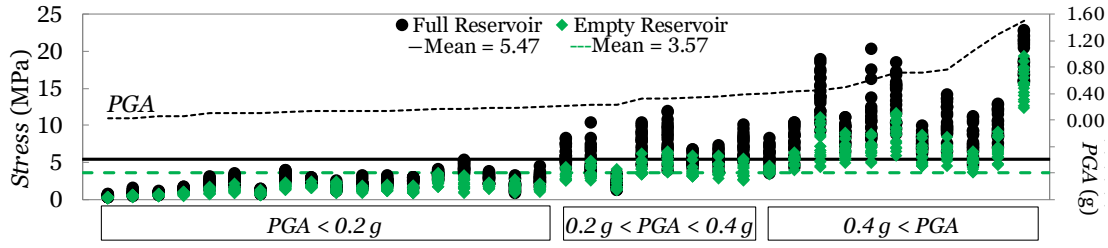
(b) H = 100 m
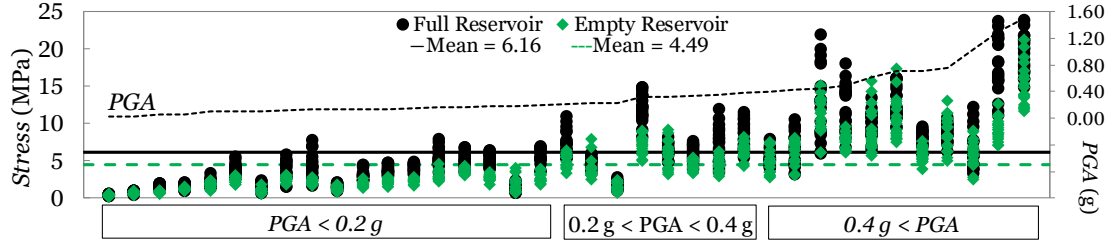
(c) H = 150 m

Figure 2.4. Maximum principal stress distributions with varying ground motions
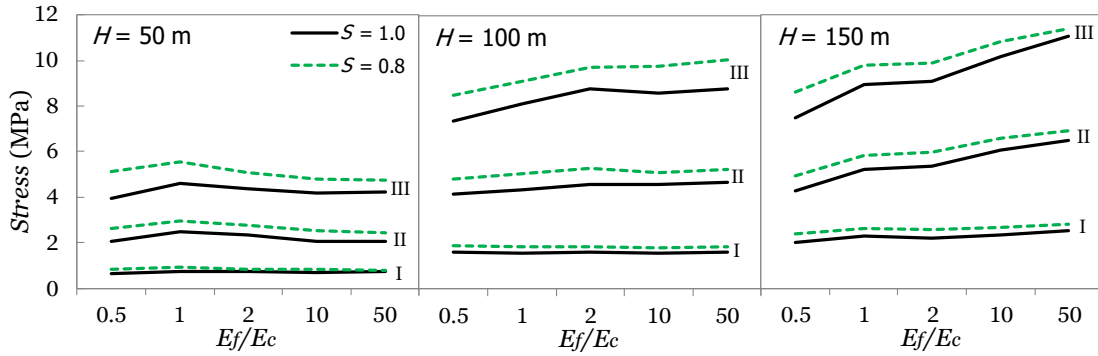
(a) Downstream slope (*S*)
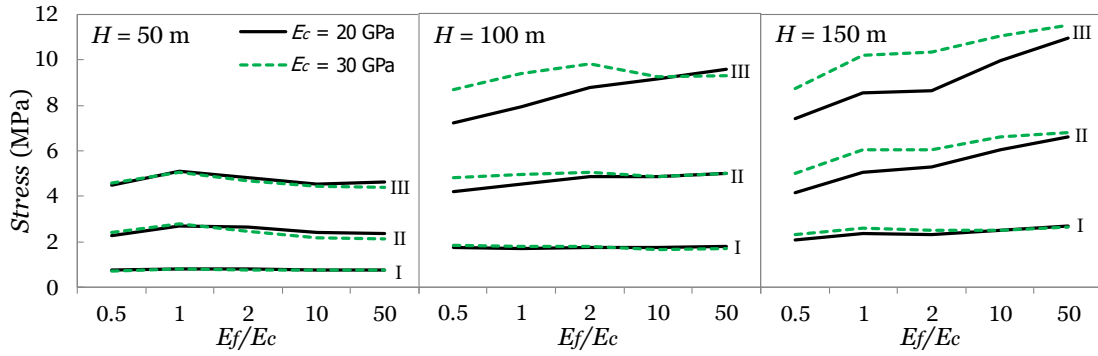
(b) Modulus of elasticity of concrete (*E$_c$*)

I: PGA < 0.2 g, II: 0.2 g < PGA < 0.4 g, III: 0.4 g < PGA

Figure 2.5. The effect of parameters on maximum principal stress

The distribution of principle tensile stresses is also important when deciding the critically stressed region under earthquakes. For this purpose, envelope of principal stress demands (σ_{max}) at the dam base were extracted and plotted by normalizing the dam base with the dam base length (L_b) and stresses with the maximum values as shown in Figure 2.6. The analysis results revealed that ground motion variability, reservoir condition, S, E_c and H had negligible effects on stress distribution along the dam base. So, all the cases related with these parameters were included in stress distribution prediction equation. The main parameter that affected the dam base maximum principal stress envelope distribution was E_f/E_c. In all cases, the maximum principal tensile stresses decreased to 20 percent of their maximum values at a distance of $0.2L_b$ from the upstream toe approximately in a linear manner. It is also interesting to note that stress envelope distributions in Figure 2.6 can be conveniently expressed in the form of a fourth order polynomial:

$$\sigma_{max}(x_b)/\sigma_{max}^u = C_1(x_b/L_b)^4 + C_2(x_b/L_b)^3 + C_3(x_b/L_b)^2 + C_4(x_b/L_b)^4 + C_5 \quad (2.4)$$

where, x_b is the distance measured from the upstream toe of the dam base. Constants C_1 to C_5 are given in Table 2.2 for different E_f/E_c values. The ability of these functions to approximate the σ_{max} distribution at the dam base is shown in Figure 2.6.

(a) $E_f/E_c = 0.5$ *(b) $E_f/E_c = 2$*
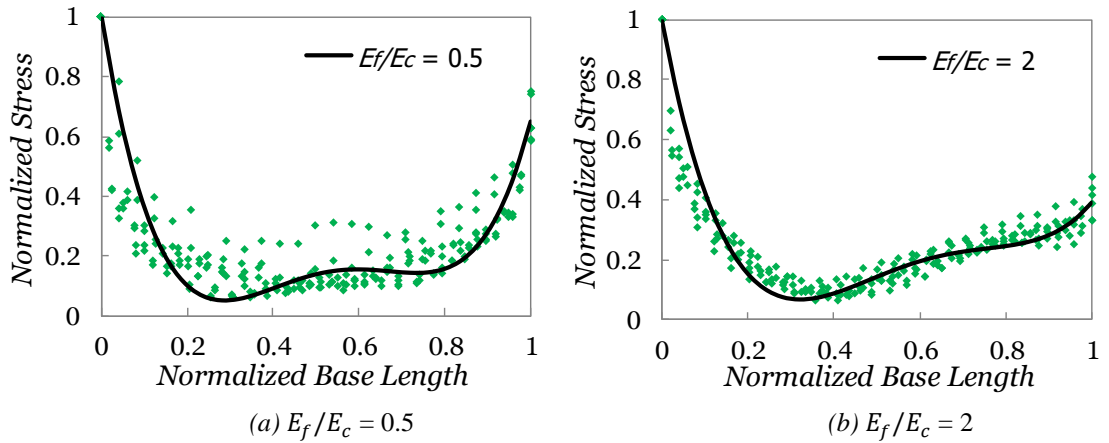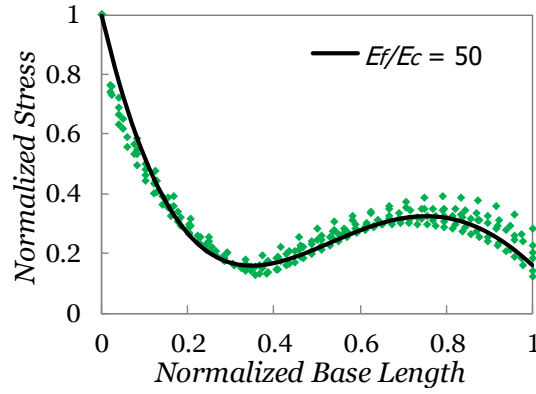
(c) $E_f/E_c = 50$

Figure 2.6. Base stress distributions

Table 2.2. *Coefficients of base stress distribution*

E_f/E_c	C_1	C_2	C_3	C_4	C_5
0.5	17.88	-38.54	29.27	-8.96	1.00
2	9.91	-24.60	21.77	7.69	1.00
50	3.77	-13.33	14.85	-6.13	1.00

The σ_{max}^u values obtained from the numerical simulations using EM was employed in a regression analysis and a stress prediction equation was developed. All important parameters that influence the stress values, namely R (0 for empty, 1 for full), E_f/E_c ($E_f/E_c = 50$ for fixed case), S, H and the spectral acceleration calculated for the fundamental mode of the dam on flexible foundation, S_{a1} (in g) were included in the prediction equation below:

$$\sigma_{max}^u = \left[-5.72S + (1.035 + 0.32R)\sqrt{H} - 0.004E_f/E_c\right]S_{a1}^{0.9} \tag{2.5}$$

In order to estimate the spectral accelerations, fundamental frequency of the dam is needed. For this purpose, dam models were analyzed under pulse type loading and the fundamental frequency was extracted for each model by using the frequency amplitude response curves. Based on fundamental frequency results following empirical equation was obtained:

$$F_1 = 78E_cH^{-1.55} + 1.77(E_f/E_c)^{0.24} - 0.045E_cR - 0.25\frac{HE_f/E_c}{1000S^2} \tag{2.6}$$

Above, F_1 represents the first mode frequency (in Hz) where E_c is in GPa. Rest of the parameters is explained above. The coefficient of the determinations (R^2) for Eq. (2.5) and Eq. (2.6) were found as 0.925 and 0.945, respectively.

In Figure 2.7(a), the stresses calculated by Eq. (2.5) are compared with EM results. It can be observed that dynamic stress prediction equations reasonably agree and can be used as a quick estimate of maximum principal stress expected due to earthquakes. Comparisons of the fundamental frequencies estimated by using Eq. (2.6) and the EM are given in Figure 2.7(b). It can be observed that proposed equation is sufficiently accurate for engineering purposes.

(a) Comparison of σ_{max} for EM and Eq. (2.5)

(b) Comparison of F_1 for EM and Eq. (2.6)
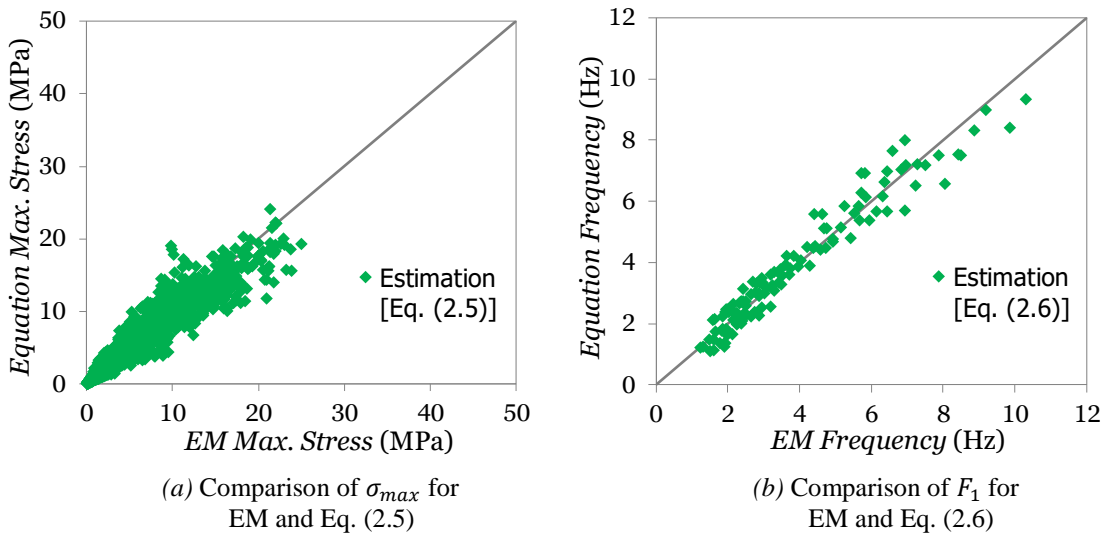
Figure 2.7. Accuracy of Eq. (2.5) and Eq. (2.6)

2.4. Effective Damping

2.4.1. Incompressible Fluid Massless Foundation Models

"Incompressible Fluid Massless Foundation Model, IFMFM" (Figure 2.1(b)) utilizes the added mass approach to model the hydrodynamic forces (Westergaard, 1933) along with the massless foundation model as proposed by USACE (1995). This modeling approach has many advantages such as allowing existing software to be utilized, ease of handling material nonlinearities in the time domain and allowing first mode static analysis or response spectrum analysis in the absence of ground motion

sets. Unfortunately, IFMFM, being extremely crude, may provide significant different results, when compared to EM results as demonstrated above. In the IFMFM, foundation is considered as a massless finite medium while stiffness contribution is taken into account with finite elements extending in a region of at least two times L_b extending all directions. In this way, the wave speed is infinity and the input motion can instantaneously reach the dam without any dynamic interaction. Massless foundation models have been commonly employed in the design and evaluation many dams in past studies (e.g., Leger and Boughoufalah, 1989, USACE, 2003 and Chuhan et al., 2009). A critical issue while conducting dynamic analysis using IFMFM is the selection of damping. In order to consider the effects of radiation damping, Fenves and Chopra (1986) proposed Eq. (2.7) based on the results of simplified dam analysis.

$$\zeta = \frac{1}{R_r R_f^3} \zeta_1 + \zeta_f + \zeta_r \qquad (2.7)$$

Above, ζ_1 represents structural damping, ζ_f represents damping due to the dam-foundation interaction and ζ_r represents damping due to the reservoir-dam interaction. R_r and R_f accounts for the effect of reservoir and flexible foundation, respectively. Eq. (2.7) is suggested by USACE (1995) for use along with IFMFMs in seismic analysis of dams. Results presented in the next section were employed by using the IFMFM with effective damping ratios calculated by Eq. (2.7). The effective damping ratios were adjusted to fit the first and third fundamental frequencies of the dam sections.

2.4.2. EM versus IFMFM Stress Results

Maximum principal tensile stress (σ_{max}^u) demands at the dam upstream toe obtained from EM and IFMFM were compared. The results were used to identify the stress errors (i.e. (σ_{max}^u from EM - σ_{max}^u from IFMFM) / σ_{max}^u from EM) obtained from IFMFM for different dam models and ground motions. The identified errors along with the examined parameters are plotted in Figure 2.8. Summary of all stress comparisons are shown in Figure 2.9.

20

Modeling the hydrodynamic effects with the added mass along with the massless foundation approach resulted in significant errors irrespective of the dam geometry. For ER cases, errors were between -60 to 10 percent. The errors were larger and more scattered for the FR conditions compared to the ER cases showing the additional inaccuracy of the added mass modeling. For the FR conditions, absolute errors tended to increase up to 100%, 130% and 150% for 50 m, 100 m and 150 m dam height. The errors usually tended to increase with decreasing E_f/E_c ratios. The variation of E_c (20 versus 30 GPa) did not result in a significant difference on estimated errors. The effect of S seemed to be important on the magnitude of errors unless the foundation was rigid.

The sign of the relative errors may also shed light whether the IFMFM (with damping ratios obtained by Eq. (2.7)) result in safe (higher than those obtained by using EM) or unsafe estimations. Safety is thought in the design sense whether the engineer over predicts (safe) or under predicts the "exact" stresses. According to the results, the main parameter that dictated the safety was E_f/E_c. If this ratio approached to the fixed base case (i.e $E_f/E_c = 50$), the number of having unsafe σ_{max}^u values tended to increase. Conversely, as the foundation rock was softer, stress errors usually grew to large values. Interestingly, E_c and S were not correlated with the sign of the errors. Although increasing H caused an increase in the stress errors, it usually provided safe side estimations. For 50, 100 and 150 m high dams, the percentage of analyses that can be labeled as unsafe were 17, 13 and 12, respectively. Significant over prediction of σ_{max}^u can be easily visualized in Figure 2.9(a) considering all the data points.

(a) $H = 50$ m, $S = 0.8$ *(b) $H = 50$ m, $S = 1.0$*

(c) H = 100 m, S = 0.8

(d) H = 100 m, S = 1.0

(e) H = 150 m, S = 0.8

(f) H = 150 m, S = 1.0
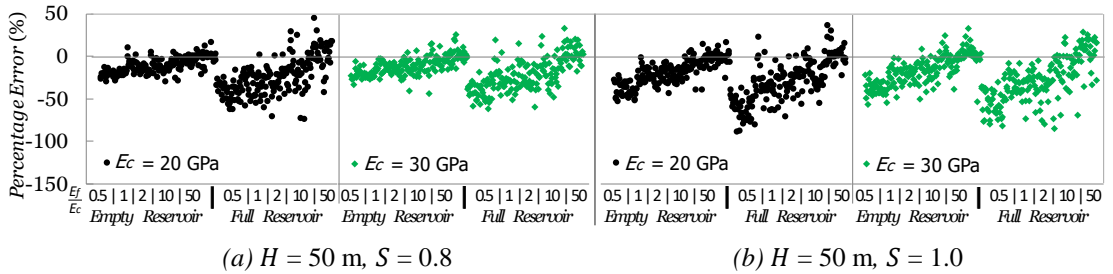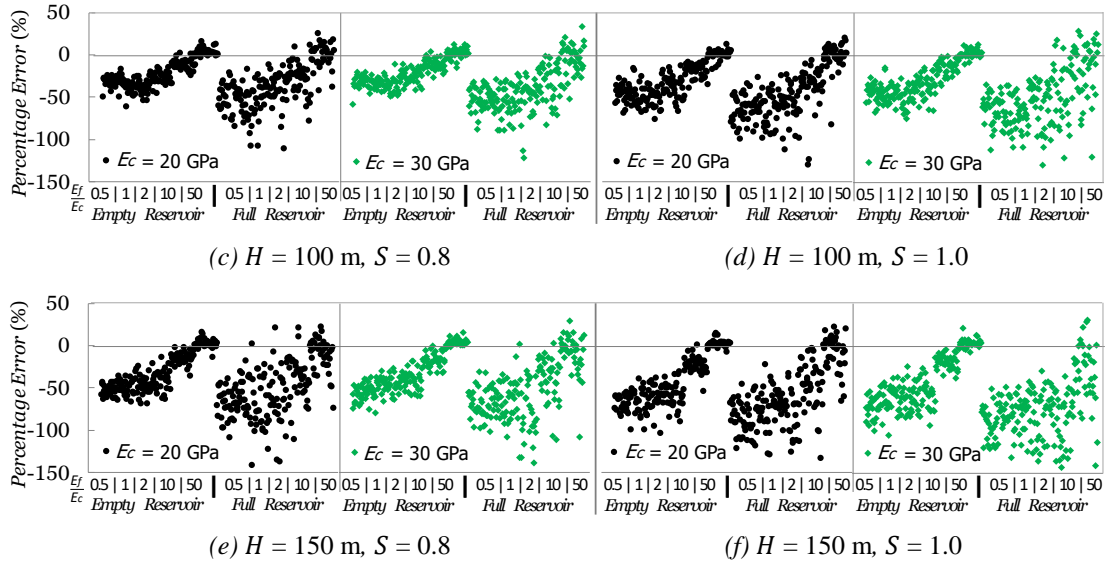
Figure 2.8. Maximum stress errors for dams

(a) IFMFM stresses with Eq. (2.7)

(b) Estimated damping ratios

(c) IFMFM stresses with Eq. (2.8)
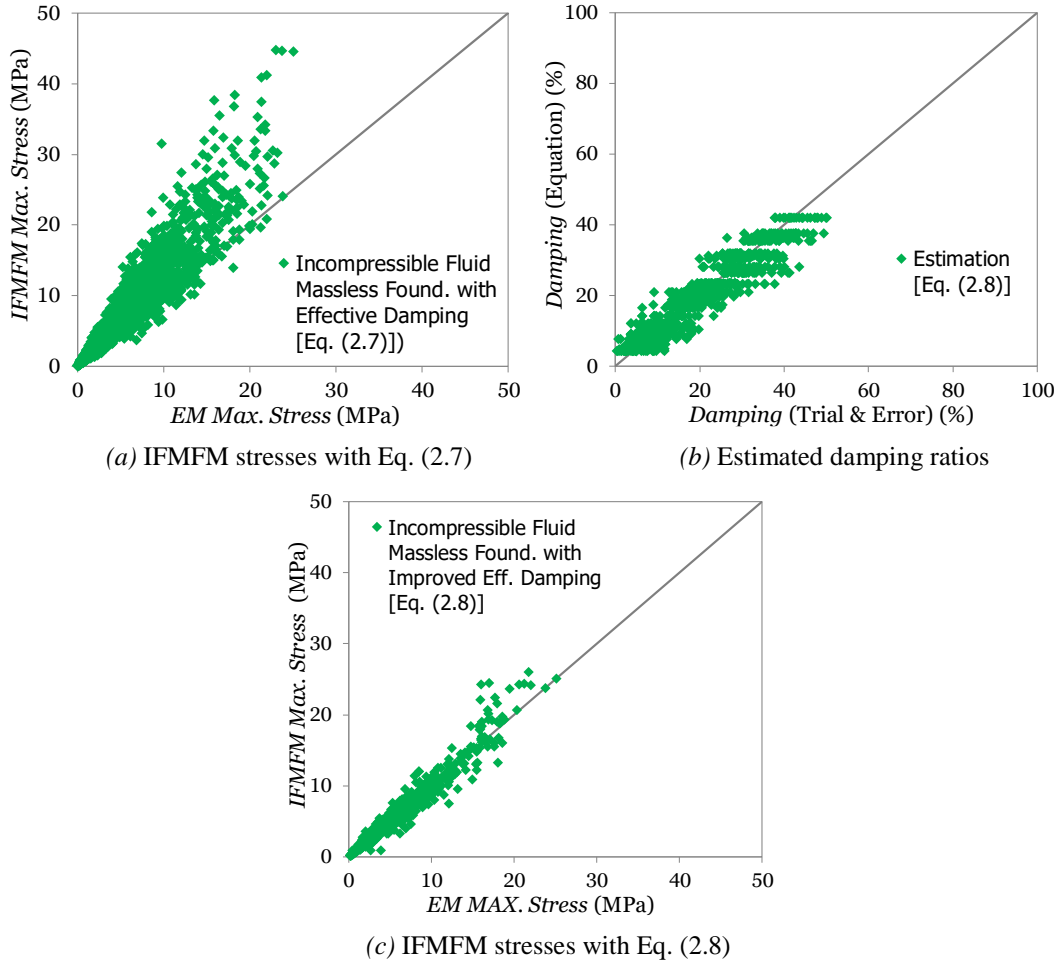
Figure 2.9. Comparisons of EM and IFMFM stresses

22

2.5. Improved Effective Damping

Aforementioned results revealed that IFMF analysis along with modified damping ratios (Fenves and Chopra, 1986) provide significant over prediction of σ_{max}^u (up to 150% in some cases). For preliminary design purposes, this situation can be considered as acceptable. However, such models, when used in nonlinear analysis may provide a false picture of the expected damage due to improper estimations of crack initiation. The over simplifications regarding fluid compressibility, frequency dependent nature of foundation stiffness, radiation damping, numerical errors due to time integration, conceptual differences between hysteretic and Rayleigh damping are the likely sources of these errors. One practical way of fixing such high stress errors is using higher damping ratios. This requires finding effective damping ratios that would provide similar σ_{max}^u for IFMFM and EM approaches.

New effective damping ratios were obtained by using an error minimization technique. Damping ratios of the IFMFM was changed until the square root of sum of $\bar{\sigma}_{base}^u$ error squares were minimized. For each case, an effective damping ratio was found by employing a trial & error process (Figure 2.10). The iterative process was stopped when the $\bar{\sigma}_{base}^u$ error between the EM and IFMFM was less than 5%.
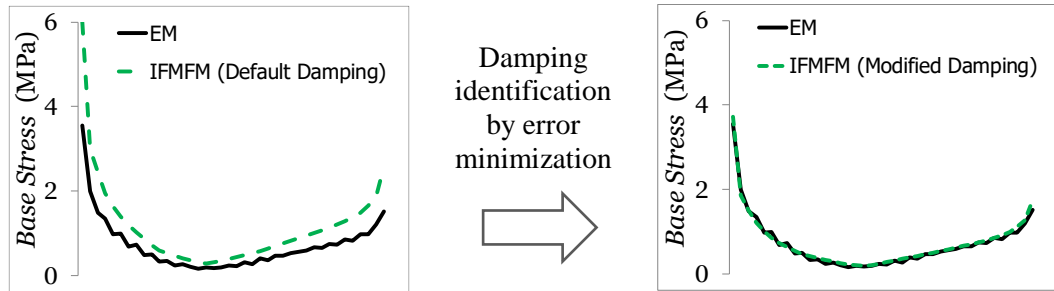
Figure 2.10. Damping ratio identification process

Earlier results in this study show that E_c had negligible effect on σ_{max}^u errors. Moreover, it was decided to compute the effective damping values only for the operation condition corresponding to the FR case. As a result, the effective damping ratios were determined for; H = 50 m, 100 m, 150 m; E_f/E_c = 0.5, 1, 2, 10, 50 and S = 0.8, 1.0. The computed effective damping ratios as a function of H and $1/(E_f/E_c)$

are given in Figure 2.11. As can be seen in the figure, effective damping ratios are proportional to $1/(E_f/E_c)$ ratios. To emphasized the correlation of $1/(E_f/E_c)$ values with damping ratios, simple linear trends are also shown. It can also be observed that the increase of S from 0.8 to 1.0 may slightly affect the lower boundaries requiring higher damping ratios.

(a) S = 0.8

(b) S = 1.0
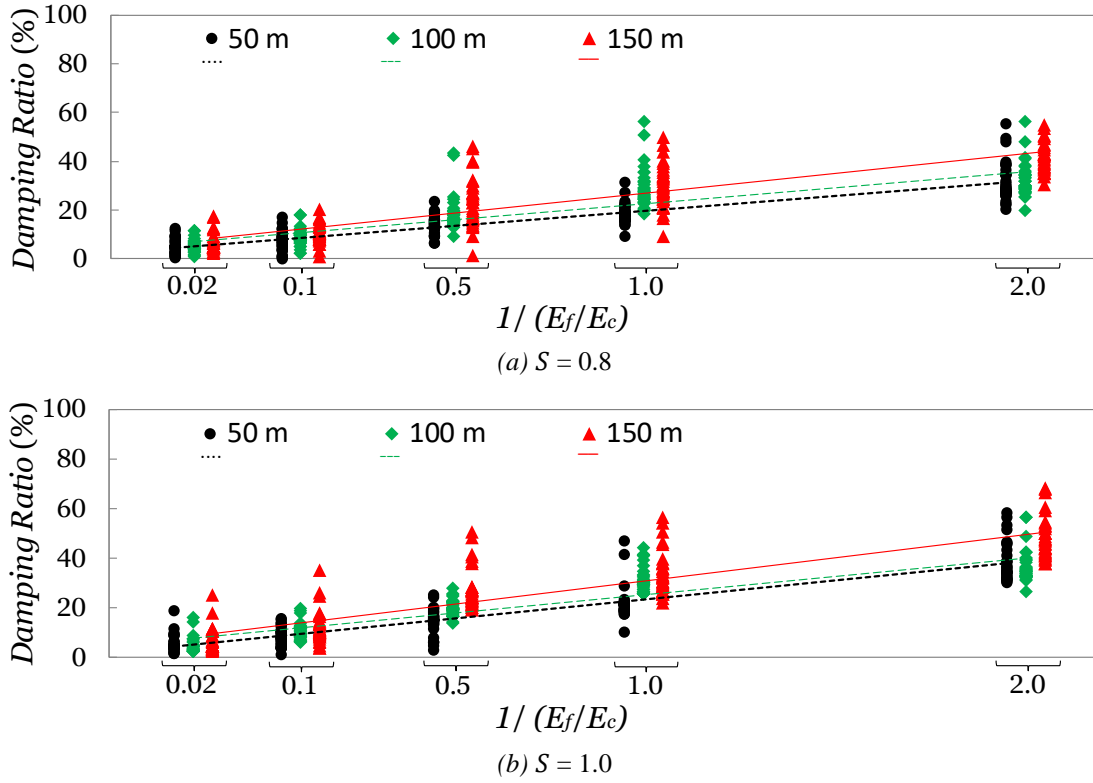
Figure 2.11. Damping ratios for full reservoir

The effective damping values obtained for each dam section and material properties were averaged for the 37 response history analyses. Results are tabulated in Table 2.3. It can be stated that, regardless of the E_f/E_c, it is necessary to assign higher effective damping for higher H or S values. Similarly, increasing $1/(E_f/E_c)$ require the use of higher damping ratio demands. In addition, effective damping ratios deviate from the assigned material damping in the EM only by a small amount for $E_f/E_c = 50$.

24

Table 2.3. *Average damping ratios (%) for FR*

	Dam Height (m)	0.02 (Fixed)	$1/(E_f/E_c)$ 0.1	0.5	1	2
S = 0.8	50	4.8	7.1	13.5	18.4	30.8
	100	5.1	8.6	18.4	28.5	32.2
	150	6.8	10.6	22.6	29.7	41.6
S = 1.0	50	5.5	8.3	14.8	21.9	37.8
	100	5.3	10.6	20.1	31.1	36.5
	150	7.2	12.4	27.2	33.5	48.1

Employing the results above, a nonlinear regression analysis was conducted to propose an equation for effective damping ratios. It should be noted that the provided equation is applicable for the dam sections with 2-dimensional numerical models and utilization of dam-reservoir and dam-foundation interactions with added masses and massless foundation methods, respectively. The proposed equation is as follows:

$$D = -0.7 + \frac{65}{H} + 0.5\left(E_c/E_f\right)^{F_1} + (0.1H + 16S)\left(E_c/E_f\right)^{0.4} \qquad (2.8)$$

In the above equation, D represents the effective damping ratio (%), F_1 represents the first mode frequency (in Hz) that can be calculated by the (Eq. 2.6). It is interesting to note that the effect of ground motion variability was not included as its use through PGA or S_{a1} did not lead to an improvement. In Figure 2.9(b), the effective damping ratio estimations of Eq. (2.8) are compared with the ones obtained from trial & error process. In order to demonstrate the ability of Eq. (2.8) in estimating σ^u_{max} employing the IFMFM, analyses were repeated with the new damping values obtained by using Eq. (2.8). Comparisons of σ^u_{max} employing IFMFM with effective damping from Eq. (2.8) and using the EM are shown in Figure 2.9(c). It can be observed that σ^u_{max} estimations are in good agreement with the EM results and the improvement of σ^u_{max} estimations upon using Eq. (2.8) instead of Eq. (2.7) is remarkable (Figure 2.9(a) versus Figure 2.9(c)).

Although the new damping values improve the accuracy of the analysis results, they may not guarantee a safe design (Figure 2.12). For that reason, a safety factor was decided to use along with the principle tensile stresses that determined by the IFMFM.

By this way, the method insures a safe dam design in an acceptable error margin. According to the analysis result with new damping values, a factor of safety (FS) value of 1.15 guarantees 90% of the results in safe side while keeping the error under 50% margin (Figure 2.13).

$\frac{E_f}{E_c}$ 0.5 | 1 | 2 | 10 | 50 | 0.5 | 1 | 2 | 10 | 50 | 0.5 | 1 | 2 | 10 | 50 | 0.5 | 1 | 2 | 10 | 50 | 0.5 | 1 | 2 | 10 | 50 | 0.5 | 1 | 2 | 10 | 50

Empty Reservoir   *Full Reservoir*   *Empty Reservoir*   *Full Reservoir*   *Empty Reservoir*   *Full Reservoir*

(a) H = 50 m   *(b) H = 100 m*   *(c) H = 150 m*
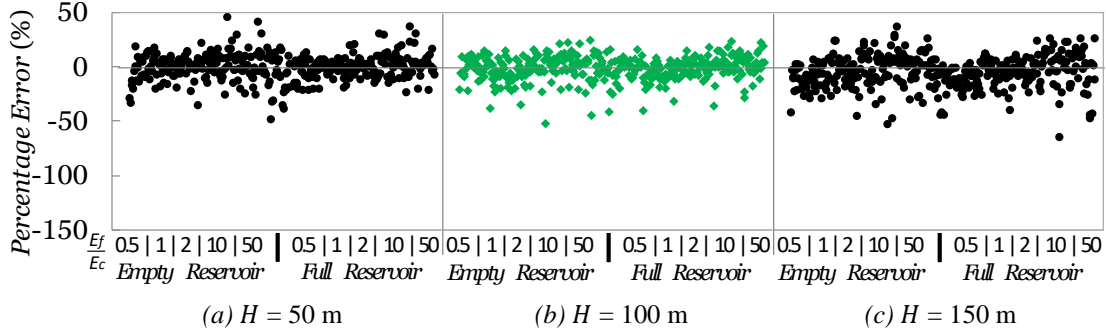
Figure 2.12. Maximum stress errors with improved effective damping

$\frac{E_f}{E_c}$ 0.5 | 1 | 2 | 10 | 50 | 0.5 | 1 | 2 | 10 | 50 | 0.5 | 1 | 2 | 10 | 50 | 0.5 | 1 | 2 | 10 | 50 | 0.5 | 1 | 2 | 10 | 50 | 0.5 | 1 | 2 | 10 | 50

Empty Reservoir   *Full Reservoir*   *Empty Reservoir*   *Full Reservoir*   *Empty Reservoir*   *Full Reservoir*

(a) H = 50 m   *(b) H = 100 m*   *(c) H = 150 m*
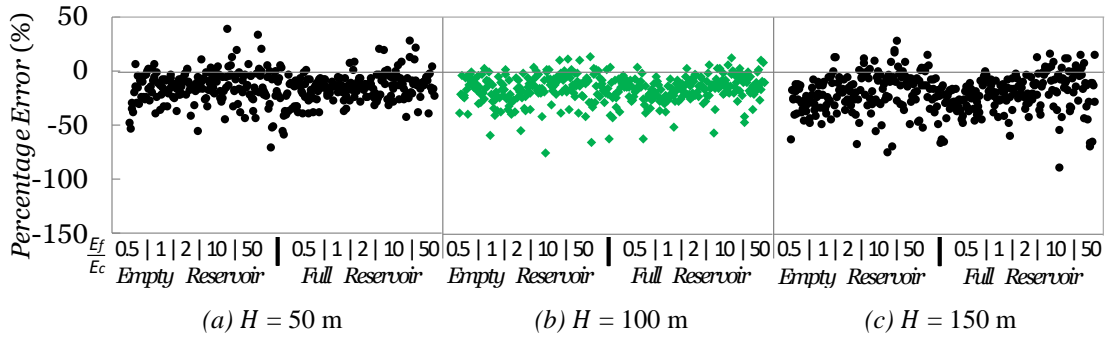
Figure 2.13. Maximum stress errors with 1.15 FS

2.6. Final Remarks

By conducting 4440 analyses with EM and IFMFM, dam base stresses and effective damping of concrete gravity dams were investigated. The maximum principal tensile stress (σ_{max}^u) at the dam upstream toe and its distribution at the dam base was studied. Results revealed that the tensile stress distribution at the base was strongly correlated with the E_f/E_c ratio. The higher dams with FR were usually exposed to higher principal tensile stress demands and the effect of E_f/E_c on σ_{max}^u was found to be more important. A simple prediction equation for σ_{max}^u was proposed as a function of R, E_f/E_c, S, H and S_{a1}. Accuracy of stress estimations using the IFMFM, which is a practical and frequently preferred analysis method for dam-foundation-reservoir

26

interaction problems, was critically evaluated. Results showed that the method along with the Eq. (2.7) led to significant errors in stress estimations. The influential variables on errors were dam height, reservoir condition and E_f/E_c. The boundaries of the stress errors usually showed larger scatter for the FR condition due to the added inaccuracy from the added mass approach. It can be stated that IFMFM usually ensured safe side stress estimations except when the E_f/E_c ratio approaches to the fixed base case. For the typical foundation rock modulus values ($E_f/E_c = 0.5$ and $E_f/E_c = 1$), the errors with IFMFM were largest for most of the cases. In this context, analysis with IFMFM revealed that the foundation model was critical and the method can provide inaccurate results when the typical E_f parameters are used. In order to minimize the stress errors caused by IFMFM, the damping ratios were adjusted by using an error minimization technique. The results showed that higher dams with low E_f/E_c ratio required significantly high damping ratios. The E_f/E_c ratio was found to be the most important variable for the damping ratios and almost a linear relationship was observed between inverse of E_f/E_c and damping ratios. The effectiveness of the new damping equation was successfully proved by comparing by the earlier numerical tests. However, one should be cautious for the high damping ratios predicted by using Eq. (2.8) due to the inability of the two-dimensional half space problems in providing an accurate picture of the actual dam site conditions.

CHAPTER 3

EARTHQUAKE DEFORMATION AND DAMAGE

3.1. Background

The dynamic interaction of hydrodynamic pressures and the concrete gravity dam was first studied by Westergaard (1933) assuming incompressible fluid in reservoir and a vertical upstream face. The early works of Chopra and his colleagues were the first modern prediction of earthquake response of dams considering the compressibility effect of the water, dam-reservoir and dam-foundation interactions making use of the finite element method (Chopra, 1966-1984). In the light of these studies, Fenves and Chopra (1985) developed a simplified analytical procedure for the fundamental mode response of concrete gravity dams to earthquake ground motion considering hydrodynamic and foundation interaction effects, separately. Continuing that study, Fenves and Chopra (1986) extended their procedure to include the simultaneous effects of dam-reservoir interaction, reservoir bottom absorption and dam-foundation interaction. The study of Saleh and Madabhushi (2010) computed the hydrodynamic pressures behind both relatively stiff and flexible model dams and the experimental data was employed as a benchmark of theoretical hydrodynamic pressures found by Westergaard's (1933) and Chopra's (1985) method. Bouaanani and Perrault (2010) developed new closed form analytical expressions systems for dam-reservoir dynamic interactions the effects of dam flexibility, water compressibility, and reservoir bottom wave absorption. Recently, Løkke and Chopra (2017) developed a finite element method for nonlinear earthquake analysis considering dam-reservoir-foundation interaction which is applicable for modeling of concrete cracking, as well as sliding and joint separation. Cracking in concrete dams is considered as the critical type of damage during strong motions. There are several numerical and experimental studies conducted to understand the crack behavior of concrete gravity dams. For example,

Bhattacharjee and Leger (1994) focused on the simulation of a model concrete gravity dam employing a coaxial rotating crack model (CRCM) and a fixed crack model with a variable shear resistance factor (FCM-VSRF). Nowadays, the need of estimating the potential risks and expected loss under earthquakes has shifted the engineers to conduct nonlinear analysis of structures including dams. A number of studies were conducted to investigate concrete cracking and estimate dam stability (e.g., Bhattacharjee and Leger, 1995, Mclean et al., 2006, Arici and Binici, 2011, Soysal et al., 2016). Sequentially linear analysis was proposed as alternative procedure to iterative solution of nonlinear finite element analysis of structures (Rots, 2001-2018). The method avoids convergence problems related to softening behavior and negative tangent stiffness by directly specifying a damage increment. The method first proposed by Rots in 2001 then used by many other studies that has been published. In 2008, DeJong et al. has developed the method such as the algorithm can handle non-proportional loading with an orthotropic cracking model that is similar to the traditional fixed smeared crack concept.

3.2. Objectives

The main objective of this part is to develop a method employing nonlinear static analysis combined with a static oscillator to calculate the dam-reservoir interaction and estimate the cracking behavior of concrete dams. For this purpose, the capacity curve of the concrete gravity dam was obtained by sequential linear analysis method. The most important advantage of this method is its being stable and convergence even if the systems subjected to severe cracking tension softening or even snapback. The method applied in the form of non-proportional load combination and the hydrostatic and gravitational loads were taken as the initial step. Total hydrodynamic load and its distribution over upstream face of the dam were estimated from a SDOF approximation of the fundamental mode of concrete gravity dam. Similarly, the inertia forces were calculated and applied the system along with hydrodynamic loads as secondary loading. The capacity curve and the crack patterns observed for the explained method were compared with the time history analysis (THA) results.

Nonlinear static procedures were employed to predict the seismic demand. By using the results of nonlinear time history analysis, the most likely crack patterns were identified which were then categorized based on dam characteristics and seismic intensities. Finally, two equations were developed for the determination of crest displacement and crack length by the results of the THA.

3.3. SLA Procedure

SLA method is an alternative to the iterative nonlinear analysis, which employs a stepwise following of the damage pattern in a continuum model. The algorithm aims to solve nonlinear behavior by sequential linear analyses instead of an iterative solution. For the method, each integration point of the elements in a finite element model has its own constitutive stress-strain relationship. The significant part of the process is identifying the integration point that the damage is expected. For that purpose, under an applied unit load, the principle stresses at each integration point are calculated by linear elastic analysis. The point, at which the ratio of principal tensile stress to tensile strength is a maximum, is selected as critical integration point. The ratio is employed as a load factor for the unit load and current state response of the system is computed. For the following step, the critical point is damaged such that the modulus of elasticity and the tensile strength of the critical integration point are reduced according to the constitutive relationship. The method is also applicable for more than two independent non-proportional loads (DeJong et al., 2008).

For the traditional iterative solution procedure, the convergence difficulties are commonly related with the negative slope of the modulus of elasticity encountered in the nonlinear material models. By the SLA, that problem is overcome by a modeling technique called the saw-tooth curve. The saw-tooth curve forms a structure that oscillates around the softening tension curve with a step-wised reduction of modulus of elasticity and strength (Figure 3.1(a)). In each step of damage, the capacity of damaged integration point is reduced as shown in figure. In this way, the elasticity modulus is always positive, and hence stability of the system is preserved. The size

of the stiffness reduction steps does not change the overall behavior, but affects the oscillations in response. For the case of this study, an optimum reduction (i.e. reduction in modulus of elasticity without effecting the results) varying between %15 to %35 of the initial modulus was selected to provide accurate results along with acceptable analysis duration. The method requires a standard finite element program with a linear elastic solver. For this purpose, a linear elastic finite element program code was developed. The program is capable of analyzing linear static, modal, and frequency response problems along with pre/post processor. According to the needs of the study, four-node isoparametric plane stress and strain elements were adopted to the program. For numerical integration over the elements, 2x2 gauss quadrature rule was followed (Cook et al., 2001).

(a) Saw-tooth stress-strain curve   *(b)* Solution algorithm
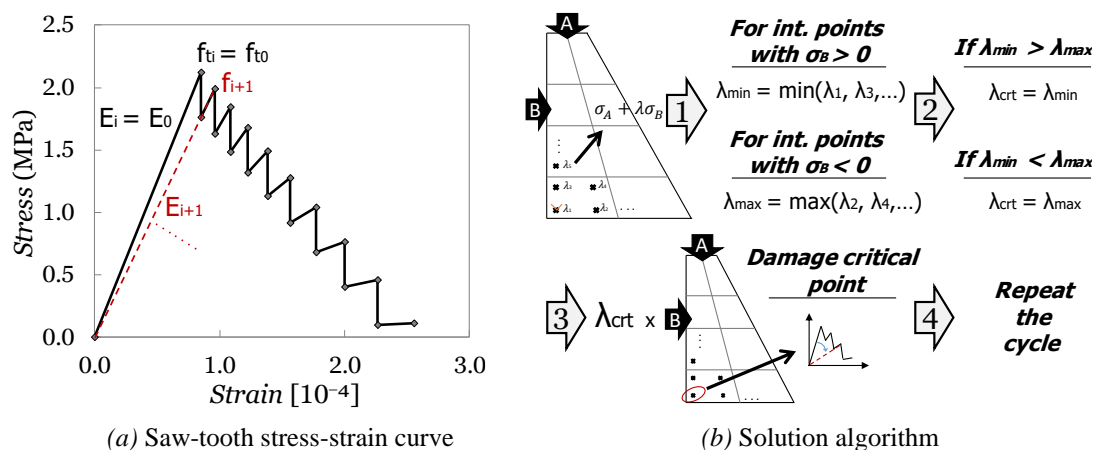
Figure 3.1. Solution algorithm and stress-strain curve

One of the significant problems with the use of the four-node plane element is a phenomenon called "shear locking". When traditional plane stress elements ($Q4$) are subjected to pure bending, due to linear shape functions, their top and bottom edges remain straight. That condition causes formation of parasitic shear. Such elements exhibit more rigid behavior than it should and generate non-existing shear stresses. The resulting supplement stresses are also related with the aspect ratio of the elements and the effect increases with increasing aspect ratios (Cook et al., 2001). To avoid the shear locking, several techniques can be used. One way of getting better results for bending related problems is applying "selective reduced integration". Since shear

32

strain is zero at the element center, selective reduced integration can be applied by evaluating shear strain in the element midpoint only (1x1 Gauss rule). Using high order elements or assumed strain elements are the other solution methods for shear locking problem. Especially assumed strain elements can be adapted to plane elements by approximating the strain field by using not only the compatible displacements but also additional incompatible displacement mods. These elements are usually called as incompatible elements ($Q6$) and have more accurate behavior than $Q4$ elements under pure bending. There are also enhanced elements ($QM6$) that have improved bending behavior with modified incompatible modes (Taylor et al., 1976 and Simo and Rifai, 1990). In the following chapters, all quadrilateral elements were evaluated critically and the most suitable one was selected for use in this study.

The material behavior was adopted to follow the concept of total strain cracking model, which is based on the smeared band cracking theory. According to the orientation of the crack plane, the crack models can be categorized as fixed and rotating crack models. For the rotating crack concept, the orientation of the crack is kept aligned with the axes of principal strains (Rots, 1988). On the other hand, according to fixed crack concept, after the initial crack is opened on an integration point, the direction of the crack is fixed (Rots, 1988). The local axis system is kept parallel and perpendicular to the initial crack direction. For both techniques, the stiffness and strength parameters are reduced according to the saw-tooth stress-strain relationship. In this study, both approaches have been used to validate various theoretical and experimental studies. Crack models employ the orthotropic material law such that an independent constitutive relationship exists in the parallel and perpendicular directions to the crack. In this way, the formation of secondary cracks can be captured. The critical point is calculated for both directions of each integration point. The orthotropic behavior of the material requires separate constitutive relation for the crack parallel and perpendicular direction. Although such modification lengthens the computation time, it improves accuracy of the technique significantly (DeJong et al., 2008). The isotropic behavior of the concrete material can be

represented by 2D plane stress equation in global axes given below (Eq. (3.1)). Until the cracking occurs, the linear behavior can be modeled with ease. Once the principal stresses exceed the tensile strength, an orthotropic material law is introduced and replaced by the isotropic material law, with a crack being formed in a local direction (σ_{ii} - ε_{ii}) perpendicular to the direction of the maximum principal stress.

$$\begin{Bmatrix} \sigma_{nn} \\ \sigma_{tt} \\ \sigma_{nt} \end{Bmatrix} = \begin{bmatrix} \frac{E_0}{1-v^2} & \frac{vE_0}{1-v^2} & 0 \\ \frac{vE_0}{1-v^2} & \frac{E_0}{1-v^2} & 0 \\ 0 & 0 & \frac{0.5(1-v)E_0}{1-v^2} \end{bmatrix} \begin{Bmatrix} \varepsilon_{nn} \\ \varepsilon_{tt} \\ \varepsilon_{nt} \end{Bmatrix} \tag{3.1}$$

After cracking, there is a reduction of the shear stiffness of the material. For the fixed crack concept, the relation of aggregate interlock to the shear strength usually included in constitute model by shear retention factor, β (Eq. (3.2)). The earlier researches have claimed that the constant shear retention factor may not capable of fully reflecting the behavior of the concrete after cracking. Therefore, constitutive models with variable shear retention factor were suggested such that the shear stiffness decreases with the crack opening (Rots, 2008). By using a constant shear retention factor, the orthotropic constitute relation of a plain stress element in its local axes can be expressed as:

$$\begin{Bmatrix} \sigma_{nn} \\ \sigma_{tt} \\ \sigma_{nt} \end{Bmatrix} = \begin{bmatrix} \frac{E_n E_t}{E_t-v^2 E_n} & \frac{vE_n E_t}{E_t-v^2 E_n} & 0 \\ \frac{vE_n E_t}{E_t-v^2 E_n} & \frac{E_t^2}{E_t-v^2 E_n} & 0 \\ 0 & 0 & \beta G \end{bmatrix} \begin{Bmatrix} \varepsilon_{nn} \\ \varepsilon_{tt} \\ \varepsilon_{nt} \end{Bmatrix} \tag{3.2}$$

For variable shear retention factor, there are different techniques exist in literature. One way of describing the reduced shear stiffness is using the isotropic definition of the shear stiffness, except using reduced elastic properties (Rots, 2008) as shown in Eq. (3.3).

$$\begin{Bmatrix} \sigma_{nn} \\ \sigma_{tt} \\ \sigma_{nt} \end{Bmatrix} = \frac{1}{1-v^2\frac{E_n E_t}{E_0^2}} \begin{bmatrix} E_n & \frac{v}{E_0}E_n E_t & 0 \\ \frac{v}{E_0}E_n E_t & E_t & 0 \\ 0 & 0 & \frac{E_{min}}{2(1+v\frac{E_{min}}{E_0})}(1-v^2\frac{E_n E_t}{E_0^2}) \end{bmatrix} \begin{Bmatrix} \varepsilon_{nn} \\ \varepsilon_{tt} \\ \varepsilon_{nt} \end{Bmatrix} \tag{3.3}$$

34

where E_n and E_t are degraded modulus of elasticity values at local directions, E_0 is initial modulus of elasticity, E_{min} is the minimum of E_n and E_t, G is shear modulus, v is Poisson's ratio, σ_{nn}, σ_{tt}, σ_{nt} and ε_{nn}, ε_{tt}, ε_{nt} are local stress and strains, respectively. It is understood that the isotropic relation does not hold for anisotropic damage, but Eq. (3.4) effectively relates the shear stiffness to a maximum of the orthotropic damage. Another constitutive relation correlates the orthotropic damage to the shear modulus was proposed by Bhattacharjee ang Leger (1993):

$$
\begin{Bmatrix} \sigma_{nn} \\ \sigma_{tt} \\ \sigma_{nt} \end{Bmatrix} = \frac{E_0}{1-\eta v^2} \begin{bmatrix} \frac{E_n}{E_0} & \frac{E_n}{E_0}v & 0 \\ \frac{E_n}{E_0}v & 1 & 0 \\ 0 & 0 & \frac{1+v}{1-\eta v^2}\left(\frac{\eta\varepsilon_{nn}-\varepsilon_{tt}}{\varepsilon_{nn}-\varepsilon_{tt}}-\eta v\right)\frac{1-\eta v^2}{2(1+v)} \end{bmatrix} \begin{Bmatrix} \varepsilon_{nn} \\ \varepsilon_{tt} \\ \varepsilon_{nt} \end{Bmatrix} \tag{3.4}
$$

where the parameter η $(0 < \eta < 1)$ is ratio between the softened elastic modulus E_n, in the direction normal to a fracture plane, and E_0, the initial isotropic elastic modulus.

The solution algorithm for the SLA method is summarized in Figure 3.1(b). For the case of two independent loads, if the self-weight and the hydrostatic forces are named as A, the hydrodynamic and inertia forces are named as B, the SLA method can have applied by following steps (Rots, 2008):

- $Load\ A$ is applied and σ_A is found for all integration points.
- $Load\ A$ is removed then $Load\ B$ is applied and σ_B is found.
- For all integration points, λ values are calculated such that $\sigma_A + \lambda\sigma_B$ would be equal to the tensile strength.

Normally, $Load\ A$ and $Load\ B$ stresses affect in different directions. In order to find the principle stresses, equations in the global directions (σ_{kk}) are:

$$
\begin{aligned}
\sigma_{xx} &= \sigma_{xx,A} + \lambda\sigma_{xx,B} \\
\sigma_{yy} &= \sigma_{yy,A} + \lambda\sigma_{yy,B} \\
\sigma_{xy} &= \sigma_{xy,A} + \lambda\sigma_{xy,B}
\end{aligned} \tag{3.5}
$$

So, the principle stresses and λ values can be found by the Eq. (3.6) and (3.7) as:

$$\sigma_{1,2} = \frac{1}{2}[(\sigma_{xx,A} + \lambda\sigma_{xx,B}) + (\sigma_{yy,A} + \lambda\sigma_{yy,B})] \pm$$

$$\sqrt{\frac{1}{4}[(\sigma_{xx,A} + \lambda\sigma_{xx,B}) - (\sigma_{yy,A} + \lambda\sigma_{yy,B})]^2 + (\sigma_{xy,A} + \lambda\sigma_{xy,B})^2} \qquad (3.6)$$

where:

$$\lambda = \frac{1}{2A}(-B \pm \sqrt{B^3 - 4AC})$$

$$A = \sigma_{xy,B}{}^2 - \sigma_{xx,B}\sigma_{yy,B}$$

$$B = f_t(\sigma_{xx,B} + \sigma_{yy,B}) + 2\sigma_{xy,A}\sigma_{xy,B} - \sigma_{xx,A}\sigma_{yy,B} - \sigma_{xx,B}\sigma_{yy,A}$$

$$C = \sigma_{xy,A}{}^2 - \sigma_{xx,A}\sigma_{yy,A} + f_t(\sigma_{xx,A} + \sigma_{yy,A}) - f_t{}^2 \qquad (3.7)$$

Each of the λ values are calculated for the integration points and compared to identify critical λ. Due to the effect of multiple loads on system, the identification of λ requires a special procedure as outlined below:

- The principle stress directions are determined for the $A + \lambda B$ combination of each integration point. Then the stresses are calculated in these directions only under *Load B*.
- The integration points that are under tension and compression stresses are identified. For the ones under tension stress, all the λ values are compared and λ_{min} is determined.
- In a similar way λ_{max} is determined for λ values under compression stress.
- If $\lambda_{max} < \lambda_{min}$, λ_{crc} is chosen as λ_{min}, otherwise λ_{crc} is not applicable and damage should be applied at $\lambda_{max} = \lambda_{crc}$.

After determination of the λ_{crc}, the method follows the below steps:

- *Load B* is scaled by λ_{crc} and the response results for $A + \lambda B$ combination are taken as the current state.

- In the next step all the loads are removed from the system and the critical integration point is degraded in the direction of crack according to saw-tooth curve given in Figure 3.1(a). The crack direction is fixed.
- The above steps are repeated until the complete failure is satisfied.

3.3.1. Hydrodynamic and Inertia Loads

The hydrodynamic pressure has a significant influence on the response of concrete gravity dams to the earthquake a ground motion. However, its effect is closely related with bottom silt deposits, height, flexibility, and shape of the dam, and the water compressibility. Although analytical solution is possible for vertical rigid dam and incompressible water assumptions (Westergaard, 1993), the response may be inaccurate under actual conditions. For example, Kotsubo (1956) showed that Westergaard's (1993) response is valid only when excitation period is larger than the reservoir's natural period. Additionally, recent research has showed that, in comparison with the compressible reservoir solution, modelling the hydrodynamic forces by added mass has led stress errors at the base of the dam, significantly for the high concrete gravity dams (see Chapter 2).

The dam-reservoir interaction problem can be analytically solved by using the wave propagation equation assuming linear compressibility and appropriate boundary conditions. If the water compressibility and the bottom absorption are considered, solution of the equation is dependent on the frequency content of the ground motion waves. If p is hydrodynamic pressure and C is the velocity of sound in water, the 2D wave equation can be represented in the time (t is time variable) domain as:

$$\frac{\partial^2 p}{\partial x^2} + \frac{\partial^2 p}{\partial y^2} = \frac{1}{C^2}\frac{\partial^2 p}{\partial t^2}$$

(3.8)

The pressure can be represented in the frequency domain as $p(x, y, t) = \bar{p}(x, y, w)e^{iwt}$ for a harmonic ground motion. Then the Eq. (3.8) becomes:

$$\frac{\partial^2 \bar{p}}{\partial x^2} + \frac{\partial^2 \bar{p}}{\partial y^2} + \frac{w^2}{C^2}\bar{p} = 0$$

(3.9)

The solution of Eq. (3.9) is possible by employing the appropriate boundary conditions. The surface waves at free surface and the reflection of waves from far end boundaries are neglected. Therefore, zero pressure condition occurs for these boundaries (Eq. (3.10) and Eq. (3.11)).

$$\bar{p}(x, H_r, w) = 0 \tag{3.10}$$

$$\lim_{x \to -\infty} \bar{p}(x, y, w) = 0 \tag{3.11}$$

By assuming a vertical upstream face, the boundary condition between dam and reservoir can be represented by ρ_r is the density of reservoir water and a_x is the horizontal frequency response acceleration as:

$$\frac{\partial \bar{p}}{\partial x}(0, y, w) = -\rho_r a_x(0, y, w) \tag{3.12}$$

The boundary condition between the absorptive rigid foundation and the reservoir is given below. In Eq. (3.13), q is the damping coefficient that accounts for the bottom absorption. It is included in the equation as a function of wave reflection coefficient $\propto$ (Eq. (3.14)) such that for full absorption, it gets the value of zero and for zero absorption, it achieves the value of 1.

$$\frac{\partial \bar{p}}{\partial y}(x, 0, w) = iwq\bar{p}(x, 0, w) \tag{3.13}$$

$$\propto = \frac{1 - Cq}{1 + Cq} \tag{3.14}$$

Eq. (3.9) can be solved with an iterative method (Fenves and Chopra, 1984) as well as with a simplified closed form formulation (Bouaanani and Perrault, 2010). The hydrodynamic pressure frequency response function is:

$$\bar{p}(x, y, w) = \bar{p}_0(x, y, w) - w^2 \sum_{i=1}^{N_d} \bar{Z}_i(w)\bar{p}_i(x, y, w) \tag{3.15}$$

where, $\bar{Z}_i(w)$ is the complex valued frequency response function, N_d is the number of structural mode shapes, $\bar{p}_0(x, y, w)$ and $\bar{p}_i(x, y, w)$ are the rigid and flexible parts of the hydrodynamic pressure function which are summation of frequency dependent

complex-valued functions of rigid and flexible parts for each reservoir mods. The dynamic response of short vibration-period structures, such as concrete gravity dams, to earthquake ground motion is primarily due to the fundamental mode of vibration (Fenves and Chopra, 1984). If only the contribution of fundamental mode is considered in the analysis, for a unit harmonic ground motion, the horizontal displacement response $\bar{u}(x, y, w)$ can be expressed by horizontal component of its fundamental mode shape $\phi_1(y)$ as:

$$\bar{u}(x, y, w) = \phi_1(y)\bar{Z}_1(w) \tag{3.16}$$

and the solution of the equation of motion of SDOF system becomes:

$$\bar{Z}_1(w) = \frac{-\tilde{L}_1}{-w^2\widetilde{M}_1 + iw\tilde{C}_1 + K_1} \tag{3.17}$$

For a SDOF system with FR, the terms $\tilde{L}_1$, $\widetilde{M}_1$ and $\tilde{C}_1$ can be evaluated by the following equations:

$$\tilde{L}_1 = L_1 + B_0(w) \tag{3.18}$$

$$\widetilde{M}_1 = M_1 + Re[B_1(w)] \tag{3.19}$$

$$\tilde{C}_1 = C_1 - w\, Im[B_1(w)] \tag{3.20}$$

in which M_1 is generalized mass, L_1 is modal parameter account for generalized inertia force, $C_1 = 2M_1\xi w_1$ and $K_1 = w_1^2 M_1$ where ξ is critical damping ratio and w_1 is fundamental vibration frequency of the ER dam. $B_0(w)$ and $B_1(w)$ are the frequency-dependent hydrodynamic parameters and reflects the dam-reservoir interaction and reservoir bottom wave absorption. According to Fenves and Chopra (1984), the term $B_0(w)$ can be interpreted as an added force, the real part of $B_1(w)$ as an added mass, and the imaginary part of $B_1(w)$ as an added damping and described as:

$$B_0(w) = -\int_0^{H_r} \bar{p}_0(0, y, w)\, \phi_1(y)dy \tag{3.21}$$

$$B_1(w) = -\int_0^{H_r} \bar{p}_1(0, y, w)\, \phi_1(y)dy \tag{3.22}$$

Addition of mass to the SDOF system due to hydrodynamic effect shortens the fundamental frequency of the dam. The fundamental frequency of FR system ($\widetilde{w}_1$) can be identified by estimating the first resonant peak of acceleration response function (second derivative of Eq. (3.16)). By employing the approximate fundamental mode solution and the fundamental frequency ($\widetilde{w}_1$), the corresponding damping ratio ($\tilde{\xi}_1$) can be evaluated by Eq. (3.23) (Fenves and Chopra, 1984). The damping ratio includes the damping caused by dam-reservoir interaction and bottom absorption.

$$\tilde{\xi}_1 = \frac{\widetilde{w}_1}{w_1}\xi_1 - \frac{1}{2M_1}(\frac{\widetilde{w}_1}{w_1})^2 \, Im[B_1(\widetilde{w}_1)] \tag{3.23}$$

Moreover, the hydrodynamic forces can be calculated by employing fundamental FR frequency and damping ratio as:

$$f_h(y) = \frac{\tilde{L}_1}{\tilde{M}_1}\frac{S_{a1}(\widetilde{w}_1,\tilde{\xi}_1)}{g}\left[\widetilde{m}(y)\phi_1(y) + gRe[\bar{p}_1(0,y,\widetilde{w}_1)]\right] \tag{3.24}$$

For an earthquake spectrum with $\widetilde{w}_1$ and $\tilde{\xi}_1$, the spectral acceleration value, $S_{a1}(\widetilde{w}_1,\tilde{\xi}_1)$ can be evaluated. $\widetilde{m}(y)$ is the total mass of the dam per unit height. Then the hydrodynamic force distribution at the upstream face of the dam can be easily calculated by Eq. (3.24). This force distribution will be later employed for the construction of the capacity curves of the FR cases. For the same S_{a1}, the total static lateral force can also be calculated. By using the fundamental mode shape and corresponding mass distribution of finite element modal response solution, the lateral inertia forces can be obtained by Eq. (3.25).

$$f_i(y) = \frac{m(y)\phi_1(y)}{\sum m(y)\phi_1(y)} \tag{3.25}$$

The combination of hydrodynamic and inertia forces will be used as the lateral load of the pushover analysis of simplified method.

3.3.2. Validation of SLA Method and Hydrodynamic Loads

In order to validate the SLA method, a number of theoretical and experimental studies were analyzed as benchmarks. At first, the accuracy of the finite element program was

validated by applying some widely used tests. Then SLA was evaluated by employing rotated crack model and fixed crack model with different shear reduction techniques (s_i). The first method (s_0) employs the widely used constant shear reduction factor, β. The second method (s_1) is a variable shear reduction technique that follows the rules of isotropic definition of the shear stiffness reviewed in DeJong et al. (2008). The last method (s_2) is another variable shear reduction technique that derived by Bhattacharjee (1993). After evaluation of SLA, hydrodynamic parameters were calculated for a concrete dam section with a vertical upstream face. By solving the equations of the hydrodynamic and inertia forces, the total lateral load and its distribution on the dam were evaluated for fundamental mode approximation. Their results were compared to the exact response solutions.

3.3.2.1. Numerical Cases

Patch Test

	Value	Unit
E_c	1	Pa
t_s	1	m
v	0.25	
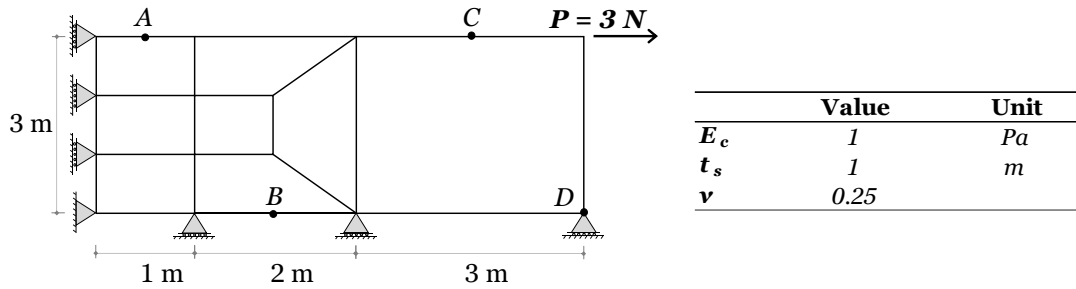
Figure 3.2. Test configuration and properties of the patch test

To verify the finite element program for its consistency and accuracy, patch tests are the first methods that come to mind. The idea of patch test is defining a finite element model that consist several elements with a specific boundary condition and loading. The patch test can be used as a benchmark for the finite element codes because the exact solution is known. A patch test for a plane stress problem with different mesh configurations and element types was proposed by Taylor et al. (1976). The pure bending test given in Figure 3.2 was tested by employing $Q4$, $Q6$ and $QM6$ elements, separately. The results are compared in Table 3.1. In the table, references 1, 2 and 3 accounts for the study of Taylor et al. (1976), Sap 2000 (2015) and TNO Diana (2016),

respectively. It can be observed that all the elements passed the patch test, while $QM6$ gave a slightly better result. $Q4$ and $QM6$ elements matched with the results of Ref. 2 and Ref. 3, respectively. $Q6$ results and reference values found slightly different. However, the results obtained with this element were found to be at a sufficient level to be used in future studies.

Table 3.1. *Stress and displacement results of different elements*

	Stress			Displacement
	A	**B**	**C**	**D**
Exact	*3.000*	*0.000*	*3.000*	*-18.00*
Q4	*3.071*	*-0.093*	*2.777*	*-17.00*
Q4 (Ref. 1)	*3.071*	*-0.008*	*2.777*	*-17.00*
Q4 (Ref. 2)	*3.071*	*-0.093*	*2.777*	*-17.00*
Q6	*3.045*	*-0.128*	*3.099*	*-17.62*
Q6 (Ref. 1)	*3.009*	*0.002*	*3.007*	*-19.66*
Q6 (Ref. 3)	*3.069*	*-0.109*	*3.049*	*-17.52*
QM6	*3.024*	*-0.066*	*3.000*	*-17.61*
QM6 (Ref. 1)	*3.024*	*-0.022*	*3.000*	*-17.61*
QM6 (Ref. 3)	*3.024*	*-0.066*	*3.000*	*-17.61*

Modal Analysis of Concrete Gravity Dam

	Value	Unit
E_c	27.5	GPa
ρ_c	2400	kg/m^3
t_s	1	m
v	0.25	
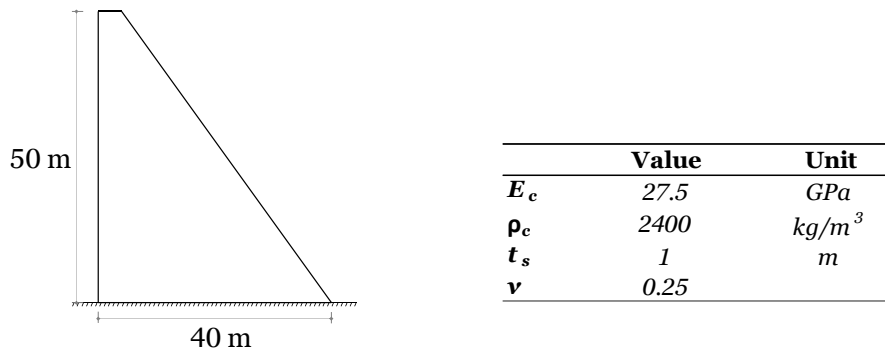
Figure 3.3. Test configuration and properties of the modal test

The natural frequencies and modal shapes of a structure can provide important information about its dynamic behavior. The modal analysis is an analytical procedure that solves the eigen values of the matrix equation, which defines the free vibration of the structure. The equation involves the assembly of stiffness and the mass matrices therefore; one can employ solution as a benchmark. For that reason, a 50 m-high

concrete gravity dam (Figure 3.3) with 0.8 downstream slope (S) was tested. The first 10 natural frequencies (w) were compared with the results of a reliable finite element programs. For the both analyses, $Q4$, $Q6$ and $QM6$ elements were employed along with material properties 27.5 GPa, 0.25 and 2400 kg/m^3 for elastic modulus, Poisson's ratio and concrete unit mass, respectively. The results are provided in Table 3.2 by using the same references above. According to the results, all elements were able to calculate the natural frequencies with sufficient accuracy. However, the $Q6$ and $QM6$ elements were more successful in predicting the higher mode frequencies of the dam.

Table 3.2. *First 10 modal frequency values (Rad/sec) of different elements*

	Mode Number									
	1	**2**	**3**	**4**	**5**	**6**	**7**	**8**	**9**	**10**
Q4	52.6	126.5	142.1	226.7	314.5	334.6	381.9	409.7	442.2	470.8
Q4 (Ref. 2)	52.6	126.5	142.1	226.7	314.5	334.6	381.9	409.8	442.2	470.8
Q6	52.0	124.2	141.3	218.6	312.4	319.2	381.5	399.3	417.6	458.0
Q6 (Ref. 2)	52.0	124.3	141.4	218.7	312.4	319.4	381.5	399.5	417.8	458.3
Q6 (Ref. 3)	52.2	125.1	141.7	222.0	313.7	326.8	381.1	405.2	432.4	462.7
QM6	52.0	124.3	141.3	218.7	312.4	319.4	381.5	399.5	417.8	458.2
QM6 (Ref. 3)	52.0	124.3	141.3	218.7	312.4	319.4	381.5	399.5	417.8	458.2

Flexural Beam Test

	Value	Unit
E_c	32	GPa
f_t	3	MPa
G_f	60	N/m
t_s	1	m
v	0.2	
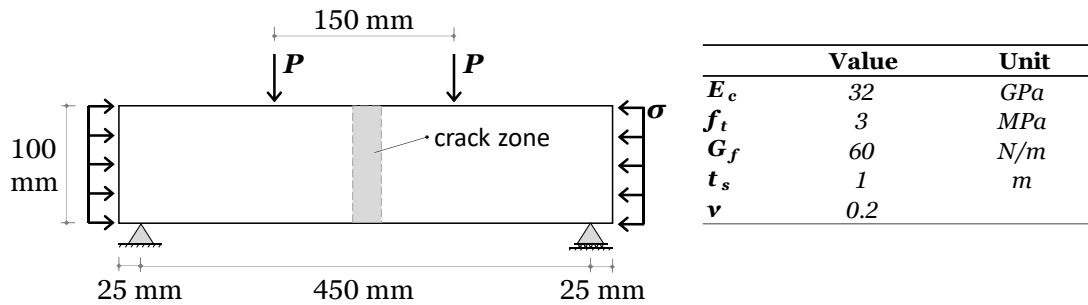
Figure 3.4. Test configuration and properties of the flexural beam test

A beam bending problem was analyzed with no pre-stress, with a 1 MPa pre-compression, and a pre-tensile stress followed by vertical loading. The middle span of the beam is in pure bending so the secondary cracks would not be expected for any cases. The original analysis was conducted by DeJong et al. (2008) by using an iterative Newton–Raphson scheme and crack mouth opening displacement with arc-

length control to achieve convergence. The test beam, material and loading details are shown in Figure 3.4. In the test system, concrete's elastic modulus, Poisson's ratio, tensile strength and the fracture energy are taken as 32 GPa, 0.2, 3 MPa and 60 N/m, respectively. The variable shear reduction (s_1) were employed for the tests. In Figure 3.5(a), the SLA results are compared with the numerical results and an almost exact match was obtained. Particularly for the tensile pre-stress test, the iterative analysis methods had difficulties to provide a successful solution. SLA method appears to be ideal for systems soften quickly so could be employed to obtain the capacity curve of the brittle structures such as concrete dams.

| (a) Force-Deformation response | (b) Crack pattern |
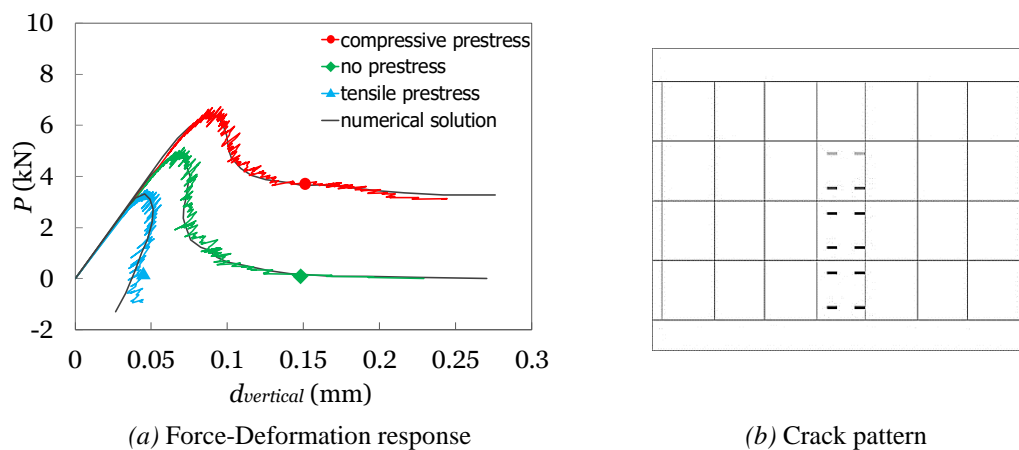
Figure 3.5. Results of flexural beam test under different lateral loading

3.3.2.2. Physical Cases

Three-Point Beam Bending Test

	Value	Unit
E_c	20	GPa
f_t	2.4	MPa
G_f	113	N/m
t_s	0.1	m
v	0.2	
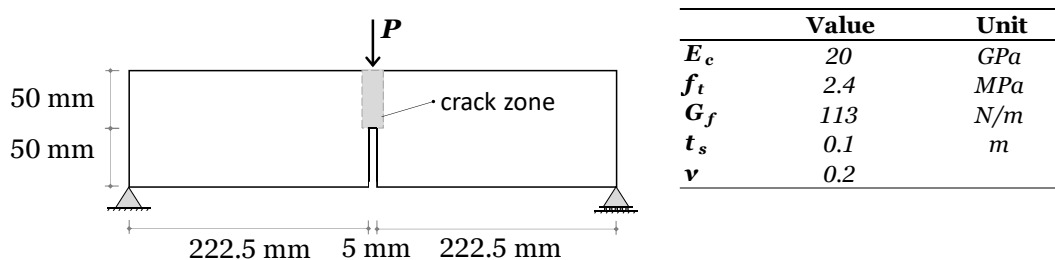
Figure 3.6. Test configuration and properties of the three-point bending beam test

The unreinforced three-point bending beam test (Körmeling and Reinhardt, 1983) has been thought as a convenient way to start comparing SLA with experimental results.

44

On the beam, a single load was applied at the mid-point aligned with an initial notch. The details of the beam and the actual crack zone are shown in Figure 3.6. The thickness of the concrete beam was reported as 100 mm. For the analysis, concrete's elastic modulus, Poisson's ratio, tensile strength and the fracture energy were taken as 20 GPa, 0.2, 2.4 MPa and 113 N/m, respectively. Further details of the test can also be found in Slobbe (2014). The Figure 3.7(a) and Figure 3.7(b) show the vertical displacement of the loading point versus applied force diagrams of $Q6$ and $QM6$ elements, respectively. Both elements were tested using two different cracking models, namely variable shear reduction with fixed crack (s_1) and rotated crack. Results show that both elements and crack models were successful in matching the maximum load and the capacity dropdown of the experimental sample. Figure 3.8 presents the corresponding crack patterns for tested elements and crack models. The differences between the crack patterns were not significant. In terms of constitutive models, while the crack distribution of the fixed crack was a little scattered, the rotated crack provided a more concentrated crack distribution.

(a) Q6   *(b) QM6*

Figure 3.7. Force-Deformation responses of different elements and crack models
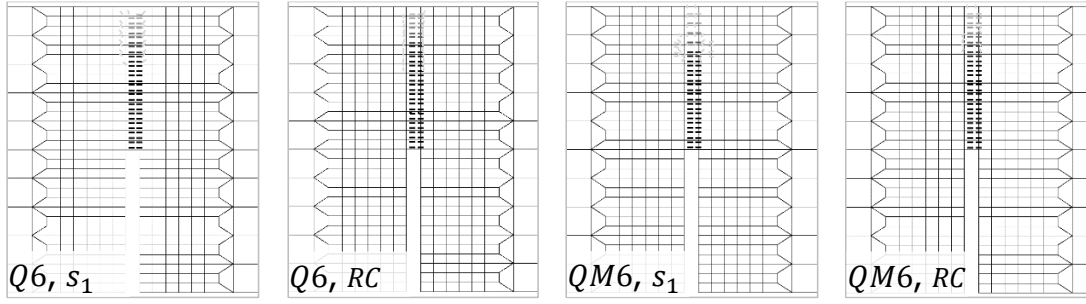
Figure 3.8. Crack patterns of different elements and crack models

Notched Shear Beam Test-1

The unreinforced single notched shear beam is an important benchmark for finite element applications to simulate shear induced cracking of concrete (Arrea and Ingraffea, 1981). On the top of the beam, loads were applied at two point with 0.13:1.0 ratio. To control the crack initiation, an initial notch was created. The test beam and the experimental crack pattern are shown in Figure 3.9.

	Value	Unit
E_c	24.8	GPa
f_t	2.8	MPa
G_f	100	N/m
t_s	0.156	m
v	0.18	
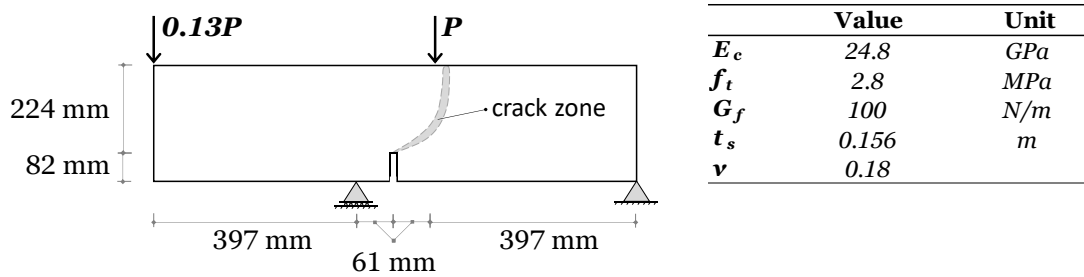
Figure 3.9. Test configuration and properties of the notched shear beam test-1

The thickness of the concrete beam is 156 mm. For the analysis, concrete's elastic modulus, Poisson's ratio, tensile strength and the fracture energy are taken as 24.8 GPa, 0.18, 2.8 MPa and 100 N/m, respectively. As shown in Figure 3.10, the $Q6$ element successfully followed the experimental results. The s_1 model provides a good match with $Q6$ element, but not with $QM6$ element. However, s_2 succeeded in matching the crack behavior for both elements. The rotated crack approach provided the most successful prediction.

46

(a) Q6   *(b) QM6*

Figure 3.10. Force-Deformation responses of different elements and crack models

Figure 3.11. Crack patterns of different elements and crack model

Notched Shear Beam Test-2

	Value	Unit
E_c	30	GPa
f_t	3	MPa
G_f	135	N/m
t_s	0.1	m
ν	0.2	

Figure 3.12. Test configuration and properties of the notched shear beam test-2

Another unreinforced single notched shear beam was tested by Nooru-Mohamed et al. (1993). At the bottom of the beam, loads were applied from two different points proportionally. A small notch was planned to initiate crack opening. The test beam and the actual crack pattern are shown in Figure 3.12. The thickness of the concrete beam is 100 mm. For the analysis, concrete's elastic modulus, Poisson's ratio, tensile strength and the fracture energy are taken as 30 GPa, 0.2, 3.0 MPa and 135 N/m, respectively. The details of the test can be found in Slobbe (2014). Figure 3.13(a) and Figure 3.13(b) show the crack mouth sliding displacement versus force diagrams of $Q6$ and $QM6$ elements, respectively. Results showed that the maximum load capacity is more dependent on the constitutive crack model. Except the s_2 results, both elements provided similar prediction of the load degradation. It is observed that s_2 and s_3 models reached higher capacity while s_0 ($\beta = 0.02$) is below the experimental value. s_1 provided the best match for the case of maximum load capacity. In Figure 3.14, corresponding crack paths are presented. s_0 and s_1 provided an average performance on predicting the true behavior. The s_2 model yielded an average performance with both elements. The last method, the rotated crack approach led to acceptable results for both types of elements.
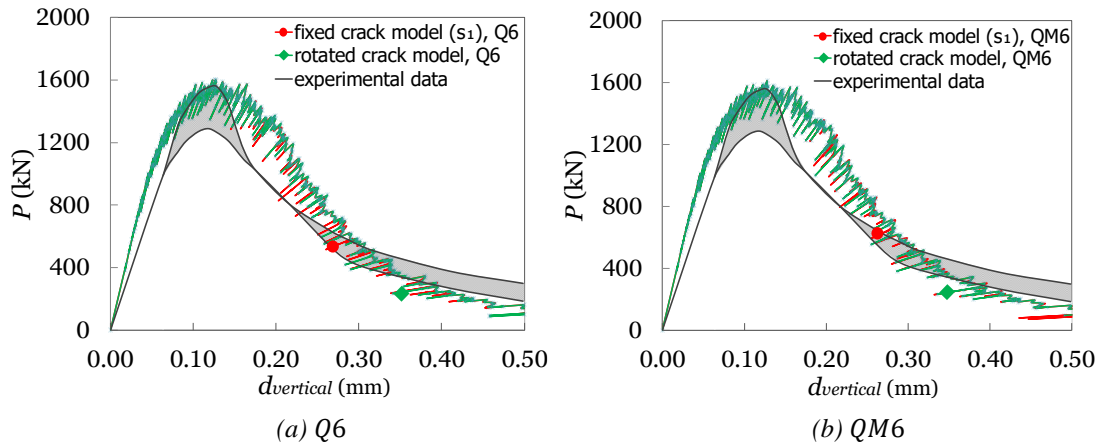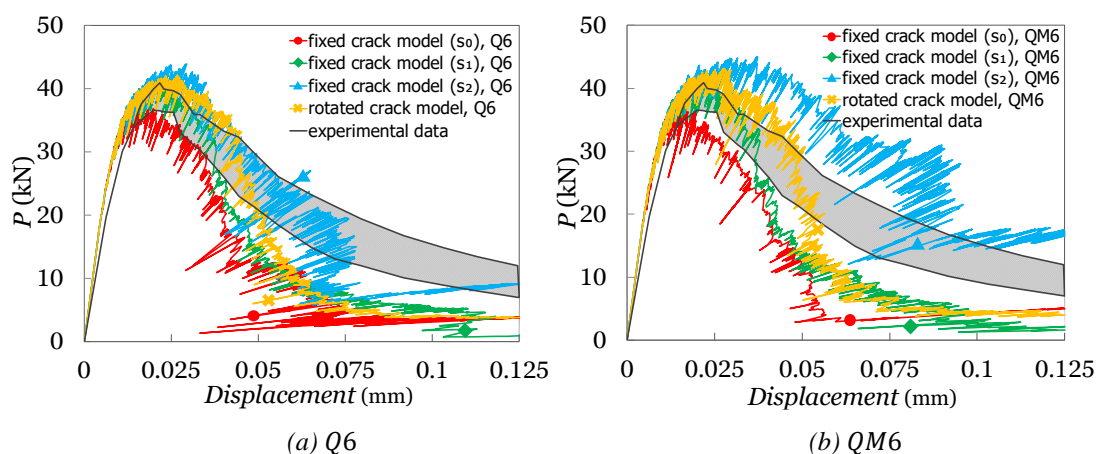

Figure 3.13. Force-Deformation responses of different elements and crack models
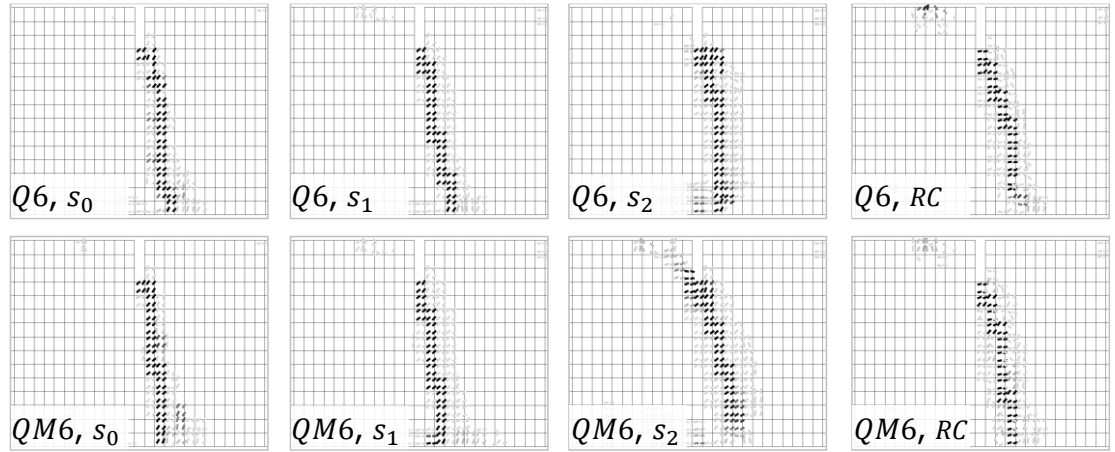
Figure 3.14. Crack patterns of different elements and crack models

Scaled Concrete Dam Test-1

	Value	Unit
E_c	35.7	GPa
f_t	3.6	MPa
G_f	184	N/m
t_s	0.3	m
v	0.1	
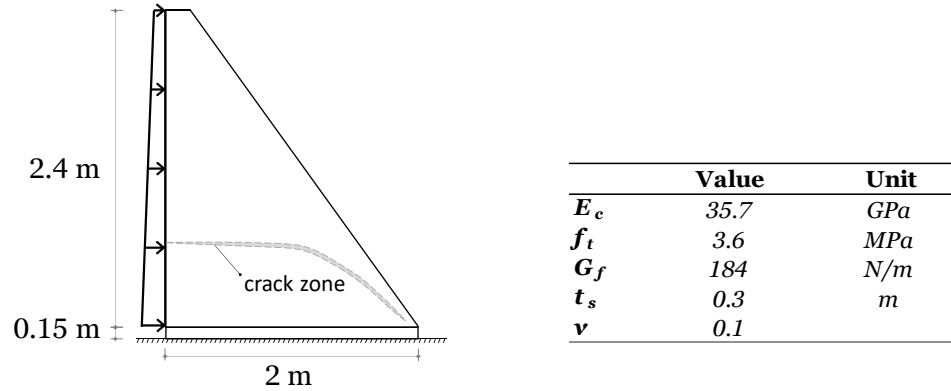
Figure 3.15. Test configuration and properties of scaled dam test-1

Carpinteri et al. (1992) tested a 1:40 scaled gravity dam. The concrete dam was fixed at its base and subjected to equivalent lateral loads (Figure 3.15). For the material properties of the dam, concrete's elastic modulus, Poisson's ratio, tensile strength, density and the fracture energy were 35.7 GPa, 0.10, 3.6 MPa, 2400 kg/m^3 and 184 N/m, respectively. The thickness was 30 cm. Neither the choice of crack models nor the different quadrilateral elements made a significant difference in the force-crack mouth opening displacement curves. For all cases, the capacity was found to be about 7% higher than the experimental ones (Figure 3.16). The crack patterns are provided in Figure 3.17. Although, the best match was obtained by the s_0 ($\beta = 0.02$) and $QM6$ element, almost all combinations succeeded in matching the curvature of the path.
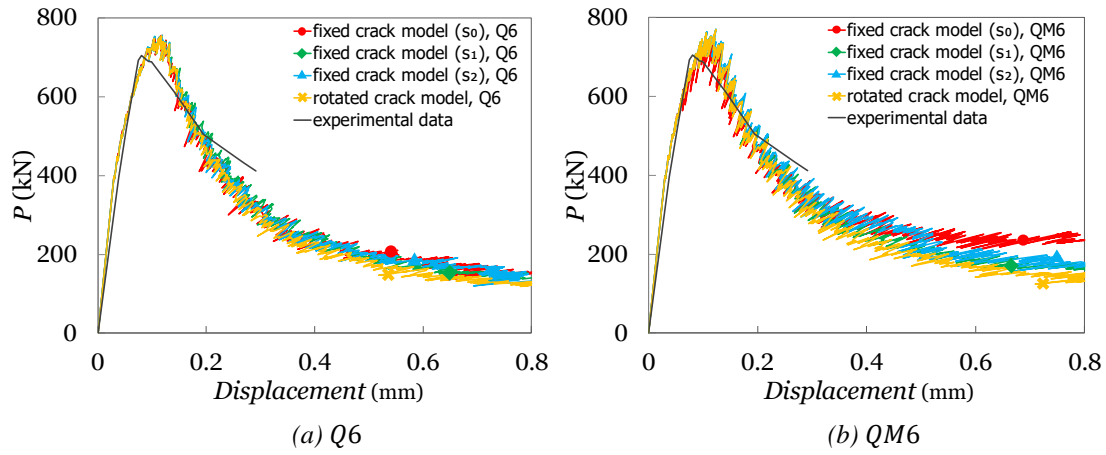
Figure 3.16. Force-Deformation responses of different elements and crack models
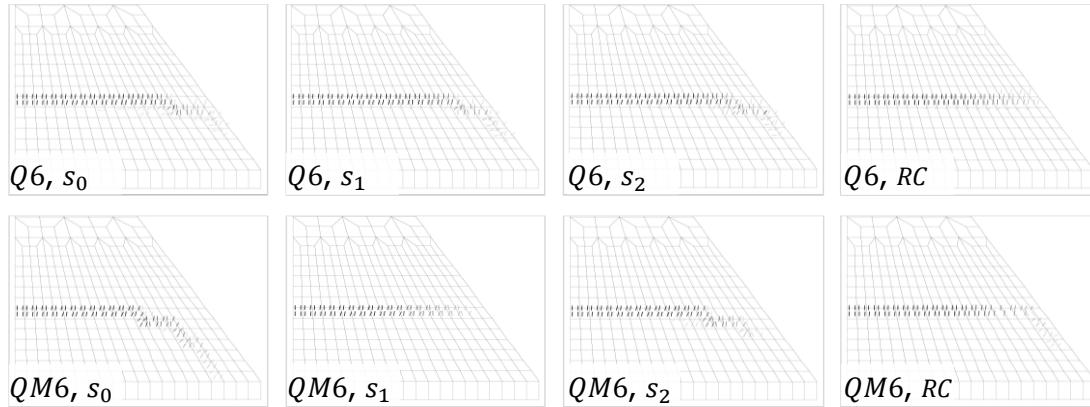
Figure 3.17. Crack patterns of different elements and crack models.

Scaled Concrete Dam Test-2

	Value	Unit
E_c	13.5	GPa
f_t	1	MPa
G_f	100	N/m
t_s	0.2	m
v	0.2	
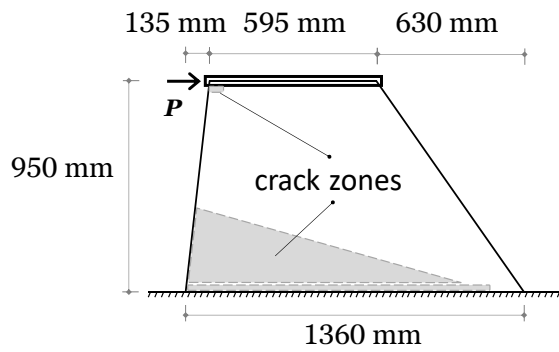
Figure 3.18. Test configuration and properties of scaled dam test-2

Alper et al. (2015) experimentally tested a scaled roller compacted concrete dam at METU Laboratory (Figure 3.18). The specimen was numerically investigated as a

benchmark of SLA. The dam was fixed at its base and subjected to the lateral load. It was reported that a vertical load of 400 kN was applied on the dam specimen to reflect proper gravitational actions. For the material properties of the specimen, concrete's elastic modulus, Poisson's ratio, tensile strength and the fracture energy were 13.5 GPa, 0.20, 1.0 MPa and 100 N/m, respectively. The thickness of dam was 20 cm. According to the results, for the stiffness of the dam an almost exact match was obtained. Additionally, the maximum lateral load capacity of the specimen was approximately matched in force-crest displacement curve (Figure 3.19). For the case of crack models, as in the previous test, s_0 ($\beta = 0.05$) and s_2 provided the best matches. The crack pattern observed during the experiment is given in Figure 3.18. As in the figure, the actual cracks started at the bottom of the section and propagates from upstream to downstream. Then additional cracks initiate from the middle height of the dam section and joins with the bottom crack. According to the results, s_0 and s_2 crack models led to the best match of the actual crack pattern (Figure 3.20). It can be said that these results in determining crack behavior are quite encouraging.
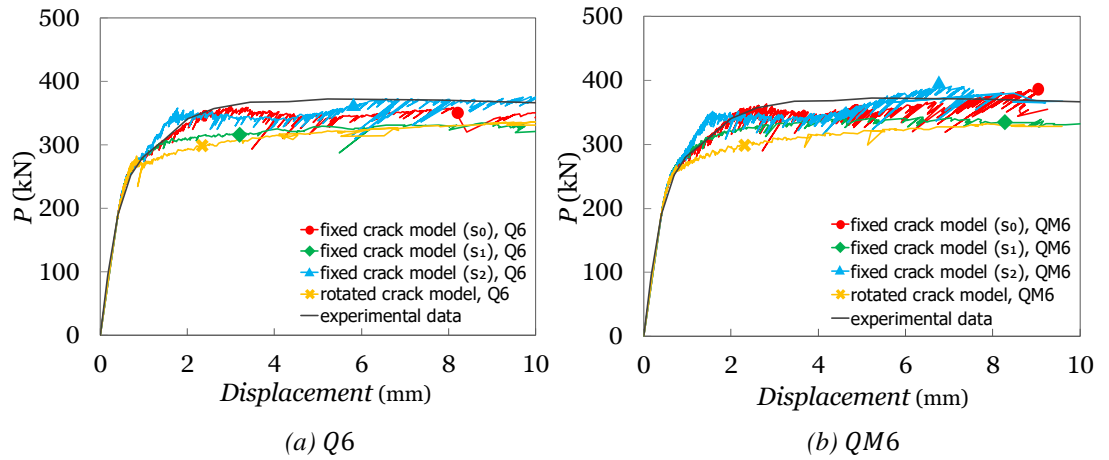
Figure 3.19. Force-Deformation responses of different elements and crack models

| Q6, s_0 | Q6, s_1 | Q6, s_2 | Q6, RC |
| QM6, s_0 | QM6, s_1 | QM6, s_2 | QM6, RC |
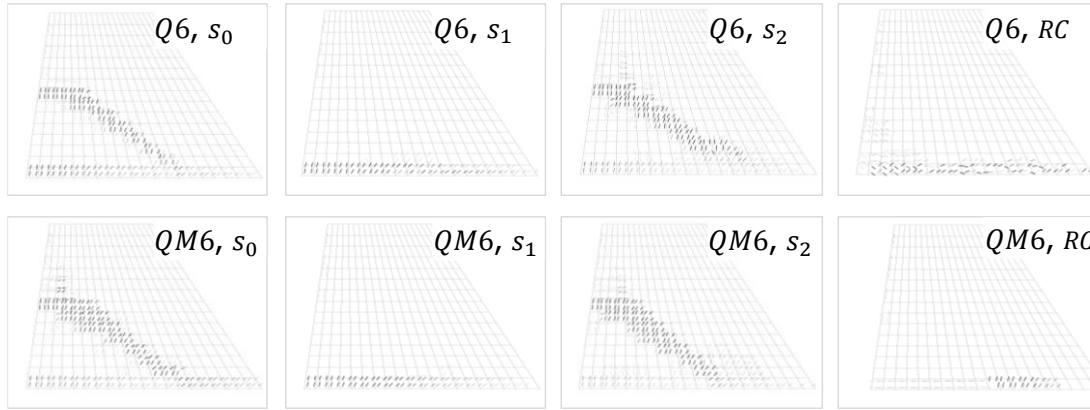
Figure 3.20. Crack patterns of different elements and crack models

3.3.2.3. Dam-Reservoir Interaction Validations

To evaluate the dynamic response of dam reservoir system, the simplified closed form formulation suggested by Bouaanani and Perrault (2010) was adopted. In his technique, the modal response of a gravity dam on a rigid foundation can be related hydrodynamic pressure by following procedure explicitly stated (see Chapter 3.3.1). To evaluate the solution, author employed a dam of 121.92 m height with vertical upstream and 0.8 downstream slopes. The material properties of the concrete were reported as 25 GPa, 0.20, 2400 kg/m^3 for modulus of elasticity (E_c), Poisson's ratio and density (ρ_c), respectively. The density of water and the velocity of pressure waves were taken as 1000 kg/m^3 and 1440 m/s. The solution was carried out with fundamental structural mode and 25 reservoir modes under unit acceleration. In the following figures, the solution presented in the original report is compared with the results of the simplified technique. The further details can be found in Bouaanani and Perrault (2010).

In the beginning, real and imaginary parts of the frequency dependent eigenvalues (λ_n) for each reservoir mode n were compared. Frequency (w) was normalized by the natural frequency of the full reservoir ($w_0 = \pi C/(2H_r)$). Calculations were made for two wave reflection coefficients (α) namely, 0.95 and 0.65. As in the Figure 3.21, real and imaginary parts of the first three eigenvalues can successfully be matched.

(a) Real part, $\alpha = 0.95$ *(b)* Real part, $\alpha = 0.65$

(c) Imaginary part, $\alpha = 0.95$ *(d)* Imaginary part, $\alpha = 0.65$
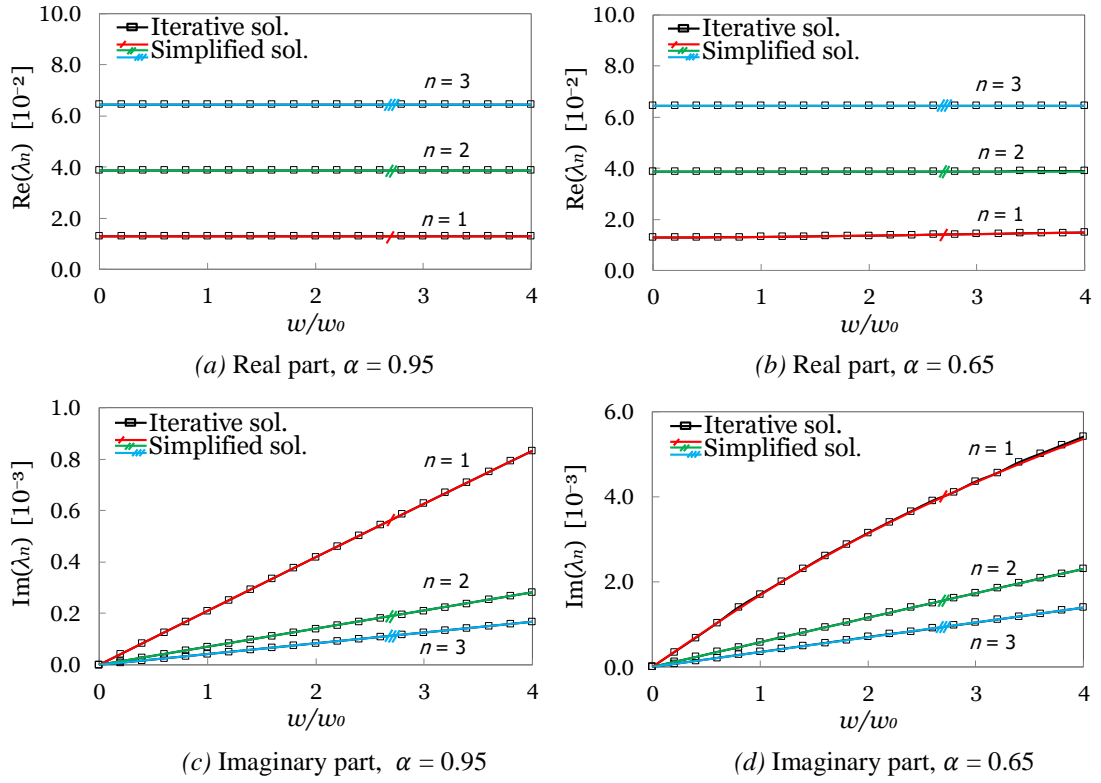
Figure 3.21. Eigenvalues with different values of α

The complex-valued hydrodynamic pressure frequency response function for horizontal direction is given in Eq (3.15). For the first mode of the dam, absolute value of rigid ($\bar{p}_0$) and flexible ($\bar{p}_i$) parts of the equation are calculated for $\alpha = 0.95$ and $\alpha = 0.65$ values, respectively (Figure 3.22). The hydrodynamic pressures are normalized by mass density of water, gravitational acceleration (g) and reservoir height. Consequently, the exact match was obtained for all cases.

(a) Rigid part, $\alpha = 0.95$ *(b)* Rigid part, $\alpha = 0.65$
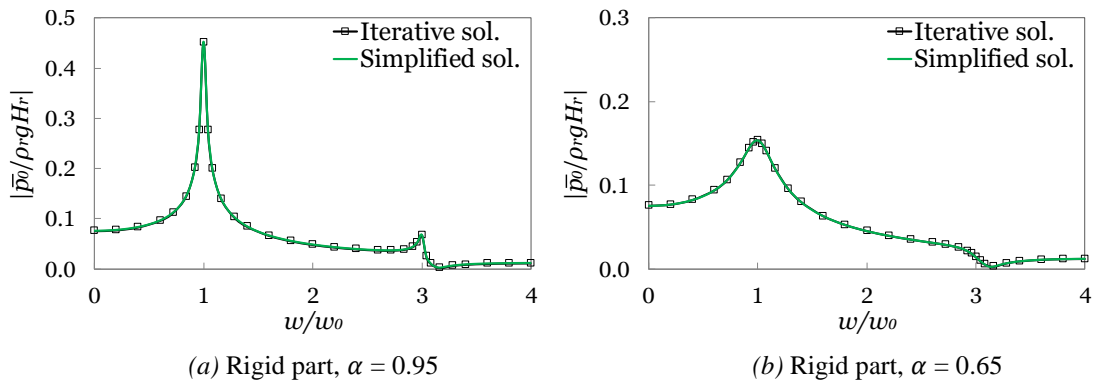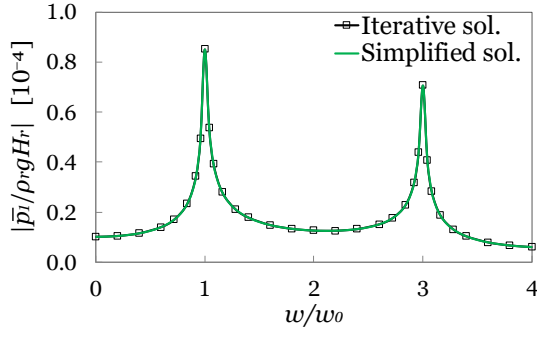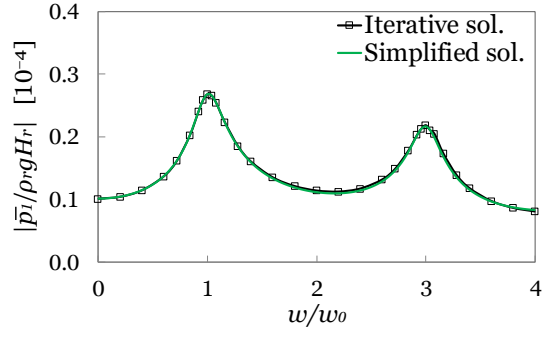
(c) Flexible part, $\alpha = 0.95$ · *(d) Flexible part, $\alpha = 0.65$*

Figure 3.22. Hydrodynamic pressure at dam heel for the first mode
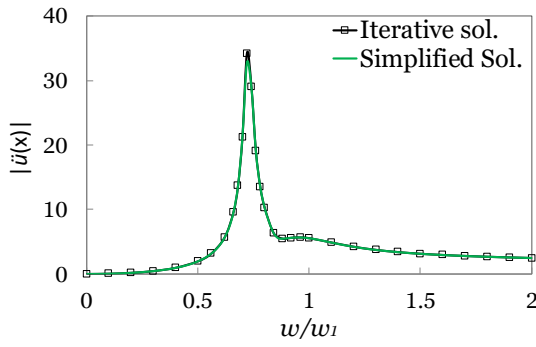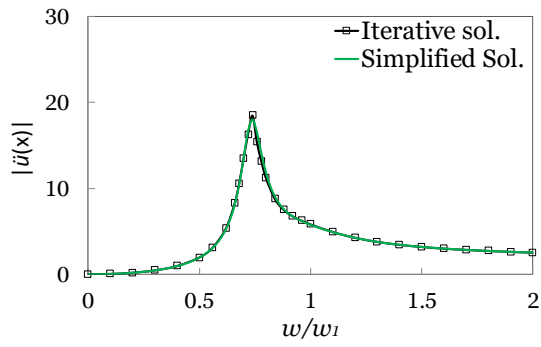
(a) E = 25 GPa, $\alpha = 0.95$ · *(b) E = 25 GPa, $\alpha = 0.65$*
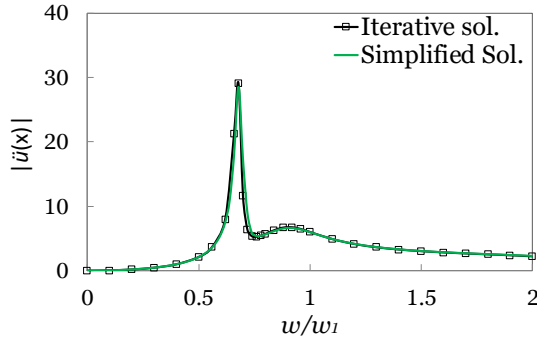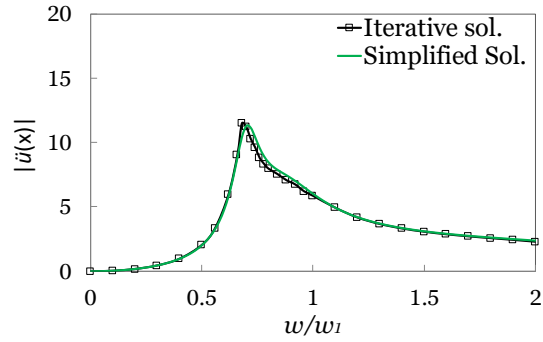
(c) E = 35 GPa, $\alpha = 0.95$ · *(d) E = 35 GPa, $\alpha = 0.65$*

Figure 3.23. Horizontal acceleration at dam crest with different values of α and E

The effects of dam-reservoir and foundation-reservoir interactions are calculated by Eqs. (3.20-3.22) as additional modal parameters. The resulting parameters represent a SDOF system in which all interaction effects are implicitly included. In Figure 3.23, the absolute value of the frequency response function of horizontal acceleration ($\ddot{u}(x)$) at the dam crest under unit acceleration with 5% damping ratio is presented.

(a) E = 25 GPa, α = 0.95 *(b) E = 25 GPa, α = 0.65*

(c) E = 35 GPa, α = 0.95 *(d) E = 35 GPa, α = 0.65*
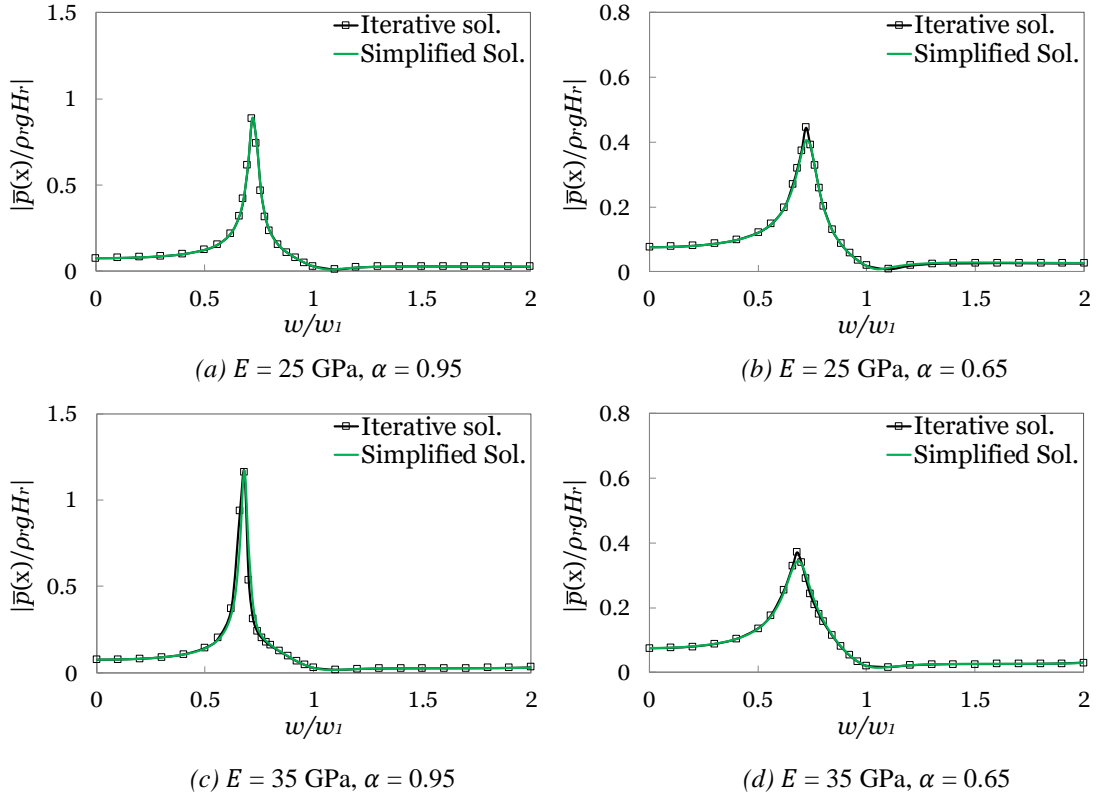
Figure 3.24. Hydrodynamic pressure at dam crest with different values of α and E

The absolute value of frequency response functions of total hydrodynamic pressure at dam heel was calculated (Figure 3.24). The results of the iterative solution were successful with the simplified method. However, for $α = 0.65$, the values at the peak level were slightly lower. This could be due to the differences in the finite element model and so the mode shape between Bouaanani and Perrault (2010) and this study.

The total hydrodynamic pressure ($\bar{p}$) distributions at the upstream face of the dam were calculated and presented (Figure 3.25) over the dam height (y). Results are given for different w/w_1 ratios, namely 0.6, 0.8 and 1.0. Except 25 GPa and $w/w_1 = 0.8$ cases, a satisfactory match was provided between the iterative and simplified methods. The next figure (Figure 3.26) shows the change in ratio of the fundamental mode frequency of the dam on rigid foundation and FR ($\tilde{T}_1$) to the one with ER (T_1). $\tilde{T}_1$ values were calculated by plotting the fundamental mode response functions and identifying the frequency corresponding to the first resonant peak, as suggested in the

55

study. The results are given in different ratios of reservoir height (H_r) and dam height (H). The reservoir interaction was extended the periods as expected. The damping ratio of the SDOF system including reservoir effects ($\tilde{\xi}_1$) was calculated by employing the formulation suggested in Bouaanani and Perrault (2010). The effect of reservoir height on the damping ratio is presented in Figure 3.27. According to the results, the simplified method is successful in accurately estimating the hydrodynamic effects.

(a) E = 25 GPa, α = 0.95

(b) E = 25 GPa, α = 0.65

(c) E = 35 GPa, α = 0.95

(d) E = 35 GPa, α = 0.65
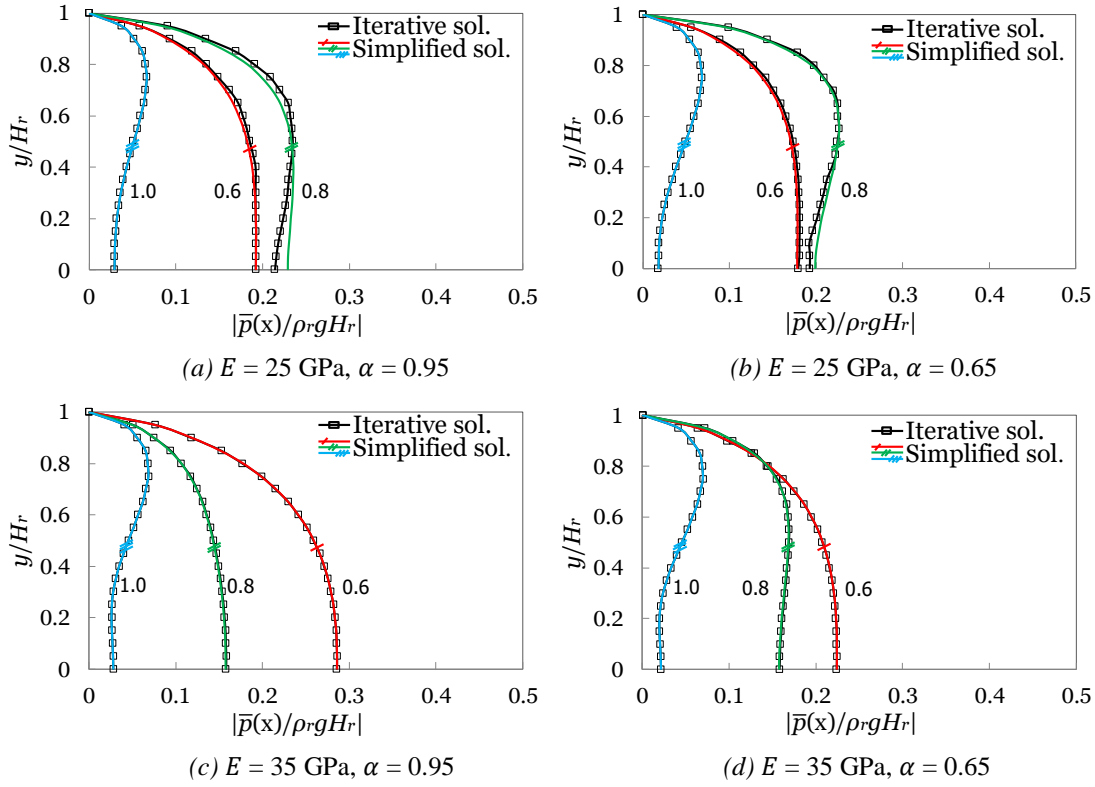
Figure 3.25. The total hydrodynamic pressure distributions over reservoir height

(a) E = 25 GPa, α = 0.95

(b) E = 25 GPa, α = 0.65

(c) E = 35 GPa, α = 0.95   *(d) E = 35 GPa, α = 0.65*
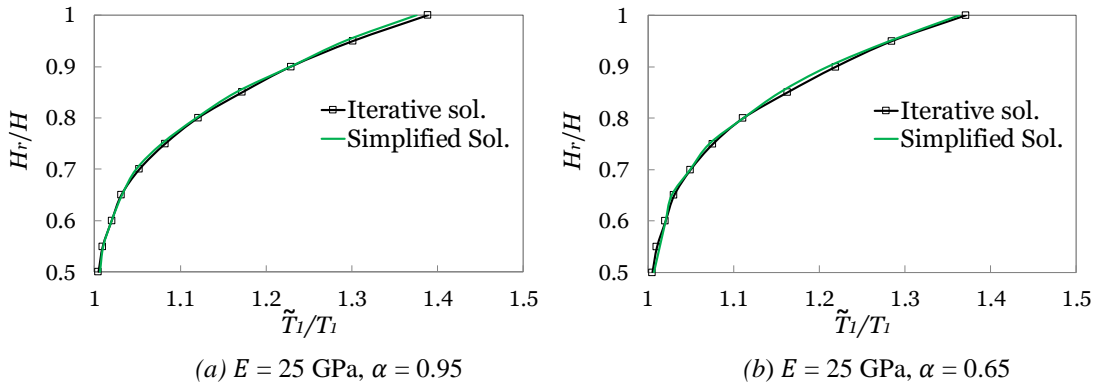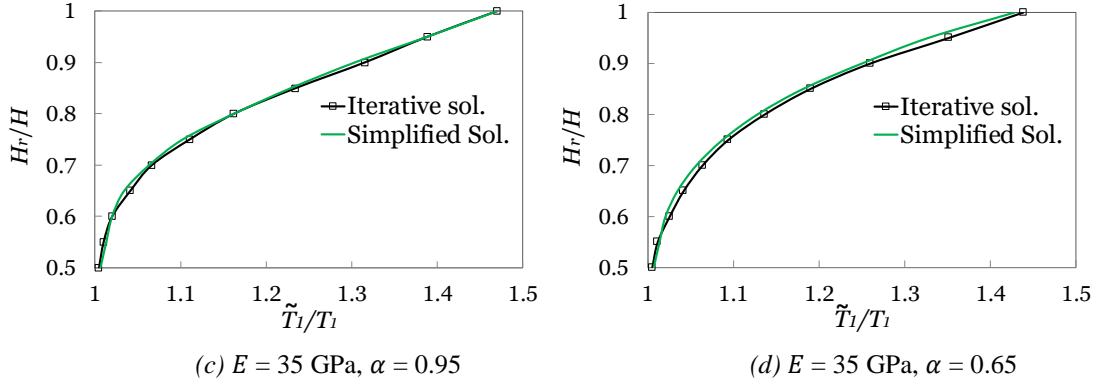
Figure 3.26. Period extension for different level of reservoir heights

(a) E = 25 GPa, α = 0.95   *(b) E = 25 GPa, α = 0.65*

(c) E = 35 GPa, α = 0.95   *(d) E = 35 GPa, α = 0.65*
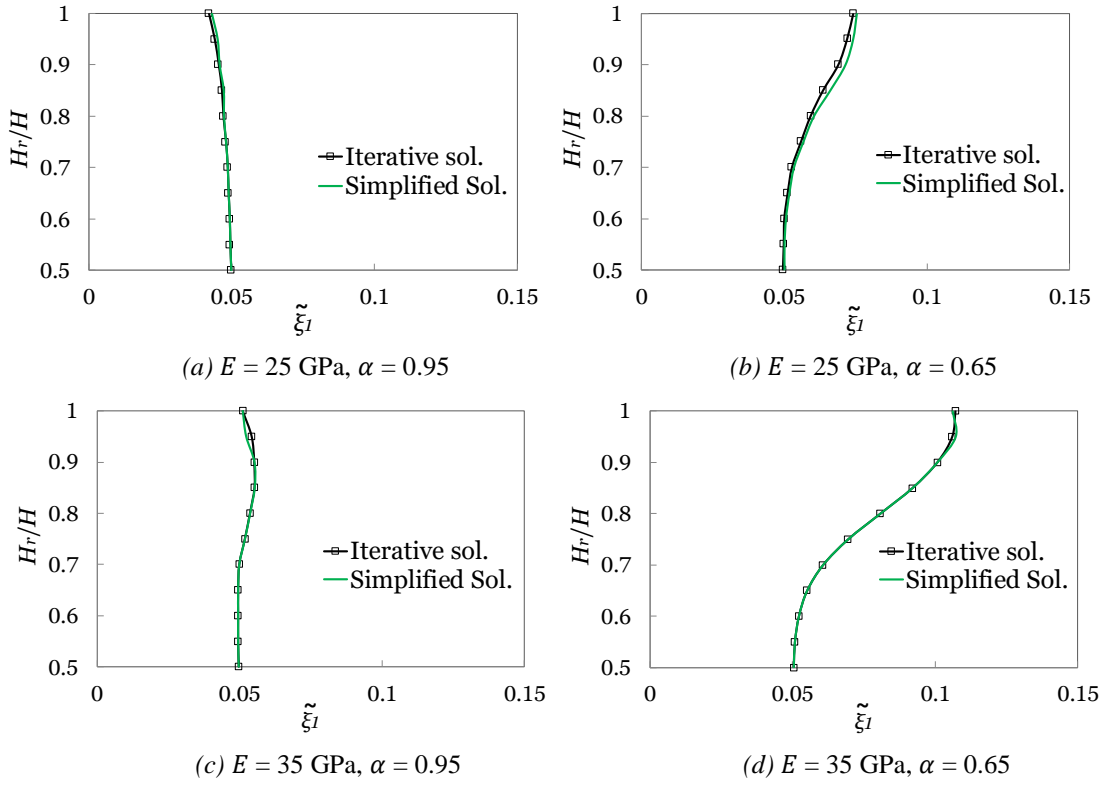
Figure 3.27. Damping ratio variation for different level of reservoir heights

The last graph regarding the validation contains the information of the main interest of this study, namely, the hydrodynamic load distribution on the reservoir surface (Figure 3.28). The hydrodynamic loads ($f_h(y)$) are normalized with hydrostatic load (F_{st}), dam height (H), and spectral acceleration ($S_{a1}(\widetilde{w}_1, \widetilde{\xi}_1)$), respectively. Load were successfully calculated for all the cases examined.

57
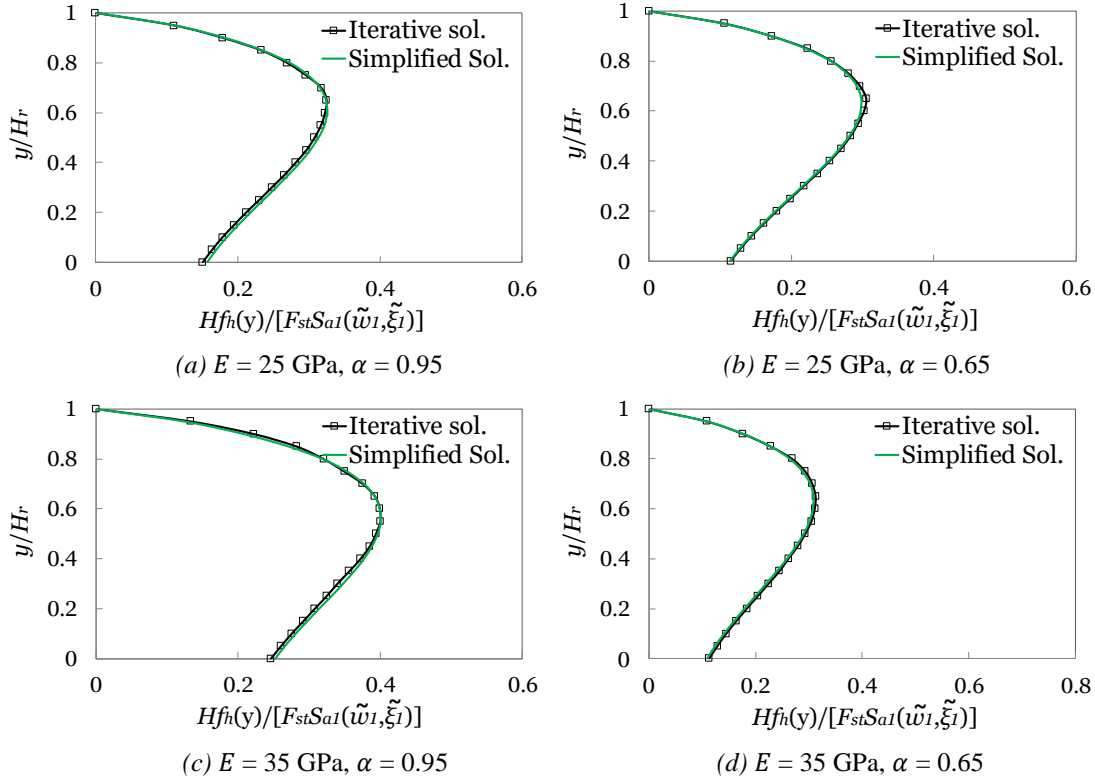
Figure 3.28. Hydrodynamic force distribution on dam

The four subplots are labeled:

(a) E = 25 GPa, α = 0.95

(b) E = 25 GPa, α = 0.65

(c) E = 35 GPa, α = 0.95

(d) E = 35 GPa, α = 0.65

With y-axes labeled y/H_r and x-axes labeled $Hf_h(y)/[F_{st}S_{a1}(\tilde{w}_1,\tilde{\xi}_1)]$, legends showing "Iterative sol." and "Simplified Sol."

3.3.3. Simplified Analysis with SLA Method

Although the time-history analysis is a powerful tool for the dam engineering, its application for dams is still a challenge. Since the water compressibility and the bottom absorption are frequency dependent, the solution should also be followed in the frequency domain. This situation usually prevents the analysis from being performed nonlinearly. Hybrid time history analysis appeared as an alternative method for both evaluating exact hydrodynamic forces and the material nonlinearity (Darbre and Wolf, 1988). However, beyond the linear limits, the validity of the hybrid method should still be evaluated. The nonlinear response of the concrete gravity dams is mostly sensitive to the material, section geometry and the ground motion characteristics. When all these effects are considered, it seems that new approaches are needed in the literature in the evaluation of such structures. Taking the advantage of the first mode being dominant, the static pushover analysis, which is specialized for the concrete gravity dams, can be a competitive alternative. In this part, the simplified

analysis of concrete dams with the SLA method will be critically evaluated by comparing the results obtained by nonlinear time history analyses.

The procedure requires that multiple methods described in the previous sections be used together. Two independent loads were employed for the procedure. Self-weight and the hydrostatic forces were selected as the primary loads (*Load A*). For the secondary loads, the modal analysis is first performed. By using the modal properties of analyzed model, the inertia and hydrodynamic load distributions are calculated. To perform the pushover analyses of ER and FR dams, these loads are used as the secondary loads (*Load B*). The summary of the methodology is presented in Figure 3.29. For this study, the displacement demands were chosen from the results of the nonlinear time history analyzes and the existing nonlinear static procedures. The exact dam sections used in the previous chapter were also used in this part. The dam heights (H) were chosen as 50, 100, 150 m. Upstream face of all dam sections were vertical and the corresponding downstream slope was selected as 0.8. Crest length of the dams were taken as 4 m, 8 m and 12 m for the dam heights of 50, 100, and 150 m, respectively. Plane stress elements ($Q6$) with 1 m thickness were selected as the quadrilateral elements. This element is sufficient in terms of stability and performance, as seen in the verification section. The finite element models of the dams are presented in Figure 3.30.
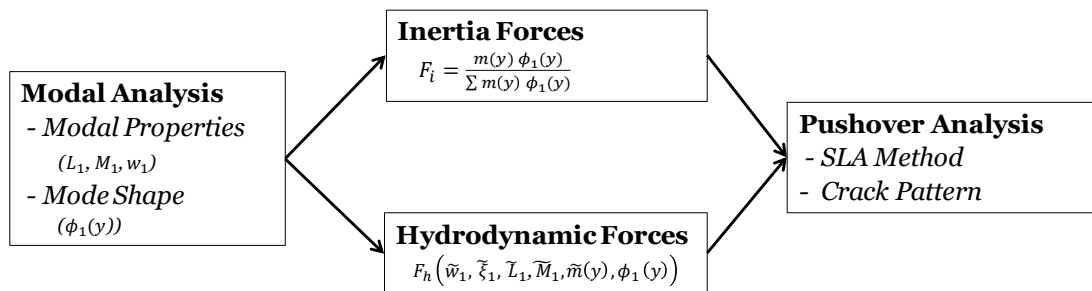
Figure 3.29. Simplified analysis algorithm

For the nonlinear dynamic analysis of dam-reservoir-foundation interaction, the finite element program Diana (TNO Diana, 2016) was used. The generic finite element model of a dam-reservoir interaction is presented in Figure 3.31(a). For the dynamic

analyses of FR dams, fluid and boundary elements were employed. These elements can successfully model the hydrodynamic behavior of the dam-reservoir interaction. However, since the analysis was done in the time domain, the solution was based on the assumption of incompressible water. The model consists of two types of quadrilateral elements and three types of boundary elements and one type of interface element, respectively. The dam body was modeled by the Q8MEM which is a four-node quadrilateral isoparametric plane stress element. The reservoir was modeled by the Q4HT which is a four-node quadrilateral isoparametric element for general potential flow analysis. The B2HT element is a two-node isoparametric boundary element for general potential flow analysis and was used to model boundary conditions. The dam-foundation interaction was modeled by a fluid-structure line interface element which is called as BL4S2 in the program. All these elements are based on linear interpolation and Gauss integration (TNO Diana, 2016).

The free surface condition was assumed as zero pressure as in Eq. (3.10). For the far end, it was assumed that no waves may be radiated by considering the boundary had been placed at sufficiently large distance (Eq. (3.11)). By assuming a vertical upstream face, the continuity between the dam and reservoir elements is satisfied by Eq. (3.12). The density of reservoir water (ρ_r) was taken as 1000 kg/m^3 and included as an input of interface elements. The boundary condition between the absorptive rigid foundation and the reservoir follows the condition given in Eq. (3.13). The damping coefficient in the equation depends on the velocity of sound in water. This parameter was taken as 1440 m/s. The material behavior follows the concept of total strain cracking model, which is based on the smeared band cracking theory (see Chapter 3.3). For the material parameters of the concrete, USACE (1995) and ACI (2005) recommendations were followed. For this study, two level of compressive strengths (f_c), 12 and 28 MPa, are selected. The corresponding elastic modulus (E_c) are calculated with Eq. (3.26) as 20 GPa and 30 GPa, respectively (USACE, 1995). In the equation, 20% dynamic loading increment is included.

$$E_c = 4750\sqrt{f_c} \qquad (3.26)$$

The following equation can be used to estimate the tensile strength (f_t) where no experimental data are available.

$$f_t = 0.35\sqrt{f_c} \qquad (3.27)$$

By using Eq. (3.27), the corresponding tensile strengths are found as 1.25 MPa and 1.85 MPa, respectively. For both materials, the fracture energy (G_f) is selected as 150 N/m (Petterson, 1981). The constitutive relation is selected as the fixed crack method with constant shear retention factor $\beta = 0.2$. The rest of the concrete parameters are taken as 0.2 for Poisson's ratio and 2400 km/m^3 for density, respectively.

The dams in Figure 3.30 have geometries similar to those investigated by Fenves and Chopra (1984) and then later by Medina et al. (1990). To understand if the reservoir effect can be represented correctly, as in aforementioned studies, the models were analyzed in frequency domain under unit horizontal acceleration with 5% hysteretic damping ratio. The material properties of the concrete were taken as 27.5 GPa, 0.20, 2480 kg/m^3 for modulus of elasticity, Poisson's ratio and the density, respectively. The density of water and the velocity of pressure waves were 1000 kg/m^3 and 1438 m/s. The magnitude of the horizontal acceleration of the crest of the dam relative to the ground acceleration are compared in Figure 3.31(b) assuming rigid foundation and ER/FR cases. A sufficient agreement is observed for the results of the finite element model and the reported boundary element method presented in the literature.
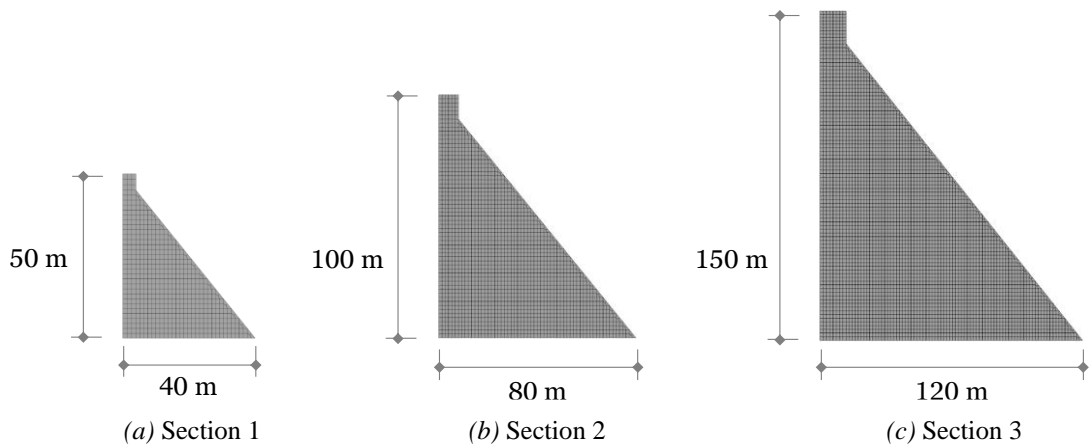
Figure 3.30. Analyzed dam sections

(a) Full reservoir model	*(b)* Unit crest acceleration
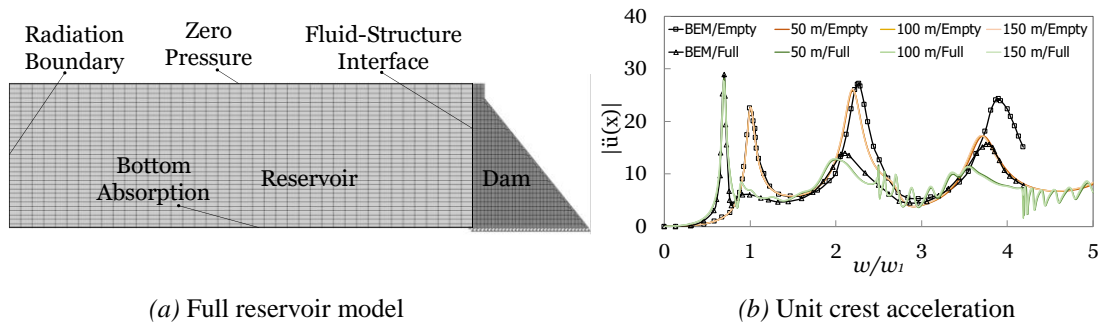
Figure 3.31. Full reservoir model and its validation

The time history analyses were utilized for thirty-seven different ground motion records (Table 2.1). The original records with 5% damping response spectrum of the ground motions are shown in Figure 2.3. All ground motions are scaled to satisfy target spectral accelerations, which is explained in following part.

3.4. Deformation and Damage

3.4.1. Analysis Procedure and Post-Process

According to Federal Guidelines for Dam Safety (Fema-65, 2005), the most important safety concern of the concrete dams subjected to earthquakes is excessive cracking, which can lead to potential instability from sliding or overturning. The guidelines note that seismic analysis is the most cost-effective way to start with the simplest and most conservative method for the problem. If the structure is able to resist the earthquake loading within a certain safety margin, then further analysis may not be necessary. If further studies are needed, they should be conducted progressively in detail. Time history analysis can successfully evaluate the seismic response of the dams during an earthquake. However, this method can be difficult when parameters such as material nonlinearity, dam-reservoir interaction, and frequency dependent damping ratio are included. The objective of conducting a pushover analysis with SLA method is provide a simple tool that can estimate nonlinear behavior of concrete dams accurately without performing a time-history analysis. However, it is not intended to replace a full 3D nonlinear time history analysis. The proposed method and its steps were explained in Chapter 3.3. In the study, the same finite element model and material

properties were used in both simplified analysis and time history analyses, respectively. The results of simplified analysis were compared with those obtained by time analysis. It was aimed to investigate whether the damage can be estimated successfully by the proposed method.

The evaluation of the proposed method will be done by comparing the cracks propagating in the dam body. To compare the damage appropriately, a particular instance of the crack distribution should be selected. For each type of analysis, these instances will be called as "critical states". From the time history analysis results, the highest deformations obtained in upstream and downstream directions were determined. Then at the exact time, the corresponding crack distributions were selected as the critical states. To identify the critical states for simplified analysis, the displacement demands should be known. To do that, the highest deformation values determined by time history analysis were used as target displacements. In addition to that, the target displacements were also calculated using the SDOF approximated nonlinear static procedures. For each target displacement, the critical state was determined and compared to those found by the time history analysis, separately. One difficulty in implementing the method was the proper comparison of damage for two different critical states obtained. A quantitative evaluation of the crack distribution on dam body was needed to compare the results of two separate method. For this reason, a new technique was developed to define cracks in a measurable manner. The method basically serves as a smoothening tool for the scattered crack schemes. The details of the technique are described below.

At the end of an analysis, the crack strains, crack orientations and their locations on the dam body was obtained for a critical state. These parameters are than used to determine an "equivalent crack length" for the dam section (Figure 3.32). The proposed methodology follows the below steps:

- For a critical state, all the primary crack strains larger than 10^{-5} were determined.

- The crack strains at different sections were determined. Each point was selected as a "starting point" (Figure 3.32(c)).

- All the integration points adjacent to the "starting point" were determined. These points were called as "eligible integration points".

- From eligible integration points, those that do not crack (remain within linear limits) were excluded.

The crack path will be found separately in the positive and negative directions, parallel to the horizontal axis. So, the following points should be repeated for both directions.

- The next point was selected from remaining eligible integration points in the desired direction.

- For the positive direction, the ones to the left (right for the negative direction) of the starting point were excluded.

- The integration point having the highest cracking strain from the remaining eligible integration points was selected as the next point of the crack path.

- The steps were repeated until no eligible integration points remain in one direction.

- After the application of the method separately on both sides, an equivalent crack path was determined as the sum of the result obtained in both directions.

- This procedure was repeated for all "starting points" with different cracking strain at different sections by visual examination of the crack strain maps.

- The crack with the largest crack length to section width among all examined level was taken as the critical crack path (Figure 3.32(c)).

By following the steps described above, the critical crack path can be obtained. The total equivalent length of the crack (L_c) is the key parameter to be used in comparing the critical states of the different analysis methods. A flowchart summarizing the method is given in Figure 3.32(a). An example of the application of the method is also presented in Figure 3.32(b). The marked dot is the starting integration point at which

the largest crack strain occurs. Then, the crack paths were determined in both directions and the equivalent crack path was determined.

(a) Proposed method of determining crack length

(b) Crack length
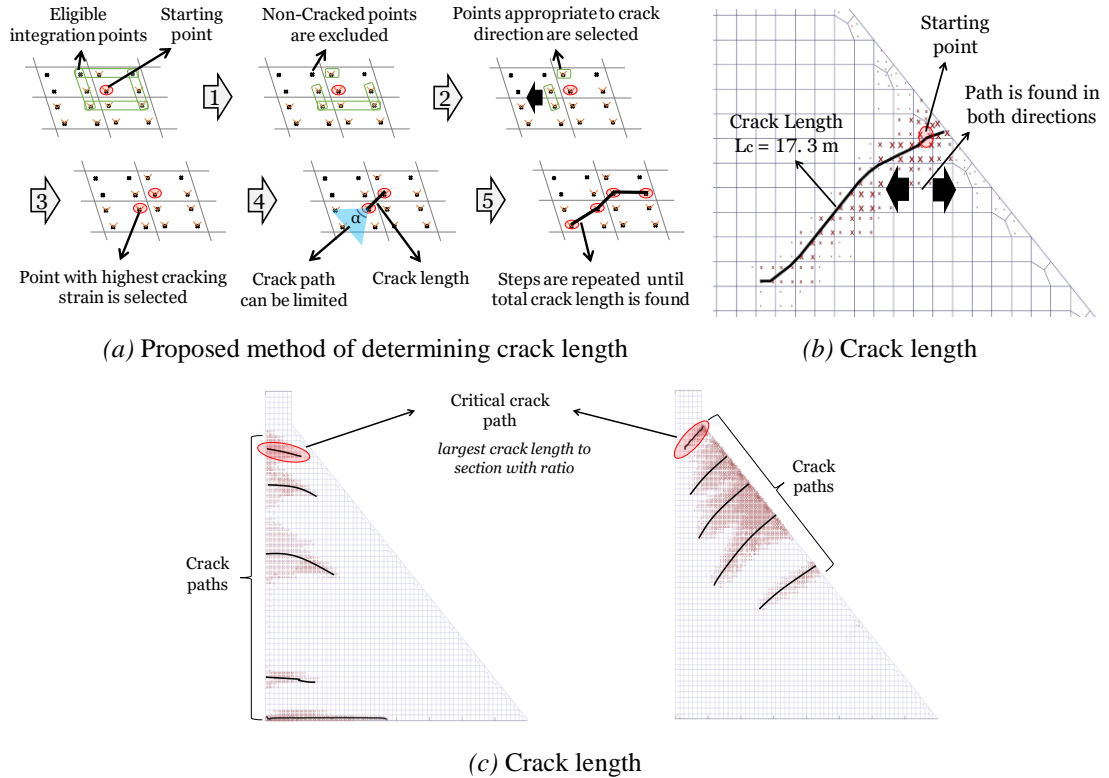
(c) Crack length

Figure 3.32. Equivalent crack length estimation

3.4.2. Ground Motion Scaling

It has been decided that the ground motion records should be scaled to a certain level of spectral acceleration to reasonably correlate the ground motion intensity and damage (cracks) on dams. First, the target design spectrum representing the typical site conditions of concrete gravity dams were selected. The provisions of ATC-40 (1996) was followed for the construction of design spectrum. The design spectrum of the ATC-40 (1996) requires calculation of the shaking intensity, which is defined as the product of the zone factor, the earthquake hazard level, and the near source factor. The average depth and magnitude of the existing earthquake set was found as 25 km and 6.6, respectively. By choosing the seismic source type without knowing slip rate (Type B) and following Table 4-5 and Table 4-6 in ATC-40 (1996), the near source

factor was found as 1.0. If the earthquake hazard level is taken as one, the zone factor may be variable. The resultant seismic coefficients simply represent the peak ground accelerations. These values were taken to be 0.4 g and 0.6 g, which served as the lower and upper bounds of the target spectra. Then, the interval was divided into 5 equal spectral acceleration levels. The soil profile type was selected as S_B which represented the typical practical cases. The seismic coefficients in ATC-40 (1996) were determined by interpolation. For the corresponding period range of the analyzed sections (*T*: 0.12 sec to 0.43 sec), the mean target spectral acceleration values were finally arranged as 1.0 g, 1.1 g, 1.2 g, 1.3 g, 1.4 g and 1.5 g, respectively. With this information, six different elastic response spectra with 5% damping ratio were constructed.

Damping ratio of concrete dam structures can be up to 20% when considering material damping, bottom absorption and radiation boundary. However, according to USACE (1995), material damping of concrete dams are limited to 5% for OBE, and 7% for SEE, respectively. For this reason, the damping ratio in this study was taken as 7%, which is common in analysis of such structures. Many studies were conducted to find the coefficient that scale the 5% damped spectra to other damping levels. There are studies that estimate this coefficient by requiring only the damping ratio, as well as requiring period or other seismic parameters. However, all these approaches suggest a damping scaling factor (*DSF*) for converting 5% damped response spectra to any desired damping level (Eq. (3.28)).

$$DSF = S_a(T, \beta_t) / S_a(T, 5\%) \tag{3.28}$$

In the equation, S_a is the spectral acceleration and β_t is the target damping ratio, respectively. For this study, NEHERP (2003) recommended DSF coefficients were employed. All the 5% damped spectra were converted to 7% damped spectra. The final elastic response spectra are presented below along with the fundamental periods of the tested dam structures (Figure 3.33).

(a) Target spectrums   *(b)* Equivalent SDOF system
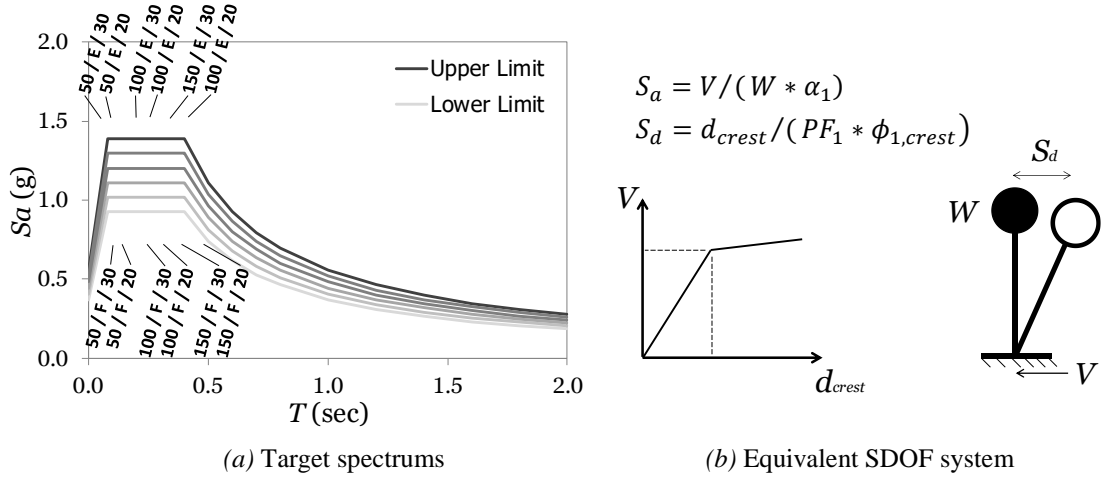
Figure 3.33. Target spectrums and equivalent SDOF system

For ground motion scaling ASCE/SEI-7 (2010) provisions are followed. According to ASCE/SEI-7 (2010), the ground motions shall be scaled such that the average value of the response spectra for the suite of motions is not less than the design response spectrum for periods ranging from $0.2T$ to $1.5T$. T is the fundamental period of the dam in the fundamental mode of the direction being analyzed. To follow the explained procedure, a computer program was developed that capable of scaling randomly selected ground motions as in the following steps;

- For each of the records calculate 5% damped response spectrum $A(T)$.
- Select a target spectrum $A'(T)$ for the same period range.
- For each ground motion records identify SF_1 which minimize the difference between target and response spectrums for a specific period value.
- By trial & error and minimization, find the SF_2 values for each record that by scaling motions with $SF_1 \times SF_2$ ensures that the mean value of the response spectra for the set of scaled motions is not less than the target spectrum over the period range from $0.2T$ to $1.5T$.

By following the described method, each of the 37 floor motions was scaled according to six levels of spectral accelerations. However, 12 type (3 dam sections, 2 type of concrete materials and ER/FR conditions) of model cases have different fundamental

periods (i.e. different period range from 0.2*T* to 1.5*T*) so for each case, the ground motion records were scaled with varying scale factors, individually. The calculated scale factors were presented according to different periods in Figure 3.34 for $E_c = 20$ GPa and in Figure 3.35 for $E_c = 30$ GPa, respectively.
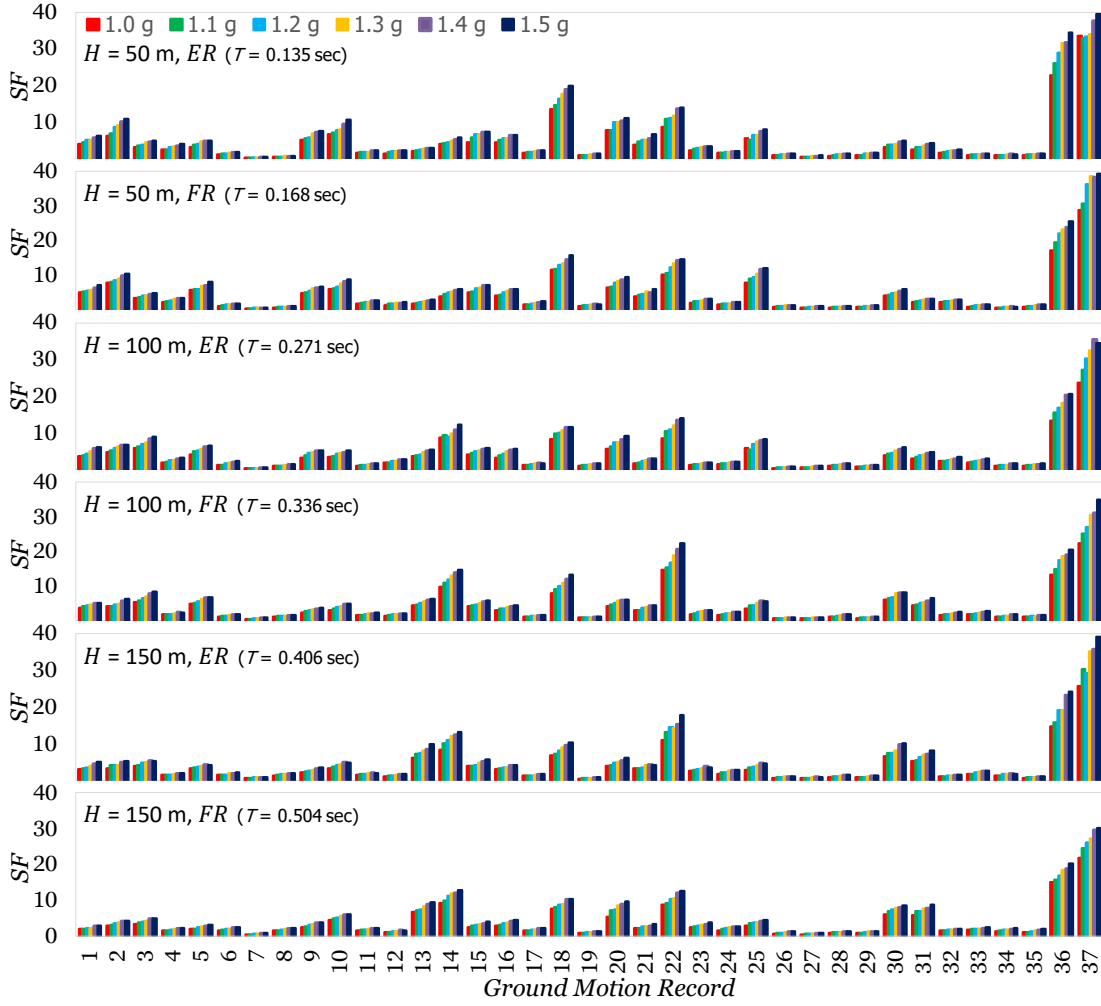
Figure 3.34. Scale factors for ground motions with $E_c = 20$ GPa

68
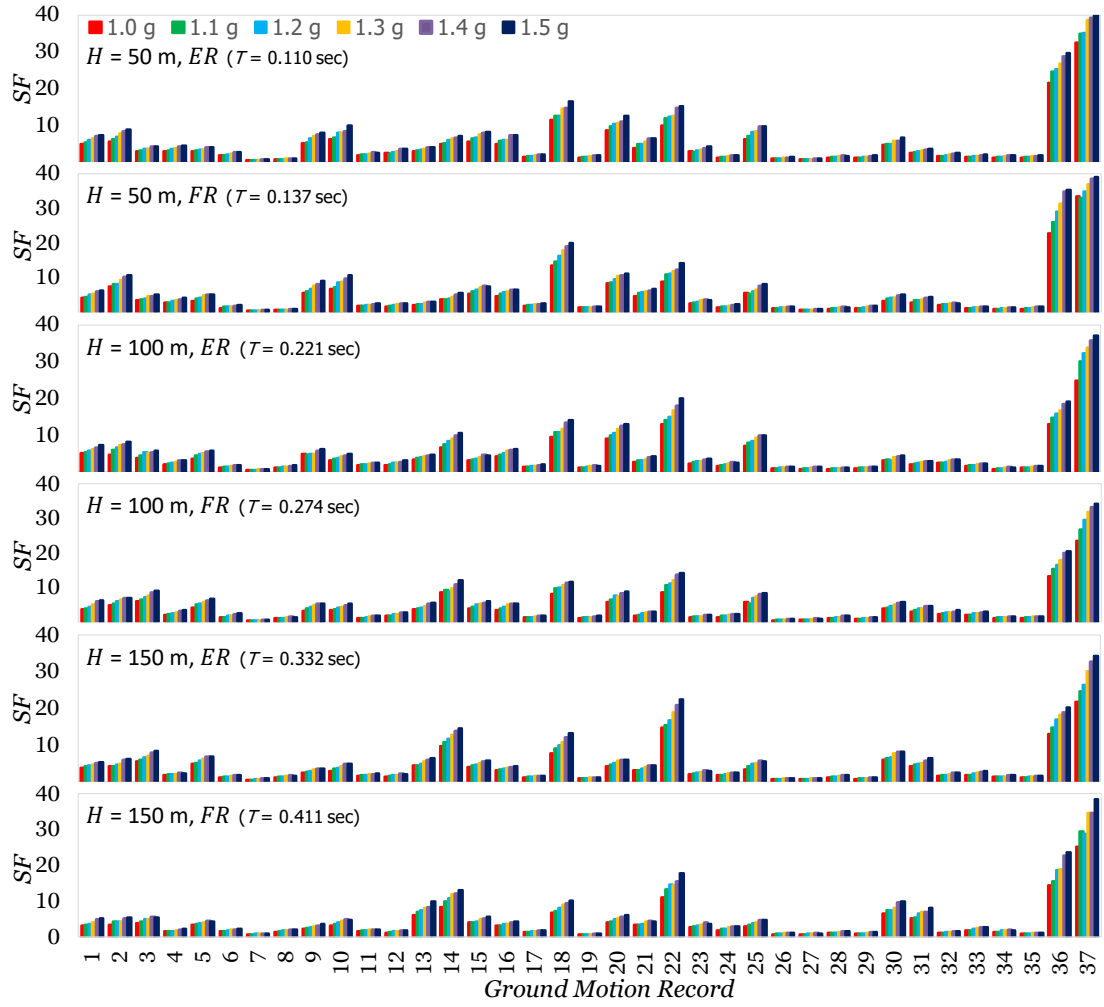
Figure 3.35. Scale factors for ground motions with $E_c = 30$ GPa

The method can lead to various combinations of scaling factors however the mean value of the response spectrum for the scaled motions should not be less than the target spectrum over the period range from $0.2T$ to $1.5T$. The response spectra of the scaled motions are shown in Figure 3.38 and Figure 3.39 for $E_c = 20$ GPa and $E_c = 30$ GPa, respectively. For each of the figures, the dashed lines represent the limits $0.2T$ and $1.5T$. As can be seen, the ground motions are satisfactorily matched to the target earthquake spectra in accordance with the rules of ASCE/SEI-7 (2010).

The spectral acceleration values corresponding to each of fundamental periods are presented at Figure 3.36 and Figure 3.37 for $E_c = 20$ GPa and $E_c = 30$ GPa, respectively. The mean of the spectral accelerations (S_a) are given in Table 3.3. For

each level of scaling, a constant spectral acceleration value will not be obtained since the coefficients can be reached at various levels. However, the standard deviation of S_a is calculated in between 0.05 g and 0.13 g, respectively.
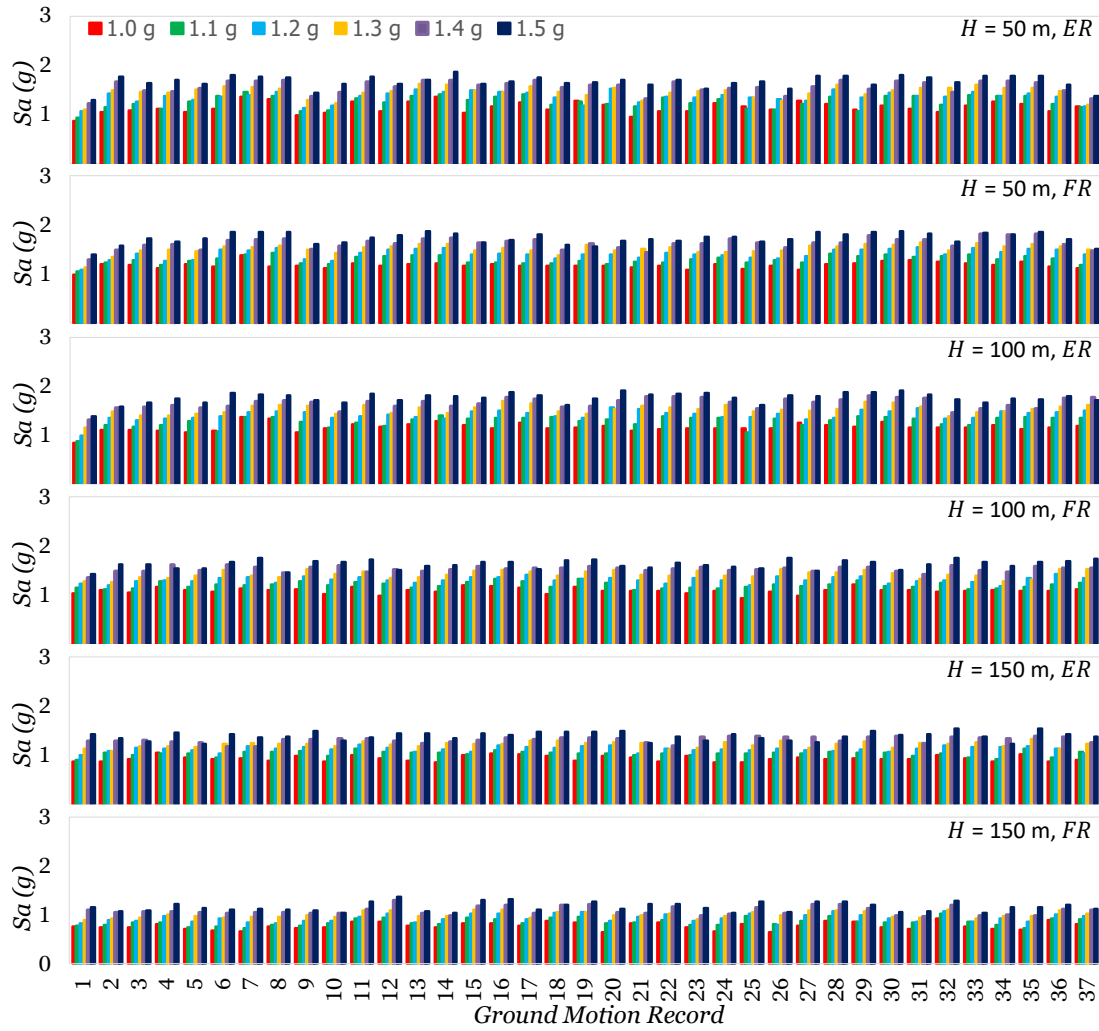
Figure 3.36. Spectral accelerations with $E_c = 20$ GPa
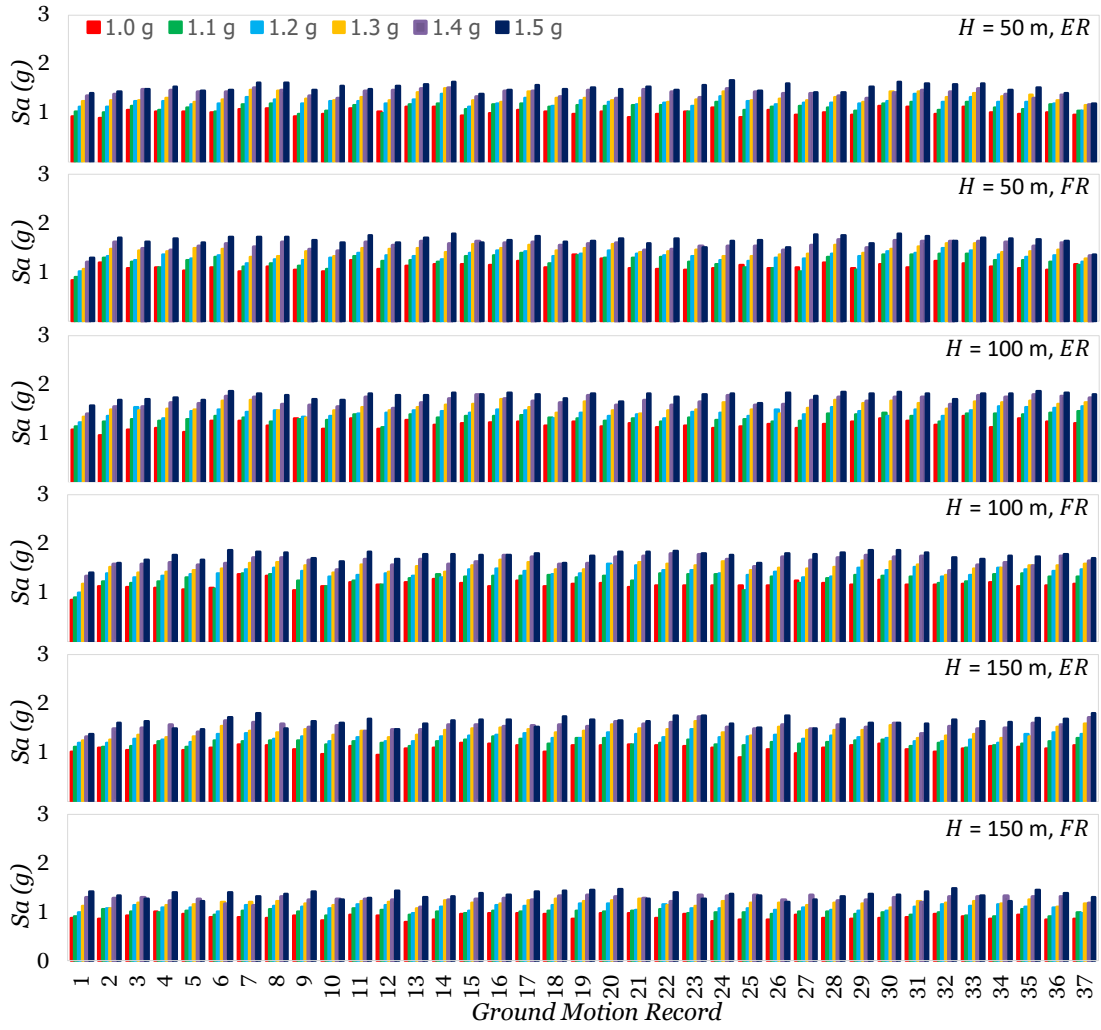
Figure 3.37. Spectral accelerations with $E_c = 30$ GPa

Table 3.3. *Mean S_a values corresponding to the fundamental periods (g)*

	Ec = 20 GPa						Ec = 30 GPa					
	Empty Reservoir			Full Reservoir			Empty Reservoir			Full Reservoir		
	50 m	100 m	150 m	50 m	100 m	150 m	50 m	100 m	150 m	50 m	100 m	150 m
1.0 g	1.14	1.16	0.92	1.18	1.09	0.78	1.02	1.18	1.09	1.12	1.16	0.91
1.1 g	1.25	1.28	1.02	1.29	1.20	0.86	1.12	1.31	1.20	1.23	1.28	1.00
1.2 g	1.35	1.41	1.12	1.41	1.30	0.94	1.22	1.43	1.30	1.33	1.41	1.09
1.3 g	1.45	1.53	1.21	1.52	1.42	1.01	1.31	1.54	1.42	1.44	1.52	1.18
1.4 g	1.56	1.65	1.30	1.63	1.52	1.09	1.40	1.66	1.53	1.55	1.64	1.27
1.5 g	1.67	1.76	1.38	1.73	1.62	1.17	1.51	1.77	1.62	1.66	1.75	1.35
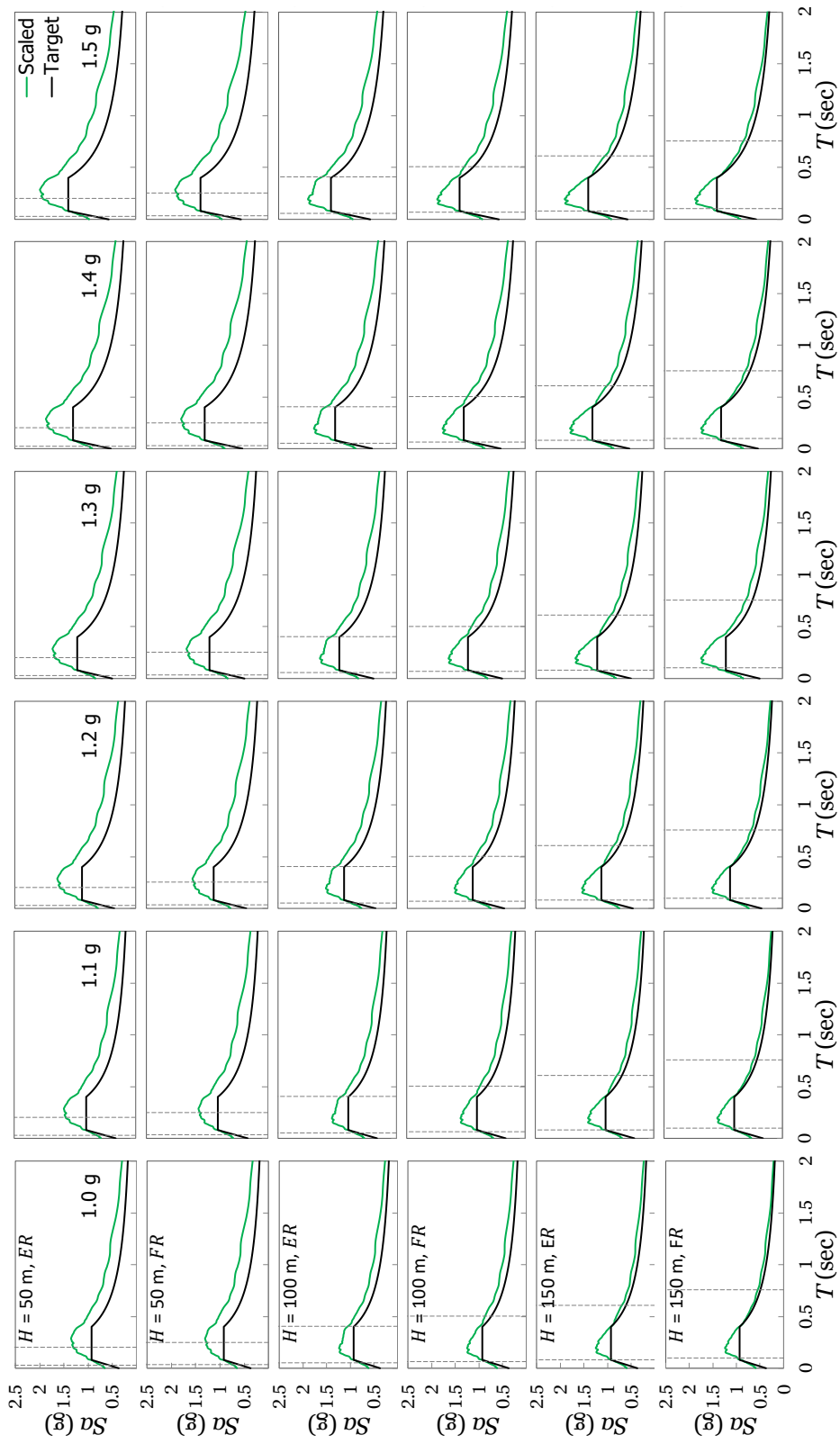
Figure 3.38. Matched spectra set with $E_c = 20$ GPa
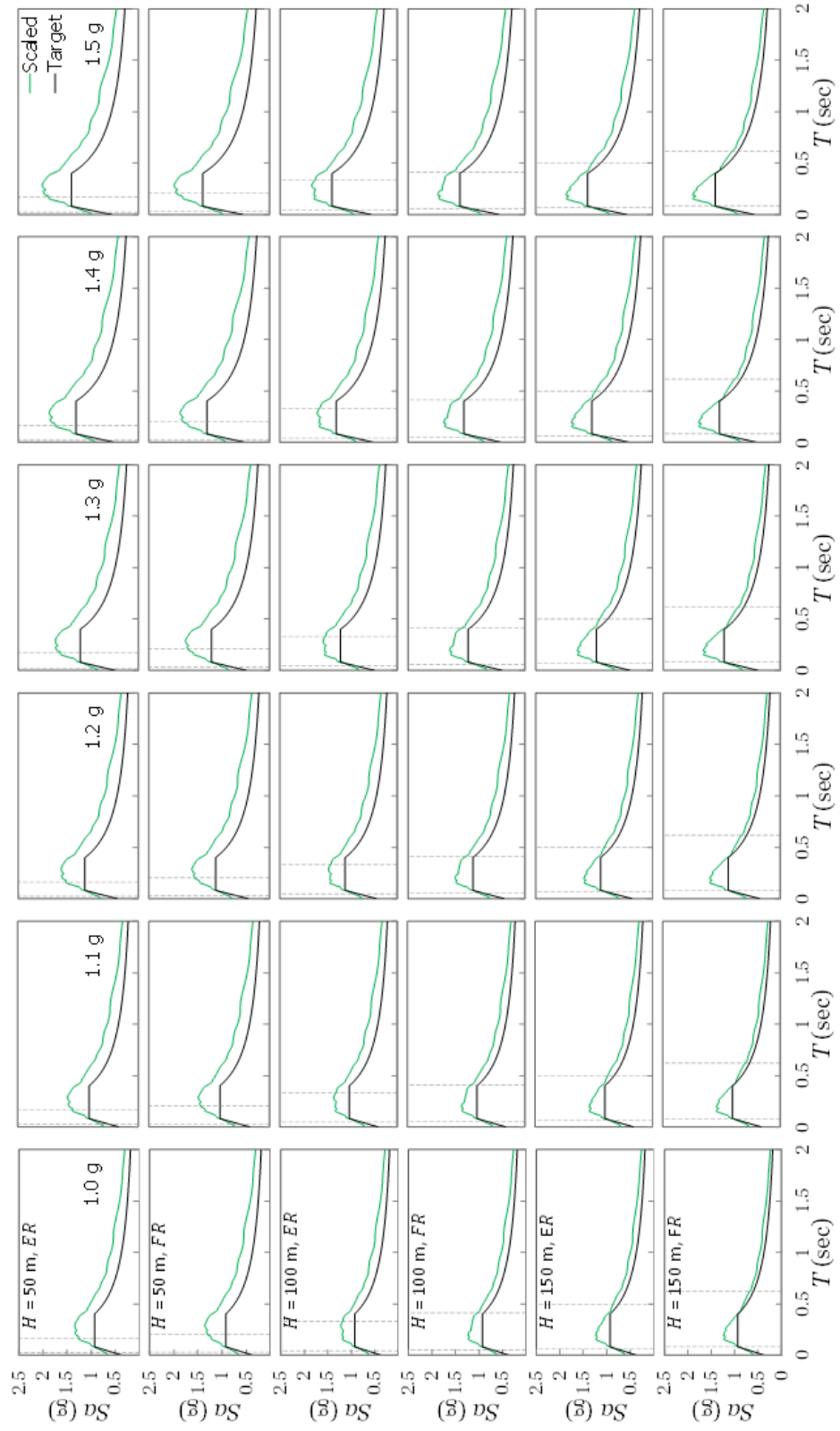
Figure 3.39. Matched spectra set with $E_c = 30$ GPa

73

3.4.3. Nonlinear Static Procedures

Nonlinear static procedures are commonly used in the structural engineering applications to predict seismic demands on structures. It is known that these approaches usually yield successful results for the fundamental mode dominant structures. The general principle of such procedures is to replace the MDOF system into equivalent SDOF one and to determine displacement demand by using the capacity curve and target spectrum (Figure 3.33(b)). Such methods usually require conversion of the capacity curve to the capacity spectrum. The transformation can be done by following equations in ATC-40 (1996):

$$PF_1 = \sum \tilde{m} \ \phi_1 / \sum \tilde{m} \ \phi_1^2 \tag{3.29}$$

$$\alpha_1 = (\sum \tilde{m} \ \phi_1)^2 / [(\sum \tilde{m}) * (\sum \tilde{m} \ \phi_1^2)] \tag{3.30}$$

$$S_a = V / (W * \alpha_1) \tag{3.31}$$

$$S_d = d_{crest} / (PF_1 * \phi_{1,crest}) \tag{3.32}$$

In the equation, $\tilde{m}$ is the mass along dam height, PF_1 and α_1 represent the fundamental mod participation factor and mass coefficient, S_a and S_d represent spectral acceleration and displacement, ϕ_1 is the fundamental mode shape, V is base shear, W is total weight of the dam and d_{crest} is crest displacement, respectively.

For known earthquake levels and dam sections, displacement demands may be calculated by using the nonlinear static procedures. The commonly used static procedures, coefficient (FEMA-356 (2000), FEMA-440 (2005)) and capacity spectrum (ATC-40 (1996), FEMA-440 (2005)) methods, SDOF nonlinear time history analysis approach was adopted in the study. The methods used to determine nonlinear displacement demands are described in following parts.

3.4.3.1. SDOF Nonlinear THA

It is possible to represent a structure with its fundamental mode as an equivalent SDOF model. The capacity curve of the MDOF system can provide the yield capacity and

the stiffness of the SDOF model. Then, the response of the SDOF model subjected to an earthquake excitation can be obtained by the solution of the differential equation. For the SDOF Nonlinear THA solution, the capacity curve was obtained by SLA. Then, the nonlinear THA was performed by employing the SDOF model.

3.4.3.2. Fema-356 Coefficient Method

Fema-356 coefficient method calculates the nonlinear displacement demand by the help of specific coefficients (C_k) obtained through statistical analysis.

$$\delta = C_0 C_1 C_2 C_3 S_a \frac{T}{4\pi^2} g \qquad (3.33)$$

In the equation, C_0 represents the coefficient that relates between actual crest displacement and equivalent SDOF system's displacement, C_1 represents the coefficient that relates between linear and nonlinear response, C_2 represents the coefficient that include the effect of pinched hysteretic shape, C_3 represents the coefficient that increased displacement due to P-Δ effects.

3.4.3.3. Fema-440 Coefficient Method

The method is obtained through the update of the coefficients (C_k) used in existing Fema-356 coefficient method.

$$\delta = C_0 C_1 C_2 S_a \frac{T}{4\pi^2} g \qquad (3.34)$$

In the equation, C_0 is identical to one in Fema-356; but for C_1 and C_2, a new calculation method has been presented. C_3 coefficient has been removed.

3.4.3.4. ATC-40 Capacity Spectrum Method

In the method, a procedure is being used in which equivalent period and damping ratios of the system are iteratively calculated. The basic principle of the method is to compare the capacity curve of the structure by the earthquake demand and estimate the target displacement. The method suggests three different calculation techniques including graphical and analytic procedures.

The capacity and demand curves are required for the application of the procedure. First, the lateral capacity of the dam was determined by SLA. The obtained base shear and crest displacement curve was converted to a spectral displacement versus spectral acceleration curve (capacity spectrum) of the SDOF system. Likewise, earthquake spectrum was defined as an acceleration versus spectral displacement and the demand was determined. The equivalent-damping ratio was calculated by the help of ductility ratio and the equivalent damping ratio coefficient. Target displacement was determined by employing the capacity spectrum, equivalent damping ratio and the earthquake spectrum. If the relative error between target displacement and estimated displacement was not in a desired level, the steps were repeated.

3.4.3.5. Fema-440 Capacity Spectrum Method

Fema-440 capacity spectrum method brought enhancements to the ATC-40 (1996) capacity spectrum method. The method proposes new formulas for the calculation of effective period and effective damping ratio, respectively.

3.4.4. Earthquake Induced Cracks

Earthquake induced cracks are shown for 37 ground motions with different spectral acceleration ranges in Figure 3.40(b). Numerical simulations revealed that concrete gravity dams are possible to experience excess cracking during large earthquakes. The location and size of these cracks are mostly dependent on dam geometry, material type, reservoir condition, soil class and ground motion characteristics. However, considering the time history analysis results, it was observed that there might be certain crack patterns, which are common in such dams.

For each analysis set (e.g H = 50 m dam with E_c = 20 GPa and ER), the results of nonlinear time history analysis were employed to identify the most likely crack patterns. Each dam section was divided into subregions with equal heights of 0.1H. Within each subregion the number of crack initiation points were determined. The highest number of crack initiation points is assumed to be the most likely crack pattern. The common crack patterns obtained with this procedure is shown in Figure 3.40 (a).

It can be stated that the crack lengths presented in Figure 3.40(a) are not the average of all records (i.e. 37 ground motion records), but the most likely crack to occur considering the ground motion. In Figure 3.40, the spectral acceleration levels are presented by the different color tones.

The results revealed some interesting information about the damage patterns of different types of concrete dams. With the assumption that concrete dams will be built on a rigid rock foundation, the most important effect in common crack pattern was the reservoir effect. For the dams with ER, the large cracks were mostly observed on the downstream face of the dams. It was observed that these cracks usually initiated from a position between half and one-third of the dam height. However, the reservoir changed the cracking behavior dramatically. For the case of FR, large cracks were mostly located at the heel of the upstream face of the dams. On the contrary, the downstream cracks were concentrated at the crest and mid region. This effect is more noticeable with increasing height of the dam. It may be seen that the crack pattern of the 150 m height dam with FR cases were quite similar regardless of the earthquake spectral acceleration and material type. Another important parameter affecting the crack pattern was the dam geometry. It is observed that the dams with smaller height were more affected by the earthquake intensity. It is also interesting to note that for higher dams the crest was in more danger of experiencing excessive damage. Additionally, 50 m height dam was the only one that suffered cracks at the heel within the ER cases. There was no significant effect of the spectral acceleration levels on crack initiation locations. However, as the earthquake level increased, the average crack lengths were mostly increased. If the effect of the material was taken into consideration, it can be said that the crack behavior of the rigid dams was less affected by the earthquake intensity.
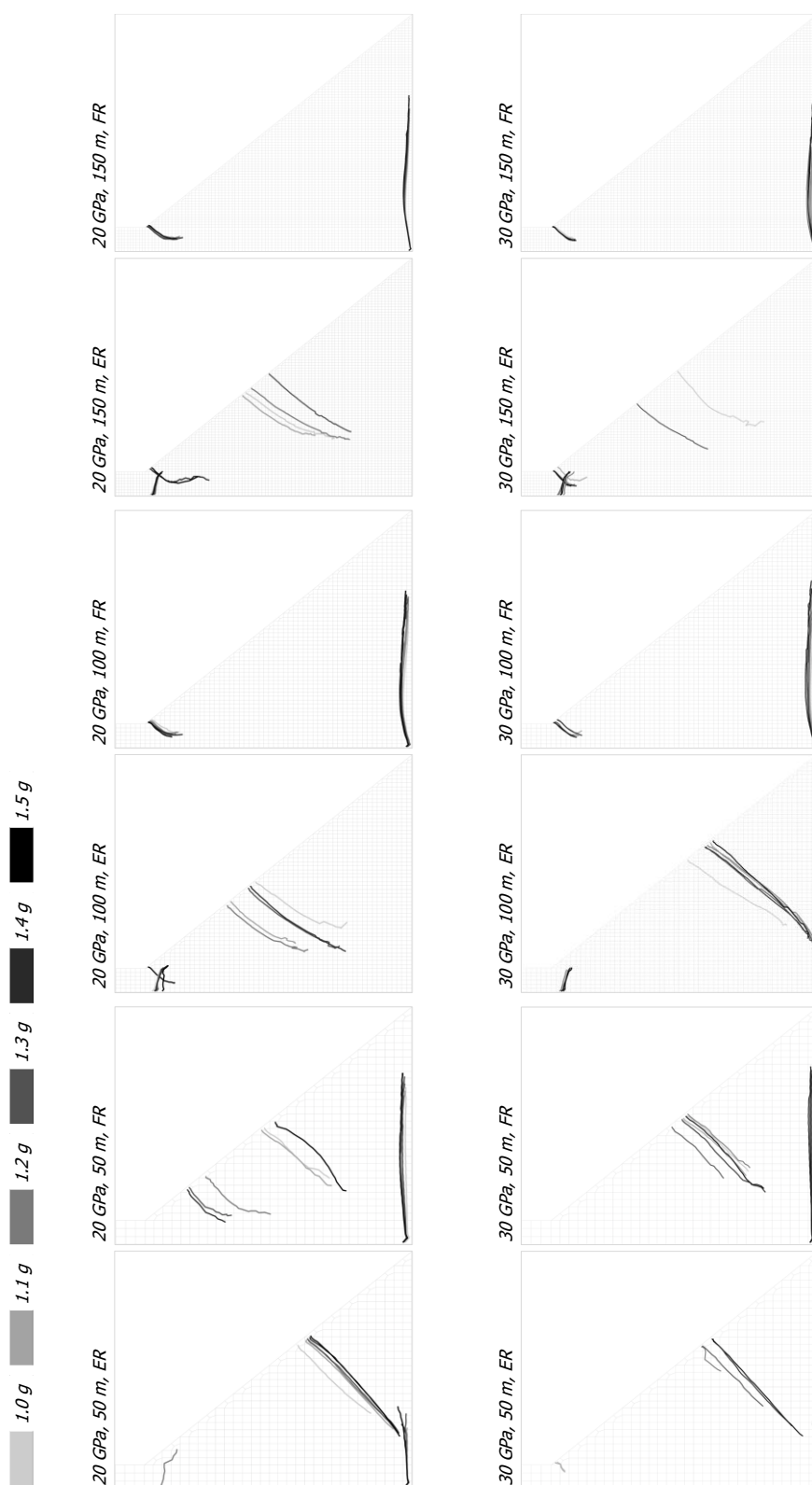
(a) Common crack patterns
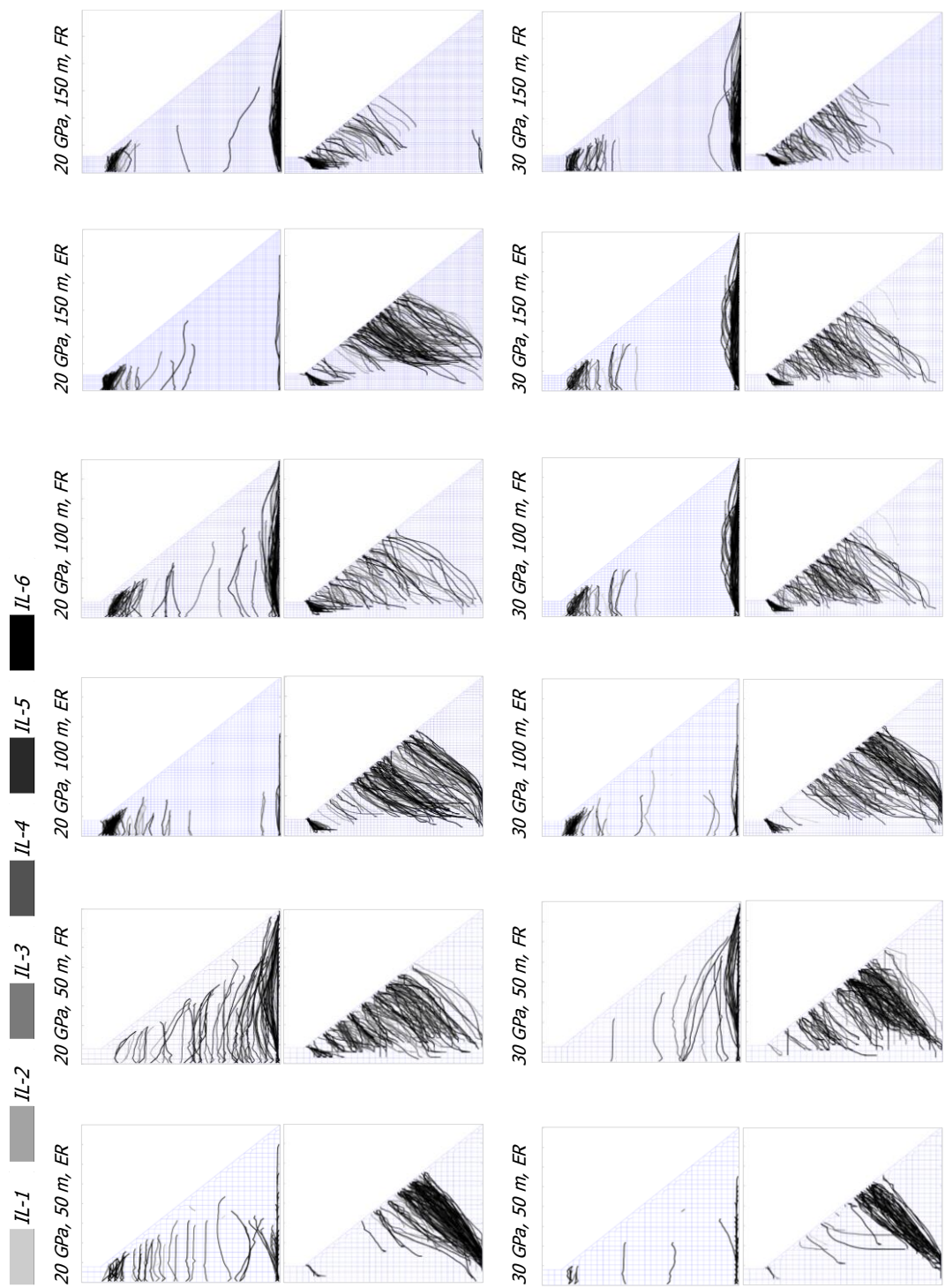
(b) All crack patterns

Figure 3.40. Crack patterns

The aforementioned results were than compared to the simplified analyses results and presented according to different spectral acceleration levels for each dam cases. For each analysis, maximum horizontal deformations of the top of the crest were reordered for upstream and downstream directions. In the following sections, the crack lengths at the time of the maximum crest deformations occurred in the time history analysis were compared with the crack lengths obtained by employing the deformations of nonlinear static procedures and SLA. A consistent measurement of the crack length is often a problem for discrete crack models. However, a successful comparison was provided by employing the proposed equivalent crack length method in Chapter 3.4.1. In order to provide a clear presentation, the results are presented in the following subsections as 50 m height dam with ER and FR, 100 m height dam with ER and FR, 150 m height dam with ER and FR, respectively. For each section, the results are given separately for two directions (upstream – negative dir., downstream – positive dir.).

3.4.4.1. 50 m Height Dam with ER

The fundamental periods of 50 m height dams with ER were found to be between 0.135 s and 0.110 s for $E_c = 20$ GPa and $E_c = 30$ GPa, respectively. While the spectral acceleration levels were between 1.0 and 1.5 g (Table 3.3), the corresponding mean S_a values increased linearly between 1.14 g and 1.67 g for $E_c = 20$ GPa (1.02 g and 1.51 g for $E_c = 30$ GPa). The comparisons of crest deformations are given in Figure 3.41 and Figure 3.42. The first noticeable detail is that the simplified methods usually underestimated the crest deformations. The mean crest displacement in the upstream direction linearly increased between 0.9 cm (1.0 g) and 4.9 cm (1.5 g) for $E_c = 20$ GPa (0.4 cm (1.0 g) and 1.9 cm (1.5 g) for $E_c = 30$ GPa), respectively. The method that gave the closest result to these values was found by CSM A/40 with 18.7% average error for $E_c = 20$ GPa (CM F/440 with 18.4% average error for $E_c = 30$ GPa). Interestingly, it was noticed that the two extreme values (1.0 g & 1.5 g) were more difficult to predict than intermediate values. Especially, for $E_c = 30$ GPa case with 1.0 g, actual crest deformations were very small and cannot be estimated successfully by any method.

Figure 3.41. Crest deformations for $H = 50$ m, ER, $E_c = 20$ GPa
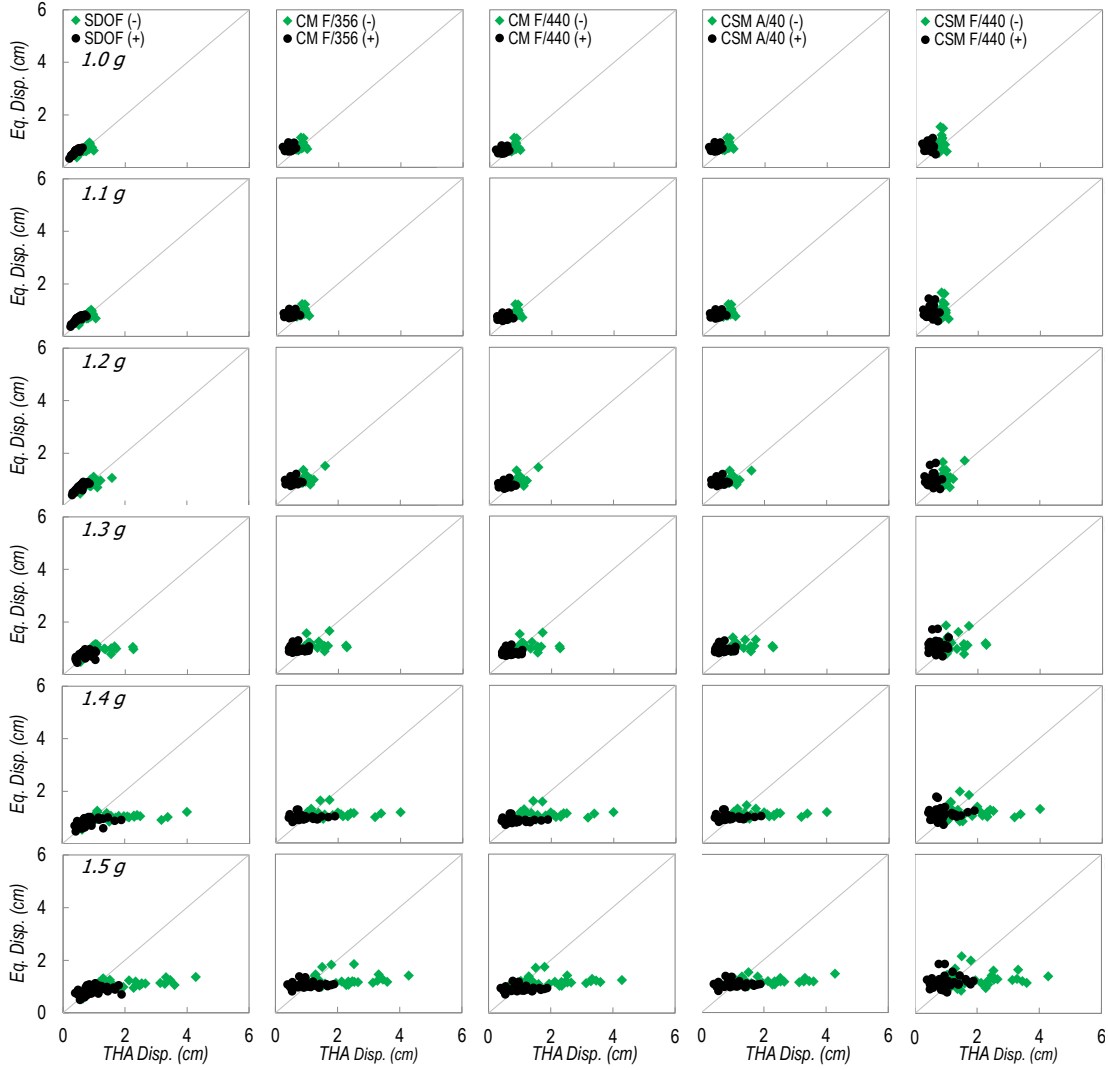
Figure 3.42. Crest deformations for $H = 50$ m, ER, $E_c = 30$ GPa

A similar behavior was observed for the crack length estimation. For $E_c = 30$ GPa case, the small deformations led to unsuccessful estimation of the crack lengths for low spectral acceleration levels. The average crack length in upstream direction varied between 16.3 m (1.0 g) and 25.0 m (1.5 g) for $E_c = 20$ GPa (3.8 m (1.0 g) and 21.2 m (1.5 g) for $E_c = 30$ GPa), respectively. In downstream the direction, these values changed between 4.9 m (1.0 g) and 10.2 m (1.5 g) for $E_c = 20$ GPa (3.2 m (1.0 g) and 9.4 m (1.5 g) for $E_c = 30$ GPa), respectively. The comparisons of the crack lengths are given in Figure 3.43 and Figure 3.44. For the crack lengths, best estimation was found by SDOF with 15.4% average error for $E_c = 20$ GPa (SDOF with 66.2% average error

82

for E_c = 30 GPa). It has seen that employing THA deformations for the crack length prediction also led accurate estimations. The excessive error for E_c = 30 GPa case is due to the behavior explained above. For this case, the average error of low spectral acceleration results (1.0 g to 1.2 g) is 119.6% whereas it is 12.9% for high spectral acceleration results (1.3 g to 1.5 g).

Figure 3.43. Crack lengths for H = 50 m, ER, E_c = 20 GPa

Figure 3.44. Crack lengths for H = 50 m, ER, E_c = 30 GPa

3.4.4.2. 50 m Height Dam with FR

The fundamental periods of 50 m height dams with FR were found as 0.168 s and 0.137 s for E_c = 20 GPa and E_c = 30 GPa, respectively. While the spectral acceleration levels were between 1.0 and 1.5 g (Table 3.3), the corresponding mean S_a values increased linearly between 1.18 g and 1.73 g for E_c = 20 GPa (1.12 g and 1.66 g for E_c = 30 GPa). The comparison of crest deformations is given in Figure 3.45 and Figure 3.46. In the case of the FR case, the displacement values increased in both directions. The mean crest displacement in the upstream direction linearly increased between 3.1 cm (1.0 g) and 7.1 cm (1.5 g) for E_c = 20 GPa (1.5 cm (1.0 g) and 4.5 cm (1.5 g) for E_c = 30 GPa), respectively. The method that gives the closest result to these values

was found as CSM F/440 with 18.1% average error for $E_c = 20$ GPa (CSM F/440 with 16.8% average error for $E_c = 30$ GPa).

Figure 3.45. Crest deformations for $H = 50$ m, FR, $E_c = 20$ GPa

Figure 3.46. Crest deformations for H = 50 m, FR, E_c = 30 GPa

The comparison of the crack lengths is given in Figure 3.47 and Figure 3.48. The average crack length in the upstream direction changed between 12.1 m (1.0 g) and 14.3 m (1.5 g) for E_c = 20 GPa (14.0 m (1.0 g) and 18.1 m (1.5 g) for E_c = 30 GPa), respectively. In the downstream direction, these values changed between 25.2 m (1.0 g) and 26.8 m (1.5 g) for E_c = 20 GPa (26.6 m (1.0 g) and 31.2 m (1.5 g) for E_c = 30 GPa), respectively. For the crack lengths, best estimation was found by CSM A/40 with 4.7% average error for E_c = 20 GPa (CM F/440 with 6.4% average error for E_c = 30 GPa). As in the previous ER case, employing THA deformations for the crack length prediction also led accurate estimations. However, the crack length calculation

86

was successfully estimated with almost all methods. This is due to the fact that crack length values were less dependent on the roof displacement in the FR models.

Figure 3.47. Crack lengths for H = 50 m, FR, E_c = 20 GPa

Figure 3.48. Crack lengths for $H = 50$ m, FR, $E_c = 30$ GPa

3.4.4.3. 100 m Height Dam with ER

The fundamental periods of 100 m height dams with ER were found as 0.271 s and 0.221 s for $E_c = 20$ GPa and $E_c = 30$ GPa, respectively. While the spectral acceleration levels were between 1.0 and 1.5 g (Table 3.3), the corresponding mean S_a values increased linearly between 1.16 g and 1.76 g for $E_c = 20$ GPa (1.18 g and 1.77 g for $E_c = 30$ GPa). The comparison of crest deformations is given in Figure 3.49 and Figure 3.50. As expected, the displacement values increased according to the results of 50 m dams. The mean crest displacement in the upstream direction linearly increased between 3.8 cm (1.0 g) and 15.7 cm (1.5 g) for $E_c = 20$ GPa (2.6 cm (1.0 g) and 10.3 cm (1.5 g) for $E_c = 30$ GPa), respectively. The method that gave the closest result to these values was found as CM F/440 with 19.2% average error for $E_c = 20$ GPa (CSM

88

A/40 with 11.2% average error for $E_c = 30$ GPa). Especially in the upstream direction, it seems that the methods had difficulty in estimating the THA values.

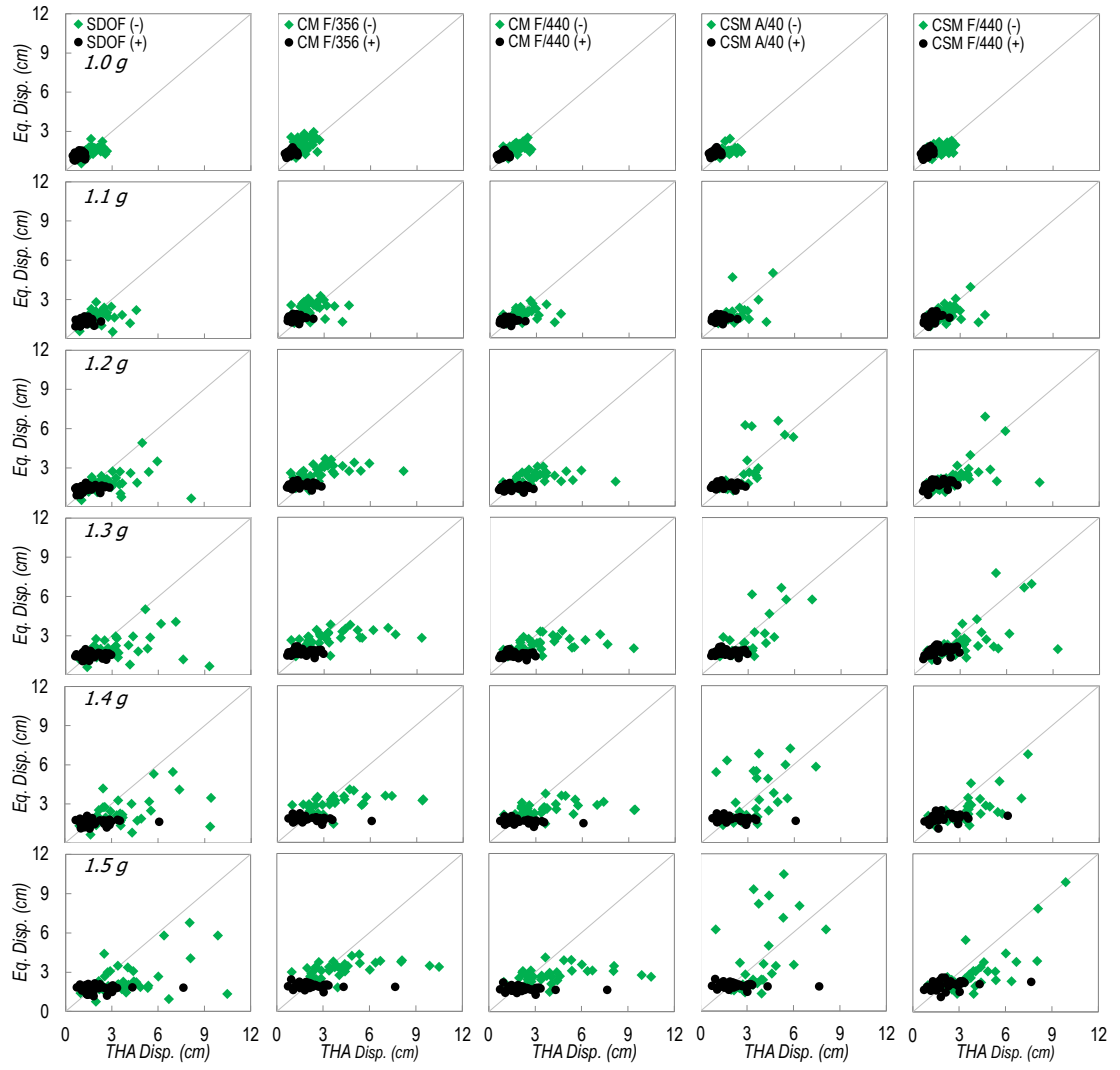*Figure 3.49.* Crest deformations for $H = 100$ m, ER, $E_c = 20$ GPa

Figure 3.50. Crest deformations for $H = 100$ m, ER, $E_c = 30$ GPa

The comparison of the crack lengths is given in Figure 3.51 and Figure 3.52. The average crack length in the upstream direction changed between 27.5 m (1.0 g) and 34.3 m (1.5 g) for $E_c = 20$ GPa (37.6 m (1.0 g) and 38.9 m (1.5 g) for $E_c = 30$ GPa), respectively. In the downstream direction, these values changed between 11.4 m (1.0 g) and 12.5 m (1.5 g) for $E_c = 20$ GPa (10.8 m (1.0 g) and 17.1 m (1.5 g) for $E_c = 30$ GPa), respectively. For the crack lengths, best estimation was found by SDOF with 9.0% average error for $E_c = 20$ GPa (SDOF with 12.3% average error for $E_c = 30$ GPa). Although the average errors for crack lengths were low, the variation in crack estimation, as seen in the graphs, was not properly reflected in the results. In particular,

this was seen in the estimation of the crack lengths for $E_c = 30$ GPa dams. It is observed that the errors in the displacement estimation significantly affected on determination of the crack length.
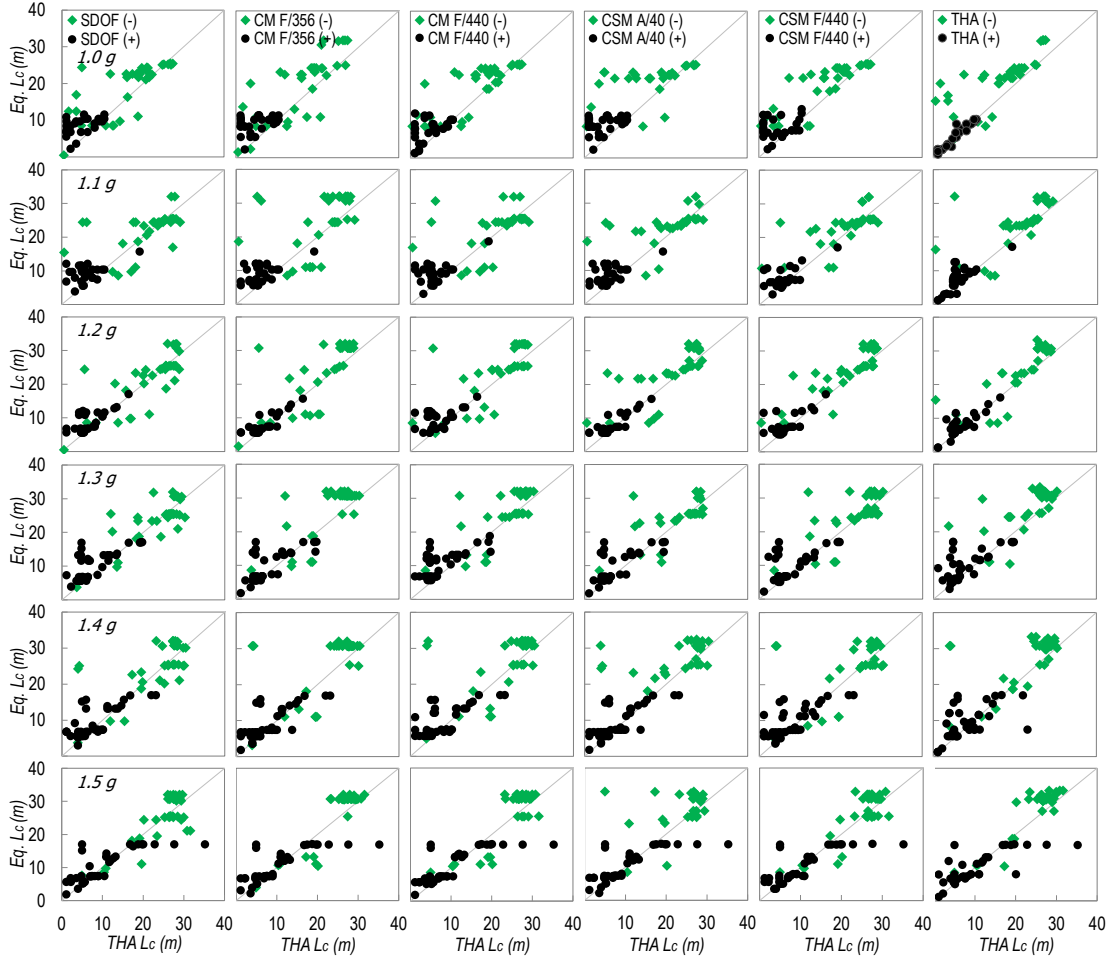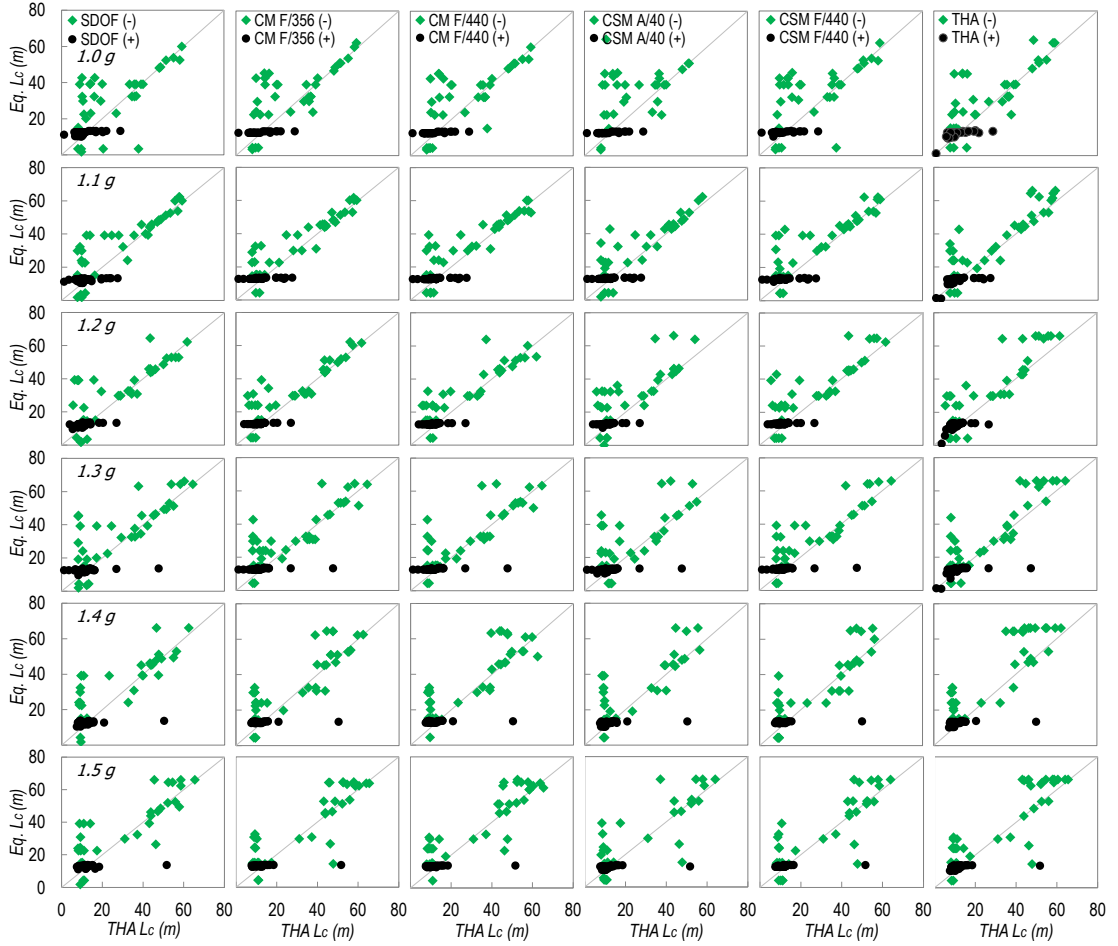

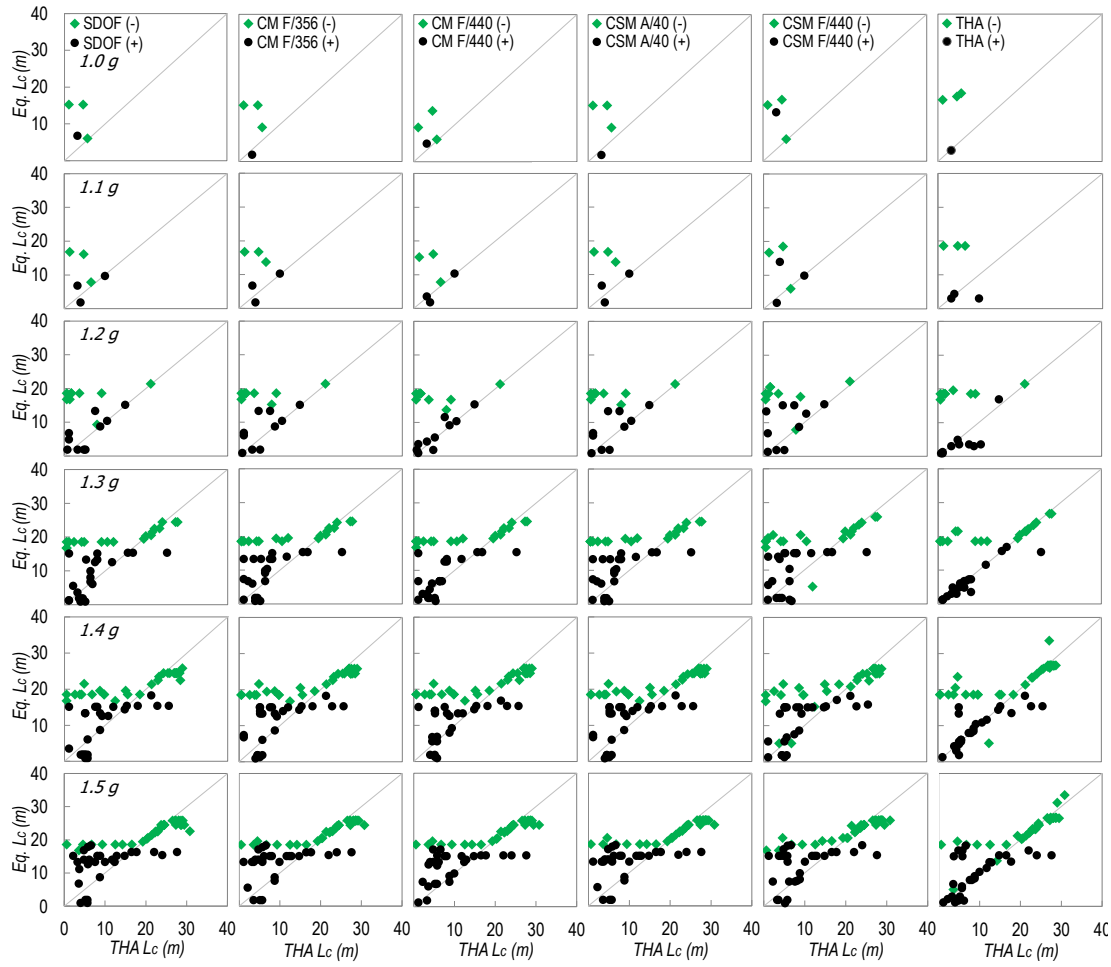*Figure 3.51.* Crack lengths for $H = 100$ m, ER, $E_c = 20$ GPa
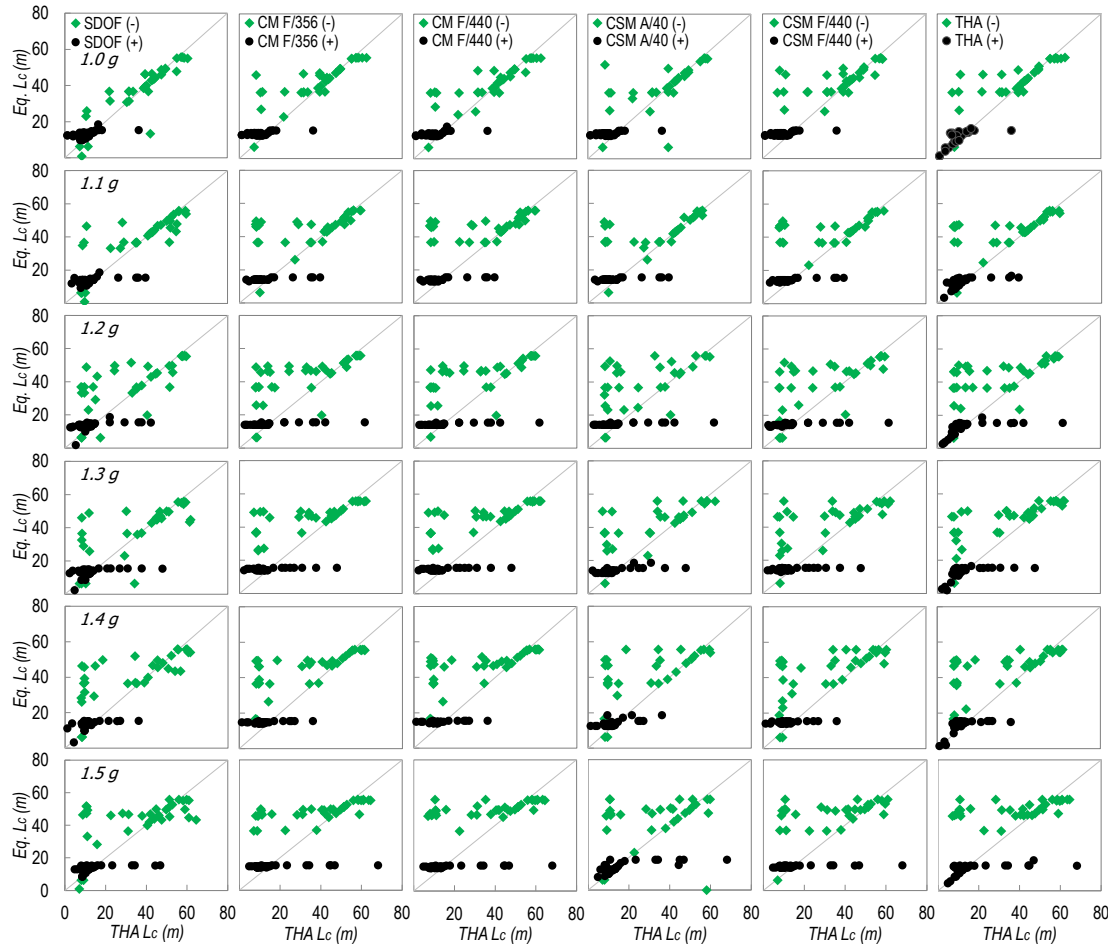
Figure 3.52. Crack lengths for $H = 100$ m, ER, $E_c = 30$ GPa

3.4.4.4. 100 m Height Dam with FR

The fundamental periods of 100 m height dams with FR were found as 0.336 s and 0.274 s for $E_c = 20$ GPa and $E_c = 30$ GPa, respectively. While the spectral acceleration levels were between 1.0 and 1.5 g (Table 3.3), the corresponding mean S_a values increased linearly between 1.09 g and 1.62 g for $E_c = 20$ GPa (1.16 g and 1.75 g for $E_c = 30$ GPa). The comparison of crest deformations is given in Figure 3.53 and Figure 3.54. Firstly, it is seen that the crest displacement estimations were more successful than the ones in ER. The mean crest displacement in the upstream direction linearly increased between 8.5 cm (1.0 g) and 16.3 cm (1.5 g) for $E_c = 20$ GPa (6.5 cm (1.0 g) and 12.9 cm (1.5 g) for $E_c = 30$ GPa), respectively. The method that gave the closest

result to these values was found as CSM F/440 with 8.5% average error for $E_c = 20$ GPa (CSM F/440 with 5.4% average error for $E_c = 30$ GPa).
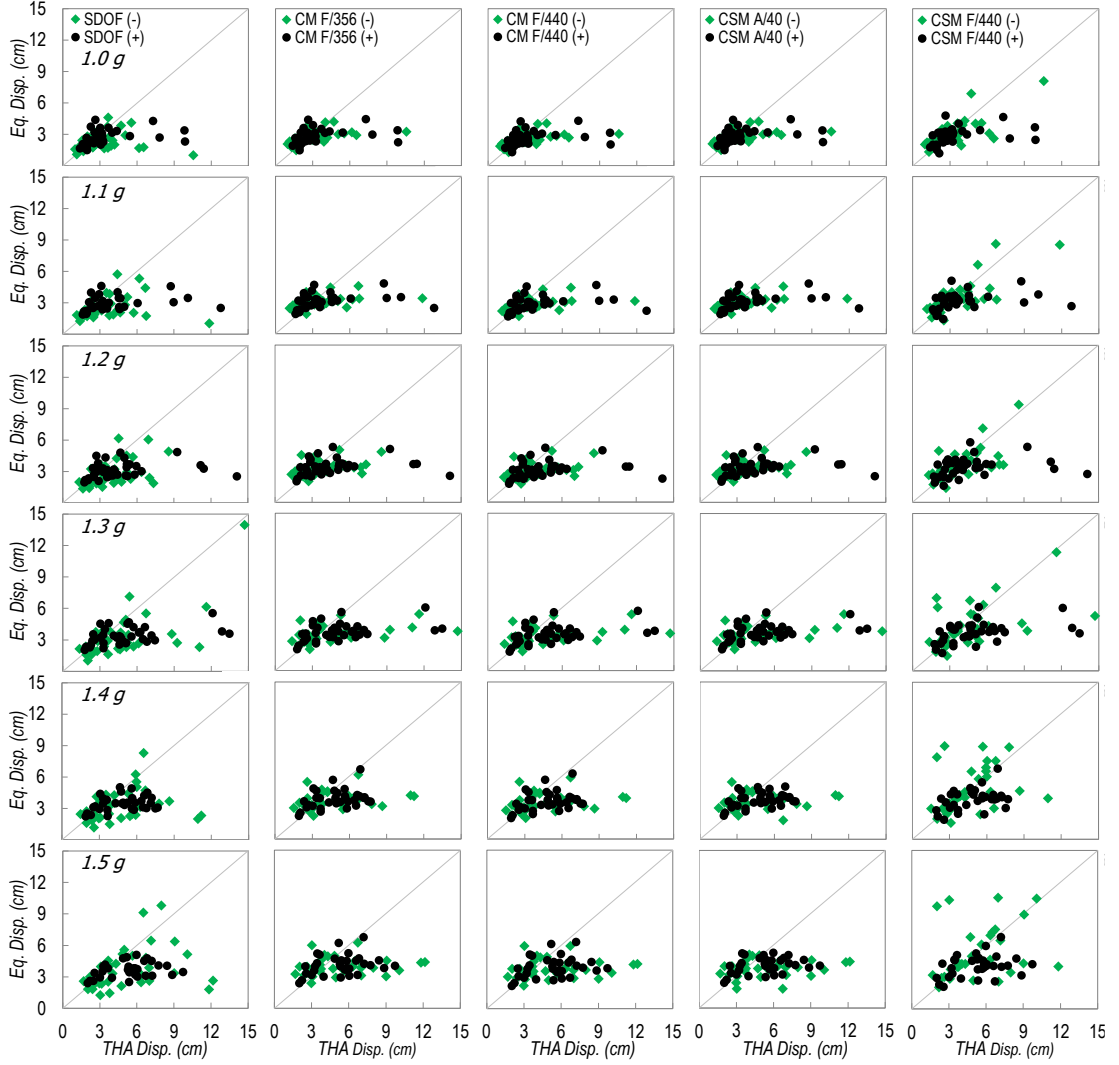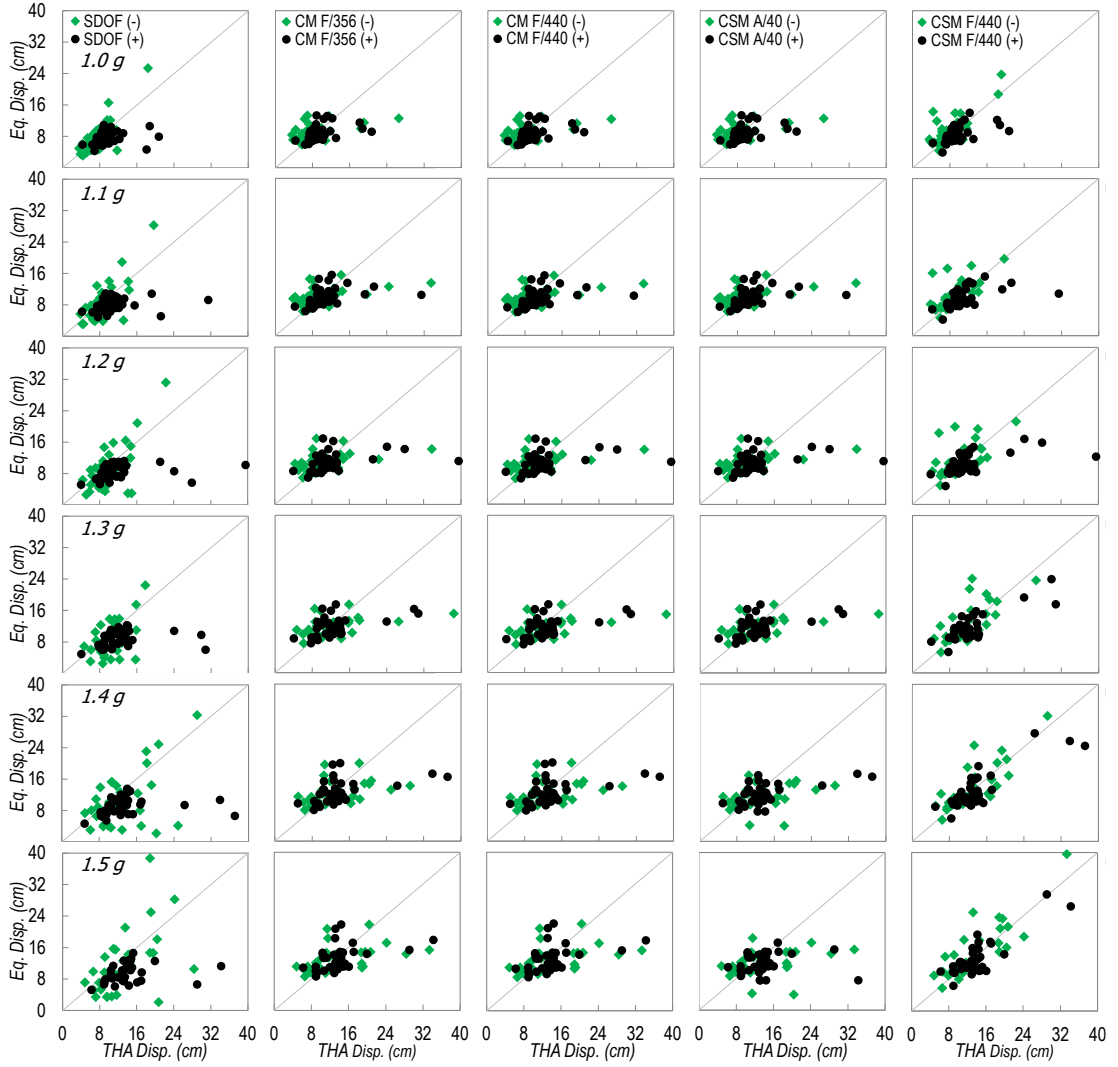

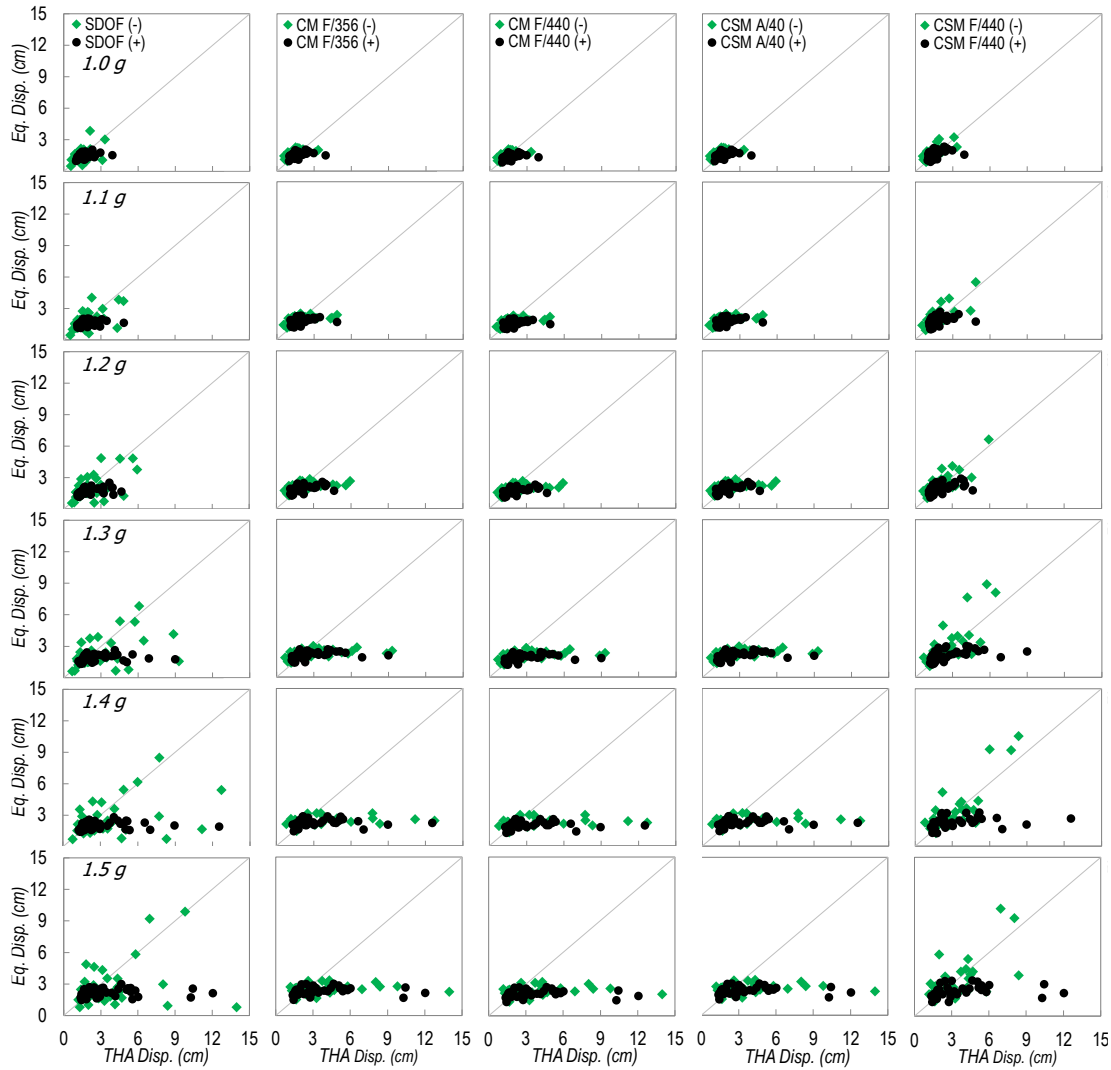*Figure 3.53.* Crest deformations for $H = 100$ m, FR, $E_c = 20$ GPa
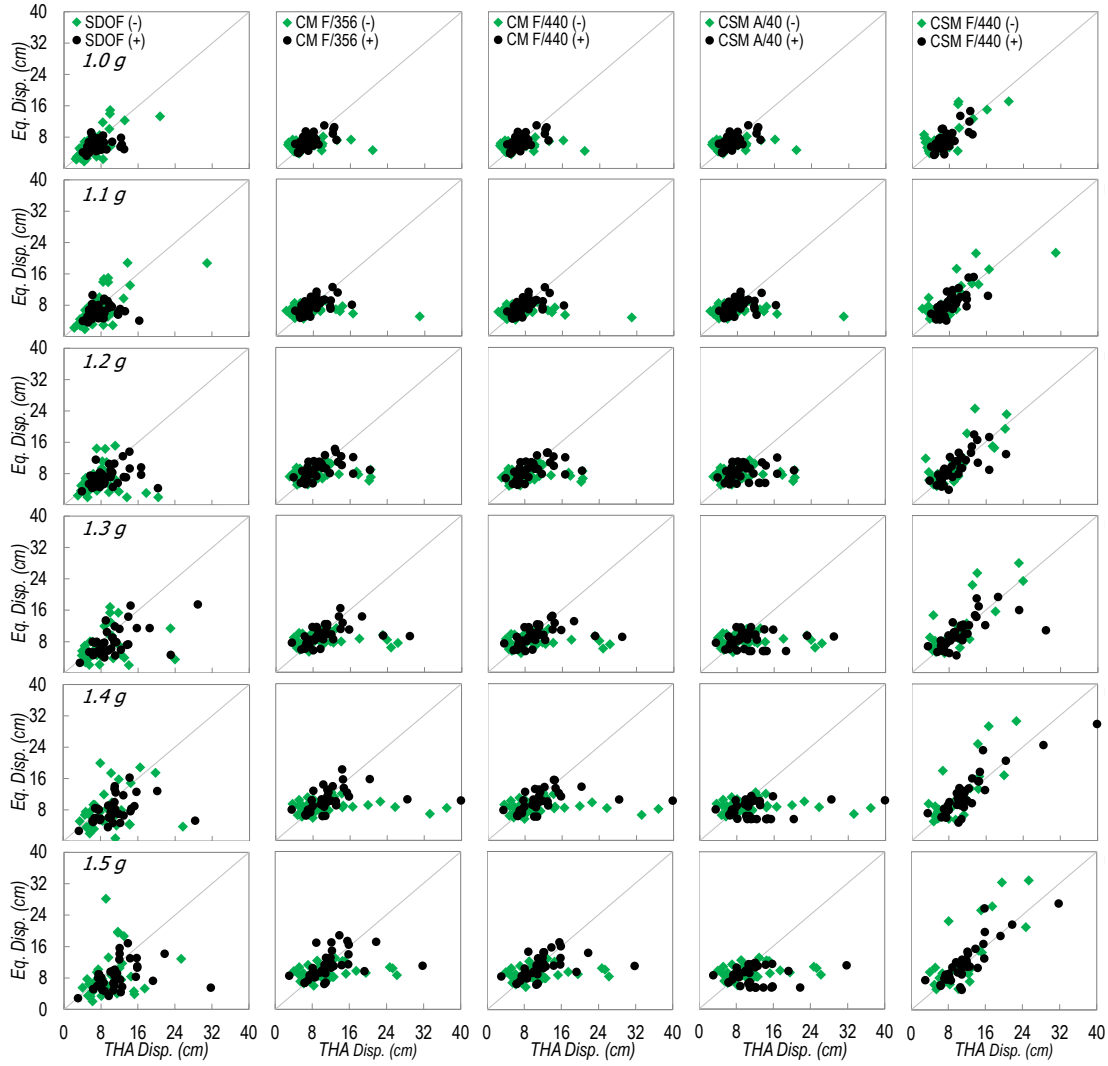
Figure 3.54. Crest deformations for $H = 100$ m, FR, $E_c = 30$ GPa

The comparison of the crack lengths is given in Figure 3.55 and Figure 3.56. The average crack length in the upstream direction changed between 16.0 m (1.0 g) and 17.6 m (1.5 g) for $E_c = 20$ GPa (15.8 m (1.0 g) and 21.5 m (1.5 g) for $E_c = 30$ GPa), respectively. In the downstream direction, these values changed between 32.9 m (1.0 g) and 38.9 m (1.5 g) for $E_c = 20$ GPa (40.5 m (1.0 g) and 42.1 m (1.5 g) for $E_c = 30$ GPa), respectively. For the crack lengths, best estimation was found by SDOF with 20.5% average error for $E_c = 20$ GPa (SDOF with 46.6% average error for $E_c = 30$ GPa). Especially for $E_c = 30$ GPa dams, the crest deformations were overestimated by all methods. Although displacement estimates were close, such a result suggests that

94

the crest displacement and crack length relationship was not closely related for this case.
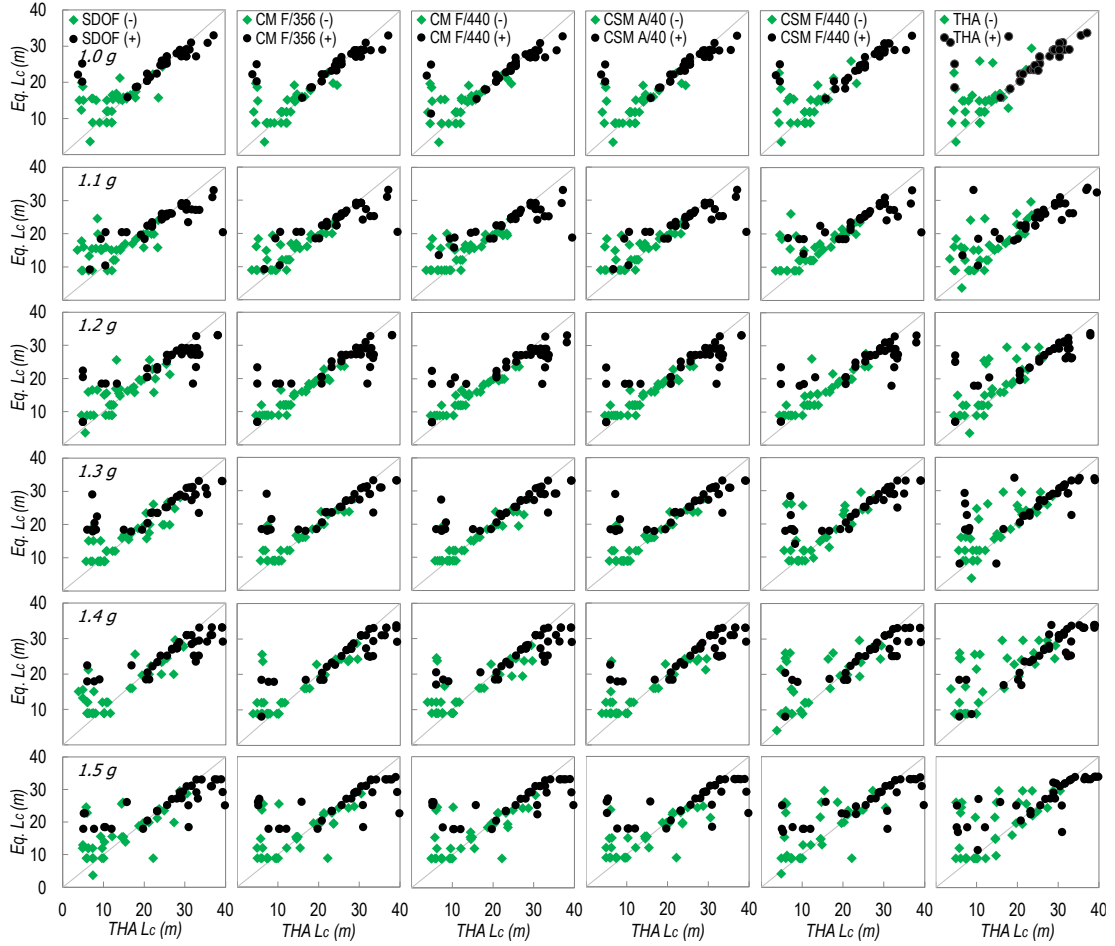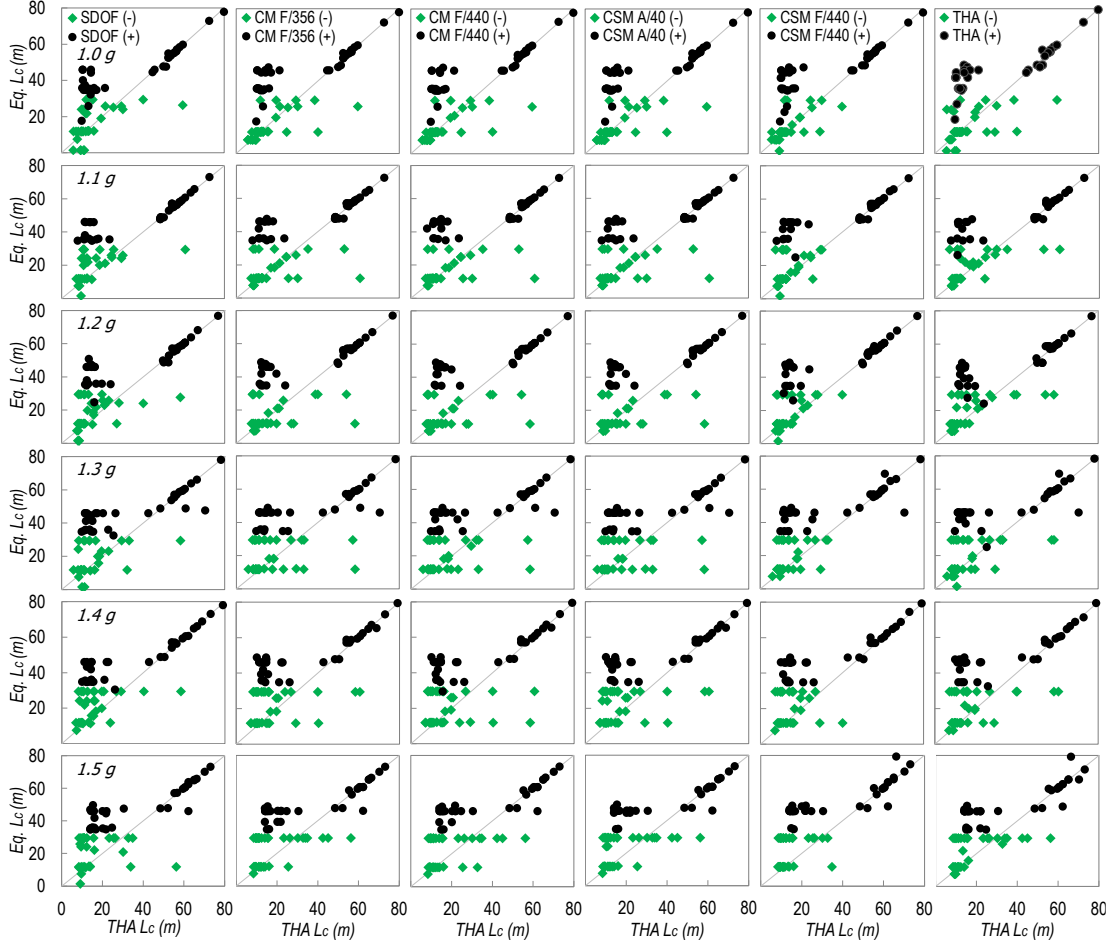

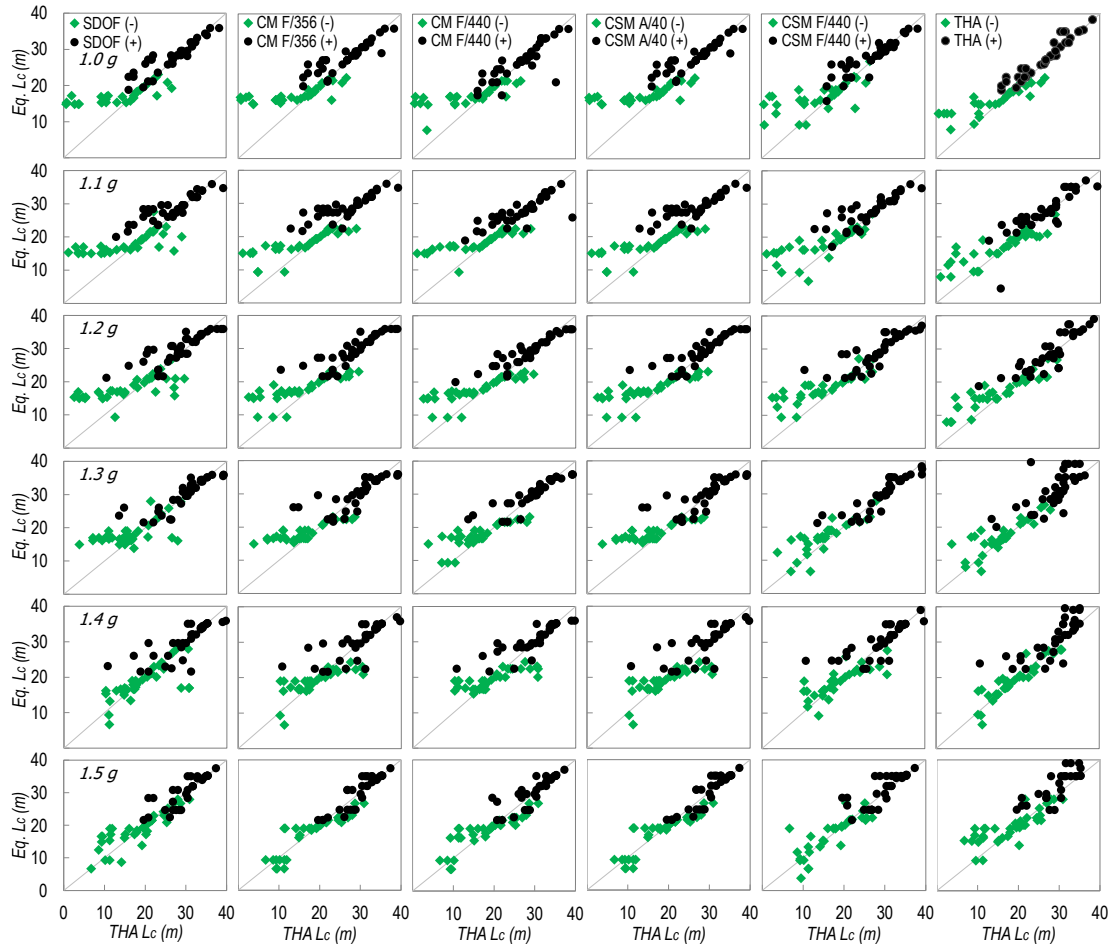*Figure 3.55.* Crack lengths for $H = 100$ m, FR, $E_c = 20$ GPa
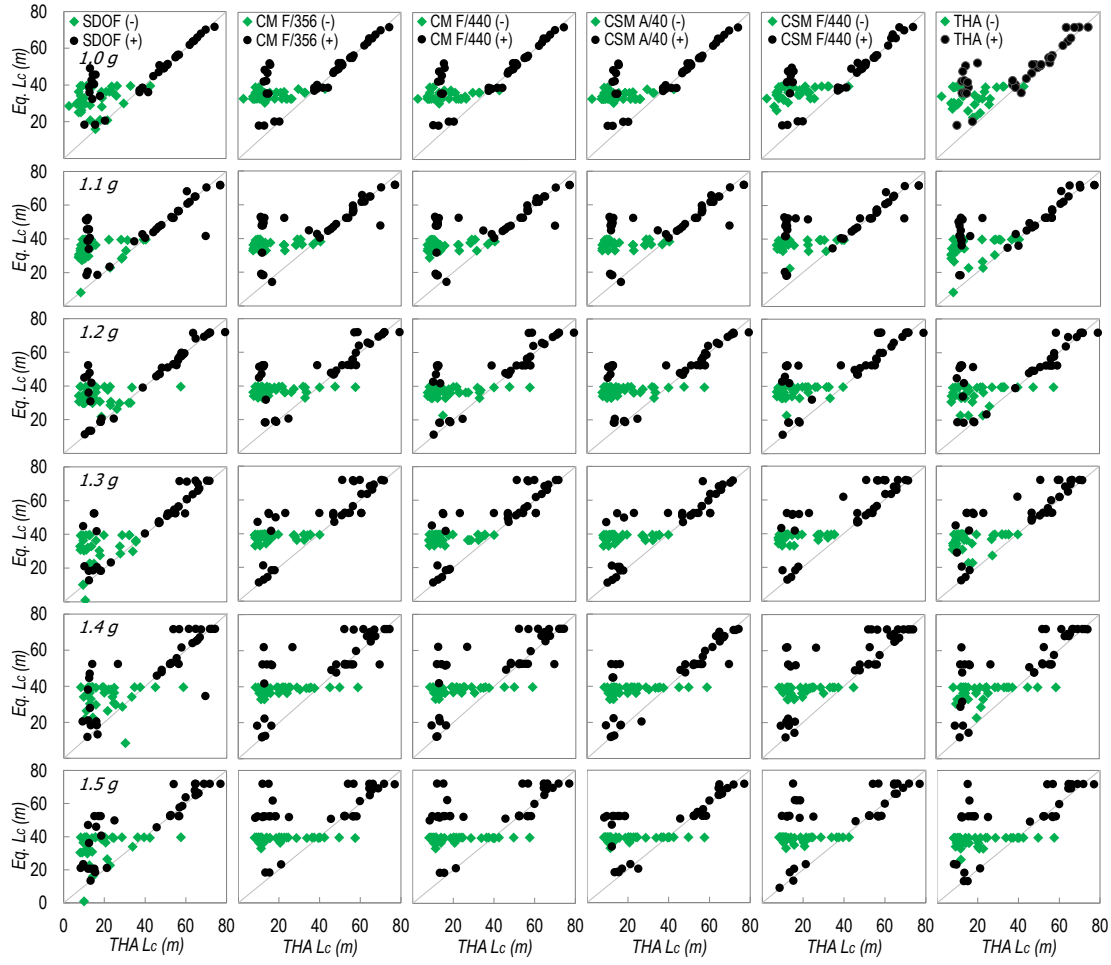
Figure 3.56. Crack lengths for $H = 100$ m, FR, $E_c = 30$ GPa

3.4.4.5. 150 m Height Dam with ER

The fundamental periods of 150 m height dams with ER were found as 0.406 s and 0.332 s for $E_c = 20$ GPa and $E_c = 30$ GPa, respectively. While the spectral acceleration levels were between 1.0 and 1.5 g (Table 3.3), the corresponding mean S_a values increased linearly between 0.92 g and 1.38 g for $E_c = 20$ GPa (1.09 g and 1.62 g for $E_c = 30$ GPa). The comparison of crest deformations is given in Figure 3.57 and Figure 3.58. For ER case, it is observed that crest displacement estimations were more successful than the dams with less height. The mean crest displacement in the upstream direction linearly increased between 4.9 cm (1.0 g) and 23.6 cm (1.5 g) for E_c = 20 GPa (4.0 cm (1.0 g) and 16.3 cm (1.5 g) for $E_c = 30$ GPa), respectively. The

96

method that gave the closest result to these values was found as SDOF with 22.8% average error for $E_c = 20$ GPa (SDOF with 25.0% average error for $E_c = 30$ GPa).
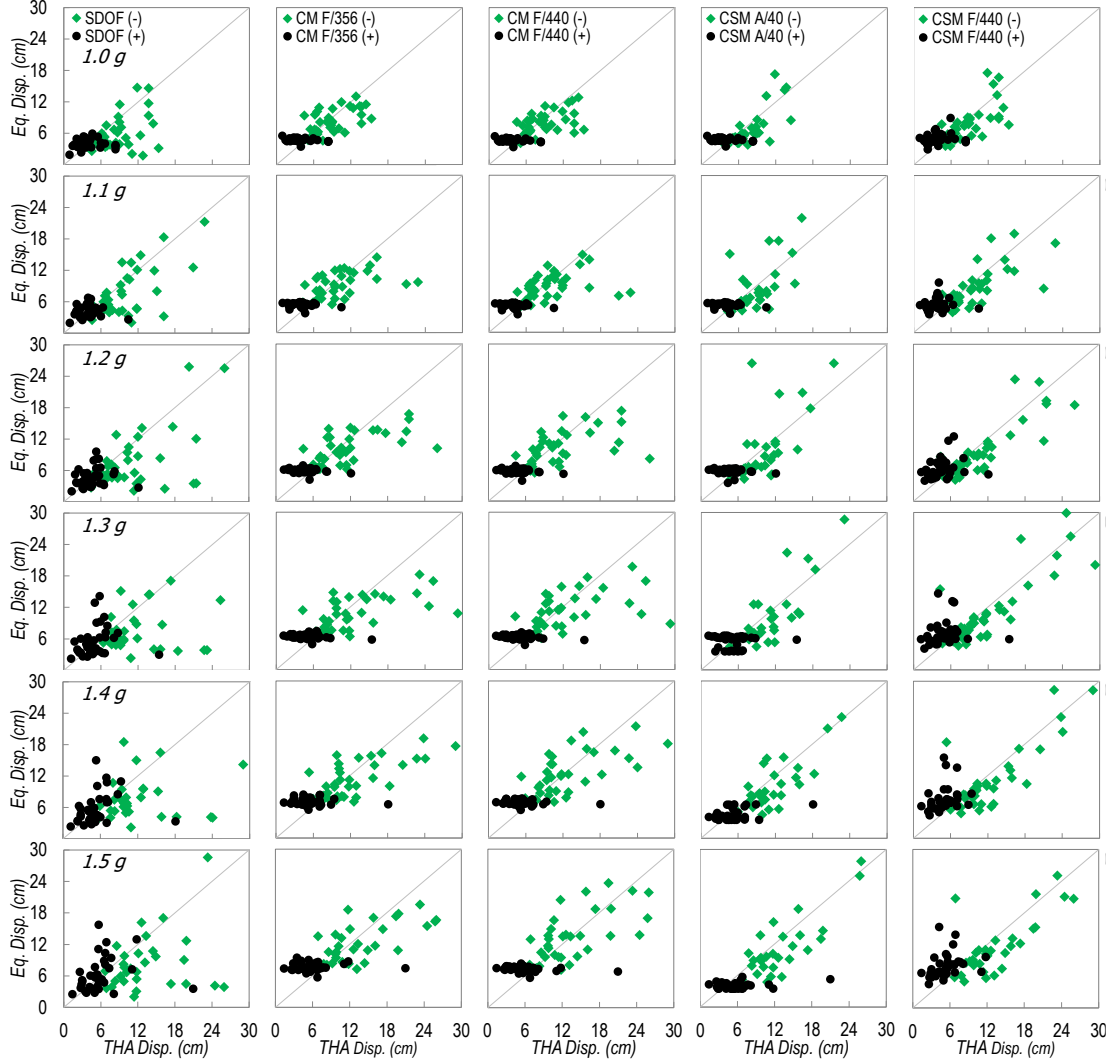

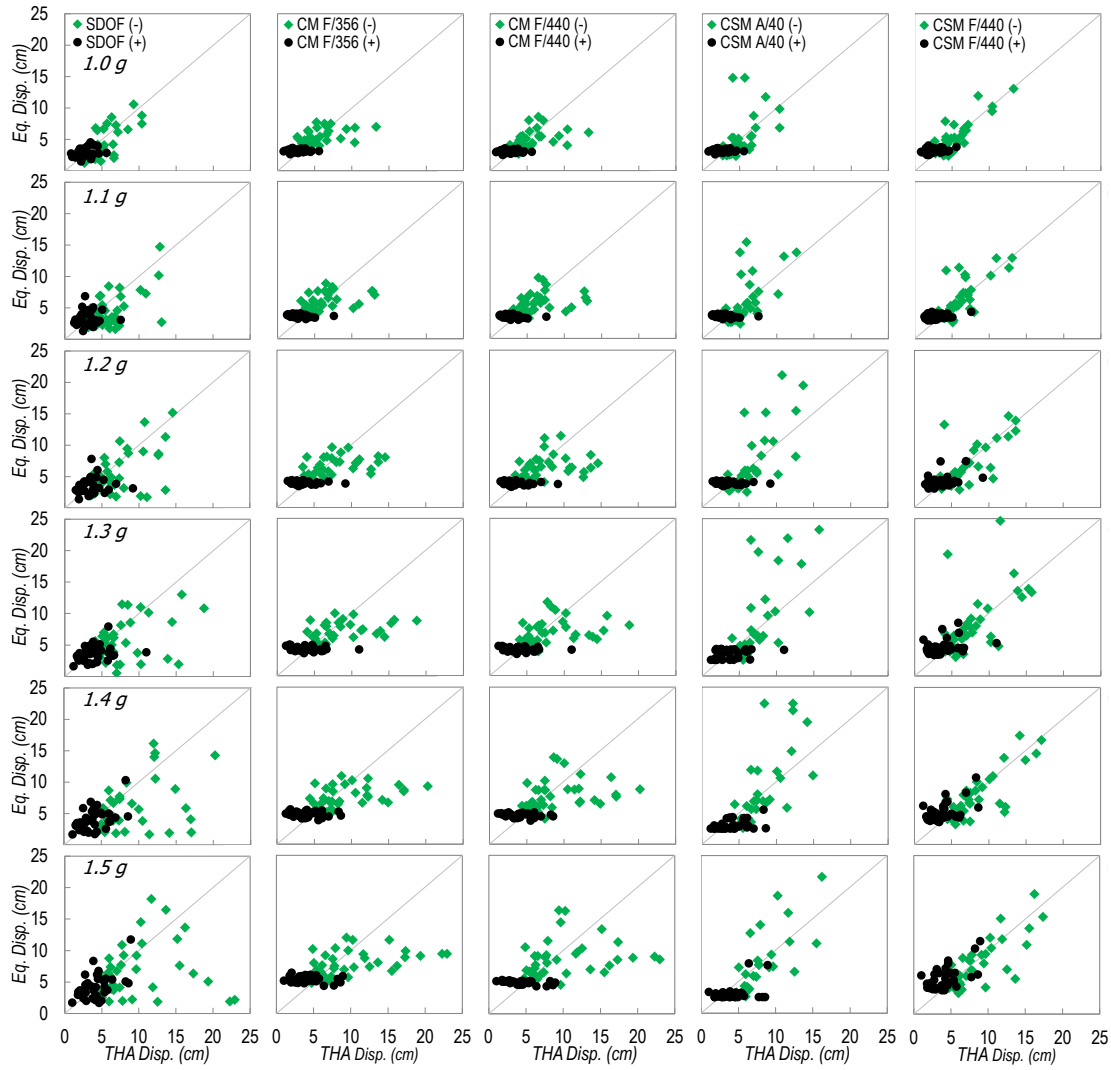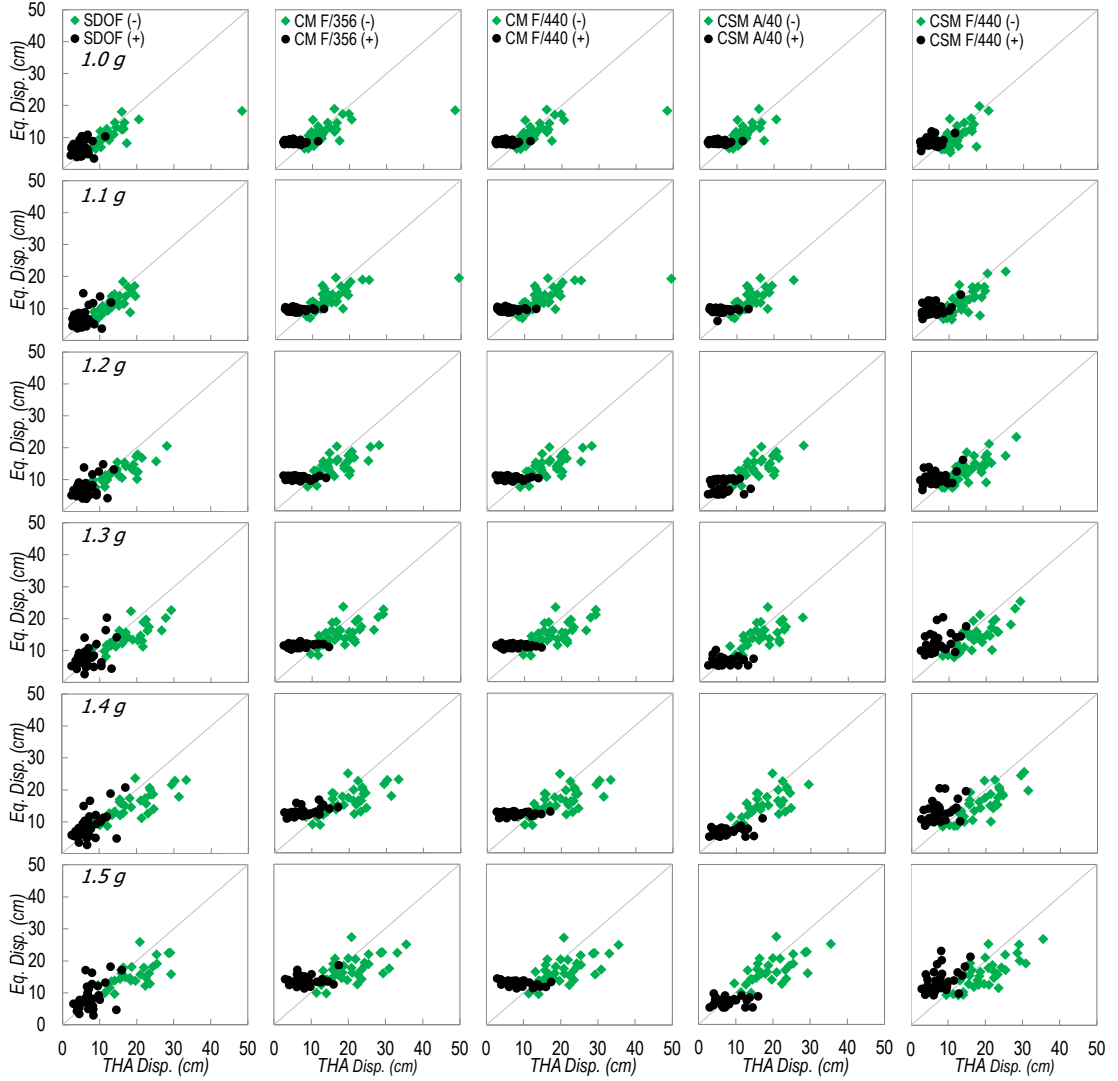*Figure 3.57.* Crest deformations for $H = 150$ m, ER, $E_c = 20$ GPa
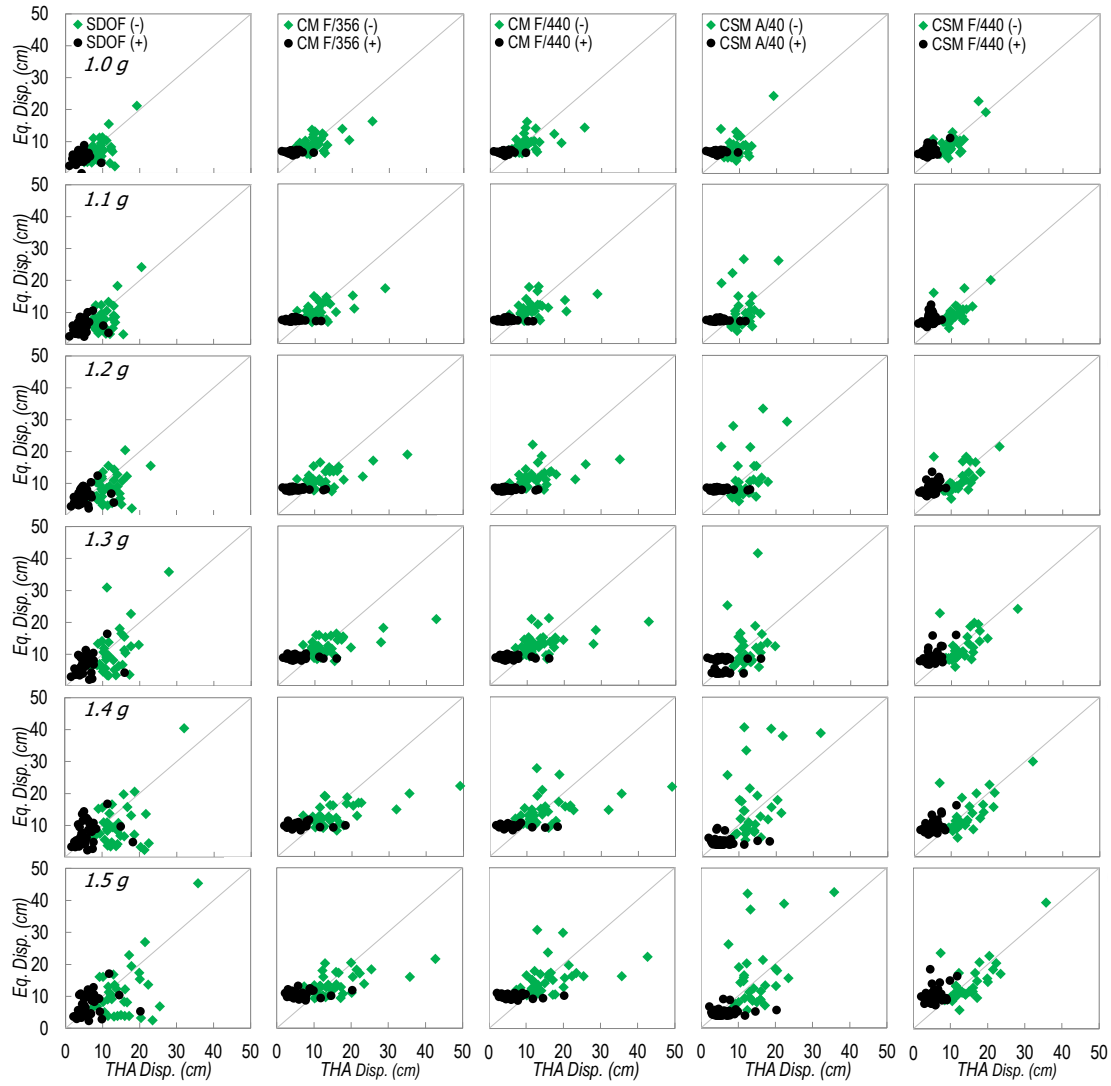
Figure 3.58. Crest deformations for $H = 150$ m, ER, $E_c = 30$ GPa

The comparison of the crack lengths is given in Figure 3.59 and Figure 3.60. The average crack length in the upstream direction changed between 38.0 m (1.0 g) and 41.5 m (1.5 g) for $E_c = 20$ GPa (39.1 m (1.0 g) and 48.3 m (1.5 g) for $E_c = 30$ GPa), respectively. In the downstream direction, these values changed between 12.4 m (1.0 g) and 18.6 m (1.5 g) for $E_c = 20$ GPa (11.7 m (1.0 g) and 16.2 m (1.5 g) for $E_c = 30$ GPa), respectively. For the crack lengths, best estimation was found by SDOF with 8.8% average error for $E_c = 20$ GPa (CM F/440 with 10.7% average error for $E_c = 30$ GPa). For ER case with 150 m height dams, negative directional cracks had mostly dominated the behavior. Although a successful match was observed for dams with E_c

= 20 GPa, errors increased at lowest and highest spectral acceleration levels of the more rigid dams.
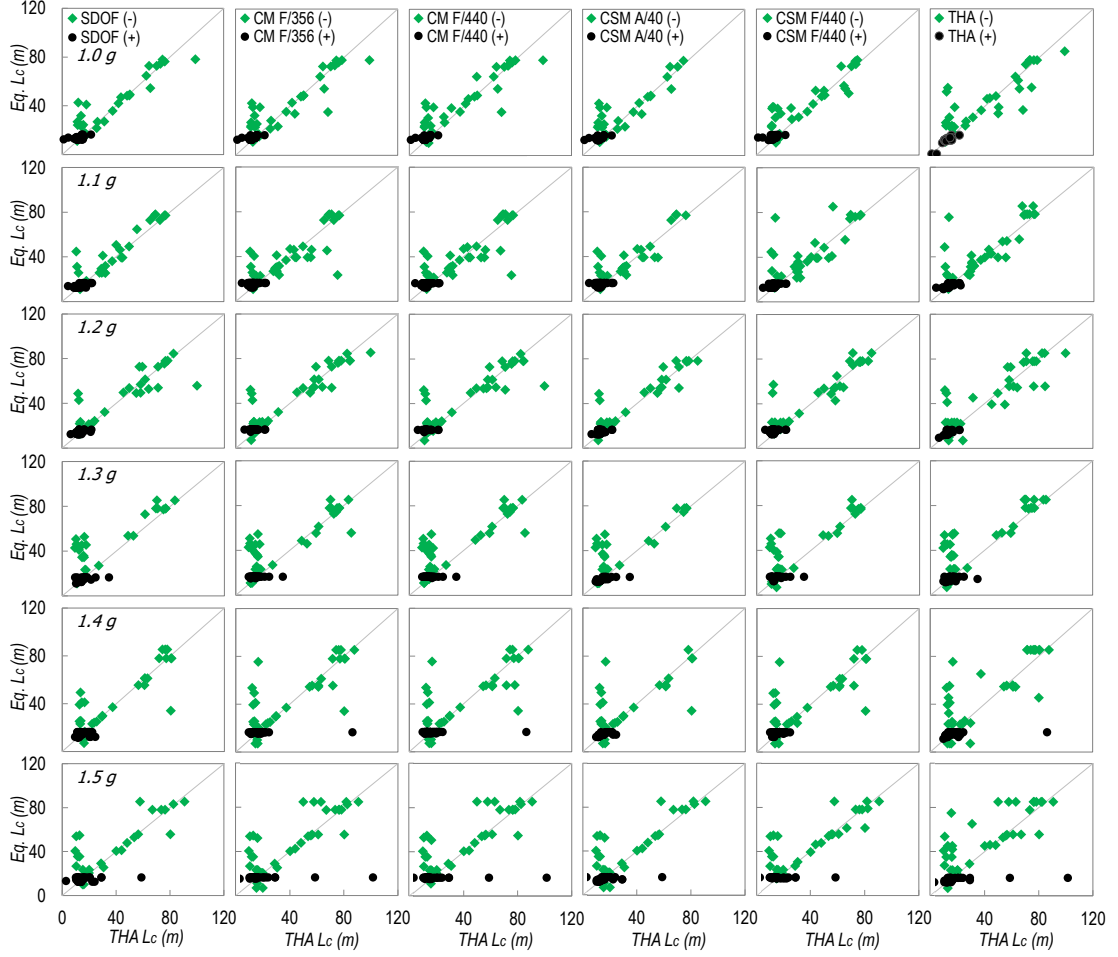
Figure 3.59. Crack lengths for H = 150 m, ER, E_c = 20 GPa
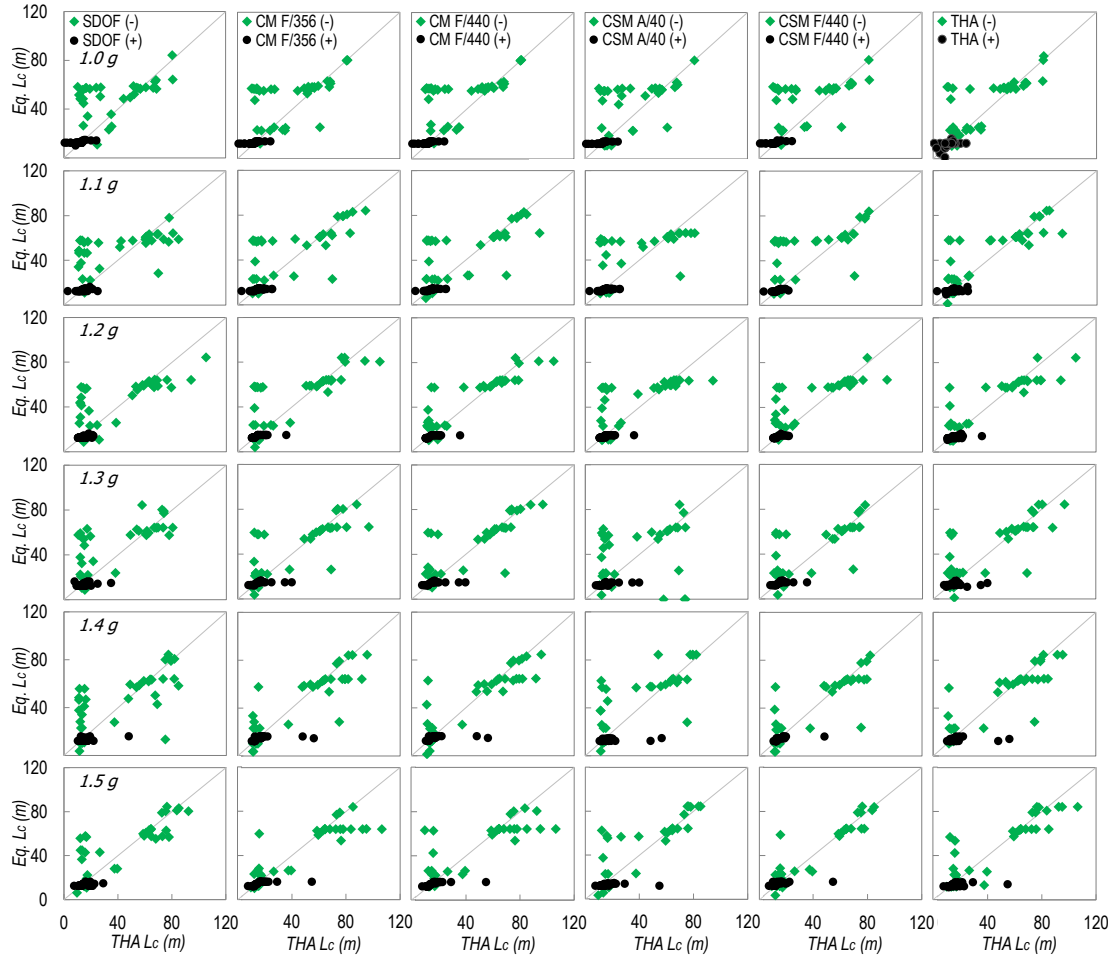
Figure 3.60. Crack lengths for $H = 150$ m, ER, $E_c = 30$ GPa

3.4.4.6. 150 m Height Dam with FR

The fundamental periods of 150 m height dams with FR were found as 0.504 s and 0.411 s for $E_c = 20$ GPa and $E_c = 30$ GPa, respectively. While the spectral acceleration levels were between 1.0 and 1.5 g (Table 3.3), the corresponding mean S_a values increased linearly between 0.78 g and 1.17 g for $E_c = 20$ GPa (0.91 g and 1.35 g for $E_c = 30$ GPa). The comparison of crest deformations is given in Figure 3.61 and Figure 3.62. The mean crest displacement in the upstream direction linearly increased between 11.3 cm (1.0 g) and 22.7 cm (1.5 g) for $E_c = 20$ GPa (9.1 cm (1.0 g) and 18.5 cm (1.5 g) for $E_c = 30$ GPa), respectively. The method that gave the closest result to

these values was found as CSM A/40 with 15.1% average error for $E_c = 20$ GPa (CM F/440 with 3.1% average error for $E_c = 30$ GPa).
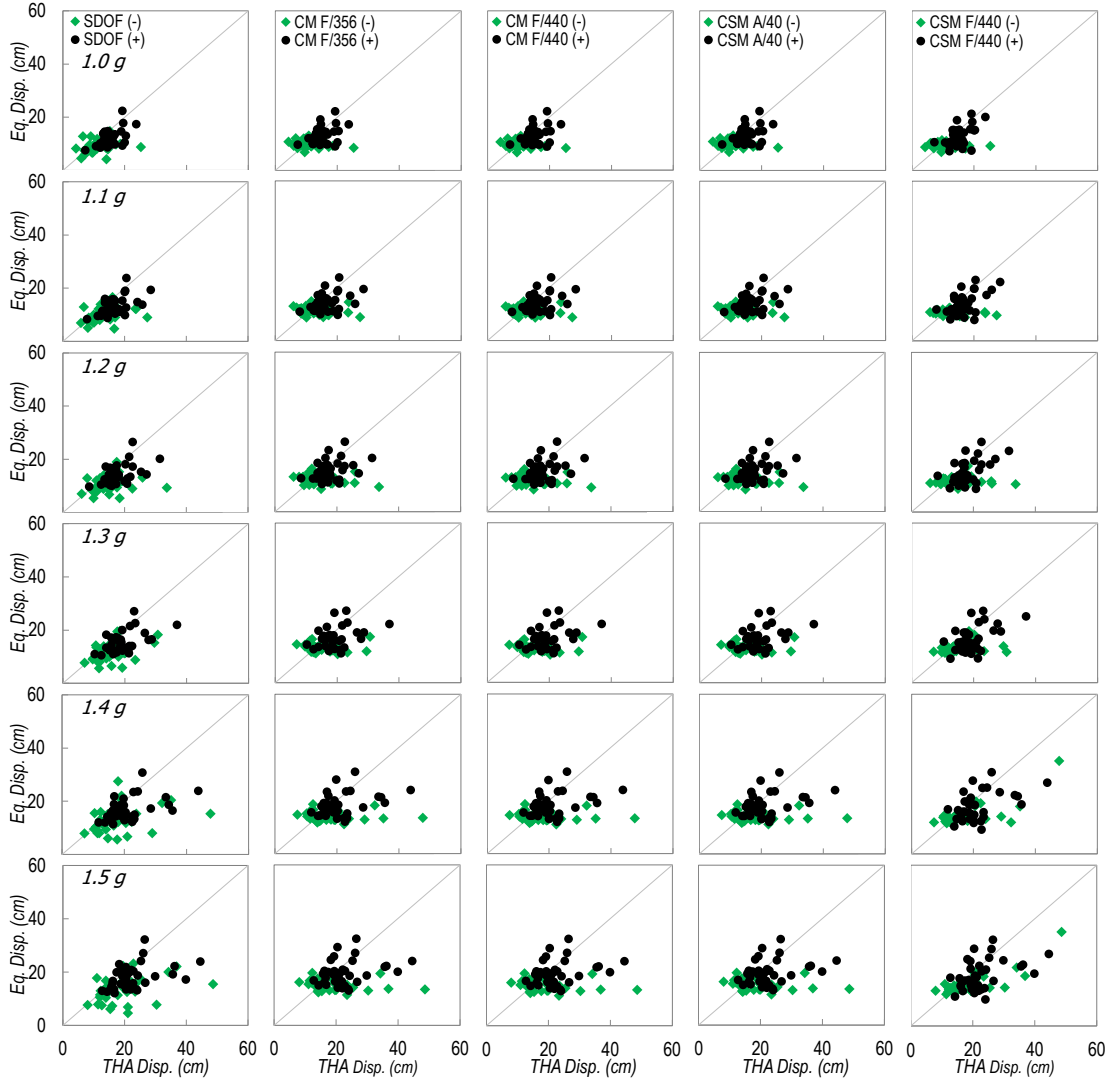
Figure 3.61. Crest deformations for $H = 150$ m, FR, $E_c = 20$ GPa
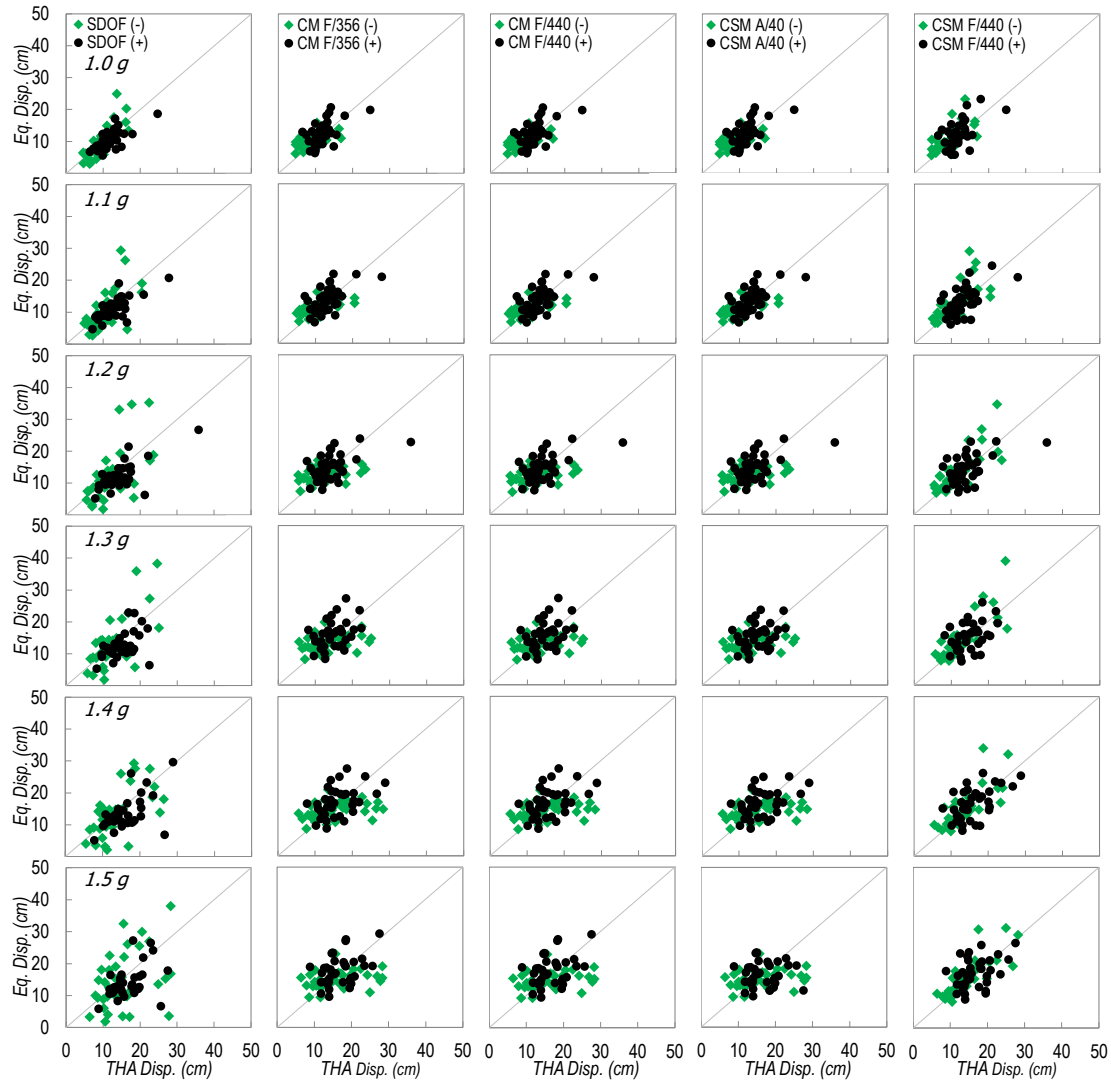
Figure 3.62. Crest deformations for $H = 150$ m, FR, $E_c = 30$ GPa

The comparison of the crack lengths was given in Figure 3.63 and Figure 3.64. The average crack length in the upstream direction changed between 18.0 m (1.0 g) and 20.5 m (1.5 g) for $E_c = 20$ GPa (17.2 m (1.0 g) and 19.3 m (1.5 g) for $E_c = 30$ GPa), respectively. In the downstream direction, these values changed between 47.4 m (1.0 g) and 59.7 m (1.5 g) for $E_c = 20$ GPa (58.0 m (1.0 g) and 60.3 m (1.5 g) for $E_c = 30$ GPa), respectively. For the crack lengths, best estimation was found by CSM F/440 with 8.3% average error for $E_c = 20$ GPa (SDOF with 31.2% average error for $E_c = 30$ GPa). Successful estimates for FR dams were also observed for this case. In

102

particular, if the crack lengths were large, it was easier to predict the values with the simplified method.
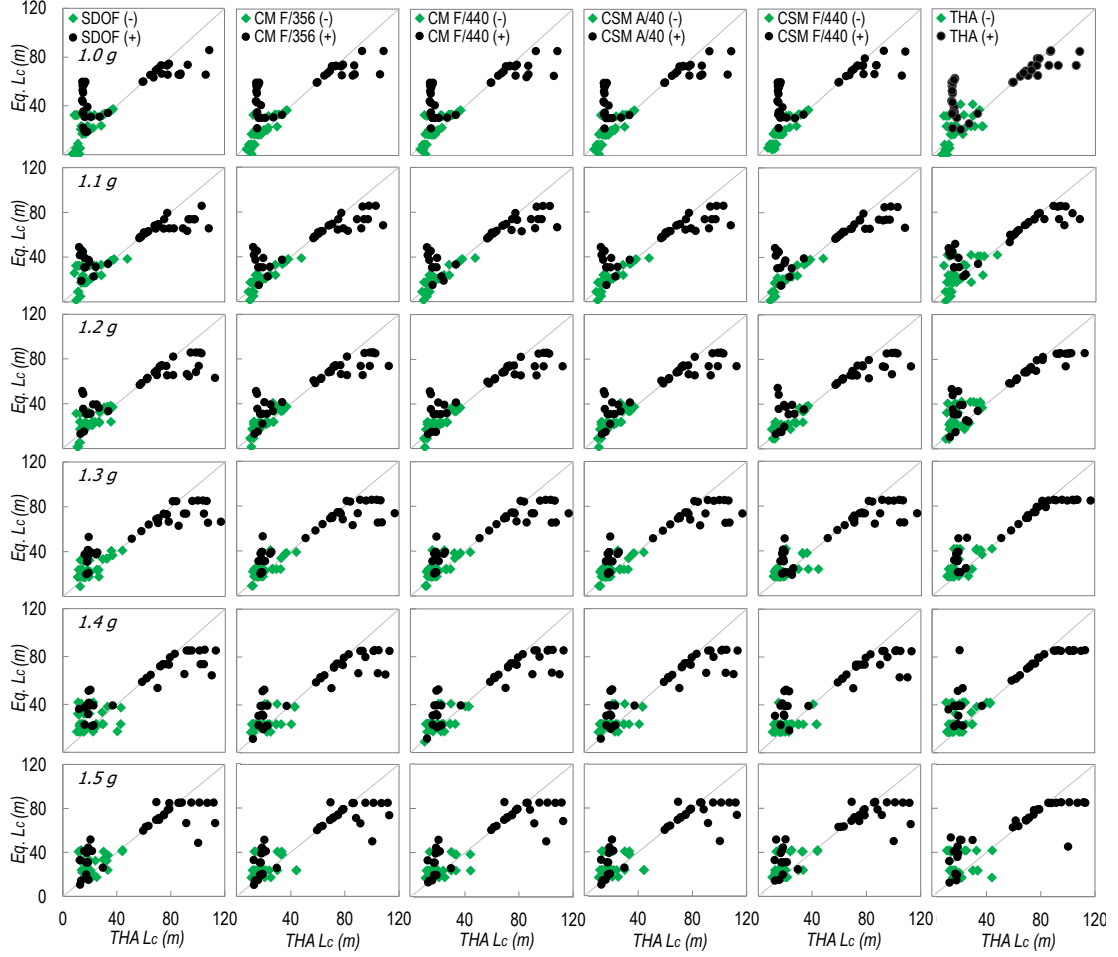
Figure 3.63. Crack lengths for $H = 150$ m, FR, $E_c = 20$ GPa

103
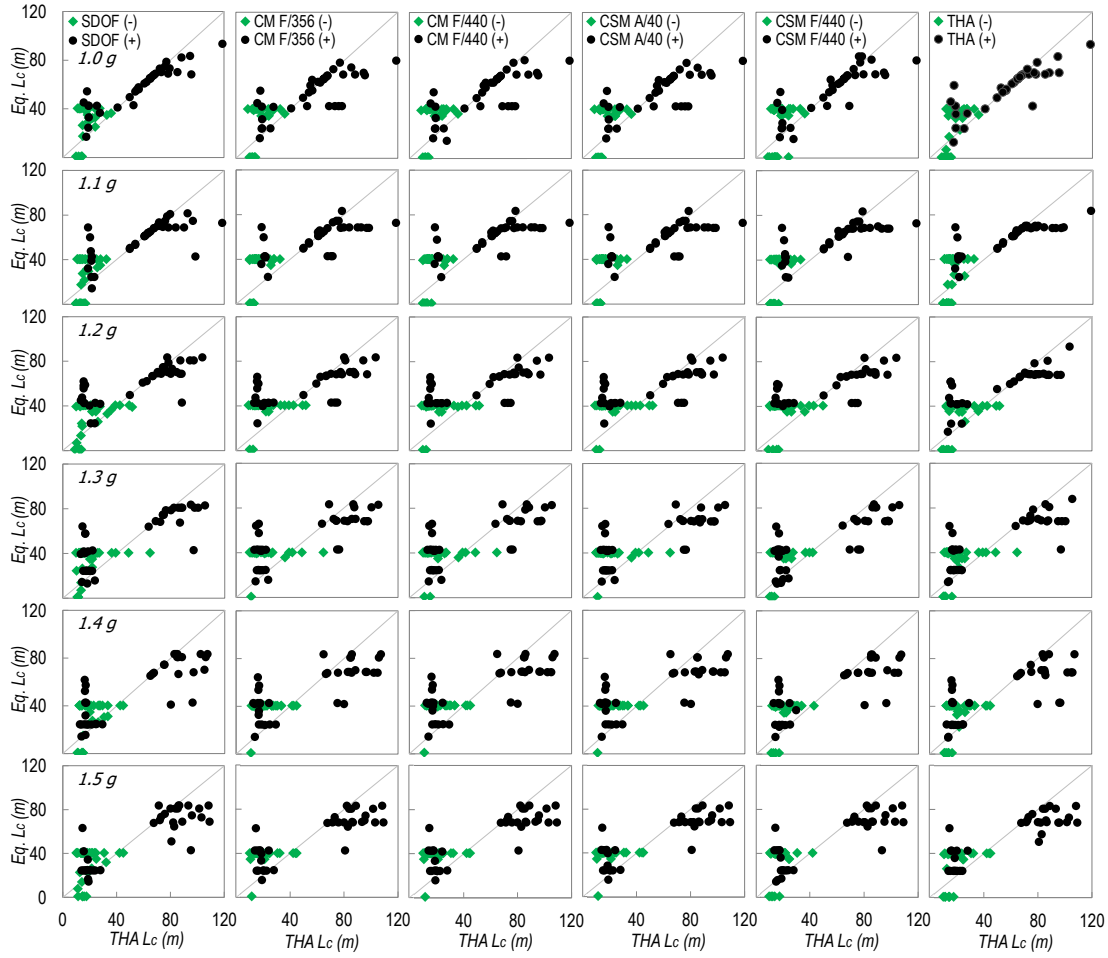
Figure 3.64. Crack lengths for $H = 150$ m, FR, $E_c = 30$ GPa

3.4.4.7. Overall Evaluation

For the statistical evaluation of the results, the mean values and standard deviations of the crest displacement and the crack length ratios were calculated. The results of each method were divided by result of the time history analysis (THA) for each ground motion record (e.g (d_{crest} for SDOF / d_{crest} for THA) or (L_c for CM F/440 / L_c for THA)), then the mean values and standard deviations were calculated. In Table 3.4 and Table 3.5 the mean crest displacement ratio and its standard deviation (in brackets) are presented for different dam heights, reservoir conditions, material parameters and spectral acceleration levels, respectively. The results are given separately for two directions (upstream - negative dir., downstream - positive dir.). As the previous figures indicate, mean d_{crest} values were usually underestimated for the simplified methods in negative

direction of ER dams. However, a reverse situation was observed in the positive direction. According to the results of the FR dams, the estimations were more accurate in the both directions. The errors were usually higher for the higher dams. In such dams, it is believed that the extreme crest displacements obtained for some ground motion records led the such difference. Such extreme d_{crest} values, which were caused by ground motion record characteristics, may not be successfully determined by the simplified methods. However, when all the results are evaluated together, it is believed that the simplified methods can sufficiently estimate the variation of d_{crest} for different H, E_c, spectral acceleration level or reservoir conditions.

Table 3.4. *Mean and standard deviation of d_{crest} for E_c = 20 GPa*

		Mean Displacement Ratio - d_{crest} [Std dev] (cm)											
		ER						FR					
		1.0 g	1.1 g	1.2 g	1.3 g	1.4 g	1.5 g	1.0 g	1.1 g	1.2 g	1.3 g	1.4 g	1.5 g
H = 50 m, Negative Dir.	SDOF	0.9 [0.2]	0.8 [0.3]	0.8 [0.3]	0.7 [0.3]	0.7 [0.3]	0.7 [0.3]	0.9 [0.4]	0.8 [0.3]	0.8 [0.3]	0.8 [0.4]	0.8 [0.4]	0.8 [0.4]
	CM F/356	1.3 [0.4]	1.2 [0.5]	1.1 [0.5]	1.0 [0.5]	1.0 [0.5]	0.9 [0.5]	1.1 [0.4]	1.0 [0.4]	1.0 [0.4]	0.9 [0.5]	0.9 [0.5]	0.9 [0.5]
	CM F/440	1.1 [0.3]	1.0 [0.3]	0.9 [0.4]	0.8 [0.4]	0.8 [0.4]	0.8 [0.4]	1.0 [0.4]	0.9 [0.4]	0.9 [0.4]	0.9 [0.5]	0.8 [0.5]	0.8 [0.5]
	CSM A/40	1.0 [0.3]	0.9 [0.4]	1.0 [0.4]	0.9 [0.4]	1.1 [1.0]	1.2 [1.1]	1.1 [0.4]	1.0 [0.4]	1.0 [0.4]	0.9 [0.5]	0.9 [0.5]	0.8 [0.5]
	CSM F/440	1.1 [0.3]	1.0 [0.4]	0.9 [0.3]	0.9 [0.4]	0.8 [0.4]	0.8 [0.3]	1.1 [0.4]	1.1 [0.4]	1.0 [0.4]	1.1 [0.7]	1.1 [0.7]	1.2 [0.8]
H = 50 m, Positive Dir.	SDOF	1.4 [0.3]	1.2 [0.4]	1.1 [0.5]	1.1 [0.5]	1.0 [0.5]	1.0 [0.5]	0.9 [0.3]	0.9 [0.3]	0.8 [0.3]	0.8 [0.3]	0.7 [0.3]	0.7 [0.3]
	CM F/356	1.6 [0.4]	1.4 [0.4]	1.3 [0.5]	1.2 [0.5]	1.1 [0.5]	1.1 [0.5]	1.0 [0.3]	1.0 [0.4]	0.9 [0.4]	0.9 [0.4]	0.8 [0.4]	0.8 [0.4]
	CM F/440	1.4 [0.3]	1.2 [0.4]	1.1 [0.4]	1.1 [0.4]	1.0 [0.5]	1.0 [0.5]	0.9 [0.3]	0.9 [0.3]	0.8 [0.3]	0.8 [0.3]	0.8 [0.3]	0.8 [0.4]
	CSM A/40	1.6 [0.4]	1.4 [0.4]	1.3 [0.5]	1.2 [0.5]	1.1 [0.5]	1.1 [0.5]	1.0 [0.3]	1.0 [0.4]	0.9 [0.4]	0.9 [0.4]	0.8 [0.4]	0.8 [0.4]
	CSM F/440	1.7 [0.4]	1.4 [0.4]	1.3 [0.4]	1.2 [0.4]	1.2 [0.4]	1.1 [0.4]	1.0 [0.3]	1.0 [0.4]	0.9 [0.4]	0.8 [0.4]	0.8 [0.4]	0.8 [0.4]
H = 100 m, Negative Dir.	SDOF	0.7 [0.3]	0.8 [0.3]	0.7 [0.3]	0.7 [0.4]	0.7 [0.4]	0.7 [0.3]	1.0 [0.3]	1.0 [0.3]	0.9 [0.4]	0.9 [0.4]	0.9 [0.4]	0.9 [0.4]
	CM F/356	1.0 [0.3]	1.0 [0.3]	1.0 [0.4]	1.0 [0.4]	0.9 [0.4]	0.9 [0.3]	1.2 [0.5]	1.2 [0.5]	1.2 [0.4]	1.1 [0.4]	1.1 [0.4]	1.1 [0.4]
	CM F/440	1.0 [0.3]	1.0 [0.3]	1.0 [0.3]	1.0 [0.4]	1.0 [0.4]	1.0 [0.4]	1.2 [0.4]	1.2 [0.5]	1.1 [0.4]	1.1 [0.4]	1.0 [0.4]	1.0 [0.4]
	CSM A/40	0.9 [0.2]	1.0 [0.5]	1.0 [0.5]	1.0 [0.5]	1.0 [0.5]	1.0 [0.6]	1.2 [0.5]	1.2 [0.5]	1.2 [0.4]	1.1 [0.4]	1.0 [0.4]	1.0 [0.4]
	CSM F/440	0.9 [0.3]	0.9 [0.2]	0.9 [0.3]	0.9 [0.5]	0.9 [0.5]	0.9 [0.4]	1.3 [0.5]	1.2 [0.5]	1.2 [0.5]	1.1 [0.3]	1.1 [0.3]	1.1 [0.3]
H = 100 m, Positive Dir.	SDOF	1.3 [0.5]	1.2 [0.5]	1.2 [0.6]	1.3 [0.6]	1.2 [0.5]	1.2 [0.6]	0.8 [0.2]	0.8 [0.2]	0.8 [0.2]	0.8 [0.2]	0.7 [0.2]	0.7 [0.2]
	CM F/356	1.6 [0.9]	1.6 [0.9]	1.6 [0.8]	1.6 [0.9]	1.6 [0.9]	1.6 [0.9]	1.0 [0.2]	1.0 [0.3]	1.0 [0.3]	1.0 [0.3]	1.0 [0.3]	1.0 [0.3]
	CM F/440	1.5 [0.9]	1.6 [0.9]	1.5 [0.8]	1.6 [0.9]	1.6 [0.9]	1.6 [0.9]	0.9 [0.2]	0.9 [0.3]	1.0 [0.3]	1.0 [0.3]	1.0 [0.3]	1.0 [0.3]
	CSM A/40	1.6 [0.9]	1.6 [0.9]	1.5 [0.9]	1.4 [1.0]	1.0 [0.5]	0.9 [0.5]	1.0 [0.2]	1.0 [0.3]	1.0 [0.3]	1.0 [0.3]	0.9 [0.3]	0.9 [0.3]
	CSM F/440	1.6 [0.9]	1.6 [0.8]	1.6 [0.8]	1.7 [0.9]	1.7 [0.8]	1.7 [0.8]	0.9 [0.2]	0.9 [0.2]	0.9 [0.3]	1.0 [0.3]	1.0 [0.3]	1.0 [0.2]
H = 150 m, Negative Dir.	SDOF	0.9 [0.2]	0.9 [0.1]	0.8 [0.2]	0.8 [0.2]	0.8 [0.2]	0.8 [0.2]	0.9 [0.3]	0.8 [0.3]	0.8 [0.3]	0.8 [0.2]	0.8 [0.3]	0.8 [0.3]
	CM F/356	0.9 [0.2]	0.9 [0.2]	0.9 [0.2]	0.9 [0.2]	0.9 [0.2]	0.9 [0.2]	1.0 [0.4]	1.0 [0.4]	0.9 [0.4]	0.9 [0.3]	0.9 [0.4]	0.9 [0.4]
	CM F/440	0.9 [0.2]	0.9 [0.2]	0.9 [0.2]	0.9 [0.2]	0.8 [0.2]	0.8 [0.2]	1.0 [0.4]	0.9 [0.4]	0.9 [0.4]	0.9 [0.3]	0.9 [0.4]	0.9 [0.4]
	CSM A/40	0.9 [0.2]	0.9 [0.2]	0.9 [0.2]	0.9 [0.2]	0.9 [0.2]	0.9 [0.2]	1.0 [0.4]	1.0 [0.4]	0.9 [0.4]	0.9 [0.3]	0.9 [0.4]	0.9 [0.4]
	CSM F/440	0.9 [0.2]	0.9 [0.2]	0.8 [0.2]	0.8 [0.2]	0.8 [0.2]	0.8 [0.2]	1.0 [0.4]	0.9 [0.3]	0.9 [0.3]	0.9 [0.3]	0.9 [0.3]	0.9 [0.2]
H = 150 m, Positive Dir.	SDOF	1.5 [0.6]	1.4 [0.5]	1.3 [0.5]	1.3 [0.5]	1.3 [0.5]	1.2 [0.5]	0.8 [0.2]	0.8 [0.2]	0.8 [0.2]	0.8 [0.2]	0.8 [0.2]	0.8 [0.2]
	CM F/356	2.0 [0.8]	2.0 [0.8]	1.9 [0.8]	1.9 [0.8]	2.0 [0.8]	2.0 [0.9]	0.9 [0.2]	0.9 [0.2]	0.9 [0.2]	0.9 [0.2]	0.9 [0.3]	0.9 [0.3]
	CM F/440	2.0 [0.7]	1.9 [0.8]	1.9 [0.8]	1.9 [0.8]	1.9 [0.8]	1.9 [0.9]	0.9 [0.2]	0.9 [0.2]	0.9 [0.2]	0.9 [0.2]	0.9 [0.2]	0.9 [0.3]
	CSM A/40	2.0 [0.8]	1.9 [0.8]	1.4 [0.6]	1.1 [0.5]	1.1 [0.5]	1.0 [0.4]	0.9 [0.2]	0.9 [0.2]	0.9 [0.2]	0.9 [0.2]	0.9 [0.2]	0.9 [0.3]
	CSM F/440	2.0 [0.7]	1.9 [0.7]	1.9 [0.8]	2.0 [0.7]	2.0 [0.7]	2.0 [0.7]	0.8 [0.2]	0.9 [0.2]	0.9 [0.2]	0.9 [0.2]	0.9 [0.3]	0.9 [0.3]

Table 3.5. *Mean and standard deviation of d_{crest} for E_c = 30 GPa*

		Mean Displacement Ratio - d_{crest} [Std dev] (cm)											
		ER						FR					
		1.0 g	1.1 g	1.2 g	1.3 g	1.4 g	1.5 g	1.0 g	1.1 g	1.2 g	1.3 g	1.4 g	1.5 g
H = 50 m — Negative Dir.	SDOF	1.0 [0.1]	1.0 [0.1]	1.0 [0.1]	0.9 [0.2]	0.7 [0.3]	0.7 [0.3]	1.2 [0.4]	1.1 [0.4]	1.0 [0.4]	1.0 [0.5]	0.9 [0.5]	0.9 [0.6]
	CM F/356	1.1 [0.2]	1.1 [0.2]	1.1 [0.2]	1.0 [0.3]	0.9 [0.3]	0.8 [0.4]	1.3 [0.4]	1.2 [0.4]	1.1 [0.5]	1.0 [0.5]	0.9 [0.6]	0.9 [0.5]
	CM F/440	1.0 [0.2]	1.0 [0.2]	1.0 [0.2]	1.0 [0.3]	0.8 [0.3]	0.8 [0.4]	1.2 [0.4]	1.1 [0.4]	1.0 [0.4]	1.0 [0.5]	0.9 [0.5]	0.8 [0.5]
	CSM A/40	1.1 [0.2]	1.1 [0.2]	1.1 [0.2]	1.0 [0.3]	0.9 [0.3]	0.8 [0.4]	1.3 [0.4]	1.2 [0.4]	1.1 [0.5]	1.0 [0.5]	0.9 [0.6]	0.9 [0.5]
	CSM F/440	1.2 [0.3]	1.2 [0.3]	1.2 [0.3]	1.1 [0.3]	0.9 [0.4]	0.8 [0.4]	1.3 [0.4]	1.3 [0.4]	1.2 [0.4]	1.3 [0.5]	1.2 [0.5]	1.2 [0.5]
H = 50 m — Positive Dir.	SDOF	1.4 [0.1]	1.4 [0.1]	1.3 [0.1]	1.2 [0.2]	1.1 [0.3]	1.0 [0.4]	0.9 [0.2]	0.9 [0.3]	0.9 [0.3]	0.8 [0.3]	0.8 [0.4]	0.8 [0.4]
	CM F/356	1.7 [0.5]	1.7 [0.5]	1.6 [0.4]	1.4 [0.4]	1.3 [0.5]	1.2 [0.5]	1.0 [0.3]	1.0 [0.3]	1.0 [0.3]	0.9 [0.4]	0.9 [0.4]	0.8 [0.4]
	CM F/440	1.5 [0.4]	1.5 [0.4]	1.4 [0.4]	1.2 [0.4]	1.1 [0.4]	1.1 [0.4]	0.9 [0.2]	0.9 [0.3]	0.9 [0.3]	0.8 [0.3]	0.8 [0.3]	0.7 [0.3]
	CSM A/40	1.7 [0.5]	1.7 [0.5]	1.6 [0.4]	1.4 [0.4]	1.3 [0.5]	1.2 [0.5]	1.0 [0.3]	1.0 [0.3]	1.0 [0.3]	0.9 [0.4]	0.9 [0.4]	0.8 [0.4]
	CSM F/440	2.0 [0.6]	1.9 [0.6]	1.8 [0.6]	1.6 [0.5]	1.5 [0.6]	1.4 [0.6]	1.0 [0.3]	1.0 [0.3]	1.0 [0.3]	0.9 [0.4]	0.8 [0.4]	0.8 [0.4]
H = 100 m — Negative Dir.	SDOF	0.8 [0.3]	0.8 [0.4]	0.8 [0.4]	0.8 [0.4]	0.7 [0.4]	0.8 [0.4]	1.0 [0.3]	1.0 [0.4]	0.9 [0.5]	0.9 [0.5]	0.9 [0.5]	1.0 [0.6]
	CM F/356	1.1 [0.3]	1.0 [0.3]	1.0 [0.3]	0.9 [0.3]	0.9 [0.3]	0.9 [0.4]	1.2 [0.5]	1.1 [0.6]	1.1 [0.5]	1.0 [0.5]	1.0 [0.5]	1.0 [0.5]
	CM F/440	1.0 [0.3]	1.0 [0.3]	0.9 [0.3]	1.0 [0.4]	1.0 [0.4]	1.0 [0.4]	1.1 [0.5]	1.1 [0.5]	1.0 [0.5]	1.0 [0.5]	1.0 [0.5]	0.9 [0.5]
	CSM A/40	1.0 [0.6]	1.0 [0.5]	1.0 [0.5]	1.1 [0.6]	1.1 [0.7]	1.0 [0.5]	1.2 [0.5]	1.1 [0.6]	1.1 [0.5]	1.0 [0.5]	1.0 [0.5]	1.0 [0.5]
	CSM F/440	1.0 [0.3]	1.0 [0.4]	1.0 [0.5]	1.1 [0.7]	1.1 [0.8]	1.1 [0.9]	1.3 [0.6]	1.3 [0.5]	1.2 [0.6]	1.2 [0.5]	1.2 [0.5]	1.2 [0.5]
H = 100 m — Positive Dir.	SDOF	1.2 [0.5]	1.2 [0.5]	1.2 [0.5]	1.1 [0.5]	1.2 [0.5]	1.2 [0.5]	0.9 [0.3]	0.8 [0.3]	0.8 [0.3]	0.8 [0.3]	0.8 [0.3]	0.8 [0.3]
	CM F/356	1.5 [0.7]	1.4 [0.6]	1.4 [0.6]	1.4 [0.8]	1.5 [0.8]	1.6 [0.9]	1.0 [0.2]	1.0 [0.2]	1.0 [0.3]	1.0 [0.3]	1.0 [0.3]	1.0 [0.4]
	CM F/440	1.4 [0.6]	1.4 [0.6]	1.4 [0.6]	1.4 [0.8]	1.5 [0.8]	1.5 [0.9]	1.0 [0.2]	1.0 [0.2]	1.0 [0.3]	1.0 [0.3]	1.0 [0.3]	1.0 [0.4]
	CSM A/40	1.5 [0.7]	1.4 [0.6]	1.4 [0.6]	1.1 [0.5]	0.9 [0.4]	0.9 [0.5]	1.0 [0.2]	1.0 [0.3]	0.9 [0.3]	0.9 [0.4]	0.8 [0.4]	0.8 [0.5]
	CSM F/440	1.4 [0.6]	1.4 [0.5]	1.4 [0.5]	1.5 [0.8]	1.6 [0.9]	1.6 [0.9]	1.0 [0.2]	1.0 [0.2]	1.0 [0.2]	1.0 [0.3]	1.0 [0.3]	1.0 [0.3]
H = 150 m — Negative Dir.	SDOF	0.8 [0.3]	0.7 [0.3]	0.7 [0.3]	0.9 [0.5]	0.7 [0.4]	0.8 [0.4]	1.0 [0.3]	1.0 [0.4]	1.0 [0.5]	1.0 [0.4]	1.0 [0.4]	1.0 [0.5]
	CM F/356	1.0 [0.3]	1.0 [0.3]	1.0 [0.3]	1.0 [0.3]	0.9 [0.3]	0.9 [0.3]	1.2 [0.4]	1.2 [0.4]	1.1 [0.4]	1.1 [0.4]	1.1 [0.4]	1.1 [0.4]
	CM F/440	1.0 [0.3]	1.0 [0.3]	1.0 [0.3]	1.0 [0.3]	1.0 [0.4]	1.1 [0.4]	1.2 [0.3]	1.1 [0.3]	1.1 [0.4]	1.1 [0.4]	1.1 [0.4]	1.1 [0.4]
	CSM A/40	0.9 [0.4]	1.0 [0.7]	1.0 [0.8]	1.0 [0.7]	1.2 [0.8]	1.2 [0.8]	1.2 [0.4]	1.2 [0.4]	1.1 [0.4]	1.1 [0.4]	1.1 [0.4]	1.1 [0.4]
	CSM F/440	0.9 [0.3]	0.9 [0.4]	0.9 [0.5]	1.0 [0.5]	1.0 [0.5]	1.0 [0.4]	1.2 [0.3]	1.2 [0.3]	1.2 [0.3]	1.2 [0.3]	1.1 [0.3]	1.1 [0.2]
H = 150 m — Positive Dir.	SDOF	1.4 [0.5]	1.4 [0.5]	1.4 [0.5]	1.4 [0.6]	1.4 [0.7]	1.3 [0.6]	0.9 [0.2]	0.9 [0.2]	0.9 [0.2]	0.9 [0.2]	0.9 [0.2]	0.9 [0.2]
	CM F/356	2.0 [1.1]	1.9 [1.0]	1.9 [0.9]	1.9 [1.0]	2.0 [0.9]	2.0 [0.9]	1.1 [0.3]	1.1 [0.3]	1.1 [0.3]	1.1 [0.3]	1.1 [0.3]	1.1 [0.3]
	CM F/440	1.9 [1.0]	1.9 [1.0]	1.9 [0.9]	1.9 [1.0]	1.9 [0.9]	1.9 [0.9]	1.1 [0.3]	1.1 [0.3]	1.1 [0.3]	1.1 [0.3]	1.1 [0.3]	1.1 [0.3]
	CSM A/40	2.0 [1.1]	1.9 [1.0]	1.9 [0.9]	1.5 [1.0]	1.0 [0.6]	0.9 [0.5]	1.1 [0.3]	1.1 [0.3]	1.1 [0.3]	1.1 [0.3]	1.1 [0.4]	1.0 [0.4]
	CSM F/440	2.0 [0.9]	2.0 [0.9]	2.0 [0.8]	2.1 [0.8]	2.0 [0.8]	2.0 [0.9]	1.0 [0.3]	1.0 [0.3]	1.0 [0.3]	1.0 [0.3]	1.1 [0.3]	1.1 [0.3]

When the standard deviations are examined, it is seen that deviations for ER dams are usually greater than the ones for FR dams. In this context, it was realized that SDOF Nonlinear THA method gave more successful results in order to determine the mean values and deviations of the crest displacement parameter. This may be due to the fact that such simplified methods seek the actual response by using certain structural and seismic parameters but they cannot include the time-dependent effects of the ground motion record. Increasing the material strength lowered the effect of previous observation such that the underestimation of results in negative direction of ER dams.

The mean crack length ratio and its standard deviation (in brackets) for different dam heights, reservoir conditions, material parameters and spectral acceleration levels are given in Table 3.7. THA* stands for the L_c estimations by using the crest displacements of THA. As in the crest displacement estimation, the crack length estimation for the positive direction of ER dams were not successful. However, a reverse situation was observed in the positive direction of FR dams. For this case, it was easier to estimate the crack length of FR in positive direction.

Table 3.6. *Mean and standard deviation of L_c for E_c = 20 GPa*

				ER						FR			
		1.0 g	1.1 g	1.2 g	1.3 g	1.4 g	1.5 g	1.0 g	1.1 g	1.2 g	1.3 g	1.4 g	1.5 g
H = 50 m — Negative Dir.	SDOF	1.4 [1.0]	1.2 [0.8]	1.1 [0.6]	1.0 [0.3]	1.2 [0.8]	1.0 [0.2]	1.4 [0.8]	1.4 [0.6]	1.1 [0.4]	1.1 [0.4]	1.3 [0.6]	1.2 [0.5]
	CM F/356	1.4 [0.9]	1.3 [1.1]	1.2 [0.8]	1.2 [0.4]	1.2 [1.1]	1.1 [0.2]	1.2 [0.7]	1.2 [0.5]	1.1 [0.3]	1.1 [0.3]	1.3 [0.8]	1.2 [0.6]
	CM F/440	1.4 [0.9]	1.2 [1.0]	1.2 [0.8]	1.1 [0.4]	1.2 [1.1]	1.1 [0.2]	1.3 [0.7]	1.3 [0.6]	1.1 [0.2]	1.1 [0.3]	1.3 [0.7]	1.2 [0.6]
	CSM A/40	1.7 [1.3]	1.3 [0.9]	1.2 [0.7]	1.1 [0.4]	1.5 [1.5]	1.3 [1.1]	1.2 [0.7]	1.2 [0.5]	1.1 [0.3]	1.1 [0.3]	1.3 [0.6]	1.1 [0.4]
	CSM F/440	1.4 [0.7]	1.2 [0.7]	1.2 [0.4]	1.1 [0.4]	1.2 [1.1]	1.1 [0.2]	1.3 [0.7]	1.3 [0.7]	1.1 [0.3]	1.3 [0.7]	1.6 [1.1]	1.3 [0.8]
	THA*	1.5 [0.9]	1.2 [0.9]	1.1 [0.3]	1.3 [0.8]	1.3 [1.0]	1.1 [0.2]	1.4 [0.6]	1.3 [0.6]	1.3 [0.4]	1.3 [0.5]	1.6 [0.9]	1.5 [1.1]
H = 50 m — Positive Dir.	SDOF	2.4 [1.8]	1.8 [0.9]	1.6 [1.0]	1.5 [0.7]	1.4 [1.0]	1.3 [0.7]	1.2 [0.9]	1.0 [0.3]	1.2 [0.8]	1.2 [0.6]	1.1 [0.5]	1.1 [0.5]
	CM F/356	2.8 [2.5]	1.7 [1.1]	1.4 [0.8]	1.4 [0.7]	1.4 [1.0]	1.3 [0.8]	1.2 [0.9]	1.0 [0.3]	1.2 [0.8]	1.2 [0.6]	1.0 [0.3]	1.2 [0.8]
	CM F/440	2.3 [2.3]	1.7 [0.8]	1.6 [0.6]	1.7 [1.1]	1.6 [1.2]	1.2 [0.7]	1.1 [0.8]	1.0 [0.3]	1.2 [0.8]	1.2 [0.6]	1.0 [0.4]	1.2 [0.8]
	CSM A/40	2.8 [2.5]	1.7 [1.1]	1.4 [0.8]	1.4 [0.7]	1.4 [1.0]	1.3 [0.8]	1.2 [0.9]	1.0 [0.3]	1.2 [0.8]	1.2 [0.6]	1.1 [0.6]	1.2 [0.8]
	CSM F/440	2.6 [2.6]	1.4 [0.9]	1.2 [0.4]	1.5 [1.0]	1.5 [1.1]	1.3 [1.0]	1.2 [0.9]	1.1 [0.4]	1.2 [0.8]	1.2 [0.6]	1.0 [0.3]	1.1 [0.5]
	THA*	1.1 [0.3]	1.3 [0.4]	1.3 [0.5]	1.6 [1.3]	1.4 [0.7]	1.2 [0.7]	1.2 [0.9]	1.1 [0.5]	1.3 [1.0]	1.2 [0.6]	1.0 [0.3]	1.2 [0.6]
H = 100 m — Negative Dir.	SDOF	1.3 [0.8]	1.2 [0.7]	1.3 [0.9]	1.3 [0.8]	1.5 [1.0]	1.4 [0.8]	1.2 [0.7]	1.3 [0.6]	1.3 [0.8]	1.3 [0.8]	1.4 [0.6]	1.3 [0.7]
	CM F/356	1.4 [0.8]	1.3 [0.6]	1.5 [1.1]	1.3 [0.7]	1.7 [1.5]	1.6 [1.3]	1.0 [0.4]	1.2 [0.7]	1.2 [0.8]	1.5 [0.9]	1.5 [0.8]	1.4 [0.7]
	CM F/440	1.3 [0.8]	1.2 [0.8]	1.4 [0.8]	1.2 [0.6]	1.7 [1.2]	1.6 [1.3]	1.0 [0.4]	1.1 [0.6]	1.2 [0.8]	1.5 [0.9]	1.4 [0.9]	1.3 [0.7]
	CSM A/40	1.7 [1.2]	1.2 [0.6]	1.6 [1.2]	1.5 [1.1]	1.9 [1.3]	1.5 [1.1]	1.0 [0.4]	1.2 [0.7]	1.2 [0.8]	1.5 [0.9]	1.5 [0.8]	1.4 [0.7]
	CSM F/440	1.5 [1.0]	1.3 [0.9]	1.5 [1.2]	1.3 [0.6]	1.4 [1.0]	1.5 [1.4]	1.1 [0.5]	1.3 [0.8]	1.3 [0.7]	1.4 [0.8]	1.5 [0.9]	1.5 [0.7]
	THA*	1.3 [0.7]	1.4 [1.3]	1.4 [0.9]	1.3 [0.6]	1.7 [0.9]	1.6 [1.4]	1.1 [0.8]	1.2 [0.7]	1.2 [0.5]	1.3 [0.8]	1.4 [0.8]	1.3 [0.7]
H = 100 m — Positive Dir.	SDOF	1.2 [0.4]	1.2 [0.6]	1.2 [0.3]	1.2 [0.5]	1.2 [0.3]	1.1 [0.3]	1.5 [0.8]	1.4 [0.7]	1.5 [0.8]	1.4 [0.7]	1.4 [0.6]	1.6 [0.7]
	CM F/356	1.3 [0.4]	1.2 [0.6]	1.2 [0.3]	1.2 [0.5]	1.2 [0.3]	1.2 [0.3]	1.7 [0.9]	1.4 [0.8]	1.5 [0.8]	1.5 [0.8]	1.6 [1.1]	1.9 [1.2]
	CM F/440	1.3 [0.4]	1.2 [0.6]	1.2 [0.3]	1.2 [0.5]	1.2 [0.3]	1.2 [0.3]	1.6 [0.9]	1.4 [0.8]	1.5 [0.8]	1.5 [0.8]	1.6 [1.0]	1.9 [1.2]
	CSM A/40	1.3 [0.4]	1.2 [0.6]	1.2 [0.3]	1.2 [0.5]	1.1 [0.3]	1.1 [0.3]	1.7 [0.9]	1.4 [0.8]	1.5 [0.8]	1.5 [0.8]	1.5 [0.8]	1.7 [0.9]
	CSM F/440	1.3 [0.4]	1.2 [0.6]	1.2 [0.4]	1.3 [0.5]	1.2 [0.3]	1.2 [0.3]	1.6 [0.9]	1.4 [0.8]	1.5 [0.8]	1.5 [0.8]	1.5 [0.8]	1.8 [0.9]
	THA*	1.1 [0.3]	1.1 [0.4]	1.1 [0.3]	1.1 [0.3]	1.1 [0.3]	1.1 [0.2]	1.7 [0.9]	1.3 [0.7]	1.5 [1.0]	1.6 [1.1]	1.5 [0.8]	1.7 [0.8]
H = 150 m — Negative Dir.	SDOF	1.1 [0.4]	1.1 [0.4]	1.0 [0.2]	1.3 [0.5]	1.2 [0.7]	1.1 [0.4]	1.2 [0.8]	1.2 [0.6]	1.1 [0.6]	1.3 [0.4]	1.3 [0.6]	1.4 [0.5]
	CM F/356	1.1 [0.5]	1.1 [0.5]	1.2 [0.7]	1.3 [0.5]	1.2 [0.8]	1.2 [0.5]	1.1 [0.4]	1.1 [0.3]	1.2 [0.3]	1.2 [0.3]	1.3 [0.4]	1.4 [0.6]
	CM F/440	1.2 [0.5]	1.1 [0.5]	1.2 [0.7]	1.3 [0.5]	1.2 [0.8]	1.2 [0.5]	1.2 [0.5]	1.1 [0.3]	1.2 [0.3]	1.3 [0.4]	1.3 [0.4]	1.4 [0.5]
	CSM A/40	1.2 [0.6]	1.2 [0.6]	1.1 [0.3]	1.3 [0.5]	1.3 [0.9]	1.2 [0.6]	1.1 [0.4]	1.1 [0.3]	1.2 [0.3]	1.2 [0.3]	1.3 [0.4]	1.4 [0.6]
	CSM F/440	1.3 [0.7]	1.3 [1.0]	1.1 [0.3]	1.4 [0.9]	1.2 [0.8]	1.2 [0.5]	1.0 [0.3]	1.1 [0.2]	1.1 [0.3]	1.2 [0.4]	1.2 [0.5]	1.4 [0.6]
	THA*	1.2 [0.7]	1.3 [0.9]	1.2 [0.8]	1.9 [1.5]	1.7 [1.5]	1.6 [1.2]	1.2 [0.6]	1.3 [0.7]	1.4 [0.6]	1.4 [0.5]	1.5 [0.7]	1.4 [0.8]
H = 150 m — Positive Dir.	SDOF	1.1 [0.2]	1.1 [0.2]	1.1 [0.2]	1.0 [0.2]	1.0 [0.2]	1.1 [0.7]	1.5 [1.0]	1.3 [0.8]	1.2 [0.6]	1.2 [0.5]	1.2 [0.6]	1.2 [0.6]
	CM F/356	1.1 [0.2]	1.2 [0.3]	1.3 [0.3]	1.2 [0.3]	1.1 [0.3]	1.2 [0.8]	1.5 [1.0]	1.3 [0.8]	1.2 [0.6]	1.2 [0.5]	1.2 [0.6]	1.1 [0.6]
	CM F/440	1.1 [0.2]	1.2 [0.3]	1.3 [0.3]	1.2 [0.3]	1.1 [0.3]	1.2 [0.8]	1.5 [1.0]	1.3 [0.8]	1.2 [0.6]	1.2 [0.6]	1.2 [0.6]	1.2 [0.6]
	CSM A/40	1.1 [0.2]	1.2 [0.3]	1.1 [0.2]	1.0 [0.2]	1.0 [0.2]	1.1 [0.8]	1.5 [1.0]	1.3 [0.8]	1.2 [0.6]	1.2 [0.5]	1.2 [0.6]	1.2 [0.6]
	CSM F/440	1.1 [0.2]	1.2 [0.2]	1.2 [0.3]	1.1 [0.3]	1.1 [0.3]	1.2 [0.8]	1.5 [1.0]	1.2 [0.8]	1.1 [0.6]	1.2 [0.6]	1.3 [0.7]	1.3 [0.7]
	THA*	1.0 [0.1]	1.0 [0.2]	1.1 [0.1]	1.0 [0.2]	1.0 [0.2]	1.0 [0.6]	1.5 [1.0]	1.4 [0.9]	1.2 [0.7]	1.2 [0.5]	1.4 [0.8]	1.3 [0.9]

Increasing the material strength led shorter L_c and made it difficult to estimate by simplified methods. So, the dams with the H = 50 m and E_c = 30 GPa provided the worst estimations for L_c parameter. According to the results, SDOF Nonlinear THA and CM F/440 methods led more successful results in order to determine the mean values and deviations of the crack length parameter. Although the results found with THA* were also successful, it should be remembered that a THA is required for use.

Table 3.7. *Mean and standard deviation of L_c for E_c = 30 GPa*

		Mean Crack Length Ratio - L_c [Std dev] (m)											
		ER						FR					
		1.0 g	1.1 g	1.2 g	1.3 g	1.4 g	1.5 g	1.0 g	1.1 g	1.2 g	1.3 g	1.4 g	1.5 g
H = 50 m Negative Dir.	SDOF	5.9 [6.5]	5.8 [6.1]	5.2 [4.8]	1.7 [1.9]	1.4 [1.3]	1.3 [0.9]	1.4 [1.0]	1.5 [1.1]	1.4 [0.8]	1.3 [0.6]	1.0 [0.2]	1.1 [0.3]
	CM F/356	6.1 [6.3]	6.1 [5.8]	5.4 [4.6]	1.7 [1.9]	1.4 [1.3]	1.3 [1.0]	1.5 [1.2]	1.4 [1.0]	1.3 [0.7]	1.3 [0.6]	1.0 [0.3]	1.0 [0.2]
	CM F/440	4.0 [3.6]	5.4 [5.5]	5.2 [4.7]	1.7 [1.9]	1.4 [1.3]	1.3 [1.0]	1.5 [1.2]	1.5 [1.1]	1.3 [0.7]	1.3 [0.6]	1.1 [0.3]	1.1 [0.3]
	CSM A/40	6.1 [6.3]	6.1 [5.8]	5.4 [4.6]	1.7 [1.9]	1.4 [1.3]	1.3 [1.0]	1.5 [1.2]	1.4 [1.0]	1.3 [0.7]	1.3 [0.6]	1.0 [0.3]	1.0 [0.2]
	CSM F/440	6.0 [6.5]	5.8 [6.1]	5.6 [5.4]	1.7 [2.2]	1.4 [1.3]	1.3 [0.9]	1.4 [1.2]	1.5 [1.0]	1.4 [0.7]	1.2 [0.5]	1.1 [0.2]	1.0 [0.4]
	THA*	7.2 [6.4]	6.9 [6.2]	5.5 [4.6]	1.7 [1.9]	1.4 [1.3]	1.2 [0.7]	1.3 [0.8]	1.3 [0.8]	1.3 [0.6]	1.2 [0.6]	1.0 [0.2]	1.2 [0.4]
H = 50 m Positive Dir.	SDOF	2.1 [0.0]	1.2 [0.8]	1.8 [1.8]	1.1 [0.7]	1.5 [2.5]	1.7 [1.4]	1.1 [0.1]	1.1 [0.2]	1.1 [0.2]	1.0 [0.2]	1.1 [0.2]	1.0 [0.1]
	CM F/356	0.6 [0.0]	1.2 [0.8]	2.1 [2.0]	1.9 [2.4]	1.7 [1.5]	1.7 [1.1]	1.1 [0.2]	1.1 [0.2]	1.1 [0.2]	1.1 [0.2]	1.1 [0.2]	1.0 [0.1]
	CM F/440	1.5 [0.0]	0.9 [0.4]	1.3 [0.8]	1.2 [1.2]	1.6 [2.4]	1.8 [1.0]	1.0 [0.1]	1.1 [0.2]	1.1 [0.2]	1.0 [0.2]	1.1 [0.2]	1.0 [0.1]
	CSM A/40	0.6 [0.0]	1.2 [0.8]	2.1 [2.0]	1.9 [2.4]	1.7 [1.5]	1.7 [1.1]	1.1 [0.2]	1.1 [0.2]	1.1 [0.2]	1.1 [0.2]	1.1 [0.2]	1.0 [0.1]
	CSM F/440	4.1 [0.0]	1.7 [1.6]	3.3 [5.2]	2.1 [2.5]	1.5 [1.1]	1.7 [1.2]	1.1 [0.1]	1.1 [0.2]	1.1 [0.2]	1.0 [0.1]	1.1 [0.2]	1.0 [0.1]
	THA*	0.9 [0.0]	0.8 [0.4]	0.8 [0.3]	0.9 [0.2]	1.0 [0.6]	1.3 [1.0]	1.1 [0.1]	1.0 [0.2]	1.1 [0.2]	1.1 [0.2]	1.1 [0.2]	1.1 [0.1]
H = 100 m Negative Dir.	SDOF	1.1 [0.6]	1.1 [0.6]	1.4 [0.9]	1.2 [1.0]	1.4 [0.9]	1.2 [0.8]	1.9 [0.8]	2.3 [1.0]	2.1 [0.9]	1.9 [1.1]	1.9 [0.8]	2.0 [1.0]
	CM F/356	1.4 [1.0]	1.7 [1.6]	1.9 [1.4]	1.9 [1.6]	1.9 [1.4]	1.7 [1.4]	2.2 [1.0]	2.6 [1.3]	2.3 [1.0]	2.5 [1.1]	2.1 [0.9]	2.2 [1.1]
	CM F/440	1.3 [0.9]	1.8 [1.5]	1.9 [1.4]	1.9 [1.6]	2.0 [1.6]	1.8 [1.6]	2.1 [1.0]	2.5 [1.2]	2.2 [1.0]	2.5 [1.1]	2.1 [0.9]	2.2 [1.1]
	CSM A/40	1.4 [1.2]	1.6 [1.4]	2.0 [1.5]	2.0 [1.7]	1.9 [1.4]	1.5 [1.1]	2.2 [1.0]	2.6 [1.3]	2.3 [1.0]	2.5 [1.1]	2.1 [0.9]	2.2 [1.1]
	CSM F/440	1.6 [1.3]	1.8 [1.5]	1.8 [1.3]	2.0 [1.7]	1.8 [1.4]	1.6 [1.2]	2.3 [1.0]	2.6 [1.3]	2.3 [0.9]	2.6 [1.1]	2.2 [0.8]	2.4 [1.1]
	THA*	1.4 [1.0]	1.6 [1.4]	1.9 [1.5]	1.9 [1.6]	1.9 [1.5]	1.8 [1.6]	2.0 [0.9]	2.4 [1.1]	2.1 [1.0]	2.4 [1.1]	2.0 [0.8]	2.1 [1.1]
H = 100 m Positive Dir.	SDOF	1.3 [0.5]	1.3 [0.5]	1.2 [0.6]	1.2 [0.6]	1.3 [0.6]	1.2 [0.5]	1.4 [0.8]	1.5 [1.0]	1.3 [0.8]	1.3 [0.8]	1.4 [0.8]	1.4 [0.6]
	CM F/356	1.4 [0.5]	1.3 [0.5]	1.3 [0.7]	1.4 [0.7]	1.4 [0.7]	1.2 [0.6]	1.5 [0.9]	1.7 [1.3]	1.5 [1.2]	1.5 [1.2]	1.6 [1.3]	1.9 [1.6]
	CM F/440	1.4 [0.5]	1.3 [0.5]	1.3 [0.7]	1.3 [0.7]	1.4 [0.7]	1.2 [0.6]	1.4 [0.9]	1.7 [1.3]	1.4 [1.0]	1.5 [1.2]	1.7 [1.3]	1.9 [1.5]
	CSM A/40	1.4 [0.5]	1.3 [0.5]	1.3 [0.7]	1.3 [0.6]	1.3 [0.6]	1.1 [0.4]	1.5 [0.9]	1.6 [1.2]	1.5 [1.2]	1.3 [0.9]	1.4 [1.0]	1.8 [1.4]
	CSM F/440	1.4 [0.5]	1.3 [0.5]	1.3 [0.6]	1.3 [0.7]	1.4 [0.7]	1.2 [0.6]	1.6 [1.1]	1.8 [1.3]	1.5 [1.2]	1.6 [1.2]	1.7 [1.4]	1.8 [1.4]
	THA*	1.2 [0.3]	1.1 [0.4]	1.1 [0.4]	1.1 [0.4]	1.2 [0.3]	1.0 [0.4]	1.6 [1.0]	1.8 [1.3]	1.6 [1.3]	1.5 [1.0]	1.7 [1.3]	1.7 [1.2]
H = 150 m Negative Dir.	SDOF	1.7 [1.1]	1.7 [1.2]	1.6 [1.1]	1.6 [1.1]	1.6 [1.3]	1.4 [1.0]	1.7 [1.1]	1.5 [1.2]	1.6 [0.9]	1.7 [1.0]	1.6 [1.0]	1.6 [0.9]
	CM F/356	1.6 [1.2]	1.7 [1.4]	1.7 [1.4]	1.2 [0.8]	1.1 [0.9]	1.1 [0.5]	1.8 [1.2]	2.2 [1.1]	2.1 [1.0]	2.2 [1.0]	2.1 [0.8]	2.2 [0.8]
	CM F/440	1.7 [1.2]	1.6 [1.4]	1.4 [0.9]	1.2 [0.7]	1.2 [1.1]	1.3 [1.2]	1.8 [1.2]	2.0 [1.2]	2.1 [1.0]	2.2 [1.0]	2.1 [0.8]	2.2 [0.8]
	CSM A/40	1.5 [1.0]	1.8 [1.5]	1.8 [1.4]	1.7 [1.3]	1.6 [1.3]	1.3 [0.9]	1.8 [1.2]	2.2 [1.1]	2.1 [1.0]	2.2 [1.0]	2.1 [0.8]	2.2 [0.8]
	CSM F/440	1.7 [1.2]	1.9 [1.4]	1.8 [1.3]	1.3 [1.0]	1.3 [1.1]	1.1 [0.5]	1.6 [1.2]	1.8 [1.3]	1.9 [1.1]	2.2 [1.0]	1.8 [0.9]	2.0 [1.0]
	THA*	1.2 [0.6]	1.3 [1.0]	1.2 [1.0]	1.2 [0.8]	1.1 [0.7]	1.2 [0.7]	1.4 [1.0]	1.6 [1.2]	1.6 [1.0]	1.8 [1.1]	1.6 [0.9]	1.8 [1.0]
H = 150 m Positive Dir.	SDOF	1.1 [0.4]	1.1 [0.6]	1.0 [0.2]	1.0 [0.2]	0.9 [0.1]	1.0 [0.2]	1.2 [0.6]	1.2 [0.7]	1.4 [0.9]	1.2 [0.7]	1.3 [0.9]	1.2 [0.8]
	CM F/356	1.1 [0.4]	1.1 [0.6]	1.0 [0.2]	1.0 [0.1]	1.0 [0.1]	1.0 [0.1]	1.1 [0.6]	1.3 [0.9]	1.4 [1.0]	1.4 [0.9]	1.5 [1.2]	1.3 [1.0]
	CM F/440	1.1 [0.4]	1.1 [0.6]	1.0 [0.2]	1.0 [0.2]	1.0 [0.1]	1.0 [0.1]	1.1 [0.6]	1.3 [0.9]	1.4 [1.0]	1.4 [0.9]	1.5 [1.2]	1.3 [1.0]
	CSM A/40	1.1 [0.4]	1.1 [0.6]	1.0 [0.2]	1.0 [0.2]	0.9 [0.1]	1.0 [0.2]	1.1 [0.6]	1.3 [0.9]	1.4 [1.0]	1.3 [0.9]	1.5 [1.2]	1.3 [0.9]
	CSM F/440	1.1 [0.4]	1.1 [0.6]	1.0 [0.1]	1.0 [0.2]	1.0 [0.1]	1.0 [0.2]	1.1 [0.6]	1.3 [0.8]	1.4 [1.0]	1.3 [0.9]	1.4 [0.9]	1.3 [0.9]
	THA*	1.0 [0.3]	1.0 [0.6]	0.9 [0.2]	1.0 [0.2]	1.0 [0.1]	1.0 [0.2]	1.2 [0.7]	1.3 [0.7]	1.4 [0.9]	1.2 [0.6]	1.3 [1.0]	1.3 [0.8]

3.4.5. Simplified Prediction Equations

The aforementioned nonlinear static procedures are generally developed for building type of structures. There is lack of studies in the literature that predict the earthquake deformations of concrete dams. This is mostly due to the fact that this information alone may not meaningful for the evaluation or the design of dams. However, these equations may be useful for the future works as similar to this study, which predicts the crack length parameter as a function of the crest displacement. In preliminary design of the dams, such equations can also shade a light for deciding on the design parameters by avoiding excessive crest deformations. The crest displacement values obtained by the results of the numerical simulations of THA was used in a regression analysis and a crest displacement prediction equation was proposed. The parameters dependent on the dam section are R (0 for empty, 1 for full), H (in m), E_c (in GPa). The rest of the parameters are related to ground motion characteristics, such as PGA (in g), HI (m/s) and ASI (m/s^2), respectively. HI is the Housner Intensity (Housner, 1952) and is calculated by the area below the velocity spectrum in the period range 0.1-2.5 sec. ASI is the Acceleration Spectrum Intensity (Von Thun et al., 1988) and is calculated by the area below the acceleration spectrum in the period range 0.1-0.5 sec.

$$d_{max} = \frac{9H + (30R - 0.13HE_c - 160)HI + ((4.5R - 6.5PGA + 34.5)H - 17E_c)ASI^2}{100}$$

(3.35)

Above, d_{max} represents the maximum crest displacement (in cm) where. The coefficient of determination (R^2) for Eq. (3.35) is found as 0.910. It was observed that the crest displacements were highly correlated with HI and ASI values of the ground motion records. In nonlinear analysis, it is interesting to note that the crest displacement was correlated with the parameters that provide a summation of velocity and acceleration spectrums rather than a single value such as spectral acceleration. In Figure 3.65(a), the crest displacement calculated by Eq. (3.35) are compared with THA results by including all the cases. It can be seen that deformation prediction equation reasonably matched the crest deformations of the THA. It's believed that, the

109

proposed equation is sufficiently accurate for the use of nonlinear crest displacement estimation of the concrete gravity dams.

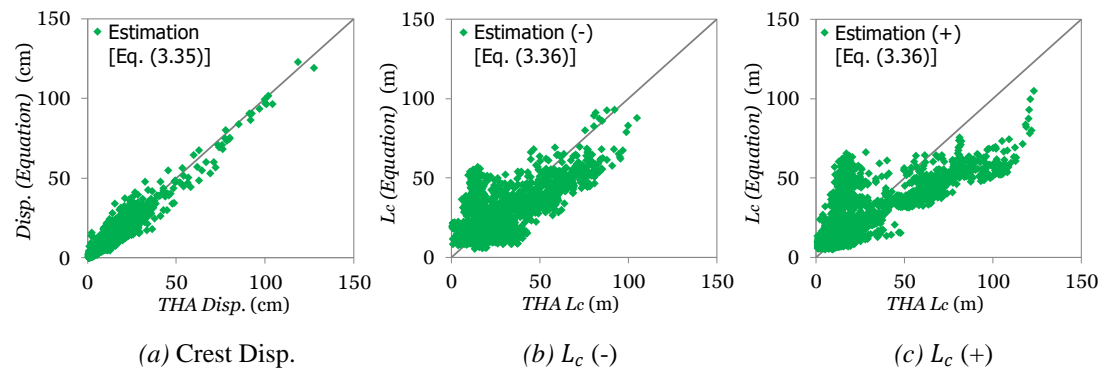*(a)* Crest Disp.   *(b)* L_c (-)   *(c)* L_c (+)

Figure 3.65. Crest displacement prediction equation comparison

Similarly, two equations were proposed for the estimation of crack length by using the THA results. In contrast to the displacements, it was observed that the crack lengths may not be easily predictable. Moreover, different characteristic behavior of the cracks in upstream and downstream directions makes it difficult to estimate the crack lengths at one time. Therefore, one equation is given to estimate the crack lengths in two directions by two different coefficient (C_n) sets. The derived equation and the coefficients are given below (Table 3.8).

$$L_c = [(C_1 + C_2R + C_3HI + C_4PGA)H + (C_5 + (C_6R + C_7HI)f_t]PGA \qquad (3.36)$$

Table 3.8. *Coefficients of crack length estimation*

Direction	C_1	C_2	C_3	C_4	C_5	C_6	C_7
Upstream	0.3	-0.25	0.04	-0.15	10.0	6.0	-0.6
Downstream	0.01	0.25	0.04	-0.05	10.0	0.5	-0.5

The parameters in the equation are explained above. The equation is recommended for dams between 50 and 150 m high. The coefficient of determinations (R^2) for Eq. (3.36) are found as 0.600, 0.650 for downstream and upstream directions, respectively. In Figure 3.65(b) and (c), the crack lengths calculated by Eq. (3.36) are compared with THA results for all the cases. As can be seen, equations could not reasonably represent

110

the analysis data. However, the proposed equations may provide a preliminary information for the crack lengths during the design or evaluation stages of the dams.

3.5. Final Remarks

By conducting 2664 analyses with THA and SLA, deformation and damage of the concrete gravity dams were investigated. The displacement (d_{max}) at the dam crest and the crack length (L_c) at the dam body were studied. It was observed that there may be characteristic crack patterns, which are dependent on the dam parameters. The most important parameter for the crack pattern was found to be the reservoir condition. For the dams with ER, the large cracks are mostly observed on the downstream face of the dams. However, for FR, large cracks were mostly located at the heel of the upstream face of the dams. The dam geometry may also affect the common crack patterns. The dams with less height were more affected by the spectral acceleration levels and for higher dams the crest is in more danger of experiencing failure. If the earthquake level increased, the average crack lengths were mostly increased as expected. It is also observed that diversity in crack lengths of the rigid dams was less affected by the earthquake intensity. According to the results, the simplified method with SLA and dam-reservoir interaction may be a promising alternative to predict cracking behavior of the concrete gravity dams. Although the crack length was estimated as a function of the crest displacement, the correct displacement did not always lead the correct crack length. In all nonlinear static procedures examined, the most successful one in displacement estimation was obtained as SDOF Nonlinear THA. The best crack length estimation was usually observed by employing the displacements of SDOF Nonlinear THA approximation. The successor simplified method was found to be CM F/440. This method was also provided promising results for both crest displacement and crack length estimations. The analysis results of the various dam cases showed that the estimation of the crack length by the first mode approximation and SLA method is possible. The higher dams with FR were usually exposed to higher crest displacements and crack lengths. Especially for the upstream direction of FR dams, the estimation of crack lengths was more successful with the simplified method.

Results revealed that the crest displacement was significantly affected by the ground motion characteristics. Moreover, the parameters describing the intensity of the ground motion (i.e. HI, ASI, AI) was strongly correlated with the nonlinear behavior of dam rather than the parameters such as S_{a1} or PGA. A simple prediction equation for d_{max} was proposed as a function of R, E_c, H, PGA, HI and ASI. It seen that Eq. (3.35) was in good agreement with the THA results. For the crack lengths, it was observed that the upstream and downstream cracks usually behave differently. So, two equations were proposed for the estimation of the crack lengths in two different directions. As in the crest displacement estimation, the THA results were used as the data set. However, crack length estimates were not successfully correlated with the analysis data. As a result, within the limits of the parameters in this study, Eq. (3.35) provided a good agreement for the estimation of the crest displacement (d_{max}). For the crack length (L_c), Eq. (3.36) provides only a rough approximation about the actual crack behavior of the dams. For the L_c estimation, the best simplified method was found to be coupled solution of SDOF nonlinear THA and the SLA. The combined results of these tools provided an acceptable accuracy for all the different cases examined.

CHAPTER 4

EARTHQUAKE DAMAGE ASSESSMENT

4.1. Background

There are many concrete dams in the world and the number is still increasing. These dams represent a significant value for the country's assets as the heritage of the next generations. Although the dams are constructed in accordance with certain design rules, it is still a potential risk because of the possible damage after an earthquake. Some dams, depending on their size and location may cause only minimal loss while large dams may cause catastrophic risks even in moderate events. The effects of a dam failure may result in loss of life, property damage, environmental effects, cultural and historical losses and social impacts, consequently, dam safety should be given one of the highest priority disaster risk management (ICOLD, 2005). Although the seismic safety assessment of concrete dams is an area of considerable work, predicting the damage on dams and their classification are still a challenge.

Leger and Leclerc (1996) examined the cracking responses of gravity dams exposed to three different types of input acceleration, namely, scaled historical records; modified historical records with Fourier amplitude spectra and synthetic records. Although they did not classify the damage on the dams, they revealed the relation between damage, the ground motion record characteristics and the dam geometry. In 2003, Tekie et al. presented a fragility assessment method for concrete gravity dams to assess their performance against seismic hazards. They investigated some interesting quantitative measures of performance such as cracking at the neck of the dam, nonlinear behavior at foundation or probability of sliding of about some specific deformation levels. In another similar study, damage state of the concrete gravity dams was studied by employing nonlinear static pushover and incremental dynamic analysis

(Alembagheri, 2013). For the analysis, they employed single concrete gravity dam section with 12 records and various spectral accelerations. They proposed three damage indexes and they observed that the damage indexes based on crest displacement can effectively estimate the damage level of the dam. The study of Hariri-Ardebili and Saouma (2015) focused on a multi-variable cumulative damage index for concrete dams by qualitatively identifying the possible failure modes. They revealed that the cracking may start at some critical locations in dam such as the neck area at the change of downstream face slope or along lift joints at various elevations etc. According to their results, the damage indices could provide quantitative failure state in terms of input dynamic motion. Soysal et al. (2016) developed a technique to quantify the damage levels on a dam using incremental dynamic analysis. They have suggested four different damage states and questioned the relation between the ground motion characteristics and damage levels. According to their results, although the crest displacement and acceleration showed weakly correlated with the damage, the spectral velocity and the peak ground acceleration correlations were promising.

4.2. Objectives

For the assessment of dams, adopting a simple approach like "safe/not safe" could be a difficult and an expensive task. Instead of following this approach, it may be appropriate to categorize damage levels more specifically. For this reason, 3 different damage states were proposed for the use of concrete dams by employing the findings of the previous chapter. These damage states were determined based on the crack lengths in the dam body. The base slip or overturning stability of the rigid block are excluded from the scope of this study. The post-earthquake effects were also included as another important factor (Leger, 1996). To include the post-earthquake effects, a plain concrete section analysis with tension softening was employed. In the analysis, increase in the water pressure was included due to the progressive crack opening. However, the pressure changes due to drainage was not considered. Finally, to evaluate the structural performance in probabilistic terms, fragility analysis was conducted. These quantitative performance measures may shed light on rehabilitation

decisions and support organizations to develop risk management policies for their dam stock.

4.3. Damage States and Assessment Procedure

To determine the damage states in concrete gravity dams, 3 levels are suggested including the crack formation trends at the upstream and downstream faces of the dam (Figure 4.1). All these damage states were based on common crack pattern findings which described in the previous section. In order to determine whether a dam is in the severe state, it was also questioned that if the cracks extend throughout the entire dam section. In such a case, it was believed that a dam might have a high risk of sliding or overturning. For damage states below this level, the sudden collapse risk of the dam is considered to be lower. However, in such cases its recommended that the dams should be rapidly rehabilitated. It should be kept in mind that, with the inclusion of post-earthquake effects, the dam may easily reach a higher level of damage state. To illustrate clearly, the 3 different damage states on the dams and their scopes are given below (Figure 4.1):
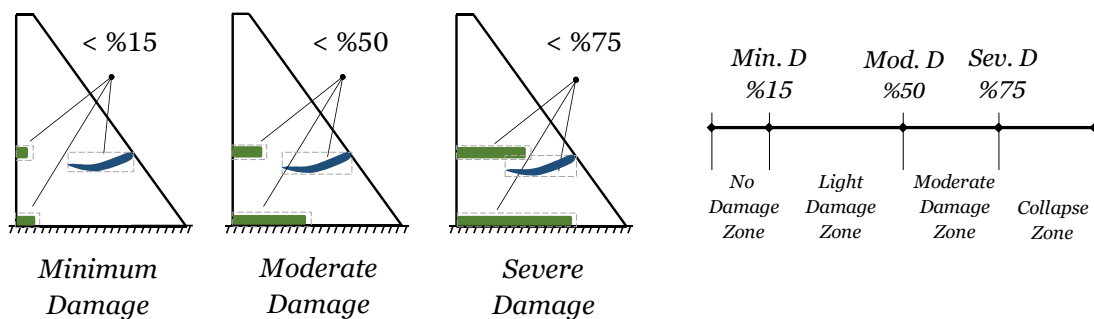

Figure 4.1. Damage states

Minimum Damage: If there is a crack on any face of the dam and its length is less than 10% of the dam section width (with respect to the its location) after an earthquake or post-earthquake. Although there is only a small crack formation on the upstream face with respect to the section width, there is a possibility that the existing crack may grow in length due to water contact.

Moderate Damage: If there is a crack on any face of the dam and its length is between 10% and 75% of the dam section width after an earthquake or post-earthquake. The difference with minimum damage state is that the crack length at upstream face is longer and the effects of post-earthquake are now more critical.

Severe Damage: If there is a crack on any face of the dam and its length is more than 75% of the section width or the cracks on the dam merge along the section after an earthquake or post-earthquake. This damage state is at the verge of collapse and is therefore very critical.

All these damage levels were assessed for all types of dam sections, earthquake records and spectral acceleration levels examined in the previous section. In the light of all this information and spectral acceleration levels, the structural performance of different dam parameters was identified by conducting fragility analysis.

To evaluate the structural performance within a probabilistic view, the damage states should be assessed to the dam sections by employing earthquake intensities and post-earthquake demands. The damage levels used in this section are based on the results of THA. The crack lengths in the dams are calculated by the method described in the Section 3.4. Damage states are determined according to the crack lengths obtained by the analysis results of each dam type with each ground motion records. To obtain the post-earthquake effect on the upstream face of the dams, a simple section analysis with tension softening is employed. The procedure used for post-earthquake response is described below (Figure 4.2). For each dam section the following steps were followed in sequence.

- Specify the crack length on the upstream face of the dam when THA is completed and calculate the axial loads including the uplift forces.
- Isolate the area where the cracking starts and accept this area as a divided concrete section (Figure 4.3).
- Draw the moment-curvature-crack length relationship for the divided section under calculated axial load.

- Determine the current moment and curvature response according to the initial crack length. The obtained curvature value is the earthquake curvature demand ($EQ\ DEMAND$).
- Unload the system toward the origin from current state.
- Calculate the new axial load including the updated uplift force over the open cracks on upstream face.
- Draw the new moment-curvature-crack length relationship for the updated axial load.
- Initially, load the system with resultant moment due to axial load, hydrostatic forces and uplift forces.
- Then, add a specific percentage (PER) of the earthquake curvature demand computed previously from the time history analysis as the post-earthquake demand ($POST\ EQ\ DEMAND$) (Eq. (4.1)).
- Recalculate the crack length.
- If calculated crack length is equal or lower than the initial length, stop the iteration. If it is larger, return to step 4 and continue.

In the procedure, it was assumed that cracks propagate parallel to the boundaries of divided section in Figure 4.3. The divided section width was taken as constant, 1 m and the f_t and G_f were selected in accordance with the dam parameters.
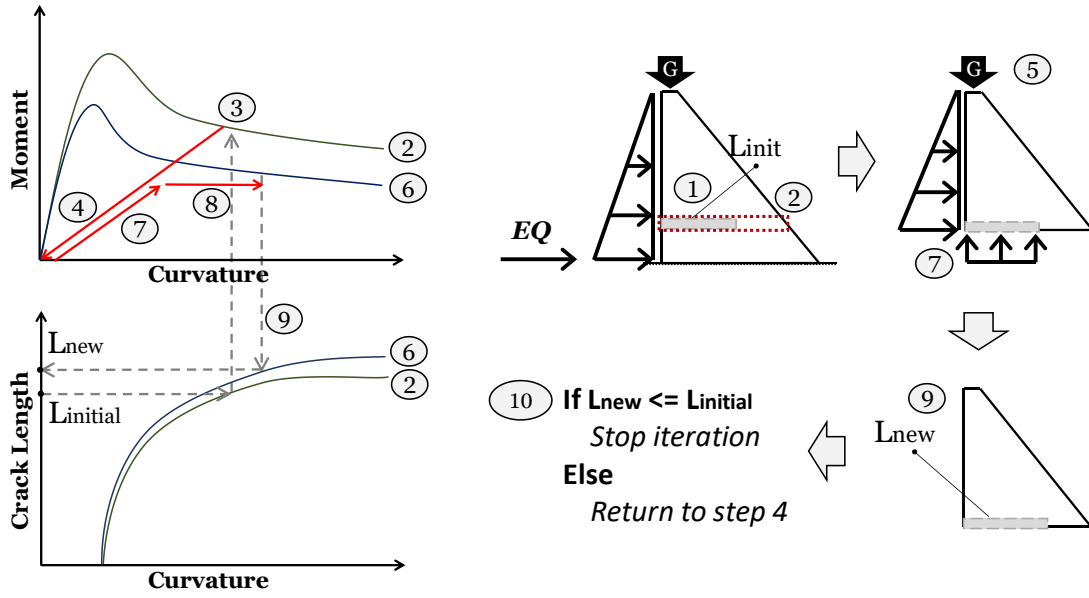
Figure 4.2. Procedure for post-earthquake response

The post-earthquake curvature demand was calculated as ratio of the earthquake curvature demand. This ratio is called as Post-Earthquake Ratio (PER) and given in Eq. (4.1). PER is related with earthquake curvature demand so; its value depends on different dam parameters and ground motion characteristics. Because aftershocks are closely related to the main earthquake, it is believed that that technique is an acceptable way of computing the post-earthquake demand.

$$PER \ = \ POST \ EQ \ DEMAND \ / \ EQ \ DEMAND \qquad (4.1)$$

PER = 0 $\rightarrow$ no post-earthquake

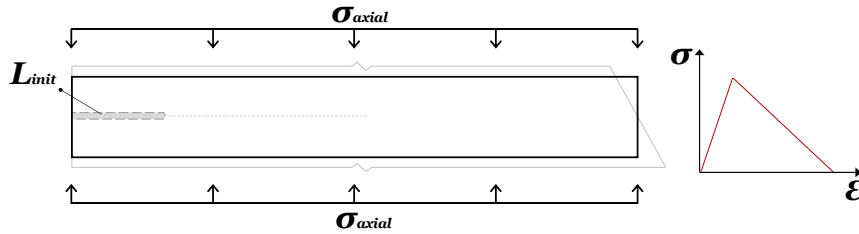PER = 0.25 $\rightarrow$ 25% of the earthquake curvature demand is added

Figure 4.3. Section analysis with tension softening

118

For the calculation of the post-earthquake effect, the area where the cracking starts was isolated and accepted as a new concrete section (Figure 4.3). Then, the failure of the concrete section in the mid-span due to the progression of the crack is idealized as follows. As the load increases, the layers in the middle region were assumed to be one of the three possible states: linear state, softening state and zero stress state. The moment and curvature for concrete section were calculated by providing a force equilibrium on the section divided by 100 layers.

$$\varepsilon_{cr} = f_t/E_c \qquad (4.2)$$

A linear tension softening curve was employed and the cracking strain was assumed as Eq. (4.2). For each dam type, their own material properties were adopted (see Section 3.3.3). For each step, the natural axis and internal forces were calculated by gradually increasing the top layer strain. The crack penetration in the section was calculated by following the step-by-step progress. As a result, damage states were determined for different earthquake and post-earthquake scenarios and all the necessary data were obtained for fragility analysis.

4.4. Earthquake Dam Assessment

The fragility analysis represents the probability of exceeding specified limit states as a function of an engineering demand parameter. Fragility is a useful tool for evaluate the structural performance within a probabilistic platform. It may give an idea about the potential of a structural system to be damaged by an earthquake event. To develop fragility curves, experimental results or analytical modelling data can be employed. In this study, the calculated damage levels were taken as limit states, and the earthquake and post-earthquake levels were taken as the demand parameters. There is not a single methodology for the determination of fragility curves, due to the uncertainty involved in estimating the damage states and the demand parameters. However, log-normal distribution is commonly used technique for the fragility curves, and this approach has been utilized in this study.

The log-normal cumulative distribution function is widely used due to its simplicity. Additionally, it generally fits observed distributions of quantities, reasonably. The log-normal distribution function can be represented by Eq. (4.3).

$$f(x) = \phi \left(\frac{\ln(x) - \mu}{\sigma} \right) \tag{4.3}$$

In the equation, ϕ represents normal distribution function and x can be assigned as the ground motion intensity parameter. Then, σ denotes the standard deviation of the natural logarithm of the ground motion intensity, μ is the mean of the natural logarithm of the ground motion intensity, respectively.

The distribution of probability of exceedance of the damage states with respect to the intensity measures represents a unique scattering. These values can be drawn as a function of ground motion intensities, respectively (Figure 4.4). A simple method was followed to generate fragility curves. The procedure is summarized below.

- First select a dam type (e.g H = 50 m dam with E_c = 20 GPa and ER), a PER level (e.g PER = 0) and a damage state (e.g Minimum Damage).
- For the selected case, determine the number of dams at the selected damage state (number of damaged dams) for each spectral acceleration level.
- For each IL, divide the number of damaged dams by total case number (37) to find the fracture (probability of exceedance) as a function of IL.
- By using the probability of exceedance values obtain the fragility curve according to log-normal distribution function.
- Fit a smooth curve by using the fragility data and least square regression.
- Repeat the procedure for all dam types and damage states.

Examples of fragility curves are given in Figure 4.4. As described, the fragility curves were constructed using the log-normal distribution function by fitting the scattered probability of exceedance values. As shown in Figure 4.4, the best fit for the probability of exceedance values are satisfied for each case.
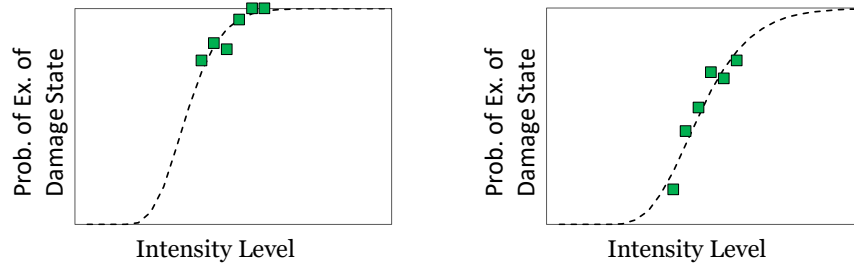
Figure 4.4. Example of fragility curves

In the following chapters, the fragility curves are presented for each section, namely 50 m height dam with ER and FR, 100 m height dam with ER and FR, 150 m height dam with ER and FR, respectively. For each damage states, the PoD values are given as a function of ground motion spectral acceleration levels including the additional post-earthquake demands. Similarly, the fragility curves of all damage states are presented for the two extreme values of the post-earthquake scenarios, namely, PER = 0 and PER = 1, respectively.

4.4.1. 50 m Height Dam with ER

The fragility curves for 50 m height dam with ER are presented in Figure 4.5 for different PER values. The figure is given for two different concrete materials, namely, $E_c = 20$ MPa and $E_c = 30$ MPa. According to the fragility curves, for all damage states with ER case, increasing the concrete strength decreased the potential of the dam to be damaged by an earthquake. Another observation is that, the effect of PER was more prominent for higher damage states and lower material rigidity. The comparison of damage states for two extreme PER values and different material types are presented in Figure 4.6. According to result, to satisfy 50% of probability of damage for severe damage, spectral acceleration levels should be around 1.8 g and 2.0 g for PER = 0 (0.7 g and 1.4 g for PER = 1), for $E_c = 20$ GPa and $E_c = 30$ GPa, respectively. As seen, the dams with low rigidity reached to the same damage level more rapidly. It can be also observed that small dams with ER were highly dependent on the PER values for severe damage state. However, for lower damage states, the effect of PER is limited. Another conclusion was that if PER = 0, the probability of observing severe damage is quite low for small dams with ER.
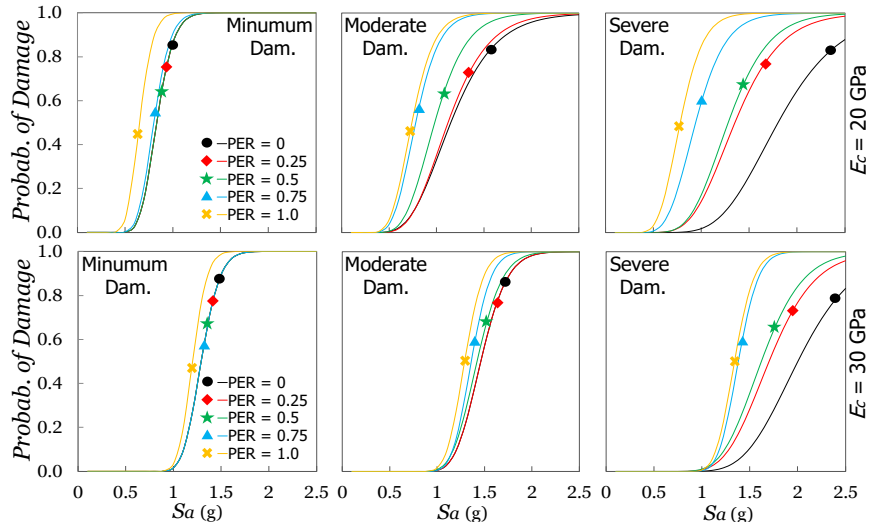
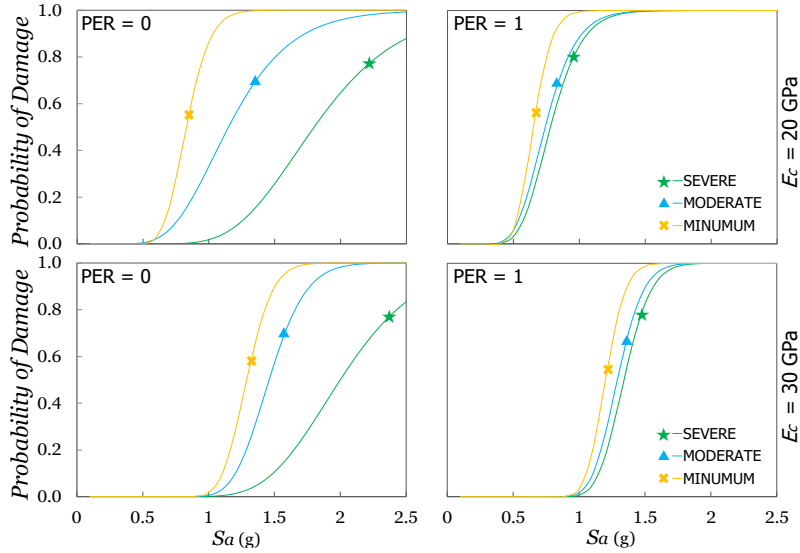*Figure 4.5.* Effect of PER on PoD for ER, $H = 50$ m

Figure 4.6. PoD for all damage states for ER, $H = 50$ m

4.4.2. 50 m Height Dam with FR

The fragility curves for 50 m height dam with FR are presented in Figure 4.7 for different PER values. For the FR dams, the change in PER did not any effect on PoD values until the moderate damage. However, its effect was significant for the moderate and severe damage states for both of the material types. Another important result is that the material strength was less effective on PoD values in compare to the ER dams. As seen in Figure 4.7, except for the minor differences, the curves of different material

types were mostly matched. The comparison of damage states for two extreme PER values and different material types are presented in Figure 4.8. According to the results, to satisfy 50% of probability of damage for severe damage, spectral acceleration levels should be around 1.3 g and 1.4 g for PER = 0 (0.7 g and 0.8 g for PER = 1), for $E_c = 20$ GPa and $E_c = 30$ GPa, respectively. For the severe damage state, a similar behavior for the ER case was also observed for the FR case. For this case, PER affected PoD significantly and increase in PER provided steeper fragility curves.
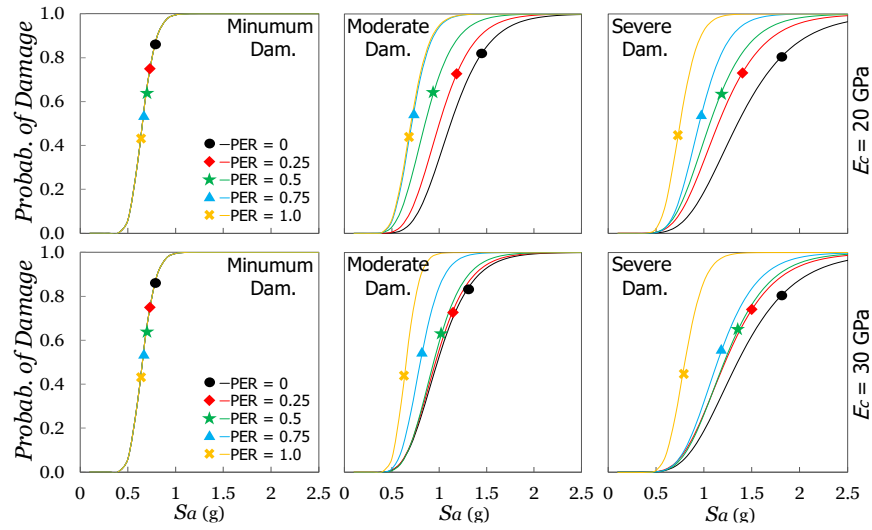

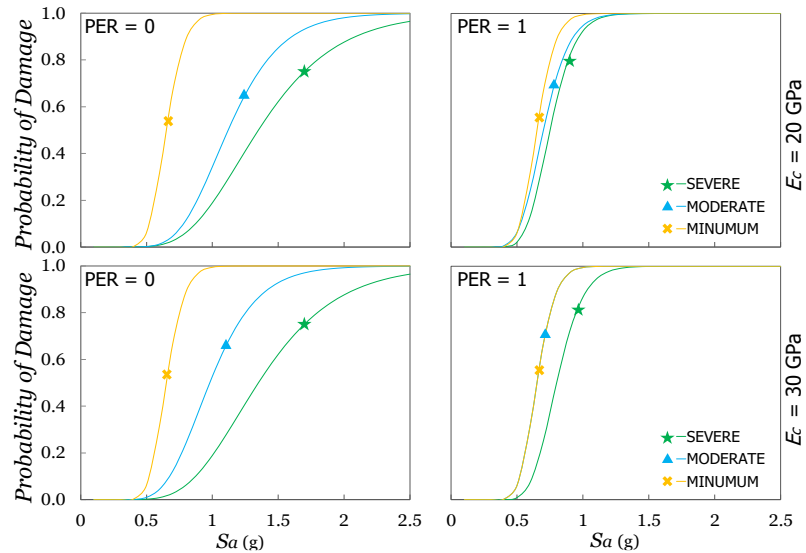*Figure 4.7.* Effect of PER on PoD for FR, $H = 50$ m

Figure 4.8. PoD for all damage states for FR, $H = 50$ m

4.4.3. 100 m Height Dam with ER

The fragility curves for 100 m height dam with ER are presented in Figure 4.9 for different PER values. According to the curves, the effect of PER on PoD values was not significant until the moderate damage state. Similarly, it was found that the material type had limited effect on any damage states. According to the results, it can be observed that the fragility curves of this case were steeper than the those of 50 m ER, especially for the moderate and severe damage states.
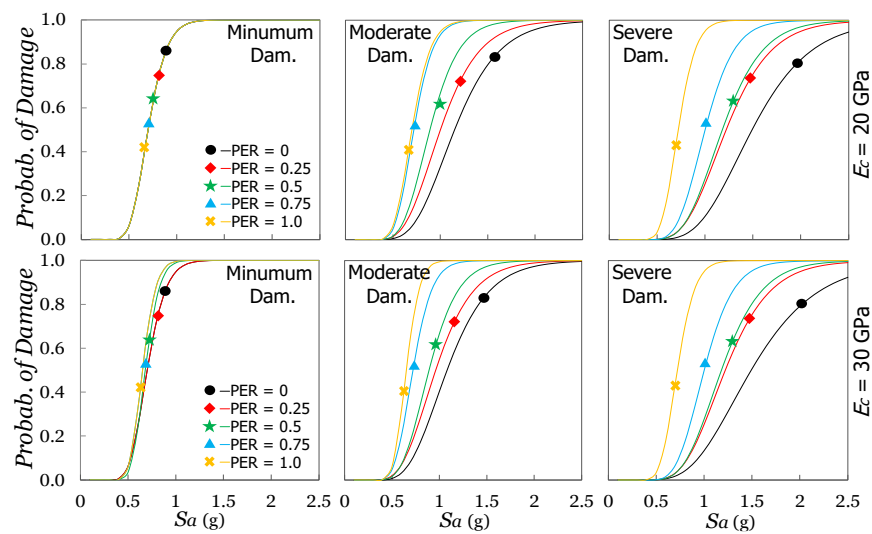

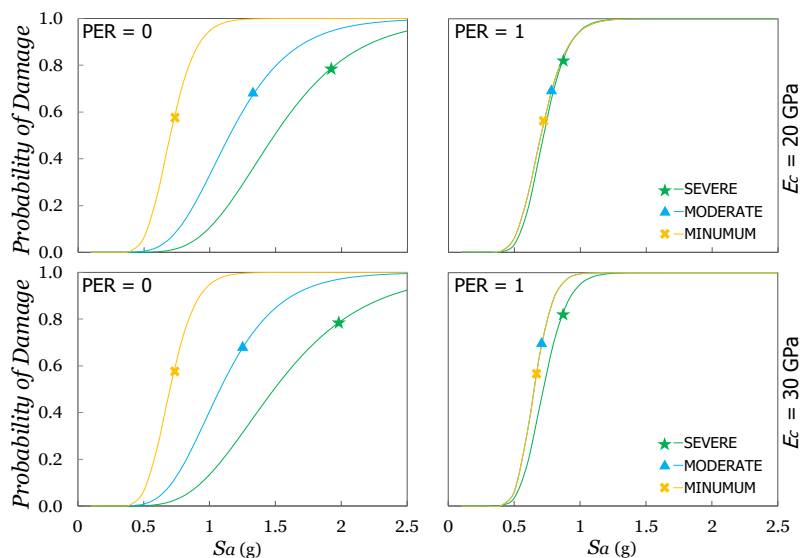*Figure 4.9.* Effect of PER on PoD for ER, H = 100 m

Figure 4.10. PoD for all damage states for ER, H = 100 m

According to Figure 4.10, to satisfy 50% of probability of damage for severe damage, spectral acceleration levels should be around 1.5 g and 1.5 g for PER = 0 (0.7 g and 0.7 g for PER = 1), for E_c = 20 GPa and E_c = 30 GPa, respectively. An interesting result was that the effect of material strength on the PoD values tended to decrease with increased dam height.

4.4.4. 100 m Height Dam with FR

The fragility curves for 100 m height dam with FR are presented in Figure 4.11 for different PER values. According to the curves, the effect of PER on fragility curves was similar to one observed for the ER case. However, for this case, the material strength was more affected on PoD at the severe damage state. The comparison of the damage for two extreme PER values and different material types are presented in Figure 4.12. According to result, to satisfy 50% of probability of damage for severe damage, spectral acceleration levels should be around 1.5 g and 1.4 g for PER = 0 (0.8 g and 0.7 g for PER = 1), for E_c = 20 GPa and E_c = 30 GPa, respectively.

Figure 4.11. Effect of PER on PoD for FR, H = 100 m
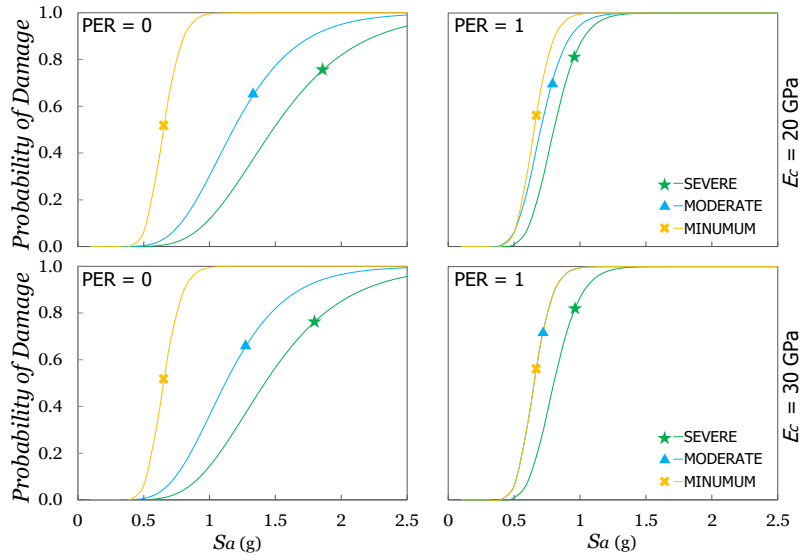
Figure 4.12. PoD for all damage states for FR, $H = 100$ m

4.4.5. 150 m Height Dam with ER

The fragility curves for 150 m height dam with ER are presented in Figure 4.13 for different PER values. According to the fragility curves, the effect of PER on PoD values were not prominent until the severe damage state. Such behavior was also observed for smaller dams. Additionally, the limited effect of material strength was only significant for the severe damage state.

Figure 4.13. Effect of PER on PoD for ER, $H = 150$ m

Figure 4.14. PoD for all damage states for ER, $H = 150$ m

The comparison of damage states for two extreme PER values and different material types are presented in Figure 4.14. According to the result, to satisfy the 50% of probability of damage for severe damage, spectral acceleration levels should be around 1.5 g and 1.4 g for PER = 0 (0.7 g and 0.6 g for PER = 1), for $E_c = 20$ GPa and $E_c = 30$ GPa, respectively.
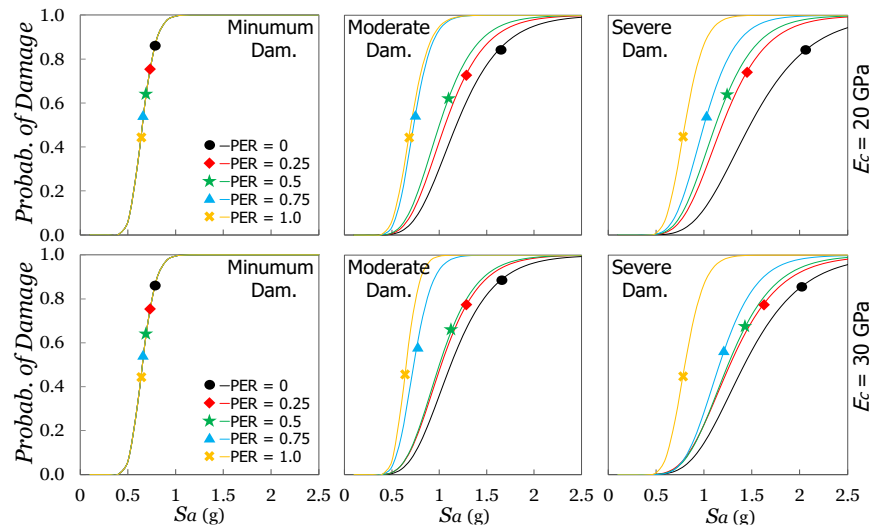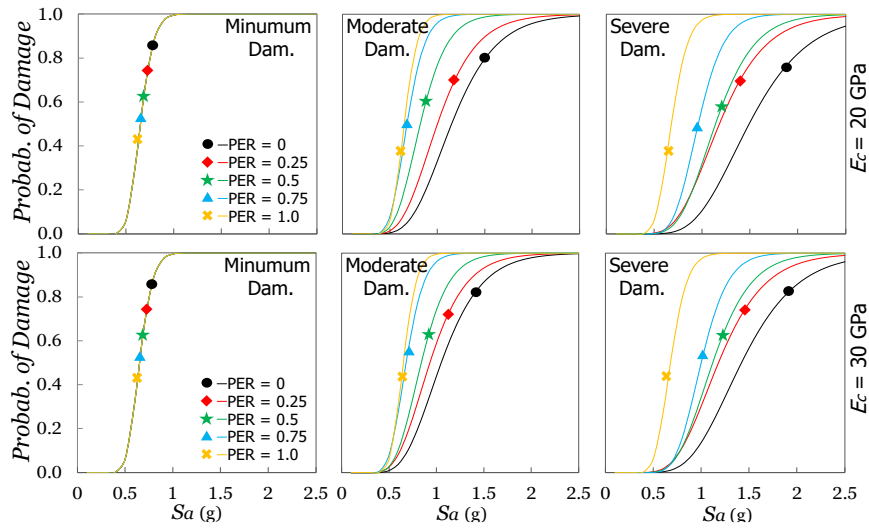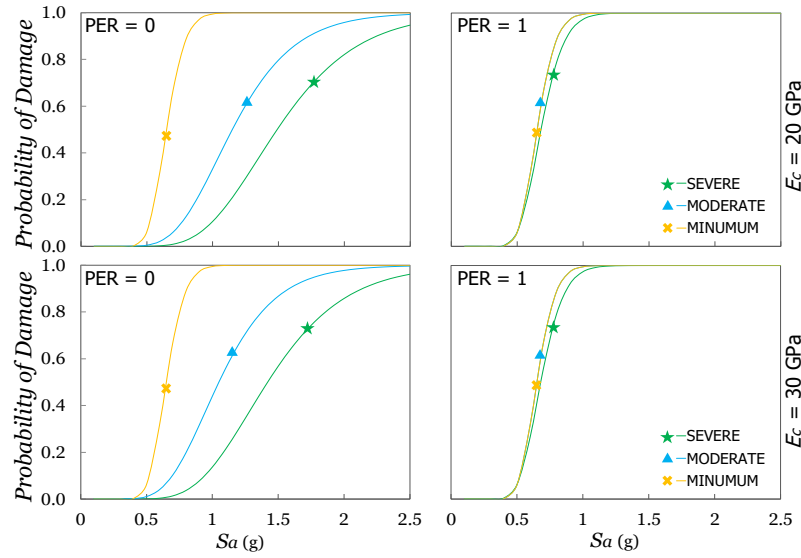
4.4.6. 150 m Height Dam with FR

The fragility curves for 150 m height dam with FR are presented in Figure 4.15 for different PER values. As in the other FR dams, the PER values were mostly effective on PoD at the severe damage state. Similarly, the effect of material strength was more significant for the severe damage state. The comparison of damage states for two extreme PER values and different material types are presented in Figure 4.16. According to result, to satisfy 50% of probability of damage for severe damage, spectral acceleration levels should be around 1.5 g and 1.6 g for PER = 0 (0.8 g and 1.0 g for PER = 1), for $E_c = 20$ GPa and $E_c = 30$ GPa, respectively. As in the 100 m height dam, the fragility curves became more steeper for increasing PER values. In addition to that, especially for larger dams, this effect was significantly important on the estimated PoD values.
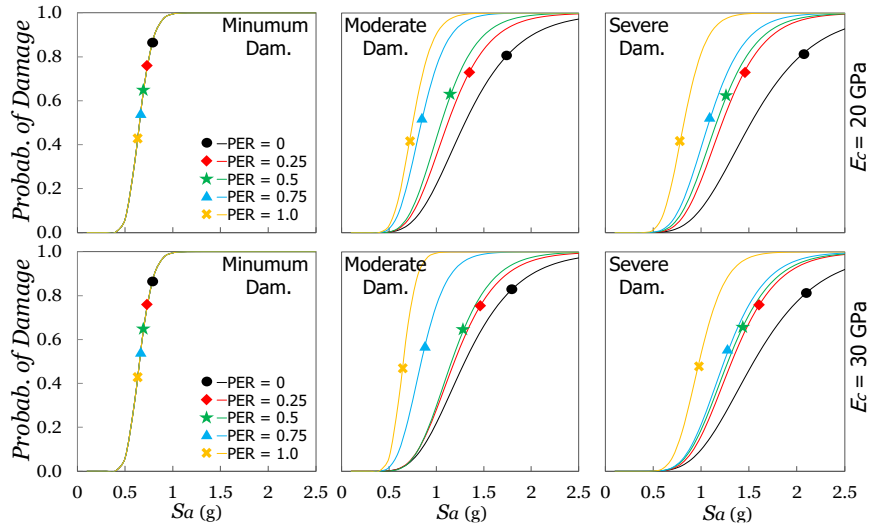
Figure 4.15. Effect of PER on PoD for FR, $H = 150$ m
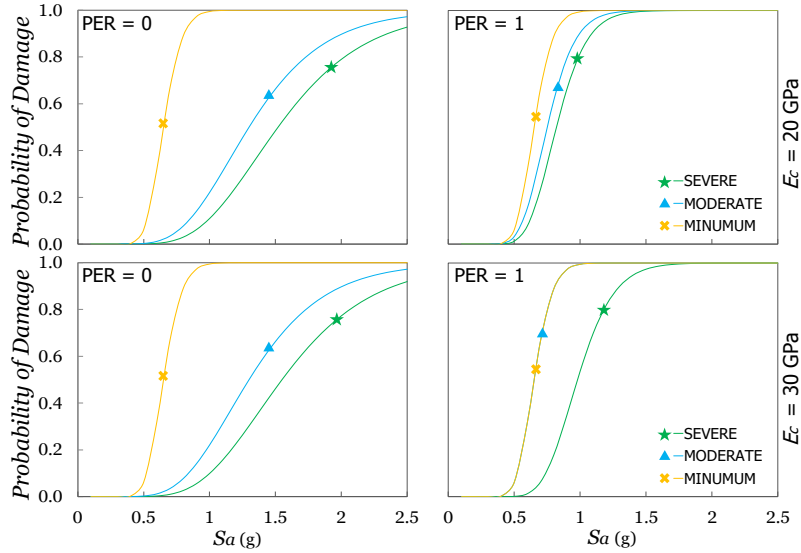
Figure 4.16. PoD for all damage states for FR, $H = 150$ m

4.4.7. Overall Evaluation

In the previous sections, the PoD values were presented for different damage levels and PER values of the dams of same height. In this section, a general evaluation was carried out by comparing the effects of the parameters such as H or reservoir condition while keeping the damage levels constant. In Figure 4.17 and Figure 4.18, PoD values for different H values were compared for both ER and FR cases ($E_c = 20$ GPa), respectively. The moderate and severe damage levels were used along with 3 PER

states, namely PER = 0, PER = 0.5 and PER = 1. The exact figures (Figure 4.19 and Figure 4.20) are also presented for $E_c = 30$ GPa. According to the results, if the damage level (severe to moderate) decreases, the fragility curves become closer. For severe damage, higher PER led steeper curves. In case of the ER dams with severe damage level, such behavior was observed more clearly.

Figure 4.17. PoD for different *H* values, $E_c = 20$ GPa, ER
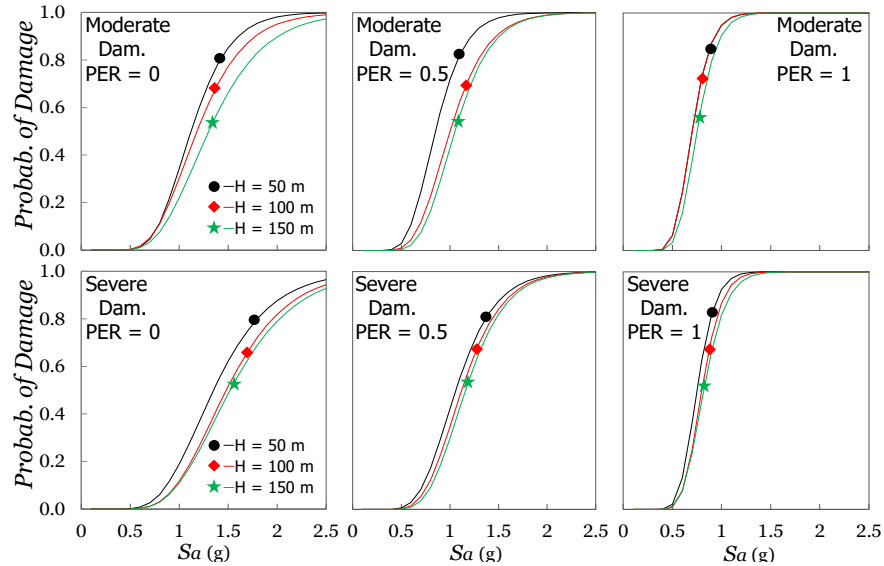
Figure 4.18. PoD for different *H* values, $E_c = 20$ GPa, FR

129

If the PER effect is neglected, the large dams with ER and small dams with FR usually had more potential to observe damage for the same spectral acceleration level. Additionally, for all the dam heights, the effect of PER was more significant for the severe damage. The aforementioned observations remained valid for the dams with higher strength concrete. However, lower strength concrete usually led more steeper fragility curves.

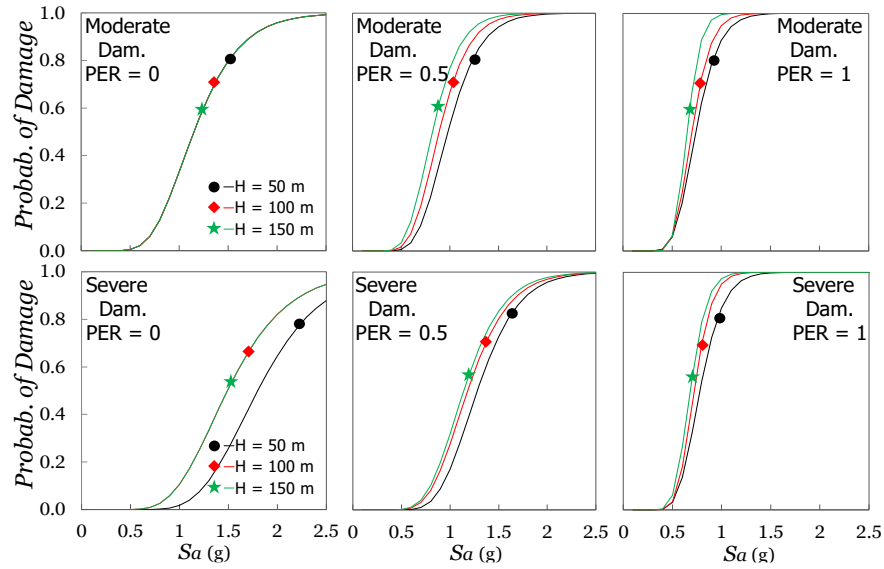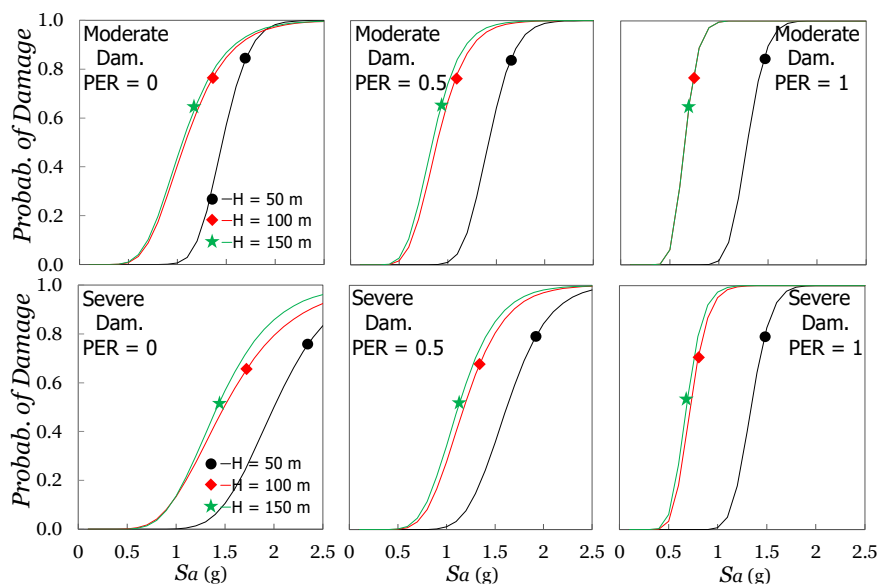*Figure 4.19.* PoD for different H values, $E_c = 30$ GPa, ER
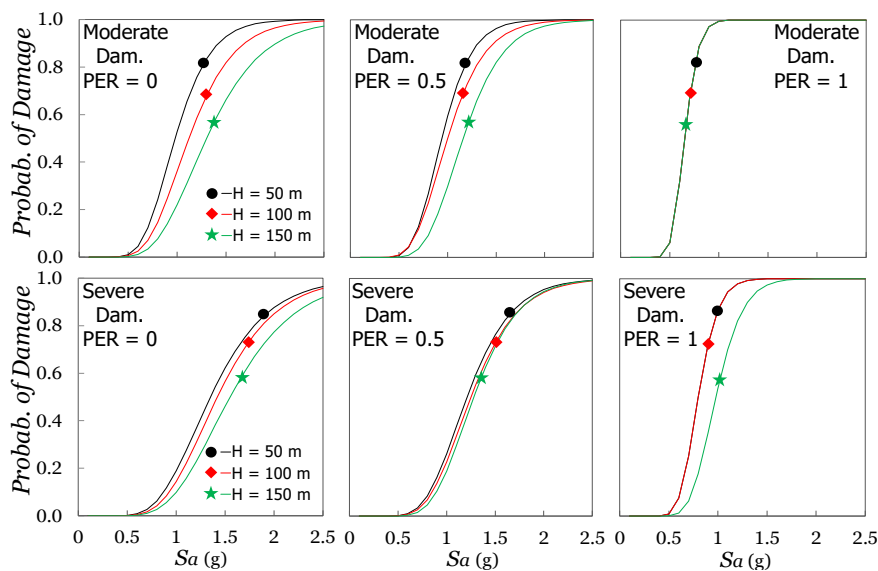
Figure 4.20. PoD for different H values, $E_c = 30$ GPa, FR

The effect of reservoir on PoD are presented in Figure 4.21 and Figure 4.22 for $E_c =$ 20 GPa and 30 GPa, respectively. For the construction of figures, the severe damage level was used along with 3 PER states (PER = 0, 0.5, 1) and 3 dam heights ($H = 50$, 100, 150 m). When PER = 0, all the dams with FR were exposed to higher PoD values for same spectral acceleration level than those with ER. However, when the PER level increased, the dams with ER provided increasingly steeper curves. Such behavior was observed for the dams with both material types and related to the assumptions made in calculation of the post-earthquake effect. As described in Section 4.4, for ER dams, overturning moments were included only due to the post-earthquake loads. However, for FR dams, hydrostatic and uplift forces were also included. For downstream face cracks, the lack of reservoir loads caused the ER dams became more vulnerable for increasing PER.
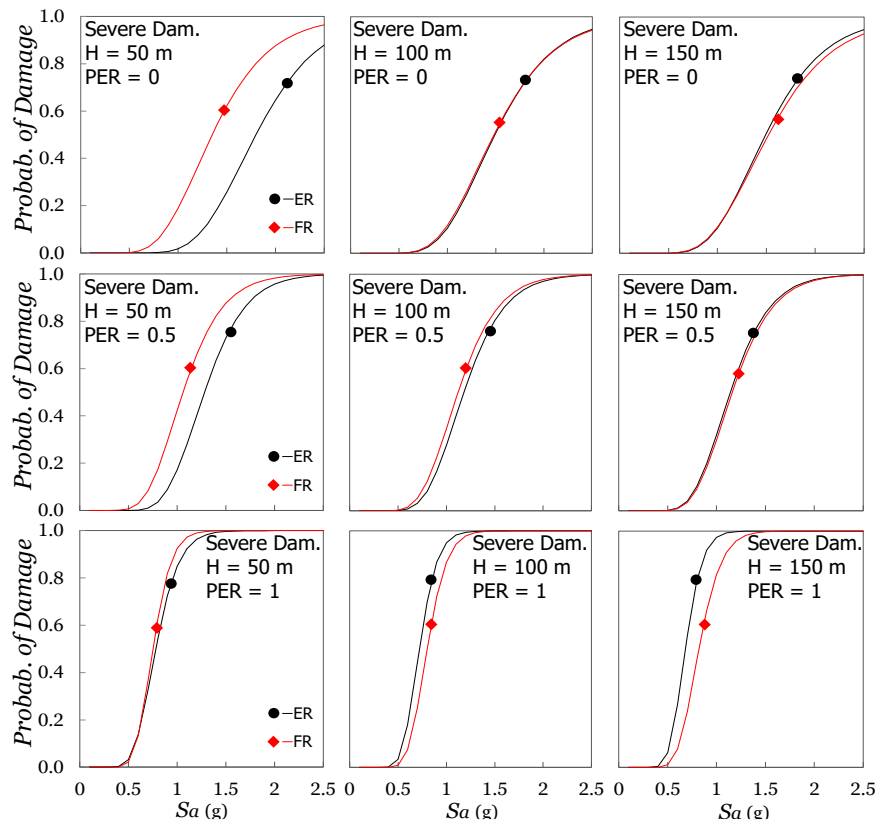
Figure 4.21. PoD for different H values, ER & FR, $E_c = 20$ GPa

131
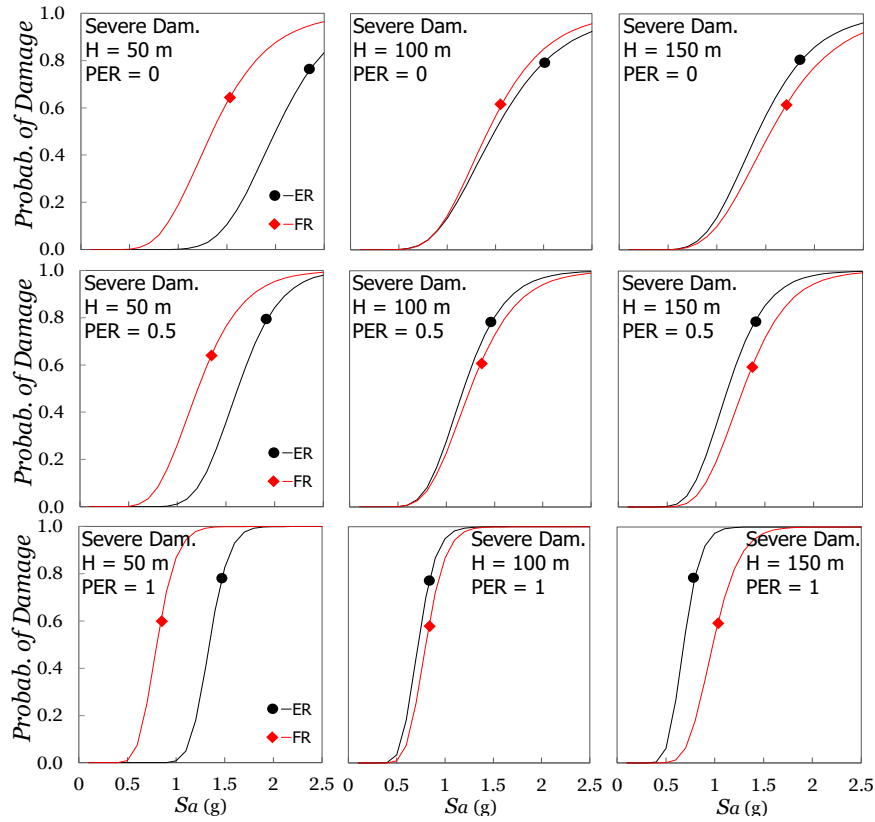
Figure 4.22. PoD for different H values, ER & FR, E_c = 30 GPa

4.5. Stepwise Assessment Method for Concrete Dams

A stepwise method for the seismic vulnerability assessment of concrete dams was described. The method includes the steps necessary for performing a simplified damage assessment based on the information obtained in the previous sections. At the beginning of the method, dam dimensions and cross-sections, material parameters and spectral acceleration level should be determined. The method can be explained step by step as follows:

- Construct a 2D finite element model of the dam section by using any software capable of performing nonlinear pushover analysis with discrete cracking.
- Conduct a modal analysis by employing the finite element model of the dam and the selected material parameters.

132

- Construct a design spectrum (e.g ATC-40 (1996)) to estimate the spectral acceleration level in terms of the spectral acceleration corresponding the fundamental period of the dam model.

- Estimate the crest displacement as the target displacement by using a simplified analysis method (Eq. (3.35) or SDOF Nonlinear THA are recommended).

- Determine the distribution of inertia and hydrodynamic forces on the upstream face of the dam as explained in Chapter 3.3.1.

- Perform a pushover analysis by using the calculated lateral forces in previous step. Using a linear tension softening material model with constant shear reduction factor (e.g $\beta = 0.2$) is recommended.

- Estimate the capacity curve (base shear-crest displacement) of the model along with the corresponding crack response for each displacement step.

- If the cracks are highly scattered, employ a crack length estimation technique similar to explained in Chapter 3.4.1.

- Employ the target displacement and crest displacement-crack length relation to estimate the crack length.

- Repeat the procedure for both upstream and downstream directions to estimate crack lengths.

- Estimate the damage state of the dam by following the instructions explained in Chapter 4.3.

Above steps were completed for a group of dams explained in Chapter 3.3. As an alternative to the above steps, the damage status of the dams can also be determined using the fragility curves given in Chapter 4.5. If the dam parameters are in the limits of this study, one can estimate the probability of damage for a damage state explained in Chapter 4.3. For this case, only design spectrum and fundamental period of the dam model is necessary to estimate the spectral acceleration level. Then it is possible to estimate the PoD values by interpolating the values for selected damage level and the relevant fragility curves.

A case study was selected to illustrate how the conceptual assessment procedure will work. The Koyna Dam, which is an important benchmark in dam engineering, was used to demonstrate the assessment procedure with a full-size concrete gravity dam. Koyna dam is located in India and was severely damaged during the earthquake in 1967. The earthquake had a maximum acceleration of 0.45 g and caused formation of cracks on the upstream and downstream faces of the dam (Chopra, 1972). The dam geometry was taken from those reported in original study. The material properties were adopted from the study of Bhattacharjee (1994). The details of the dam and the actual crack zone are shown in Figure 4.23. The concrete dam was 103 m high and fixed at its base (Figure 4.23). For the material properties of the dam, concrete's elastic modulus, Poisson's ratio, tensile strength, density of the concrete and the fracture energy were 25.0 GPa, 0.20, 1.0 MPa, 2450 kg/m^3 and 200 N/m, respectively. The thickness was 1.0 m with $Q6$ plane stress elements. The density of water and the velocity of pressure waves were taken as 1000 kg/m3 and 1440 m/s. The reservoir height and wave reflection coefficient were taken as 75 m and 1.0, respectively.
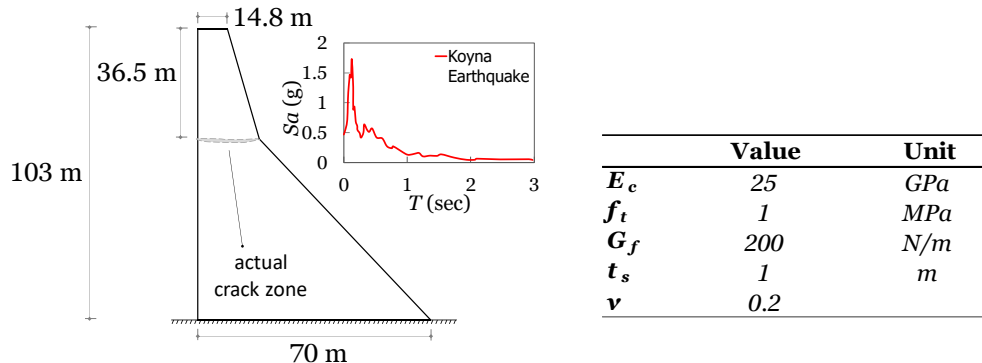
Figure 4.23. Characteristics of Koyna dam

To assess the dam, previously explained steps were followed. The SLA program was used as a finite element tool. First, a modal analysis was conducted. The fundamental period of the dam was 0.385 sec which was also consistent with the value (0.326 sec with E_c = 30 GPa) given by Chopra (1972). Instead of construction of a design spectrum, the acceleration spectrum (%5 damping ratio) of the Koyna earthquake was employed (Figure 4.23). Fema-440 coefficient method (2005) was used to estimate

the crest displacement for its simplicity. By using the equation in Chapter 3.4.3.3, the target displacements for upstream and downstream directions were found as 4.1 cm and 4.0 cm, respectively. Then procedure in Chapter 3.4.1 were performed in both directions by using the calculated lateral forces. In the analyses linear tension softening material model with constant shear reduction factor ($\beta = 0.2$) was employed. The crack response curves (crack length-crest displacement) were estimated in both directions. According to the target displacements, the corresponding crack lengths was found as 14.2 m and 22.4 m for upstream and downstream faces of the dam, respectively (Figure 4.24).
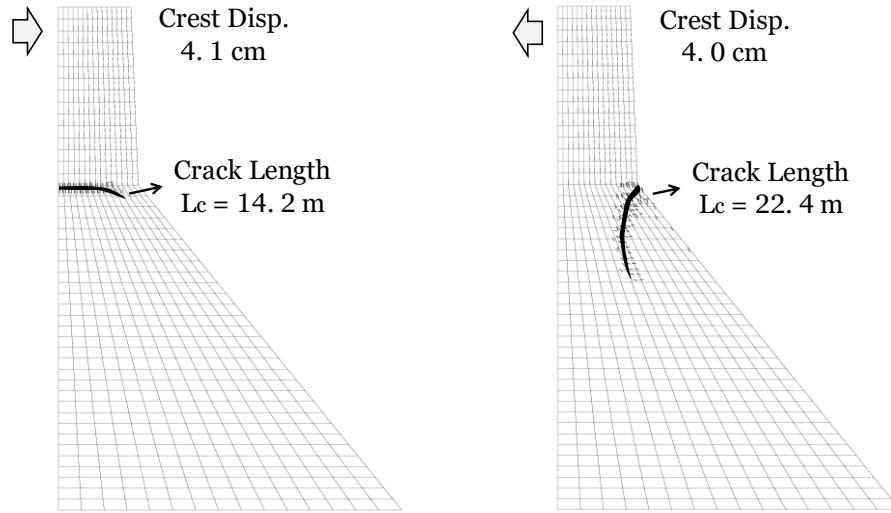
Figure 4.24. Crack patterns for upstream and downstream directions

The damage state of the dam was estimated by following the instructions explained in Chapter 4.3. According to the cracking response, the cracks on both faces of the dam merge along the same section at 65 m level. Such crack response satisfies the condition of the severe damage state. In this case, the Koyna dam exceeded the severe damage level and the it is considered unsafe. By using H = 50 and $E_c = 30$ GPa curves (Chapter 4.4.4) with $S_a = 0.6$ g, Koyna dam exceeded the minimum damage level by 40% probability and the minimum damage level by 10% probability, respectively.

4.6. Final Remarks

For the damage assessment of the dams, 3 different damage states were proposed and called as "minimum damage, moderate damage and severe damage", respectively. The damage states were basically categorized by the crack distribution on upstream and downstream faces of the dams which were also based on the predicted common crack patterns. The damage states were applied to the dams by using the results of 2664 analysis with THA method. They were related to the dam characteristics such as geometry and material type, and seismic properties such as intensity and post-earthquake effect. The post-earthquake effect was included as a moment-curvature relationship by using a simple plain concrete section analysis approach with a linear tension softening. The post-earthquake curvature demand was included as ratio of the earthquake curvature demand and called as Post-Earthquake Ratio (PER). For the PER calculation, the progressive increase in the water pressure on the crack openings was also considered. The effect of water pressure was found to be a significant parameter on growth of new cracks. The performance of the dams was investigated in probabilistic terms. For that reason, the probability of exceedance of the damage states (PoD) were defined as a function of the spectral acceleration levels. For each dam height, material type and reservoir condition, fragility curves were constructed. Additionally, 5 levels of PER (PER = 0 to PER = 1) were included to estimate the effect of post-earthquake. According to the results, PER values did not have a significant effect on fragility curves until the moderate damage state. However, for moderate and severe damage states, increasing the PER level resulted in steeper fragility curves. For ER dams, overturning moments were included only due to the post-earthquake loads. However, for FR dams, hydrostatic and uplift forces were also included. For downstream face cracks, the lack of reservoir loads caused the ER dams became more vulnerable for increasing PER. For smaller dams with ER, increasing the concrete strength usually decreased the potential of the dam to be damaged by an earthquake. Additionally, the effect of PER was more prominent for such dams with lower material rigidity. For smaller dams with FR, the material strength was less

effective on PoD values in compare to the ER dams. An interesting result was that the effect of material strength on the PoD values tended to decrease with increased dam height. For the large dams, the effect of material strength was only significant for the severe damage state. Such behavior was not observed for smaller dams. For the ER case, the increase in the dam height usually increased the PoD values for the same earthquake intensities. However, for the FR case, the fragility curves were steeper for the smaller dams. In this context, among the cases examined, 150 m height dam with ER and 50 m height dam with FR were determined to be the dams with highest risk of earthquake damage. Overall, it was found that such quantitative performance criteria can able to create a perception in terms of seismic response and damaging potential of concrete dams.

CHAPTER 5

CONCULUSION

The purpose of the thesis is to evaluate the seismic behavior and performance of the concrete gravity dams subjected to earthquakes by employing linear and nonlinear analysis techniques. For that reason, simplified analysis techniques were proposed and their results were critically compared with the results of time history analysis, which is considered as the state of art approach for the seismic performance assessment. The thesis mainly divided into three parts which can be summarized as earthquake stresses and effective damping estimation, earthquake deformation and damage estimation and earthquake damage assessment, respectively. All these parts required the use of different tools and methods as well as the different outcomes.

In the first part, it was aimed to estimate the earthquake induced dam stresses for aforementioned dam sections as a function of dam geometry and material parameters. Various analyses were conducted by a simplified method (IFMFM) and an exact method (EM). Their results were employed to evaluate the stress errors upon using massless foundation models with added mass approach along with the apparent damping. These results were also used to drive prediction equations that can estimate the maximum principal tensile stress demand and their distribution along the dam base as well as the effective damping for use in response history analysis in the time domain. According to the results:

- The most significant finding was that the tensile stress distribution at the base was strongly correlated with the E_f/E_c ratio.
- Similarly, the E_f/E_c ratio was found to be the critical variable for the damping ratios of IFMFM and the relationship between inverse of E_f/E_c and damping ratios is almost linear.

- The new damping equation was proven successful, compared to previous numerical tests. However, it should be noted that for higher dams on the soft soil (i.e. 150 m an $E_f/E_c = 0.5$), significantly higher damping ratios can be observed.

In the second part, it was aimed to develop a reliable and effective nonlinear static analysis technique that can accurately estimate the cracking response of concrete dams including the dam-reservoir interaction. For that reason, a method called sequential linear analysis (SLA) was adopted and the capacity curves of the various concrete gravity dams was obtained. The dams were selected as in previous chapter. A technique based on the SDOF approximation of the fundamental mod was employed to calculate total hydrodynamic load and its distribution over upstream face of the dam. Taking advantage of the first mode being dominant, the static pushover analyses were conducted by employing SLA method and their results were compared with ones obtained by nonlinear time history analyses. The capacity curves obtained by SLA and simplified prediction equations were used together to approximately estimate the cracking schemes obtained by THA. At this stage, suggesting an acceptable comparison technique for the highly scattered cracking schemes was a great challenge. THA results were also used to fit equations for estimating the crest displacement and crack length. According to the results:

- It was found that crack patterns can be categorized for different dam types. While, the large cracks observed on the downstream face of the ER dams, they are mostly observed on the upstream face of the FR dams.
- The reservoir condition was the most important parameter of crack formation and location. For crest displacement and crack length estimations, best nonlinear static procedures were SDOF and CM F/440, respectively.
- Although there was not a strong correlation between the crest displacement and the crack length, SLA method still provided promising results to predict cracking behavior of concrete dams. An interesting result was that the intensity

parameters (i.e. HI, ASI) was provided a better correlation with the nonlinear behavior than the parameters such as S_{a1} or PGA.

In the third part, it was aimed to evaluate the structural performance of dams in probabilistic terms. To do that, 3 different damage states were suggested by investigating the crack distributions on upstream and downstream faces of the dams. For this study, the results of THA were employed. For dam types and the intensity parameters described in previous chapter, the fragility curves were constructed by evaluating the probability of exceedance of the damage states (PoD) as a function of spectral acceleration levels. A simplified plain concrete section was used to calculate the post-earthquake effects by following an iterative moment-curvature solution. The post-earthquake effect was considered as ratio of the earthquake curvature demand and called as Post-Earthquake Ratio (PER). According to the results:

- For severe damage state, increasing the PER level resulted in steeper fragility curves for almost all the cases. This was more critical for the FR dams because increase in PER values extended the cracks and increased the internal uplift forces.

- The material strength was affected the PoD values mostly for the smaller dams with ER. For the large dams, the effect of material strength was only significant for the moderate and severe damage states.

- The fragility curves were steeper for the smaller dams with FR and large dams with ER. So, 150 m height dam with ER and 50 m height dam with FR were the dams with highest risk of earthquake damage.

This thesis aims to evaluate earthquake response of the concrete gravity dams within the perspective of widely used practices in literature. For the linear and nonlinear analyses, 2D finite element method has been employed. This is due to the fact that, dams are quite large structures, but in the finite element method, the element size is important and this leads to the creation of numerous elements. However, if the irregular dam geometries and geological conditions are considered 2D and 3D analysis

results may not agree well. If the computational requirements can be met, performing the same analysis in 3D environment may provide more realistic seismic behavior for concrete gravity dams. In the linear analysis part, it found that the most critical parameter on stress evaluation is E_f/E_c ratio. However, in this study, the nonlinear analyses were conducted on fixed foundation by considering the assumption of concrete dams usually built on rock. So, further work may be conducted to understand the effect of dam-foundation interaction on the nonlinear behavior of the concrete gravity dams. Another case is that, the crest displacement and crack length correlation suggested in this thesis could not provide a successful estimation for all the cases. For this reason, it could be better to correlate the crack length with the displacement profile of the dam or the relative displacement of certain points on dam, instead of a single crest displacement. Another development can be achieved by proposing a new procedure for dynamic analysis with SLA method. Such solution can be a competitive alternative to time history analysis for its advantages such as avoiding convergence problems related to tension softening or scattering behavior of discrete cracking approach.

REFERENCES

Akpinar, U., Binici, B. and Arici, Y., 2014. Earthquake stresses and effective damping in concrete gravity dams. Earthq. Struct., 6(3), 251-266.

Alembagheri, M. and Ghaemian, M., 2013. Seismic assessment of concrete gravity dams using capacity estimation and damage indexes. Earthq. Eng. Struct. Dynam., 42, 123-144.

Aldemir, A., Binici, B., Arıcı, Y., Kurc, O., Canbay, E., 2015. Pseudo-dynamic testing of a concrete gravity dam. Earthq. Eng. Struct. Dynam., 44, 1747-1763.

American Concrete Institute, 2005. Building code requirements for structural concrete. ACI 318-05, Farmington Hills, 432 pp.

Arici, Y. and Binici, B., 2011. Seismic safety assessment of Andiraz dam. BAP Report No. 2010-03-03-1-00-20, Civil Eng. Dept., METU, Ankara, TR.

Arrea, M. and Ingraffea, A.R., 1981. Mixed-mode crack propagation in mortar and concrete. Dept. of Structure. Eng., Cornell Univ., Rep. 81-13.

ASCE/SEI, 2010. Minimum design loads for buildings and other structures. American Society of Civil Engineers, 7-10.

ATC-40, 1996. Seismic evaluation and retrofit of reinforced concrete buildings. Applied Technology Council.

Bhattacharjee, S.S. and Leger, P., 1993. Seismic cracking and energy dissipation in concrete gravity dams. Earthq. Eng. and Struct. Dynam., 22(11), 991-1007.

Bhattacharjee, S.S. and Leger, P., 1994. Application of NLFM models to predict cracking in concrete gravity dams. ASCE Struct. Eng., 120, 1255-71.

Bhattacharjee, S.S. and Leger, P., 1995. Fracture response of gravity dams due to rise of reservoir elevation. Journal of Struct. Eng., 121(9), 1298-1305.

Bouaanani, N. and Perrault, C., 2010. Practical formulas for frequency domain analysis of earthquake-induced dam-reservoir interaction. Journal of Eng. Mech., 136(1), 107-119.

Bougacha, S., Roësset, J. and Tassoulas, J., 1993. Dynamic stiffness of foundations on fluid-filled poroelastic stratum. Journal of Eng. Mech., 119(8), 1649-1662.

Carpinteri, A., Valente, S., Ferrara, G., and Imperato, L. 1992. Experimental and numerical fracture modeling of a gravity dam. Fracture mechanics of concrete structures, Z. P. Bazant, ed., CRC, Boca Raton, FL, 351-360.

Chopra, A.K., 1966. Hydrodynamic pressures on dams during earthquakes. Report No. UCB/EERC-66/2-A, Earthq. Eng. Research Center, Univ. of California, Berkeley, CA.

Chopra, A.K., and Chakabarti, P., 1972. The earthquake experience at Koyna dam and stresses in concrete gravity dams. Earthq. Eng. Struct. Dynam., 1(2), 151-164.

Chuhan, Z., Jianwen, P. and Jinting, W., 2009. Influence of seismic input mechanisms and radiation damping on arch dam response. Soil Dynam. and Earthq. Eng., 29, 1282-1293.

Computers and Structures, Inc., 2015. SAP 2000 Nonlinear, Version 18.0.0, Structural Analysis Program, Berkeley, CA.

Cook, R.D., Malkus, D.S., Plesha, M.E. and Witt R.J., 2001. Concepts and applications of finite element analysis. John Wiley and Sons.

Darbre, G.R. and Wolf, J.P., 1988. Criterion of stability and implementation issues of hybrid frequency-time domain procedure for nonlinear dynamic analysis. Earthq. Eng. Struct. Dynam., 16, 569-581.

Dasgupta, G. and Chopra, A.K., 1977. Dynamic stiffness matrices for homogeneous viscoelastic half-planes. Report No. UCB/EERC-77/26, Earthq. Eng. Research Center, Univ. of California, Berkeley, CA.

DeJong, M.J., Hendriks, M.A.N. and Rots, J.G., 2008. Sequentially linear analysis of fracture under non-proportional loading. Eng. Fracture Mech., 75, 5042-5056.

FEMA-356, 2000. Prestandard and commentary for the seismic rehabilitation of buildings. Federal Emergency Management Agency. Washington, DC.

FEMA-440, 2005. Improvement of nonlinear static seismic analysis procedures. Federal Emergency Management Agency. Washington, DC.

FEMA-65, 2005. Federal guidelines for dam safety: earthquake analyses and design of dams. Federal Emergency Management Agency. Washington, DC.

Fenves, G. and Chopra, A.K., 1984. EAGD-84: A computer program for earthquake analysis of concrete gravity dams. Report No. UCB/EERC-84/11, Earthq. Eng. Research Center, Univ. of California, Berkeley, CA.

Fenves, G. and Chopra, A.K., 1985. Simplified earthquake analysis of concrete gravity dams: combined hydrodynamic and foundation interaction effects. Journal of Eng. Mech., 111(6), 736-756.

Fenves, G., Chopra, A.K., 1986. Simplified analysis for earthquake resistant design of concrete gravity dams. Report No. UCB/EERC-85/10, Earthq. Eng. Research Center, Univ. of California, Berkeley, CA.

Hariri-Ardebili, M.A. and Saouma, V., 2015. Quantitative failure metric for gravity dams. Earthq. Eng. Struct. Dynam., 44, 461-480.

Housner, G.W., 1952. Spectrum intensity of strong-motion earthquake. Proceeding of the symposiucm on earthquake and blast effects on structures. Earthq. Eng. Research Institute, 20-36.

ICOLD, 2005. Risk assessment in dam safety management. A reconnaissance of benefits, methods and current applications. Bull. 130.

Javanmardi, F., Leger, P. and Tinawi, R., 2005. Seismic water pressure in cracked concrete gravity dams: Experimental study and theoretical modeling. Journal of Struct. Eng., 131(1), 139-150.

Kormeling, H.A., Reinhardt, H.W., 1983. Determination of the fracture energy of normal concrete and epoxy modified concrete. Tech. rep. 5-83-18. Technical report, Delft Univ. of Technology, Delft, 72, 107.

Kotsubo, S., 1959. Dynamic water pressure on dams due to irregular earthquakes. Mem. Fac. Eng., Kyushu Univ., 18(4), 119-129.

Leger, P. and Boughoufalah, M., 1989. Earthquake input mechanisms for time-domain analysis of dam-foundation systems. Eng. Struct., 11, 37-46.

Leger, P. and Leclerc, M., 1996. Evaluation of earthquake ground motions to predict cracking response of gravity dams. Eng. Struct., 18(3), 227-239.

Lokke, A. and Chopra, A.K., 2017. Direct finite element method for nonlinear analysis of semi-unbounded dam-water-foundation rock system. Earthq. Eng. and Struct. Dynam., 46(8), 1267-1285.

Lotfi, V., Roesset, J.M. and Tassoulas, J.L., 1987. A technique for the analysis of the response of dams to earthquakes. Earthq. Eng. and Struct. Dynam., 15(4), 463-490.

Lotfi, V. and Arabshahi, H., 2008. Earthquake response of concrete gravity dams including dam–foundation interface nonlinearities. Eng. Struct., 30, 3065-3073.

Mclean, P., Leger, P. and Tinawi, R., 2006. Post-processing of finite element stress fields using dual kriging based methods for structural analysis of concrete dams. Finite El. in Analysis and Design, 42, 532-546.

Medina, F., Dominguez, J. and Tassoulas, J., 1990. Response of dams to earthquakes including effects of sediments. Journal of Struct. Eng., 116(11), 3108-3121.

145

NEHRP, 2003. Recommended provisions for seismic regulations for new buildings and other structures. Federal Emergency Management Agency.

Nooru-Mohamed, M.B., Schlangen, E., Mier, J.G.M., 1993. Experimental and numerical study on the behavior of concrete subjected to biaxial tension and shear. Advanced Cement Based Mat., 78(1), 22-37.

Petersson, PE., 1981. Crack growth and development of fracture zones in plain concrete and similar materials. Report TVBM-1006, Division of Building Mat., Lund Institute of Technology, Lund, Sweden.

Rots, J.G., 1988. Computational modeling of concrete fracture. Delft Univ. of Technology, Delft.

Rots J.G., 2001. Sequentially linear continuum model for concrete fracture. Fracture Mech. of Concrete Struct., 831-9.

Saleh, S. and Madabhushi, S.P.G., 2010. An investigation into the seismic behavior dams using dynamic centrifuge modeling. Earthq. Eng., 8, 1479- 1495.

Slobbe, A.T., Hendriks, M.A.N. and Rots, J.G., 2014. Smoothing the propagation of smeared cracks. Eng. Fracture Mech., 132, 147-168.

Soysal, B.F., Binici, B. and Arici, Y., 2016. Investigation of the relationship of seismic intensity measures and the accumulation of damage on concrete gravity dams using incremental dynamic analysis. Earthq. Eng. Struct. Dynam., 45, 719-737.

Simo, J.C. and Rifai, M.S., 1990. A class of mixed assumed strain methods and the method of incompatible modes. Num. Methods in Eng., 29(8), 1595-1638.

Taylor, R.L., Beresford, P.J., and Wilson E.L., 1976. A non-conforming element for stress analysis. Int. Journal for Num. Methods in Eng., 10(121), 1-1219.

Tekie, P.B. and Ellingwood, B.R., 2003. Seismic fragility assessment of concrete gravity dams. Earthq. Eng. Struct. Dynam., 32, 2221-2240.

TNO Diana, 2016. User's Manual, R. 10.1.

USACE, 1995. Seismic design provisions for roller compacted concrete dams. No. EP-1110-2-12, United States Army Corps of Engineers.

USACE, 2003. Time-history dynamic analysis of concrete hydraulic structures. EM 1110-2-6051, United States Army Corps of Engineers.

Von Thun, J.L., Roehm, L.H., Scott, G.A. and Wilson, J.A., 1988. Earthquake ground motions for design analysis of dam. Geotech. Special Publication, 20, 463-481.

Westergaard, H.M., 1933. Water pressures on dams during earthquakes. Trans. of the American Society of Civil Eng., 98, 418-434.

CURRICULUM VITAE

PERSONAL INFORMATION

Surname, Name   : Akpınar, Uğur
Nationality   : Turkish (TC)
Date and Place of Birth : 7 September 1984, Giresun
Phone   : +90 506 490 00 30
E-mail   : e149281@metu.edu.tr

EDUCATION

Degree	Institution	Year of Graduation
MS	METU Civil Engineering	2010
BS	METU Civil Engineering	2008
High School	Mehmet Emin Res. High School, Ankara	2003

WORK EXPERIENCE

Year	Place	Enrollment
2016-Present	Metu Civil Engineering	Civil/Software Engineer
2013 August	HidroDizayn	Project Engineer
2010 August	Metu Civil Engineering	Research Assistant

FOREIGN LANGUAGES

Advanced English

PUBLICATIONS

1. Ozcebe, G., Kurt, E., Binici, B., Kurc, O., Canbay, E. and Akpınar, U. "Performance Comparisons of Seismic Assessment Methods with PSD Test Results of a Deficient RC Frame", ATC-SEI Conference on Improving the Seismic Performance of Existing Buildings and Other Structures, 319-330 (2009)

2. Ozcelik R., Akpinar U., Binici B., "Experimental and Analytical Examination of Deficient RC Frames Retrofitted with Chevron Braces", 14. European Conference of Earthquake Eng., 1-8 (2010)

3. Akpinar U., Ozcelik R., Binici B., "The Effect of Infill Wall on Seismic Performance of Deficient RC Dtructures", Compdyn Conference on Computational Methods in Structural Dynamics and Earthquake Eng., 1-10 (2011)

4. Ozcelik R., Binici B., Akpinar U., "Nonlinear Dynamic Analysis of Structural Steel Retrofitted Reinforced Concrete Test Frames", 5th International Conference on Advanced Computational Eng. and Experimenting, 1-11 (2011)

5. Ozcelik, R., Akpinar, U., Binici, B., "Seismic Retrofit of Deficient RC Structures with Internal Steel Frames", Advances in Structural Eng., 14: 1205-1222 (2011)

6. Akpinar U., Aldemir A., Binici B., "Different Analysis Strategies for RCC Dam Design", 5th International Conference on Advanced Computational Eng. and Experimenting, (2011)

7. Kurt, E.G., Binici, B., Kurc, O., Canbay, O., Akpinar, U., and Ozcebe, G., "Performance of a Seismic Deficient Reinforced Concrete Test Frame with Infill Walls", Earthquake Spectra, 27:817-834 (2011)

8. Ozcelik R., Akpinar U., Binici B., "Nonlinear Dynamic Analysis of Structural Steel Retrofitted Reinforced Concrete Test Frames", Mechanics and Properties of Composed Materials and Structures, 71-82 (2012)

9. Aldemir A., Akpinar U., Arici Y., Binici B. "Seismic Design and Performance of an High RCC Dam", 15th World Conference on Earthquake Eng., (2012)

10. Aldemir A., Akpinar U., Arici Y., Binici B., "Seismic Two and Three Dimensional Nonlinear Dynamic Analysis of an RCC Dam", 10th International Conference on Advances in Civil Eng., (2012)

11. Ozcelik R., Binici B., Akpinar U., "Seismic Retrofit of Non-Ductile Reinforced Concrete Frames with Chevron Braces", Proceedings of the Institution of Civil Engineers-Structures and Buildings, 166: 326-341 (2013)

12. Akpinar, U., Binici B., "The Effect of Infill Wall Collapse on the Deformation Estimations of RC Frames", Journal of Civil Eng. and Science, 2:171-177 (2013)

13. Akpinar U., Aldemir A., Binici B., "Different Analysis Strategies for Roller Compacted Concrete Dam Design", Design and Analysis of Materials and Eng. Structures, 32:117-134 (2013)

14. Akpinar U., Binici B., Arici Y., "Earthquake Stresses and Effective Damping in Concrete Gravity Dams", Earthquakes and Structures, 6:251-266 (2014)

HOBBIES

Computer technologies, movies, sports (walking, exercise, running)